



Bristol Robotics Laboratory

---

PhD Thesis:  
**Towards Tactile Sensing Active Capsule  
Endoscopy**

---

BRISTOL ROBOTICS LABORATORY

UNIVERSITY OF THE WEST OF ENGLAND

NOVEMBER 2017

APPROXIMATELY 39,840 WORDS

*Author:*  
Benjamin A Winstone

*Supervisor:*  
Prof Sanja DOGRAMADZI  
Prof Chris MELHUISH  
Prof Tony PIPE  
Dr Mark CALLAWAY

## Abstract

Examination of the gastrointestinal(GI) tract has traditionally been performed using tethered endoscopy tools with limited reach and more recently passive untethered capsule endoscopy with limited capability. Inspection of small intestines is only possible using the latter capsule endoscopy with on board camera system. Limited to visual means it cannot detect features beneath the lumen wall if they have not affected the lumen structure or colour. This work presents an improved capsule endoscopy system with locomotion for active exploration of the small intestines and tactile sensing to detect deformation of the capsule outer surface when it follows the intestinal wall. In laboratory conditions this system is capable of identifying sub-lumen features such as submucosal tumours.

Through an extensive literary review the current state of GI tract inspection in particular using remote operated miniature robotics, was investigated, concluding no solution currently exists that utilises tactile sensing with a capsule endoscopy. As a result, further investigation was made into tactile sensing technologies, methods of locomotion through the gut, and methods to support an increased power requirement for additional electronics and actuation.

Criteria defined a need for a soft formed sensor and flexible bodied locomotion system. The existing biomimetic tactile sensing device, Tactip, has been redesigned to fit the form of a capsule endoscopy. The cylindrical Tactip has been validated using artificial submucosal tumours in laboratory conditions. Exploring the new form factor and device's ability to detect surface deformation when travelling through a pipe like structure with varying lump obstructions, sensor data was analysed and used to reconstruct the test environment as a 3D render. A second experiment has explored the use of classifier algorithms to successfully discriminate between three tumour characteristics; shape, size and material hardness.

Bio-inspiration has come from earthworm peristaltic locomotion, which share similar operating environments. A soft bodied peristaltic worm robot has been developed that uses a tuned planetary gearbox mechanism to displace tendons that contract each worm segment. Gearbox parameters have been optimised to maximise distance and pull force in a set diameter pipe. Experimentation in a laboratory constructed pipe environment has shown that using only one actuator, three independent worm segments can be controlled. This configuration achieves comparable locomotion capabilities to that of an identical robot with an actuator dedicated to each individual worm segment. These two developments have been integrated to demonstrate successful simultaneous locomotion and sensing to detect an artificial submucosal tumour embedded within the test environment.

Finally, additional sensing and locomotion payload have created a need for additional power beyond what is available from current battery technology. Early stage work has reviewed wireless power transfer (WPT) as a potential solution to this problem. Methods for optimisation and miniaturisation to implement WPT on a capsule

endoscopy have been identified with a laboratory built system that validates the methods found.

This thesis has developed a novel method for sub-lumen examination. With further efforts to miniaturise the robot it could provide a comfortable and non-invasive procedure to GI tract inspection reducing the need for surgical procedures and accessibility for earlier stage of examination. Furthermore, these developments have applicability in other domains such as veterinary medicine, industrial pipe inspection and exploration of hazardous environments.

## Acknowledgements

Foremost, I would I would like to thank the guidance and assistance of my project supervisors; Prof Chris Melhuish, Prof Tony Pipe, Dr Mark Callaway and Prof Sanja Dogramadzi. Despite all their busy schedules, they always made time to offer advice and guidance. I would like to give an extra thank you to Prof Sanja Dogramadzi who spent many hours reading and advising my publications and this thesis, and Dr Mark Callaway who brought both invaluable medical enthusiasm and insight in to the project. In addition, a particular thank you must go to the BRL technician Ian Horsfield for his patience and perseverance to help develop the wireless power transfer system whilst having an especially heavy work load.

I gratefully acknowledge that this work has been made financially possible by the Above and Beyond Research Funding Committee, <http://www.aboveandbeyond.org.uk/> and Severn Deanery <http://www.severn deanery.nhs.uk/>. Without their charitable donation none of this research would have been possible. Furthermore, the University of the West of England have also contributed financially to support this study.

A PhD is not just an intellectual challenge, but also a personal one. Without the patience, understanding and support of family and friends I would not have been able to get beyond my doubts and tackled the hurdles to achieve the results I have. I hope I have made my parents proud, and I dedicate this thesis to them.

# Contents

<b>1</b>	<b>Introduction</b>	<b>11</b>
1.1	The Problem . . . . .	11
1.2	Examination and Diagnosis . . . . .	12
1.2.1	Traditional Endoscopy . . . . .	12
1.2.2	Capsule Endoscopy . . . . .	14
1.2.3	Clinical Value of Capsule Endoscopy . . . . .	16
1.3	The role of palpation in diagnostics . . . . .	17
1.4	Summary . . . . .	19
1.4.1	Research Question . . . . .	19
<b>2</b>	<b>Literature Review</b>	<b>20</b>
2.1	Introduction . . . . .	20
2.2	Existing Research . . . . .	20
2.2.1	Locomotion . . . . .	21
2.2.1.1	Capsule Robots with Off-board Actuation . . . . .	22
2.2.1.2	Capsule Robots with On-board Actuation . . . . .	26
2.2.1.3	Pipe Inspection Robots . . . . .	29
2.2.1.4	Bio-inspired Locomotion Robots . . . . .	31
2.2.1.4.1	Inchworm Locomotion . . . . .	33
2.2.1.4.2	Peristaltic Locomotion . . . . .	34
2.2.1.5	Actuation For Tooling . . . . .	36
2.2.1.6	Actuators . . . . .	38
2.2.2	Wireless Power Transfer . . . . .	39
2.2.2.1	Wirelessly Powered Robots . . . . .	39
2.2.2.2	Health Considerations of WPT . . . . .	42
2.2.2.2.1	Wireless Power Through the Human Body . . . . .	42
2.2.2.2.2	Effect of Magnetic Field on Humans . . . . .	44
2.2.2.2.3	Pathology of Electromagnetic Field Exposure . . . . .	46
2.2.3	Tactile Sensing . . . . .	47
2.2.3.1	The Human Sense of Touch . . . . .	47
2.2.3.2	Existing Tactile Sensors . . . . .	48
2.2.3.3	Biologically Inspired Tactile Sensing - Tactip . . . . .	51
2.2.3.4	Tactile Sensors for Examination . . . . .	51
2.2.3.5	Identifying a Novel Technological Approach to Tactile Sensing . . . . .	55
2.3	Proposal . . . . .	56

2.3.1	Research Objectives . . . . .	58
2.3.2	Considerations of Proposal . . . . .	59
2.4	Work Plan . . . . .	60
<b>3</b>	<b>Tactile Sensing</b>	<b>62</b>
3.1	Introduction . . . . .	62
3.1.1	Technology Selection . . . . .	64
3.2	Proof of Concept Study . . . . .	65
3.2.1	Standard Tactip Design . . . . .	68
3.2.2	Tactip Design and Manufacture Process . . . . .	70
3.3	Methodology . . . . .	71
3.3.1	Cylindrical Tactip Concept - Design Challenges . . . . .	71
3.3.2	Design Solution . . . . .	72
3.3.2.1	Optical System Design . . . . .	73
3.3.2.2	3D Printed Cylindrical Tactip Capsule Design . . . . .	76
3.3.2.3	Limitations of 3D Printing . . . . .	79
3.4	Experiment - Characterisation of Cylindrical Tactip, Lump Detection . . . . .	80
3.4.1	Experiment Hypothesis . . . . .	80
3.4.2	Experiment Design . . . . .	80
3.4.2.1	Sensing Algorithm . . . . .	81
3.4.3	Results . . . . .	85
3.5	Chapter Conclusion . . . . .	86
<b>4</b>	<b>Tactip Data Analysis with Classifier Systems</b>	<b>89</b>
4.1	Introduction . . . . .	89
4.1.1	Hypothesis . . . . .	91
4.2	Review - Classification of Tactile Data . . . . .	91
4.3	Methods for Exploring Classification of Tactip Data . . . . .	92
4.4	Experiment 1 - Cylindrical Tactip Relationship With Force . . . . .	94
4.5	Experiment 2 - Classification of Tactip Interaction with Artificial Tumour Objects . . . . .	96
4.5.1	Experiment environment . . . . .	96
4.5.2	Sensing algorithm . . . . .	98
4.5.3	Classifier systems . . . . .	99
4.6	Results . . . . .	102
4.6.1	Lump detection . . . . .	102
4.6.2	Circumferential lump size . . . . .	103
4.6.3	Lump hardness . . . . .	104
4.6.4	Optimisation . . . . .	105
4.7	Chapter Conclusion . . . . .	106
<b>5</b>	<b>Integration of Capsule Locomotion and Tactile Sensing</b>	<b>108</b>
5.1	Introduction . . . . .	108
5.2	Peristaltic Locomotion Actuator Mechanism . . . . .	110
5.2.1	State Driven Actuator Mechanism . . . . .	111

5.3	Optimising Parameters . . . . .	114
5.3.1	Tendon Offset . . . . .	115
5.3.2	r1:r2 Ratio . . . . .	116
5.3.3	Effeciency Improvement of Gearbox . . . . .	117
5.4	Robot Design - Gearbox Design Test Platform . . . . .	118
5.4.1	Experiment 1 - Force Distribution Test . . . . .	118
5.4.2	Experiment 2 - Locomotion on a Flat Surface . . . . .	119
5.4.3	Experiment 3 - Locomotion Through a Confined Space . . . . .	120
5.4.4	Experiment 4 - Locomotion Through a Confined Space With Pay- load . . . . .	122
5.4.5	Transferring Mechanism Parameters to a Gearbox Drive Mechanism	123
5.5	Integration . . . . .	125
5.5.1	Experiment 5 - Locomotion of Soft-Bodied Peristaltic Robot with Integrated Cyidrical Tactip Tactile Sensor . . . . .	127
5.5.1.1	Locomotion . . . . .	127
5.5.1.2	Sensing . . . . .	128
5.6	Results . . . . .	128
5.6.1	Integration Data Classification Predictions . . . . .	130
5.7	Chapter Conclusion . . . . .	130
<b>6</b>	<b>A Review of Wireless Power for Capsule Endoscopy</b>	<b>134</b>
6.1	Introduction . . . . .	134
6.2	Wireless Power Design Principles . . . . .	135
6.2.1	Circuit Design Principles . . . . .	135
6.2.2	Predicting System Performance . . . . .	136
6.2.3	Exploring Coil Design . . . . .	137
6.2.4	Identifying Requirements For Endoscopy Applicable WPT . . . . .	141
6.3	Proof of Concept Circuit design . . . . .	143
6.3.1	Amplifier Circuit . . . . .	143
6.3.1.1	Class E Amplifier Design . . . . .	145
6.3.1.2	Benchmark of Class E Amplifier Design . . . . .	147
6.3.1.3	WPT Circuit Effeciency . . . . .	148
6.4	Chapter Conclusion . . . . .	149
<b>7</b>	<b>Conclusions</b>	<b>151</b>
7.1	Summary of Research Findings . . . . .	151
7.1.1	Background Issues . . . . .	151
7.1.2	Aims and Objectives Revisited . . . . .	153
7.2	Contributions to Aims and Objectives . . . . .	153
7.2.1	Tactile Sensing . . . . .	153
7.2.2	Classification of Tactip Data . . . . .	154
7.2.3	Locomotion . . . . .	154
7.2.4	Wireless Power . . . . .	155
7.3	Limitations of this Study . . . . .	156

7.4	Future Work . . . . .	157
<b>Appendices</b>		<b>160</b>
<b>Appendix A Wireless Power Principles</b>		<b>161</b>
A.1	Electromagnetic equations . . . . .	161
A.1.1	Magnetic Field Strength . . . . .	161
A.1.2	Magnetic Flux Density . . . . .	163
A.1.3	Magnetic induction . . . . .	165
A.1.4	Transformer theory . . . . .	166
A.1.5	Mutual Inductance . . . . .	168
A.2	Circuit Design Principles for Wireless Power . . . . .	169
A.2.1	Circuit principles . . . . .	169
A.2.1.1	Impedance . . . . .	170
A.2.1.2	Resonance . . . . .	172
A.2.1.3	Frequency . . . . .	173
A.2.2	Component Calculations . . . . .	175
A.2.2.1	Basic circuit design . . . . .	175
A.2.2.2	Resistance of a coil . . . . .	175
A.2.2.3	Inductance of a coil . . . . .	176
A.2.2.4	Calculating the tuning capacitance . . . . .	177
A.2.2.5	Reflected Load . . . . .	178
A.2.2.6	Equivalent T Circuit Linear Transformer . . . . .	178
A.3	Estimating The Effect of Solenoid Parameters on Efficiency . . . . .	179
A.3.1	Estimating The Effect of Distance on emf . . . . .	179
A.3.2	Estimating Maximum Achievable Efficiency . . . . .	180
A.4	Class E Amplifier Design Equations . . . . .	182
A.5	Class E Amplifier Ver 2.0 Schematic Design . . . . .	185

# List of Figures

1.1	Main components of the gastrointestinal(GI) tract . . . . .	12
1.2	Endoscopy videoscope system. . . . .	13
1.3	Givenimaging PillCam . . . . .	15
1.4	Comparison of images taken by PillCam and Endocapsule . . . . .	15
2.1	Typical cross section of the gut, showing the structure of the gut wall. . .	21
2.2	Honda et al 1996, helix and magnet microrobot . . . . .	22
2.3	Spiral helix around capsule, Sendoh et al 2003 . . . . .	23
2.4	Microassembled robot, Yesin et al 2006 . . . . .	23
2.5	Mathieu et al 2006, magnetic propulsion of microrobot inside MRI machine	24
2.6	Yi et al 2004, ferromagnetic polymer actuation . . . . .	24
2.7	Dreyfus et al 2005, linear chain of colloidal magnetic particles linked by DNA . . . . .	25
2.8	Guo et al 2007, wireless swimming microrobot . . . . .	25
2.9	Quirini et al. 2008 legged capsule design . . . . .	26
2.10	Carta et al. 2008 capsule design . . . . .	27
2.11	Wireless powered miniature robot for colon inspection . . . . .	27
2.12	Chen et al. 2013 Spiral legged robot for colon inspection . . . . .	28
2.13	Norton et al. 2016 RollerBall robot for intraluminal locomotion . . . . .	28
2.14	Diagram demonstrating inchworm locomotion. . . . .	32
2.15	Diagram demonstrating earthworm peristalsis [1]. . . . .	33
2.16	Inchworm robot based on Chen 2013 . . . . .	34
2.17	Peralstaltic worm robot, Boxerbaum 2012 . . . . .	35
2.18	Woods et al. 2013 capsule endoscopy with actuated needle . . . . .	37
2.19	Yim et al. 2013 capsule endoscopy with magnetically actuated micro- grippers . . . . .	38
2.20	Kosa et al 2008, steerable swimming microrobot for the MRI . . . . .	41
2.21	Cross section of glabrous skin . . . . .	48
2.22	BioTac cross section . . . . .	49
2.23	TACTIP, bio-inspired tactile sensing device. . . . .	52
2.24	Schostek et al. 2006 tactile laproscopic tool . . . . .	53
2.25	Roke et al. 2013 tactile laproscopic tool . . . . .	54
3.1	Tactile sensing capsule endoscopy. . . . .	67
3.2	Tactip demonstrating lump detection. . . . .	67
3.3	Average shading algorithm presented by Roke et al. 2011 [2] . . . . .	68
3.4	Blob detection algorithm presented by Assaf et al. 2014 [3] . . . . .	69

3.5	Texture discrimination experiment presented by Winstone et al. 2013 [4]	70
3.6	Tactip mould assembly.	71
3.7	Catadioptric panoramic mirrors	73
3.8	Cylindrical Tactip design.	74
3.9	View of cylindrical Tactip presented by catadioptric panoramic lens mirror.	75
3.10	Relationship between physical papillae pins and the columns and rows reference in the machine vision analysis	76
3.11	Relative pixel to distance ratio for radial and axial movement of pins	76
3.12	Complete 3D printed cylindrical Tactip skin.	77
3.13	Cross section view of tactip capsule assembly.	78
3.14	Exploded arrangement of cylindrical Tactip capsule endoscopy design.	79
3.15	View of fractured 3D printed skin.	80
3.16	Experiment setup, ABB IR120 pushing tactile sensing through rigid tube containing raised lumps.	82
3.17	Raw camera image showing calibration state and example contact with lump	82
3.18	Unwrapped 360° panoramic image capture with identified pin positions.	83
3.19	Localised group of pins subjected to skin contact showing the pins within the contact region separate.	83
3.20	Location of maximum pin separation and angular position along length of test pipe.	84
3.21	3D reconstruction of test environment built from data captured by the cylindrical Tactip sensor.	86
4.1	Range of test lumps used	93
4.2	Maximum deflection distance.	94
4.3	Experiment setup for characterisation of sensor force to pin displacement relationship.	94
4.4	Pin displacement against known force and lump shape	95
4.5	Pin displacement hysteresis.	96
4.6	Raw camera image showing calibration state and unwrapping of the image	97
4.7	Vector representation of pin displacement	98
4.8	Localised group of pins subjected to skin contact showing the pins within the contact region separate.	99
4.9	Examples of contact with each of the three lump sizes	100
4.10	Example of the effects of lump size and shape on sensor data used as input to classifier system.	101
4.11	Example of test lump in relation to lump coverage classification	102
4.12	Example of all 3 soft test lump pieces	104
4.13	Visualisation of the optimised classifier input data format	106
5.1	Phased linear tendon pull with single rotary actuator.	111
5.2	The Effect of Radii Ratio on Resulting Loci Path	113
5.3	General arrangement of planetary gearbox.	114

5.4	Varying to distance of tendon release point 'a'. . . . .	115
5.5	Comparison of effective clamping period when varying tendon offset in gearbox mechanism. . . . .	116
5.6	Comparison of ideal, simple armature and planetary gearbox produced waveforms. . . . .	117
5.7	Experimental peristaltic worm platform. . . . .	118
5.8	Force distribution experiment arrangement. . . . .	118
5.9	Force distribution results graph. . . . .	119
5.10	Tracked loci of worm skin segment apex. . . . .	120
5.11	Side view of experiment tunnel with worm robot. . . . .	121
5.12	Front view of experiment tunnel. . . . .	121
5.13	Front view of worm robot showing the gearbox mechanism made from two connected counter rotating gears. . . . .	124
5.14	Side view of the robot worm design. . . . .	124
5.15	3D printed worm robot with the gearbox that drives optimised peristaltic worm locomotion. . . . .	125
5.16	CAD model of integration of locomotion and sensing modules. . . . .	125
5.17	Built assembly of integrated of locomotion and sensing modules. . . . .	126
5.18	Integrated robot assembly inside test environment with addition of artificial tumour lump. . . . .	126
5.19	Total row deformation whilst traveling through test environment driven by the peristaltic worm locomotion robot developed in chapter 5 . . . . .	129
5.20	Row data after a high-pass Butterworth filter has been applied . . . . .	130
5.21	3D plots of individual papillae pin movement throughout experiment period for each of the 5 captured rows . . . . .	131
5.22	Lump predictions from integration data passed to classification systems used in previous experiments. . . . .	133
6.1	Measured against calculated mutual inductance of two identical ten turn $13.3\mu H$ coils. . . . .	136
6.2	Demonstration of the effect of both k and Q on system efficiency. Broken lines represent U and solid lines represent $\eta$ . . . . .	137
6.3	Demonstration of the effect of solenoid parameters on Q and inductance. . . . .	139
6.4	Demonstration of the effect of solenoid parameters on mutual inductance at various distances of separation. . . . .	140
6.5	Four coil high-Q resonant circuit diagram . . . . .	141
6.6	Comparison of performance between non-resonant, low-Q resonant and high-Q resonant power transfer system taken from [5]. . . . .	142
6.7	Circuit diagram of initial WPT prototype powered directly from signal generator. . . . .	143
6.8	Left: Close up of WPT coil arrangement. Right: Experiment set up showing the coils, signal generator and oscilloscope. . . . .	143
6.9	Typical Class E amplifier circuit. . . . .	144

6.10	Left: Class E power amplifier prototype circuit. Right: Class E power amplifier PCB circuit . . . . .	145
6.11	Class E power amplifier design schematic. . . . .	146
6.12	WPT system powering a 3W light bulb. . . . .	147
6.13	Axial scan of power transfer from 40mm to 120mm separation. . . . .	148
6.14	Axial scan of power transfer from 40mm to 140mm separation. . . . .	148
6.15	WPT efficiency scan 20mm to 130mm coil separation . . . . .	149
A.1	Example magnetic field . . . . .	162
A.2	Biot-Savart current loop . . . . .	163
A.3	Solenoid magnetic field . . . . .	164
A.4	Permanent bar magnet moving through an induction coil . . . . .	165
A.5	Primary coil produces emf voltage in secondary coil. . . . .	166
A.6	Fundamental formation of a transformer. . . . .	167
A.7	RCL primary circuit. . . . .	170
A.8	Voltage phase difference between AC components. . . . .	170
A.9	Total reactance is the sum of all reactance vectors. . . . .	172
A.10	The peak values symbolise the resonant frequency of a specific combination of capacitor and inductor. . . . .	173
A.11	Simple air cored transformer circuit. . . . .	175
A.12	Reflected Load. . . . .	178
A.13	Reflected Load. . . . .	179
A.14	Estimated emf output over a range of distances. . . . .	180
A.15	Primary resonant circuit load over frequency range. . . . .	181
A.16	Class E power amplifier schematic version 2. . . . .	185

# List of Equations

3.1	Tactip capsule pixel translation . . . . .	83
5.1	Tendon displacement 'h', simple armature scenario . . . . .	111
A.1	Magnetic field strength, H . . . . .	162
A.2	Magnetic flux density of a current loop, B . . . . .	163
A.3	Magnetic flux density of a solenoid, B . . . . .	164
A.4	Magnetic flux, $\Phi$ . . . . .	164
A.5	Electromotive force, emf $\xi$ . . . . .	165
A.6	Permeability of free space, $\mu_o$ . . . . .	167
A.7	Transformer voltage to turn ratio . . . . .	167
A.8	Mutual inductance, M . . . . .	168
A.11	Coeffecient of coupling, k . . . . .	169
A.14	Capacitive reactance, $X_c$ . . . . .	171
A.15	Inductive reactance, $X_l$ . . . . .	171
A.17	Impedance, Z . . . . .	172
A.18	Resistance of coil, R . . . . .	175
A.20	Inductance of coil, L . . . . .	176
A.27	Tuning capacitance, C . . . . .	178
A.28	Reflected load, $Z_R$ . . . . .	178
A.30	Figure of merit, U . . . . .	180
A.31	Quality factor, Q . . . . .	181
A.32	Maximum achievable efficiency, $\eta_{opt}$ . . . . .	182
A.33	Class E amplifier equations . . . . .	182

## List of Related Publications

- B. Winstone, C. Melhuish, and S. Dogramadzi, A Novel Bio-inspired Tactile Tumour Detection Concept for Capsule Endoscopy, in Biomimetic and Biohybrid Systems: International Conference, Living Machines, pp. 442-445, 2014.
- B. Winstone, Biomimetic Tactile Sensing Capsule, In Biomimetic and Biohybrid Systems: International Conference, Living Machines, pp. 113-122, Springer, 2015.
- B. Winstone, C. Melhuish, T. Pipe, M. Callaway, and S. Dogramadzi, Towards Bio-inspired Tactile Sensing Capsule Endoscopy for Detection of Submucosal Tumours, IEEE Sensors Journal, no. c, pp. 848-857, 2017.
- B. Winstone, T. Pipe, C. Melhuish, M. Callaway, A. C. Etoundi, and S. Dogramadzi, Single motor actuated peristaltic wave generator for a soft bodied worm robot, Proceedings of the IEEE RAS and EMBS International Conference on Biomedical Robotics and Biomechatronics, vol. 2016-July, pp. 449-456, 2016.

## List of Formative Publications

- B. Winstone, G. Griffiths, C. Melhuish, T. Pipe and J. Rossiter, "TACTIP - Tactile fingertip device, challenges in reduction of size to ready for robot hand integration," 2012 IEEE International Conference on Robotics and Biomimetics (ROBIO), Guangzhou, 2012, pp. 160-166.
- Winstone, B. et al., 2013. TACTIP - Tactile Fingertip Device , Texture Analysis Through Optical Tracking of Skin Features. In Biomimetic and Biohybrid Systems: International Conference, Living Machines. pp 323-334

The following introductory chapter will discuss the importance the problems encountered during internal examination and diagnostic procedures of the human body. With these problems identified, both current solutions will be considered along side ideas for potentially more effective solutions. In particular a focus is made towards the use of miniature robotics that can be operated remotely to perform tasks similar to endoscopy tools, but without the discomfort for the patient limitations of access.

### **1.1 The Problem**

The term GI tract describes the main organs of the digestive system. These include oesophagus, stomach, small intestine, cecum, colon and rectum, see Fig.1.1. The GI tract is a crucial part of the human working system and so any problems that occur in the GI tract can potentially lead to life threatening situations if left untreated. The full extent of the GI tract offers a diverse range of environmental conditions, which contribute to the difficulty in minimally invasive examination. In particular one should consider the varying levels of viscosity and muscular tension applied to the GI tract when identifying a method for an endoscopic tool to travel from entrance through to a desired location. Endoscopy plays an important role in the diagnosis of premalignant conditions of the oesophagus. Early diagnosis of premalignant conditions provides opportunity to prevent or diagnose oesophageal cancers.

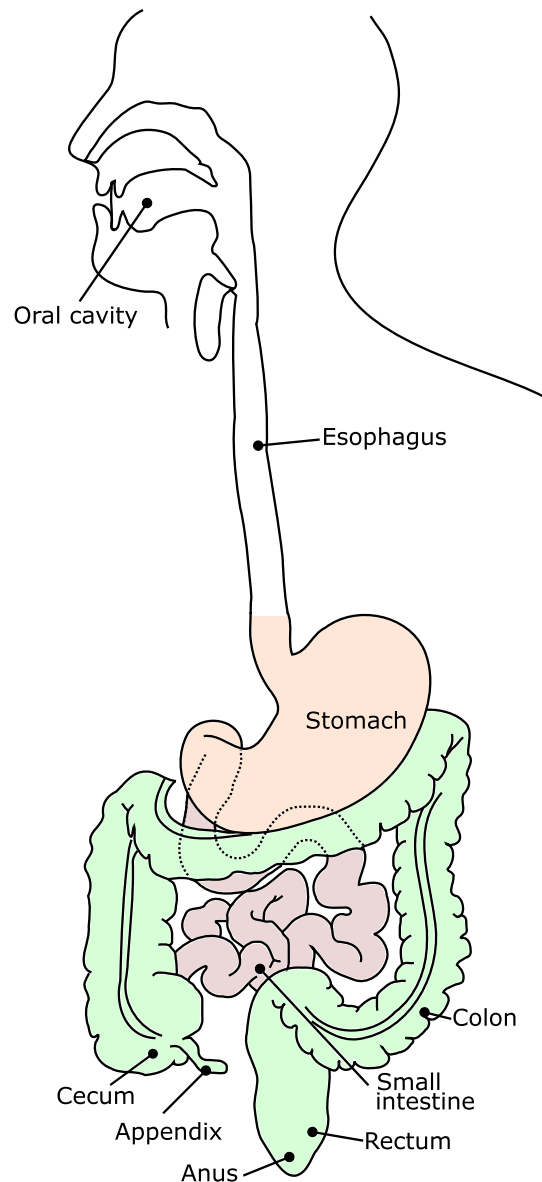


Figure 1.1: Diagram showing the main components of the gastrointestinal(GI) tract.

## 1.2 Examination and Diagnosis

### 1.2.1 Traditional Endoscopy

Endoscopy is the process of looking inside the body using an endoscope. Endoscopes are rigid or flexible tubes that use fibre-optics or cameras to visualise tissues in natural orifices, see Fig.1.2. There are a number of different endoscopy procedures that target different areas of the body, however gastroscopy and colonoscopy are the most common.

Examination of the GI tract has traditionally been performed using endoscopy tools that allow a surgeon to see the inside of the lining of the digestive tract, typically called

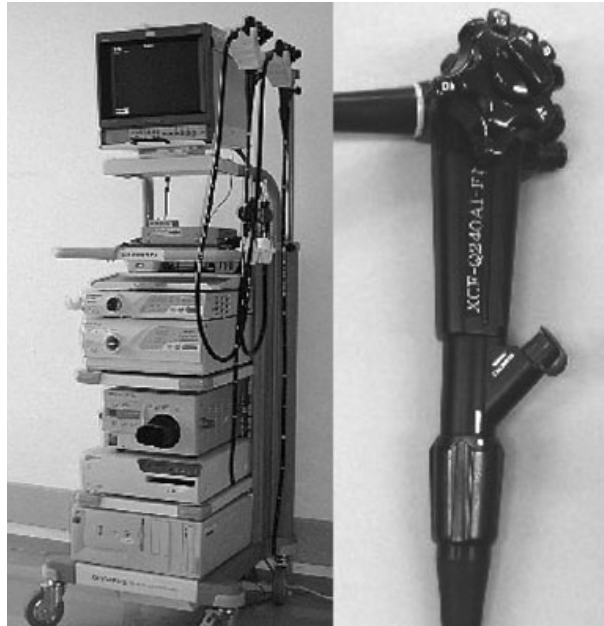


Figure 1.2: Endoscopy videoscope system. With permission of John Wiley and Sons, Japan Gastroenterological Endoscopy Society, Newly Developed Autofluorescence Imaging Videoscope System For The Detection Of Colonic Neoplasms, June, 2005, 235-240, Nakaniwa et al. [6]

esophagogastroduodenoscopy. This practice is indicated for a number of pathologies such as suspected gastrointestinal bleeding, dysphagia (difficulty swallowing), suspected gastrointestinal ulceration and malignancy. Further to direct visualisation, a biopsy can be taken for histological examination of the tissue, further aiding diagnosis. Following on from diagnosis the endoscope can be used for a number of interventions including surgery, removal of foreign bodies and injection therapy (localised delivery of pharmaceuticals).

Endoscopy can be an uncomfortable and very invasive procedure for the patient. Complications encountered during endoscopy procedures are very infrequent, however it is possible that perforation and tearing can occur and from this bleeding may start at the site of damage. Some endoscopy procedures may require anaesthetic due to the discomfort levels of the patient, which will later require a recovery period after the procedure in order for the anaesthetic to wear off. Other effects of an endoscopy procedure are minimal, possibly leaving some temporary pain due to minute bruising but the patient should be fully recovered and able to continue with normal activities within 24 hours. Compared to invasive surgery, endoscopy procedures are low impact both physically and financially.

The procedure does have limitations with regard to reach. The alimentary canal in an adult is approximately 5m long and consists of several flexures and valves, making the passage of an endoscope cumbersome and limited by length. For this reason the distal portion of the small intestine, consisting of the distal duodenum and jejunum, is beyond the reach of traditional endoscopes, making diagnosis via observation at this location difficult.

With regard to advanced endoscopic procedures typically used on the upper GI tract, endoscopic retrograde cholangiopancreatography (ERCP) combines the use of an endoscope with fluoroscopy, where by radiographic contrast is injected in to a targeted area identified with the endoscope. This radiographic contrast is then observed using X-ray imaging, and the movement of the contrast indicates the condition within the patient. Recent development of the magnetic resonance cholangiopancreatography (MRCP) typically replaces this procedure for its minimally invasive nature. Another alternative which also mostly focuses on the upper GI tract, but occasionally on the lower also, is endoscopic ultrasound. Endoscopic ultrasound combines endoscopy with ultra sound imaging to obtain internal images in the chest and abdomen.

### 1.2.2 Capsule Endoscopy

Capsule endoscopy describes a swallowable capsule with self contained microsystem, similar to a traditional drug delivery capsule. This capsule provides a platform to achieve similar procedures to more traditional methods of endoscopy but without the restrictions of a tethered system. The idea of swallowing a small capsule with an internal sensing system that can communicate to outside of the body goes as far back as 1957 when R. Stuart Mackay presents the idea of RF transmission of the temperature and pressure within the human body [7]. Limitations of technology at the time did not allow for practical development of such a device, but with modern advances in digital, RF and materials technology a complex and capable capsule system is feasible. Later in 1998 NASA registered a patent with John Hopkins University that describes a swallowable pill that transmits the internal temperature of the body for use in monitoring astronauts during space expeditions. An obvious ambition of a swallowable capsule is to perform and transmit imaging from inside the body. Wireless capsule endoscopy (WCE) is a passive imaging system in the form of a large pill swallowed by the patient to inspect the GI tract by use of an internal imaging camera. In addition to a camera, the capsule

also requires suitable lighting to assist in image acquisition. A capsule endoscopy allows a more comfortable examination for the patient through the entire GI tract, and can perform examination past the reach of traditional endoscopy.



Figure 1.3: PillCam Courtesy of [8]. ©2016 IEEE

PillCam capsule endoscopy [9] is a commercial product used within the medical industry as a minimally invasive endoscopy tool, see Fig.1.3. The pill is swallowed by the patient and an internal camera records the journey through the GI tract. The PillCam measures 26mm in length and 11mm in diameter, transmits images at between two and eight frames per second which are downloaded to a receiver carried by the patient. The device is powered by silver oxide batteries able to last over five hours of recording.

A currently less popular but more recent entrant to the commercial market is the Olympus EndoCapsule, [10]. At first look, both the PillCam and EndoCapsule are very similar devices, however Cave et al. have compared the two systems in clinical trials concluding that the EndoCapsule produces better imaging due to more sufficient lighting and high quality cameras, [11], see Fig. 1.4.



Figure 1.4: Comparison of images taken by PillCam and Endocapsule respectively. Reprinted from *Gastrointestinal endoscopy*, 68/3, Cave et al, "A multicenter randomized comparison of the Endocapsule and the Pillcam SB.", 487-94, 2008, with permission from Elsevier, [11].

Spada et al. report a case study [12] identifying the advantages of the PillCam over traditional endoscopy. The work concludes that the PillCam can be a feasible and

safe diagnostic tool, and may represent an alternative in cases of difficult or incomplete colonoscopies. Triantafyllou et al. [13] evaluate whether WCE can achieved complete colon examination after failure of conventional colonoscopy to visualise the caecum. Of twelve patients with previous failed colonoscopy, six were also unsuccessful in achieving complete examination with WCE. Their findings conclude that the incomplete WCE examination was due to reasons such as tumour growth protruding from the lumen wall or foreign bodies not removed during the preparation procedure.

Capsule endoscopy suffers from three problems: Firstly, it is a passive device with lack of human control, which means that the route and direction is subject to peristalsis action of the gut. This can lead to the camera potentially missing problem areas presenting incomplete or misleading diagnosis. The second problem is that due to the size restrictions, battery capacity has to be limited. Finally, the third problem is that it is purely for diagnostics and has no treatment capabilities.

The surgical robotics group, part of the bio robotics institute at Polo Sant'Anna Valdera, Italy, have made great effort in understanding the requirements and suggesting solutions for capsule endoscopy. Menciassi et al. [14] acknowledge that although there have been great developments in laparoscopic robot surgery, endoscopic robot technology has fallen behind. Endoscopic capsules exist, but they are passive and do not meet the standard of a micro-robot with substantial autonomy. They have also reviewed many attempts at developing an effective actuation method for wireless endoscopy, concluding that forces required to achieve locomotion are not trivial and batteries of appropriate size are inadequate in capacity for the power requirements of locomotion. This suggests that wireless power induction may be able to generate and maintain power requirements for this kind of locomotion.

### 1.2.3 Clinical Value of Capsule Endoscopy

As mentioned earlier, the benefit of the capsule endoscopy lies in its ability to view the small bowel beyond the duodenum and proximal to the colon. There are a number of pathologies that can occur in the small bowel, such as tumours, strictures and ulceration as part of an inflammatory bowel condition such as Crohn's disease. Currently capsule endoscopy is indicated for obscure gastrointestinal bleeding that has not been explained using traditional endoscopy.

To explore the relative usefulness of capsule endoscopy in clinical practice, its role

in diagnosing Crohn's disease in patients who are symptomatic of the disease, but who have not been diagnosed following traditional endoscopy are considered. Crohn's disease is an inflammatory bowel condition that can occur anywhere along the alimentary canal, with ulcers that can perforate the lining of the bowel and cause bleeding. A study, by De Bona et al [15], looked into the use of capsule endoscopy for the diagnosis of Crohn's disease. The study contained 38 patients with suspected Crohn's disease not diagnosed with colonoscopy. The capsule endoscopy resulted in 13 diagnoses of Crohn's, thus demonstrating the high diagnostic yield of the technology. A study, by Chong et al [16], sought to compare the capsule endoscopy with push enteroscopy and enteroclysis for the diagnosis of Crohn's disease in patients with traditional endoscopy and colonoscopy. The capsule endoscopy identified a greater number of erosions, which are indicative of Crohn's, and produced a similar diagnostic yield compared to the other two investigations.

It thus seems that capsule endoscopy is of real clinical benefit in terms of establishing a diagnosis. One area of further investigation is the long term benefit of earlier diagnosis using capsule endoscopy, both in patient outcome and in terms of economic factors. Capsule endoscopy is currently more expensive than traditional endoscopy and much less widely available. If the system is to be introduced to more hospitals, it is likely that a financial benefit to its use would form the basis for any argument for its introduction. Future studies may also wish to look at the use of capsule endoscopy for conditions not currently indicated for by NICE guidelines [17], with the hope of adding weight to its value.

### **1.3 The role of palpation in diagnostics**

Shi et al. [18] discuss the importance of the GI tract motility and how failings in motility can be an indication of more serious GI diseases. Shi presents a sensing capsule to measure pressures encountered through the journey of the GI tract as an indication of GI tract motility. Direct contact sensing has long been a common practice for diagnosis in the vast majority of medical fields. Cox et al. [19] explained why skin palpation is important and presents reassurance to the patient but is also an underestimated examination of motility that identifies tenderness, consistency, induration, depth and fixation. Palpation of skin is used to identify strained muscles, skeletal breaks and

deformed growths amongst other signs of ill health. Tactile sensing and palpation are included in the medical training.

In 2011 Kume et al. [20] investigated development of an articulated robotic endoscopic tool. Although articulation showed evidence of easing the challenge of insertion, they clearly state that force and tactile feedback in an endoscopy tool would limit unintended application of excessive insertion force. Further support for tactile sensing in remote surgical systems is discussed by Chaudhary et al. [21]'s review of medical robotics as a current technology.

”Surgical robots also increase the scope and effectiveness of MIS as key advantages of robotic surgery include the requirement of small incision, high accuracy and ability to repeat identical motions, less pain, less scarring, less bleeding, lower risk of infection, shorter hospital stays, quicker recovery time and return to normal activities, 3D vision, motion scaling, fluid movement, wrist articulation capability, remote sensing technology, tremor filtering, ergonomically intuitive sensing, 25 times more magnification, multiple instruments entrance system, haptic feedback and tele-surgery with tele-proctoring and it also has some limitations including absence of tactile or haptic information, surgeon’s judgment, high cost and not being able to use qualitative information.”

Chaudhary clearly feels that tactile and haptic sensing are key features lacking in today’s robotic medical technology. Whilst this statement refers to MIS and not endoscopy technology it is considered that there is an overlap in context regarding the natural environment and safety requirements. Laparoscopic tooling must enter confined delicate orifices with only the guidance of cameras located at the end of the tool and kinaesthetic feedback through the tool itself. Standard endoscopy uses only one tool with a vision system at the tip and vague kinaesthetic feedback from the winding elastic structure of the gut. The addition of force and tactile feedback would greatly enhance the accuracy in force application of and direction of an endoscopy tool.

With the development of haptic technology the opportunity for remote palpation is becoming increasingly feasible. It could be possible for a midwife to assess the orientation of a pregnancy whilst being in another location, or an orthopaedic surgeon to gauge the severity of a broken bone before arriving to treat the patient. Furthermore this technology could create entirely new opportunities for internal tissue remote palpation.

When considering the idea of tactile sensing inside the body it becomes apparent

that normal restrictions such as scale no longer exist. Whilst typically when a medical practitioner palpates a patient the scale ratio between their hands and the patient is 1:1. They are bound to the sensitivity of their fingertips and kinaesthetic feedback. If a robot were small and sensitive enough it could be possible to identify a higher fidelity of information than currently achieved by human hands alone. For example, polyps are early indications of a tumour but they start very small with little discrimination from normal healthy tissue until the cancer progresses further and harder tissue forms. If technology were capable it would be feasible to sense these smaller indications of a tumour and scale up the feedback such that human hands can feel and discriminate between healthy and early stage non healthy tissue.

This concept is new within the research field, and whilst examples exist within tethered and predominantly laparoscopic tooling, nothing yet exist developing a wireless capsule with tactile sensing and palpating capabilities.

## **1.4 Summary**

This introductory chapter has highlighted the limitations of current diagnostic technology used inside the body. In particular capsule endoscopy overcomes many limitations encountered by endoscopy systems but at the cost of losing control of direction and integration of any additional tooling. Gaining access to these hard to reach regions of the body provides opportunity to implement further examination procedures, such as tactile exploration, if the technology were developed to enable this. Furthermore, the importance of tactile information used in diagnosis has been highlighted. This raises the following research question;

### **1.4.1 Research Question**

Can an untethered tele-operated robot endoscopy be deployed inside the body to obtain tactile information from the intestinal tract that could lead to a greater understanding of tissue health beyond that of current technologies used?

#### **2.1 Introduction**

The following chapter will review the current technology and research relating to the problems and ideas raised in Chapter 1. The outcome of this review will identify areas of high need and or novelty within the problem space, leading to a proposal of further investigations and development of a final solution. The following review will cover locomotion, power and sensing technologies applicable to capsule endoscopy.

#### **2.2 Existing Research**

The spectrum of potential robotic applications in medicine is broad, from assistive living through to rehabilitation and surgery. With regards to minimally invasive examination and potentially surgical applications to replace endoscopic treatment, development has been confined to academic research, with the PillCam being the only commercially available miniature diagnostic vessel adopted by the NHS. The following section will look at developments towards miniature robots for examination and localised surgery. Beyond medical applications, developments in robotics for remote operation in pipe inspection or exploration of unsafe environments offer examples of locomotion and actuation which are relevant to the pipe like environment of the human GI tract. The aim to develop tactile sensing for capsule endoscopy will require a review of current

tactile sensing technologies. Finally, with the increased mechanical and electrical load from additional technology, a review of research using a wireless power source will be presented.

### 2.2.1 Locomotion

The passive nature of capsule endoscopy limits its potential to provide localised treatment because it lacks the ability to both maintain position within the GI tract and in a controlled manner travel towards a set location. Additionally, capsule endoscopy has no active method to provide treatment or take local samples for biopsy. In order to identify an effective method of actuation through the GI tract, the environment of the GI tract must be defined. Fig.2.1 shows the typical cross section of the gut. A robot making its way through the gut will have direct contact with the most inner layer of gut wall, the mucosa. The mucosa encases the open space called the lumen. The exact make up of the mucosa differs between regions of the GI tract and deals with different physiological functionalities. The next layer is known as the submucosa and contains connective tissue, blood vessels and nerve branches to both adjacent layers of mucosa and muscularis externa. The muscularis externa contains two layers of overlapping muscles, one layer to prevent backward travel of food, and the other to shorten the tract. These are the basic elements that achieve the peristalsis of the GI tract which would apply external forces on to a capsule endoscopy.

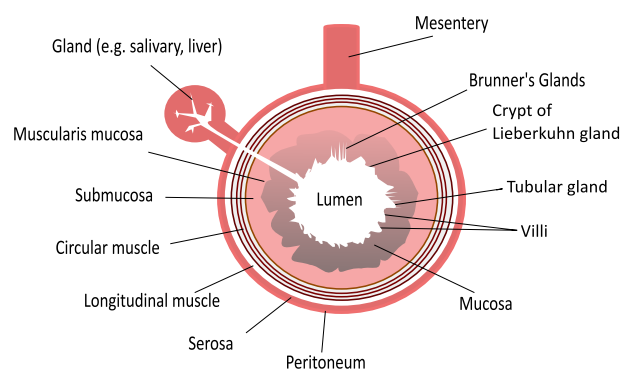


Figure 2.1: Typical cross section of the gut, showing the structure of the gut wall.

At the small scales required to propel endoscopy through tight passages inside the body, there are a number of potentially useful locomotion methods. For example a robot can achieve locomotion through the influence of external forces such as magnetism, or internal forces from onboard actuators. The range of onboard actuation

spans from traditional motors to actuated polymers. The implementation of these actuators determines the particular method of locomotion. These methods include;

- Vibration
- Leg or paddle based walking and crawling
- Wheel based rolling
- Inchworm locomotion
- Peristaltic worm locomotion

First to be reviewed is the use of external forces to achieve an off board actuation, in particular magnetic fields, to push magnetic vessels through the intestines.

### 2.2.1.1 Capsule Robots with Off-board Actuation

Honda et al. [22] have developed a 21mm long helix that imitates a bacterial flagellum, see Fig.2.2. At the head of the helix is a  $1\text{mm}^3$  permanent magnet, and the remainder of the body is a coiled copper wire. Using a rotational varying magnetic field, they have successfully shown that the robot can swim through high viscosity liquids by rotating like a screw.

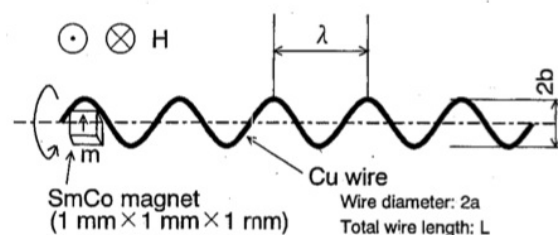


Figure 2.2: Helix and magnet microrobot, Honda et al. ©1996 IEEE [22].

An extension of this work presented in [23], used a coil wrapped around a capsule housing the magnet inside the capsule to achieve magnetic influenced locomotion, see Fig.2.3. Their work focuses on medical uses where the GI tract can provide access to target areas of the body. The experiment shows the robot swimming or crawling through an artificial intestine successfully. The work of Honda et al. has also been pursued further by Bell et al. in [24], where the size of the micro swimming robot has

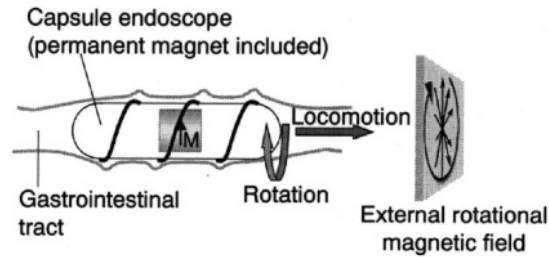


Figure 2.3: Spiral helix around capsule, Sendoh et al ©2003 IEEE [23].

been reduced with coils of  $40\mu\text{m}$  in length,  $3\mu\text{m}$  in diameter, and  $150\text{nm}$  helix strip thickness.

Yesin et al. [25] presents a three dimensional structure microrobot micro-assembled from multiple parts from electroplated nickel and laser cut steel, see Fig.2.4. The microrobot is moved through viscous liquids with the gradients of directional magnetic fields.

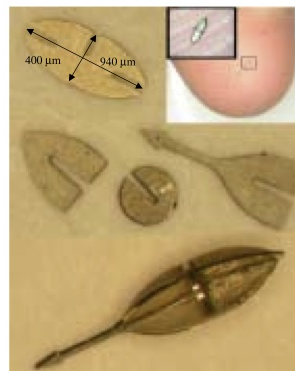


Figure 2.4: Microassembled robot, Yesin et al ©2006 IEEE [25].

Mathieu et al. investigate the potential for using the magnetic force produced from a standard MRI machine to propel medical microrobots [26], see Fig.2.5. Their results show that in the larger blood vessels where the diameter of the microdevices could be as large as a couple of millimetres, the few tens of  $\text{mT}/\text{m}$  of gradients required for displacement against the relatively high blood flow rate is well within the limits of clinical MRI systems. If it is necessary that the microrobot is smaller (ferromagnetic core diameter less than  $600\mu\text{m}$ ), modification of the MRI machine would be required.

Yi et al. [27] developed a swimming microrobot driven by FMP (Ferromagnetic polymer) actuators under magnetic field, Fig.2.6. The robot is of size  $3\text{mm} \times 2\text{mm} \times 0.4\text{mm}$  and can swim through a water filled tube when the magnetic intensity is higher

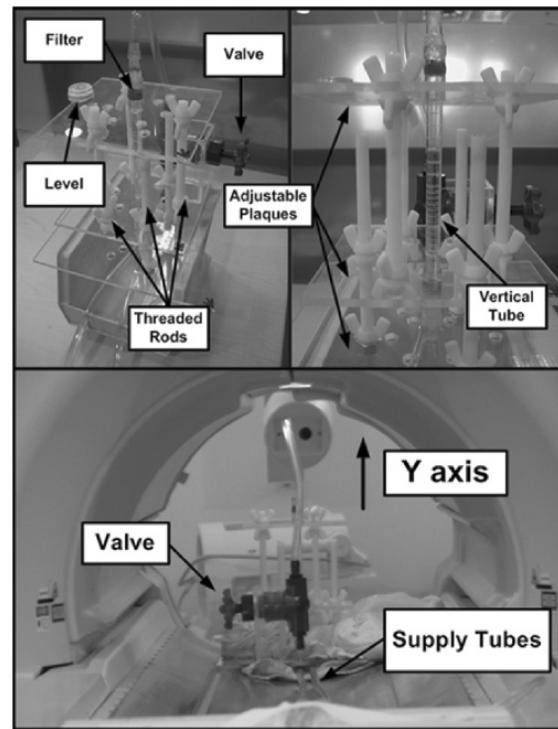


Figure 2.5: Experiment proving magnetic propulsion of microrobot inside a working MRI machine, Mathieu et al ©2006 IEEE [26]

than 8mT and the frequency is about 10Hz achieving a speed of 0.3-1.0mm/s. The swimming speed can be controlled by modifying the intensity of magnetic field.

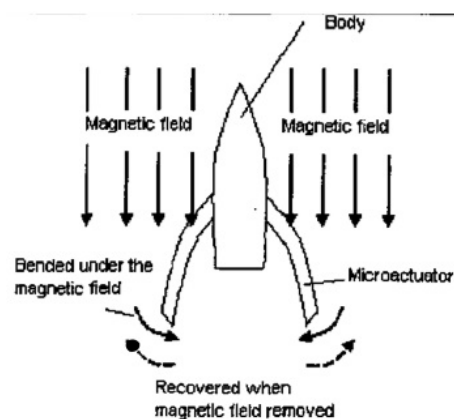


Figure 2.6: Microrobot presenting ferromagnetic polymer actuation Yi et al ©2004 IEEE [27]

Dreyfus et al. [28] presents a linear chain of colloidal magnetic particles linked by DNA and actuated by a magnetic field to achieve undulating motion that causes the microrobot to swim, Fig.2.7. This system can act as a flexible artificial flagellum.

Guo et al. [29] presents another wireless swimming microrobot that can be manip-

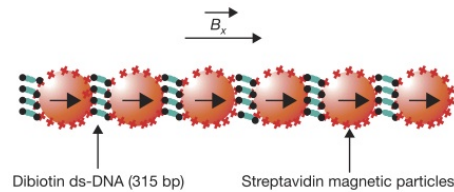


Figure 2.7: Dreyfus et al 2005, linear chain of colloidal magnetic particles linked by DNA. Reprinted by permission from Macmillan Publishers Ltd: Nature [28], ©2005

ulated inside a pipe by adjusting an external magnetic field. Moving the microrobot along a narrow area such as blood vessels has great potential for application in microsurgery. At the head of the robot is a permanent magnet and the tail is made from a polyimide film, see Fig.2.8. This microrobot achieves speeds of up to 40mm/s. Similar behaviour has been demonstrated with onboard actuation. Abdelnour et al. [30] present novel actuation with small IPMC actuated micro swimmers using magnetic resonant coupling WPT. WPT is explored later in subsection 2.2.2. These swimming robots present evidence that using external forces generated by a magnetic field, or with local actuation, the robots state can be affected, leading it to achieve locomotion through a liquid filled environment. This suggests that a similar approach could be applied to endoscopy if the GI tract is filled with liquid during the procedure.

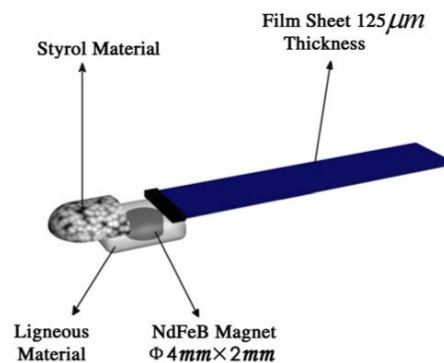


Figure 2.8: Wireless swimming microrobot. With permission of Springer, Microsystem Technologies, Development of a novel type of microrobot for biomedical application, 14, 2007, 307-314, Guo et al. [29]

Whilst off board actuations offers less challenging small mechanics and electronics, reducing power requirements and overall size, it presents limited degrees of control and dexterity and increased potential of interference of data with the strong magnetic fields used to influence motion. Onboard actuation offers potential for a range of degrees of control and dexterity, but at the cost of challenging mechanics and control,

and increased quality of data acquisition with digital communication links that are not compromised by strong magnetic fields. Miniaturisation of mechanics is an ongoing research topic, whilst actuation of multiple degrees of freedom with a magnetic source has shown little success. Therefore, on-board actuation shows most potential for achieving the objectives outlined at the end of this chapter.

### 2.2.1.2 Capsule Robots with On-board Actuation

Achieving active motion around the GI tract can enable targeted diagnostic and treatment procedures. It can overcome the peristaltic, uncontrolled motion and allow the capsule to achieve detached inspection of the intestinal tissue. Quirini et al. [31; 32] have developed a capsule robot with active locomotion that is achieved through four insect like legs driven by one central motor, see Fig.2.9. Quirini concludes that an additional stage of actuation would increase the effectiveness of locomotion but double the power requirements from 200mW to 400mW. This raises a key point in capsule design, that potentially more complex actuation can lead to more effective locomotion but at a cost of increased power requirements. This paddling leg like locomotion method has also been developed by [33; 34; 35].

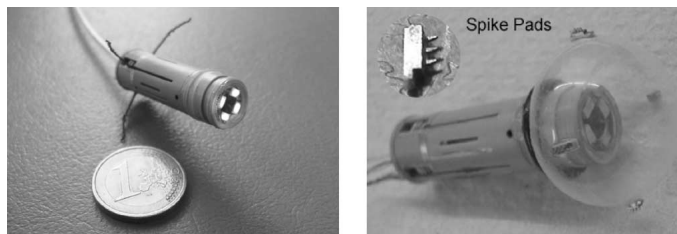


Figure 2.9: Quirini et al. 2008 legged capsule design, ©2008 IEEE.

In 2008 Carta et al. [36], present a capsule powered by wireless induction, see Fig.2.10. The locomotion is achieved with four micro-propellers which are capable of pushing the capsule through liquid. This requires the patient to have digested polyethylene glycol (PEG) before the procedure. The increased power potentially makes extra actuation suggested by Quirini more feasible. Research at the 820 Institute, Shanghai Jiao Tong University, first presented by Gao et al. [37], shows efforts towards a truly wireless capsule endoscopy. Using an inchworm like locomotion methods that incorporates inflating balloons to achieve clamping, they have developed a robot capable of locomotion through a plastic tube, and also a pig intestine to better replicate a human

like application, see Fig.2.11. In addition to the locomotion payload, a camera has also been added with capable wireless data transmission at 30 fps.

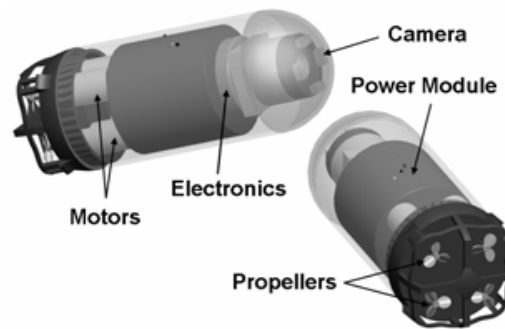


Figure 2.10: Carta et al. 2008 capsule design, ©2008 IEEE

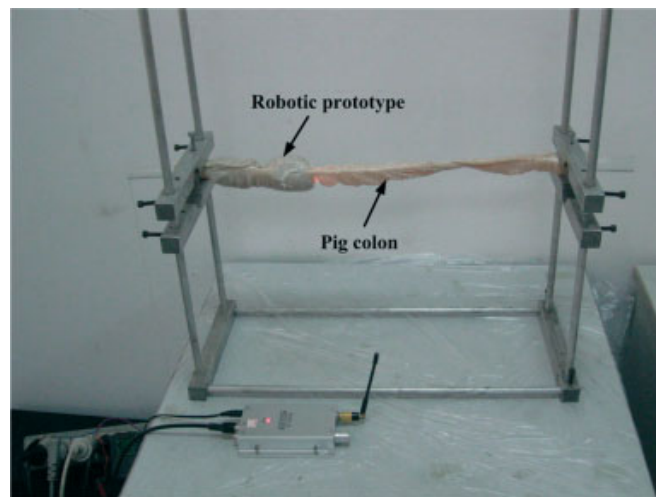


Figure 2.11: Gao et al. 2011 wireless powered miniature robot for colon inspection. With permission of John Wiley and Sons, International Journal of Medical Robotics and Computer Assisted Surgery, A robotic endoscope based on minimally invasive locomotion and wireless techniques for human colon, January, 2011, 256-267, Gao et al. [37]

The same research group have developed this concept further. Presented by Chen et al. [38], they have pursued the inchworm locomotion but opted for a legged method based upon the Archimedean spiral, see Fig.2.12. The new design takes into account the risks of rigid materials moving inside the GI tract potentially tearing the tissue, whilst reducing the overall size of the capsule. Later Gao presented further improvements on the clamping mechanism, [39].

A final approach to locomotion has been presented by Norton et al. [40] with the RollerBall robot, see Fig. 2.13. The RollerBall is a tethered intraluminal robot that

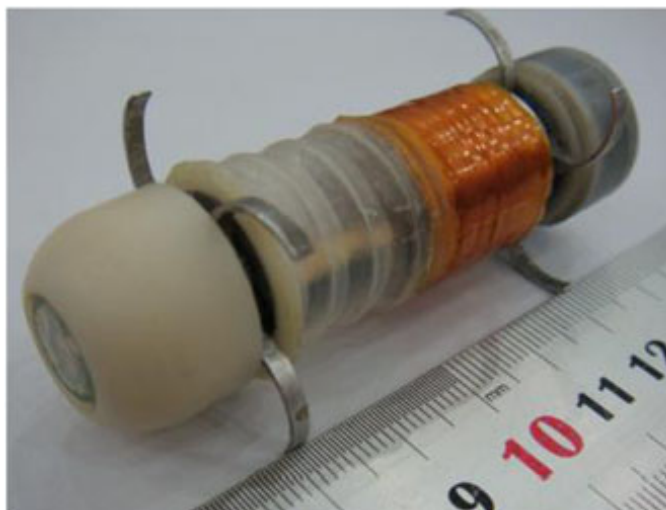


Figure 2.12: Chen et al. 2013 Spiral legged robot for colon inspection. With permission of John Wiley and Sons, *Int J Med Robotics Comput Assist Surg*, A wireless capsule robot with spiral legs for human intestine, May, 2013, Chen et al. [38].

uses wheeled locomotion to traverse the length of a fluid-filled colon. RollerBall uses an expansion method to maintain wheel contact with the varying diameter test pipes with promising success, although currently control of the mechanism is manual. Future work intends to integrate a closed loop system to maintain the wheel contact.

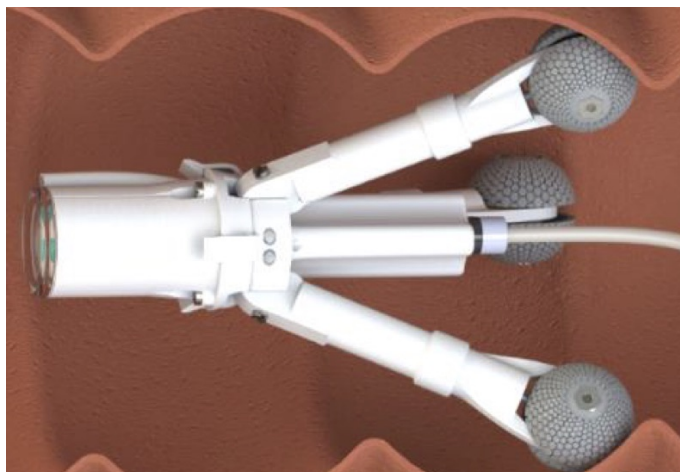


Figure 2.13: Norton et al. 2016 RollerBall robot for intraluminal locomotion. ©2016 IEEE

Table 2.1 summarises the examples of locomotion discussed. Legged and propeller based actuation have received the most development, however they do suffer limitations. Propelled capsules required an appropriate fluid environment in order to operate which cannot be guaranteed. Legged and paddle based capsules struggle to move backwards along the lumen or maintain a fixed position Furthermore, legs offer a risk of tissue

damage due to sharp and hard protrusions. Although slower, inchworm locomotion offer a safer solution. The RollerBall offers more speed however current results are limited to manual control.

### 2.2.1.3 Pipe Inspection Robots

The target environment of the medical endoscope, the GI tract, is akin to pipes and tunnels. Whilst there is substantial existing research in to endoscopy robots, attention should also be paid to similar approaches in pipe inspection and robots designed for hard to reach places. Cho et al. 2009 [59] review the current state of soft biomimetic robotics, many of which are take inspiration from small animals or insects due to their skills in traversing confined complex terrain. Notable references include the iSprawl cockroach robot [60], Stickybot [61] and Trimmer et al. caterpillar robot [43] which use pneumatic cylinders, directional adhesive materials and SMA actuators respectively. These robots use specific material properties to achieve flexible bodies more suitable to these challenging environments. Reflecting on nature and exploring alternative materials for design of an active capsule endoscopy is often found in attempts to create an innovative locomotion solution.

Typical approaches to industrial pipe inspection use various configurations of wheels to maintain contact with the surrounding walls. For example Roh et al. 2001 [44], Tatar et al. 2007 [45] and more recently Kim et al. [46] have all chosen a similar approach of multi-wheeled platforms that apply active pressure on the surrounding pipe walls. Kwon et al. 2012 [62] took this design further and used caterpillar like tracks to increase traction. Common throughout these designs is the multi-segment nature of the robot. This allows the robot to bend around the corners of the pipe. More complex designs include the spiralling wheeled snake like robot [63; 64] Gough-Stewart parallel platform inspired inchworm.

With regard to novel pipe inspection robots beyond the typical wheeled systems, Neubauer et al. [47] developed a spider like pipe climbing robot with multiple legs. Four years later Robmann et al. [48] presented a similar but more mechanically complex robot. Perhaps the most impressive is the 'MORITZ' robot, Zagler et al. 2003 [49] with eight individually articulated legs and articulated central section. Whilst legged-type

Table 2.1: Summary of Robot Locomotion

Robot	Reference	Size	Locomotion Method	Velocity
Honda et al.	[22]	21 mm	Magnetic Propulsion	25 mm/s
Sendoh et al.	[23]	8 x 20 mm	Magnetic Propulsion	25 mm/s
Bell et al.	[24]	40 $\mu\text{m}$ x 3 $\mu\text{m}$	Magnetic Propulsion	3.9 $\mu\text{m/s}$
Yesin et al.	[25]	409 $\mu\text{m}$ x 940 $\mu\text{m}$	Magnetic Propulsion	0.5 mm/s
Yi et al.	[25]	3 mm x 2 mm x 0.4 mm	Magnetic Propulsion	1 mm/s
Dreyfus et al.	[28]	24 $\mu\text{m}$	Magnetic Propulsion	N/K
Gao et al.	[29]	40 mm x 10 mm	Magnetic Propulsion	40 mm/s
Quirini et al.	[32; 31; 14; 35]	11 x 25 mm	Legged locomotion	170 mm/min (in vivo test)
Carta et al.	[36; 41; 42]	15 x 41 mm	Propellor swimming	N/K
Chen et al.	[38]	16 x 31 mm	Inch worm	34.6 mm/min
Park et al.	[33]	15 x 43 mm	Legged / Paddles	170 mm/min (in vivo test)
Norton et. al RollerBall	[40]	95 x 38 mm	Roller wheels	22 mm/s
Trimmer et al.	[43]	N/K	SMA spring actuators	N/K
Roh et al.	[44]	109 mm x 500 mm	Articulated wheeled segments	9 m/m
Tatar et al.	[45]	min dia 140, max dia 200 mm	Articulated wheeled segments	N/K
Kim et al.	[46]	dia 150 mm	Articulated wheeled segments	25 mm/s
Neubauer et al.	[47]	8 cm x 32 cm	Articulated legs	N/K
Robmann et al.	[48]	N/K	Articulated legs	40 mm/s
Zagler et al.	[49]	N/K	Articulated legs	N/K
Menciassi et al.	[50]	24 mm 15 mm	Inchworm	N/K
Zarrouk et al.	[51]	160 mm	Inchworm	5 mm/s
Aguayo et al.	[52]	576 mm x 52 mm	Worm / snake	N/K
Yamashita et al.	[53]	520 mm x 150 mm	Peristaltic worm	N/K
Omori et al.	[54]	N/K	Peristaltic worm	N/K
Seok et al.	[55]	N/K	Peristaltic worm	40 mm/s
Boxerbaum et al.	[56; 57; 58]	22 cm x 50 cm	Peristaltic worm	1 m/s

locomotion is promising with respect to flexibility to adapt to the changing shape of the terrain it has the failing of both increased power requirements and computational overhead to account for the complex kinematics of extra articulation. As discussed earlier in the chapter, power is a rare resource inside the human body limited by the current power density of modern batteries. Increasing the power requirement to achieve complex articulation is strongly discouraged unless additional power access can be achieved.

#### **2.2.1.4 Bio-inspired Locomotion Robots**

As discussed in section 2.2.1.2 a number of actuation methods are available that could fit the performance, power and size requirements of capsule endoscopy. Furthermore, Gao 2011 [37] suggests a number of different approaches to locomotion; biomimetic, legged and paddling. Gao states a main design requirement for any actuated capsule endoscopy is that it should achieve minimally invasive locomotion with minimal damage to organs or stimulation to the nervous system. This would suggest a soft peristalsis like locomotion similar to the workings of the GI tract rather than hard moving arms, legs or probes. Section 2.2.1 shows the GI tract to be a soft and wet pipe like environment. Menciassi and Dario, [50] investigate bio-inspired solutions for locomotion in the gastrointestinal tract. Their publication states that there is a medical need to develop more powerful tools for micro-endoscopy. More specifically they state "Understanding motion and perception systems of 'lower animal' forms, such as parasites, worms, insects and snakes can help to design and fabricate bio-inspired robots able to navigate in tortuous, slippery and difficult-to-access cavities of the human body". Understanding the methods used by animals that move through environments akin to the GI tract will help to design a robot to replicate such capabilities. The following section discusses the bio-inspired locomotion methods relevant to capsule endoscopy.

There are two types of worm like locomotion, inchworm and peristalsis (earthworm). Inchworm is the name of the larvae of moths of the family Geometridae. Inchworms employ a locomotion method whereby they pull the hind end forwards whilst gripping the surface with its front end, then push the front end forwards whilst gripping with the hind end see Fig.2.14. Two key features in inchworm locomotion are the ability to grip the surface and ability to push and pull between the front and hind ends.

The earthworm is native to soil and moves by means of peristalsis. Locomotion is

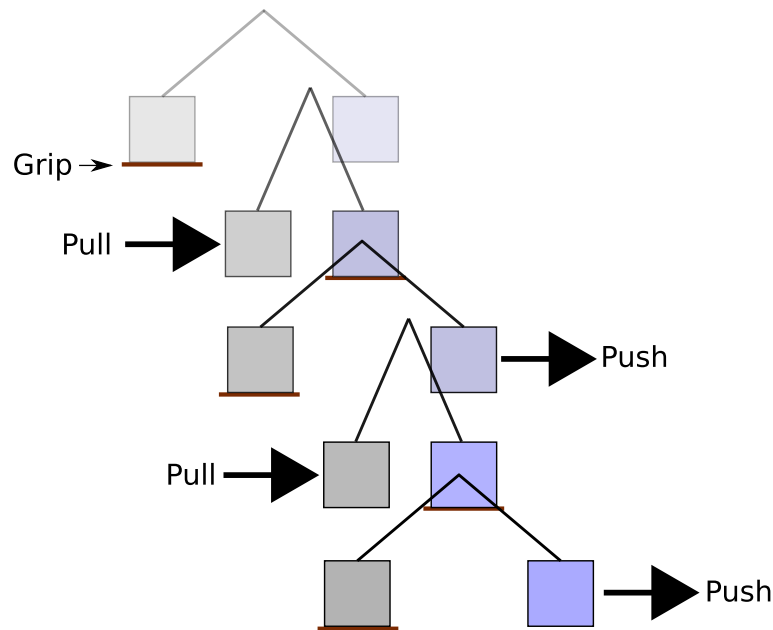


Figure 2.14: Diagram demonstrating inchworm locomotion.

achieved by waves of muscular contractions along the length of the hydrostatic skeleton that shorten and lengthen segments of the body. Whilst the shortened segment anchors to the environment surface, the lengthened segment advances the body along the trajectory, see Fig. 2.15. A combination of circular muscles and longitudinal muscles create these extension and contraction movements respectively. As a segment contracts longitudinally it will expand creating increased friction and locking action to the surrounding environment. The clamping action provides the opposing forces to allow the remaining segments to extend longitudinally and advance the body of the worm forwards, see Fig.2.15.

A clear physical difference between the inchworm and the earthworm are the mechanisms used to grip to the surface. Inchworms have small legs at both the front and hind of the body but not along the length. These legs are used to grip or pinch on to the surface. Earthworms have small bristles along the length of the body called setae. Setae can also be found in other forms in nature such as on the base of gecko feet to aid adhesion or the mouths of crustaceans to aid in holding food. When a segment of the earthworm expands it pushes the setae in to the surface in order to achieve a solid grip. From this position the rest of the body can reach forwards.

Earthworm's traditional environment, tunnels/tubes created within the soil, coupled with the worms use of peristalsis share many similarities with the human GI tract

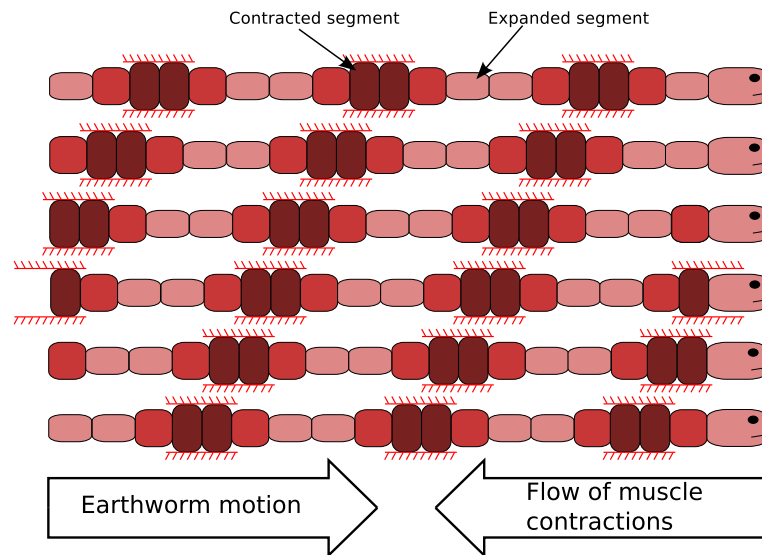


Figure 2.15: Diagram demonstrating earthworm peristalsis [1].

and the use of peristalsis to move food through the system. Acknowledging the similarities between the worm environment and the human intestines, understanding of worm locomotion will be beneficial in identifying effective methods to apply in robot design.

**2.2.1.4.1 Inchworm Locomotion** There are many examples of inchworm robots, [65; 66; 51], as described in section 2.2.1.2. Chen et al. [38] have developed an inchworm inspired robot capsule, see Fig.2.12. The locomotion method is based upon using two expanding actuators each at opposing ends of one linear actuator. As one actuator clamps to the surrounding environment by expanding, the other clamp releases and the linear actuator either extends to push the front or contracts to pull the rear further along the trajectory. A model of this design has been built for this study in order to understand its effectiveness, see Fig.2.16. This model uses one geared DC motor to drive a central lead screw, and two micro servos one for each of the clamping actuation. The model built was cumbersome in locomotion where the rigid legs would catch on surfaces creating a stall state for the motors. This led to over heating and excessive current requirement. The design is very rigid and not a compliment to a soft surrounding environment which could risk damage to the patient. This conflicts with Gao's design requirement noted in section 2.2.1.4. This leads to the decision that an alternative method of locomotion using a softer system should be investigated.

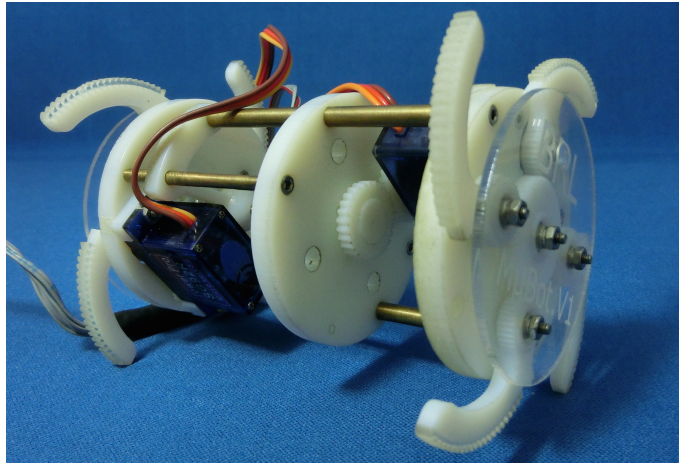


Figure 2.16: Inchworm robot based on Chen 2013.

**2.2.1.4.2 Peristaltic Locomotion** A considerable contribution to this field takes inspiration from natural peristaltic locomotion of an earth worm movement. This is a logical path to pursue considering how the peristaltic action of the gut would complement the motion of the worm, and how suited worm like movement is for tight winding tunnels or pipes. More generally inspiration is also taken in snakes for multisegment robots, [67; 55; 58; 68; 69]. In the last several decades, many robotics researchers have developed peristaltic locomotion robots [52], [70], [53] and [71]. There are similarities among peristaltic locomotion robots; DC motors, solenoid actuators, shape memory alloy (SMA), and pneumatic-high frequency drives can all achieve high velocity of locomotion. From active capsule endoscopy to industrial pipe inspection and space exploration annelid and more particularly earthworm locomotion demonstrates an effective method for inspection of hard to reach spaces. Earthworm locomotion uses waves of muscular contractions along the length of the worms hydrostatic skeleton described as peristaltic locomotion. Several worm like platforms have been developed and reported. Within the context of medical applications, peristaltic locomotion provides an action similar to the muscular contractions within the gastrointestinal (GI) tract. A robot capable of both maintaining a stall state by resisting the muscular gut action and also moving through the GI tract to a specific location would greatly open up the potential of technology towards targeted diagnostic and treatment procedures. Efforts have been made towards active capsule endoscopy [31], [36] in particular Zuo et al. [72], Yan et al. [73] and Zarrouk et al. [51] present peristaltic earthworm robots and Gao et al. [37] present an inchworm like locomotion using inflating balloons to achieve clamping seg-

ments. All these examples exhibit successful locomotion in test environments varying in likeness to a natural intestinal tract.

Other examples exist of robots designed for more generic applications. Omori et al. [54] present a seven segment worm with two actuators in each segment capable of bidirectional linear movement and cornering. Whilst being a successful example of peristaltic worm locomotion each segment requires two actuators which increases complexity, size, power requirements and control. Towards a more simple design Seok et al. [55] present the meshworm a soft robotic platform that exhibits peristaltic locomotion. This worm robot used micro NiTi coil actuators wrapped around a soft braided body. This robot is mechanically simple and naturally robust through its compliance. It does however require a specific control sequence to achieve locomotion.



Figure 2.17: Peristaltic worm robot, Boxerbaum 2012. ©2012 IEEE.

Boxerbaum's [56; 57; 58] robot uses a combination of single DC motor actuator to pull multiple out of phase tendons and a sequence of hydraulic hoop actuators (apply radial contraction) along the length of the body, see Fig.2.17. A sinusoidal wave of muscular contractions are achieved by rotation of the DC motor that pulls tendons through Bowden cables that are connected in a mesh formation that has anisotropic properties (has different physical properties in different directions). This is combined with contracting hydraulic hoops that can constrain and direct shape deformation, i.e. cause greater or lesser body extensions. This robot offers motion very similar to the peristaltic motion of the human gut, however, the design's high number of individual components may be too complicated to achieved with a miniaturised robot for capsule endoscopy. On reflection of the design characteristics some features are valuable for a small capsule endoscopy. In particular, to minimise the number of actuators it could be driven from a single motor if parts or segments can move with a phase offset from each

other. Additionally, the principle of a deforming outer surface provides opportunity to comply with surroundings. If the outer surface is deformable it could maintain contact with the gut wall to allow tactile sensing as a further ability of the capsule endoscopy. Miniaturisation of this system may present problems when reducing the size of the mechanical joints of the body. Likewise, Yeo et al. [74] developed a serial chain large scale peristaltic locomotion robot using multiple actuators which can travel along a guiding track. The robot has two solenoid actuators on each side of the cart (one for gripping and one for extending).

Such a driving mechanism could be linked with the concept presented by Rone et al. [75] whereby a multi-segment robot is driven by actuated tendons through Bowden to produce waveforms traveling the length of the robot to achieve locomotion. In Rone's work the waveforms are ripple like, similar to snake movements. Peristaltic motion, as seen in worms, could also be achieved with this approach with an appropriate soft walled multi-segmented robot which expands and contracts when the tendons are pulled. The single drive motor used by Boxerbaum can be combined with Rone's cable actuation of robot segments to achieve locomotion. Furthermore, the actuation profile of each tendon can be controlled by a gearbox or cam profile.

In order to develop robots capable of exploration of confined spaces, in particular for use in the human body exploration, simpler mechanical design would aid miniaturisation and robustness of the robot. The examples discussed use multiple actuators or complex designs that require more complex control signals. Boxerbaum's worm uses a relatively simple drive mechanism however more recently Horchler et al. [76] have further developed the work of Boxerbaum by adding multiple actuators along the length or the body further complicating the control system. A gap has therefore been identified that shows a lack development towards a mechanically simplified peristaltic worm robots.

#### **2.2.1.5 Actuation For Tooling**

Active locomotion of capsule endoscopy does not lead to a complete solution of endoscopic treatment and diagnostics tool for the gastrointestinal tract. A capsule with active locomotion can be seen as a vessel to provide a payload. That leads to the full potential being realised. Three clear applications stand out; they are targeted drug delivery such as radiotherapy, accurate tissue biopsy and localised tactile sensing.

In 2007 Moglia et al. [77], presented a review of the current achievements towards multipurpose robotics wireless capsule endoscopy. Moglia highlights the benefits of locomotion to provide therapy as well as targeted diagnostics, but acknowledged that a complete system any where near ready for use in human patients has not been achieved. The review suggested that robotics and new MEMS technology would play a key role in further development of such a system. In 2011 Woods et al. [78] had presented a first attempt at capsule endoscopy with the ability to take tissue samples for biopsy or provide drug delivery. Their proposed miniature robot houses one degree of actuation that protrudes a small cylindrical needle. This needle is intended to remove enough tissue such that a biopsy can be performed once the capsule is retrieved from the patient. The concluding comments state that the capsule has drawbacks being dependent on the peristalsis of the gut in order to move through the GI tract and having no mechanism to hold its position whilst injecting the needle. By 2013, Woods et al. have developed this capsule further to incorporate an expanding mechanism that locks the capsule in the gut for the period required to remove the sample, see Fig.2.18. The mechanism can increase the robot's circumference by 75% in order to resist the peristaltic motions of the gut and hold the robot in place. No experimental results have yet been published on the effectiveness of this design.

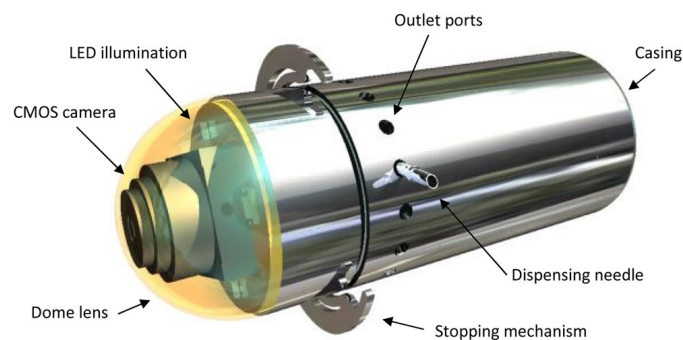


Figure 2.18: Woods et al. 2013 capsule endoscopy with actuated needle. ©2013 IEEE

Further development of a biopsy mechanism can be seen in [79] and [80], using magnetic force to manipulate the state of the effector causing it to capture tissue samples. Yim et al. employs a collection of micro-grippers tethered to a capsule endoscopy see Fig.2.19 whilst Simi et al. have developed a rotating cutting mechanism along the length of a capsule endoscopy.

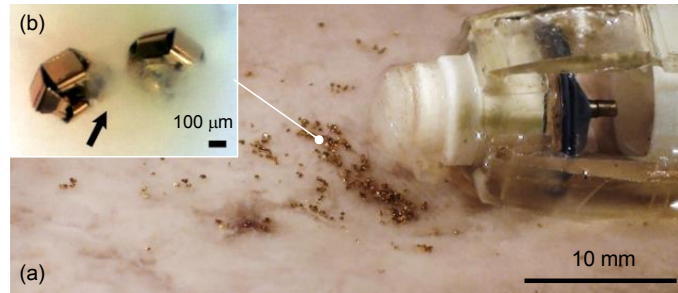


Figure 2.19: Yim et al. 2013 capsule endoscopy with magnetically actuated micro-grippers. ©2013 IEEE

### 2.2.1.6 Actuators

A variety of actuation methods are applicable to the locomotion mechanisms discussed, from more typical DC motors, shape memory alloy (SMA) to piezo motor and electro-active polymers. Table 2.2 summarises these technologies. Piezo motor technologies offer good opportunity for miniature strong actuation, but at high cost and control signal complexity. The Squiggle motor developed by New Scale Technologies, works using a piezo tube around a studded shaft. As the tube buckles from exposure to an electrical source it pushes the shaft along. An advantage of piezo motors are that they can be made as small as  $1.8 * 1.8 * 6$  mm, and have a good strength to weight ratio, 0.3 N stall force. The squiggle motor has already been used in medical application by Allen et al. [81], where a minimally invasive tool has been developed for cardiac intervention where a squiggle motor is used as actuation of a miniature robot. Another example of a micro robot using piezo actuators is presented by Qihong et al. [82], where a peristaltic squirming robot is composed of three linear actuators between contracting segments.

The advantages of SMA actuators are that they can be located directly on to the joint reducing size, however they lack strength and are greatly affected by the environmental conditions. Although they are controlled by current in order to generate the required heat, environmental temperature can cause unwanted changes in physical form. So in order to achieve predictable behaviour, controlled environmental conditions are needed to regulate temperature and performance, which would not be easily achieved inside the human body. A research example of a capsule using SMA actuators has been presented by Kim et al. [83; 84] where the SMA actuators are used to slide gripping setae along the length of the body to push the capsule forwards along a tube

like environment.

Both types of EAPs, IPMCs and dielectric, provide a range of actuation motions which can be designed in to their form, but require either high voltages or high currents. It should be noted that both high current and voltage increase harm when in contact with tissue, so use of such actuation would require significant safety measures. EAPs are still a relatively new technology which is not mass produced, and presents challenges in manufacturing in a laboratory environment. Their control and response is dependant on the challenging build quality. They offer potential as a good custom solution, but for this work are not yet predictable or reliable enough for this development stage.

Piezo electric motors offer a good compromise between achieving small form factor whilst retaining strength and reliability, but at a high cost for single unit prototyping. If they were to fit within the budget of this work they would be the first choice. All accept DC motors are either too unpredictable or affected by environmental conditions. DC motors are predictable, low cost and easily controlled. In this development stage closed loop position controlled DC motors will be used. However, suggested future developments would explore piezo electric motors.

## **2.2.2 Wireless Power Transfer**

The ideas discussed in section 2.2.1 all require additional sources of energy to achieve new motions in capsule endoscopy. Whilst current battery technology is insufficient for supplying these new loads whilst also fitting within size requirements of a capsule, wireless power transfer (WPT) may offer a solution of continuous power which can charge or power in real time, a capsule endoscopy. This section will discuss the current advances in WPT in the context of capsule endoscopy, and then health effects on the human body.

### **2.2.2.1 Wirelessly Powered Robots**

Wireless power transfer (WPT) can already be seen in household products such as electric toothbrush charging stations, and some mobile phone charging stations. Research examples of wireless power transfer can be seen in biomedical implants such as [85; 86]. In 2007 MIT first demonstrated powering a 60W light bulb at 40% efficiency over 2 meters [87], then later in 2008 Intel demonstrated the same experiment but with 75% efficiency [88]. Maximum power transfer is achieved using the concept of magnet-

Type	Description	Advantages	Disadvantages
DC motors	A DC motor is a rotary actuator built on the principles of Lorentz Law. A non-rotating permanent magnet provides magnetic forces to push a rotating electro magnetic armature.	Low cost, relatively small and easy to control	Requires additional sensors for position control. Gearbox needed for slower speeds
Piezo motors	Utilises phenomena that piezoelectric materials changes shape when exposed to an electrical source. These small movements push and pull rotary and linear mechanisms.	Can be very small, low power	Complicated control signal, high cost.
Shape Memory Alloy (SMA)	Shape memory alloy (SMA) is a smart metal which returns to its pre-deformed shape when heated.	Can be located directly on to the joint reducing size	Lack strength, affected by environmental temperatures, high power requirements.
Ionic Polymer Metal Composite (IPMC)	Ion containing synthetic polymers that display muscle like electromechanical behaviour when composited with a conductive material. Subjected to an electric signal they deform in such ways as twisting, rolling, torsioning or turning.	Can be made small, actuation form can be designed to suit requirement and low voltage activation	Manufacture is challenging, control is challenging and high current (safety risk)
Dielectric field activated polymers	Actuated by electrostatic forces between two polymers, acting much like a large capacitor. Require large voltages, from hundreds to some times thousands of volts but can achieve greater forces than IPMCs	Stronger than IPMCs and actuation form can be designed to suit requirements.	Manufacture is challenging, control is challenging and extremely high current (safety risk)

Table 2.2: Summary of Actuator Technology

ically coupled resonance [87] whereby the primary and secondary coils share magnetic resonant frequencies. Similar to mechanical resonance, the system is able to transfer maximum energy much like when a singer holds the correct note to shatter a glass. In the context of electromagnetic coils, the resonant frequency is identified when the AC properties of the driving circuit have minimum impedance.

Some years before the work of MIT and Intel’s development of large scale WPT, Lenaerts et al. had considered the idea of WPT for endoscopy, [89]. Further development of this concept is shown by both Yan et al. [73] and Carta et al. [42]. Yan et al. take the concept of WPT further by presenting inchworm locomotion capable of moving through a pig intestinal canal. Movement is provided by small DC motor driven linear actuators.

Deyle et al.[90] introduces an inexpensive, low complexity power surface system capable of simultaneously providing wireless power and bidirectional communication from a surface to multiple mobile robots. This system enables continuous operation of

a swarm-sized population of battery-less robots. The work demonstrates the capabilities to transmit power through the air wirelessly without any contact. [91; 92] present a practical use of wireless power in a medical example to power implants from an external power source. The idea of powering robots wirelessly with an induction loop is plausible, and the idea of powering a robot that exists inside the human body is also plausible.

Using an MRI machine to power a capsule endoscopy, has an added advantage of the MRI producing a real time image by which to infer the robot's location inside the body. Kosa et al.[93; 94] present promising work towards MRI powered and actuated microrobots, using both static and radio frequency magnetic fields inherently available in the MRI machine to generate propulsion force. The device has three tails, each with two coils. Using magnetic forces the three tails allow the robot to swim. The robot can be powered either by a non magnetic battery, or the RF magnetic field of the MRI. Whilst there are a number of examples of using the MRI to magnetically move a microrobot around the body, little seems to have been done on using the MRI to power a microrobot electrically.

Specifically, Kosa uses the RF field ( $B_1$ ) of the MRI to provide power to operate the tails. Coupling in power provides important advantages. One is that coils made of copper magnet wire are compatible with the MRI. Another advantage is that power can be provided at any time by running the scanner, unlike batteries that can lose charge during the procedure. Kosa seems to be at the leading edge of this research field using both piezo and magnetic tails.

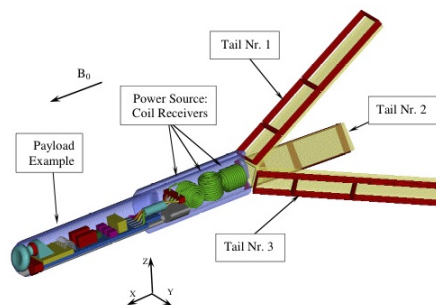


Figure 2.20: Kosa et al 2008, steerable swimming microrobot for the MRI. ©2008 IEEE

A number of capsule endoscopy robots have been identified in Section 2.2.1.2. Carta et al. [36] present wireless capsule stating that wireless induction provides considerably more power (200 mW) than two button cells (25mW) that would be suitable for a

capsule in regards to its size. Gao et al. [37] presents another wireless powered capsule endoscopy achieved with a surrounding Helmholtz coil and resonant frequency of 216 KHz. Experimental results show a maximum power transfer of 680mW with perfect conditions (transmitter and receiver alignment and distance) and minimum power transfer of 378mW for imperfect conditions for a system with total power requirement of 330mW. The same research group later developed another capsule robot with improved locomotion methods, Chen et al. [38], optimising the power transfer with ferrite cores added to the receiving circuits in order to achieve better transfer efficiency.

### 2.2.2.2 Health Considerations of WPT

The effects of WPT, and radio frequency (RF) technology on the human body have raised questions about safety both short and long term. So considerations must be made in account of any potential risks of using WPT for capsule endoscopy. Whilst other RF technologies have been subjected to studies regarding safety [95], often transmission frequency and power differ too much to be comparable with WPT.

**2.2.2.2.1 Wireless Power Through the Human Body** The transmission of wireless power across living tissue raises a number of challenges. The first factor that must be considered is the attenuating properties of living tissue on the magnetic field produced by the transmitter coil. This first factor is further complicated by the differing properties, in this respect, of different types of tissue that the magnetic field will have to traverse in the human body, such as bone, fat and muscle. The next factor to consider is that of positional stability, such that the transmission of power will need to be relatively constant, as the device passes through the body. Finally, the orientation stability of the system must be considered, such that the power transfer remains stable with varying rotations about its axis of the device.

A 2009 study, by Zhang et al [96], investigates the transmission of power across living tissue. In this study, the authors used a 6.9MHz transmitter and a receiver implanted in the core of an agar jelly representation of a human head. Two methods of assessing the transmission of power were used, an LED as an indicator of the transfer of power and a resistor system to give an indication of power output at the receiver coil. The results showed that the LED light was activated and that 105mW of useful power was received at the receiver coil, from an input of 320mW at the primary transmitter

coil. This power transfer was achieved across 80mm of agar tissue substitute, showing that as the distance decreased the power transfer efficiency increased. The second part of the study used a living laboratory pig weighing 20kg. Under anaesthetic, the receiver coil was placed 6cm below the skin in the pig's colon. The primary transmitter coil was placed 10cm above the skin and the measurement tool utilised was an LED light. The results demonstrated successful power transfer across the living tissue, indicated by the light intensity of the LED.

A 2010 paper by Xin et al [97] explored how the transfer of power varied with a point in space relative to the primary transmitter coil. The experimental equipment consisted of a Helmholtz primary coil transmitter and a receiver probe comprising of 3 receiver coils arranged along the x, y and z axis. The transmitter coil, in this case, was set to 400 kHz and had an input power of 25 Watts. The results of this experiment showed that power transfer across an axis can be relatively even, with peaks of efficiency at the regions closest to the coils. The study demonstrated that the average power output at the receiver probe was 750mW, with a 310mW output under the worst geometric conditions. The study also looked at the power transfer efficiency in relation to the rotation of the receiver around its axis, demonstrating peak efficiencies at 0 degrees and 180 degrees. Thus this study demonstrated that a relatively even field of power transfer can be created, thus giving rise to the positional stability mentioned earlier. The study, however, also showed that there was a greater variance in terms of orientation stability, with more than 50 percent difference between optimum orientation power transfer and worst orientation power transfer. It should be noted that this effect had been reduced by the use of a 3D receiver coil arrangement. A point of note for the next section of this paper is that the maximum SAR levels in this study were 0.329 Watts/Kg below the limits set out by the ICNIRP and the current density at maximum was 3.2 amps/m<sup>2</sup> below the standards set out by the same institution.

A 2010 paper by Poon et al [98] looks at how the frequency of the driving current in the primary coil can change the efficiency of power transmission when applied to different mediums of interference. The paper shows that there is a balance between higher frequencies, which permit greater power transfer, and lower frequencies, which reduce tissue absorption loss. The paper concluded that the optimum frequency exists in the GHz range. The paper also took into account the variation in optimum frequency when considering different tissue types such as fat (8.64 GHz), muscle (3.93 GHz) and

skin (4.44 GHz). The paper also demonstrated the inverse correlation between optimum frequency and depth of receiver coil below tissue and at 6cm, which is comparable to the depths, required for a capsule endoscope, the optimum frequency was approximately 2.75 GHz.

With regard to the parameters for the proposed system, it appears that at the frequency range of 4.5 to 12 MHz, power transfer is indeed possible through living tissue. Further to this, there appears to be a reasonable degree of positional stability, such that the variance of power transfer was shown to be relatively small, with strong peaks at regions around the coils themselves. However, these papers do raise points of interest with regards to limitations of the proposed system. Firstly, the literature indicates that the optimum frequency for power transfer across living tissue lies in the GHz range. The models using MHz driving frequencies have been shown to transfer power of up to 750mW with an input power of 25 watts, considering the low efficiency in this model and the possibility for larger power requirements depending on the increased functionality of the capsule endoscopy, the proposed system may need to look into the utilisation of higher frequencies to meet efficiency demands. Secondly, the matter of orientation stability needs addressing, as this was shown to vary at a greater degree than compared to positional stability. The use of multiple receiver coils was shown to reduce the variation but further study is needed to establish if this variation will fall to an acceptable level for clinical use.

**2.2.2.2.2 Effect of Magnetic Field on Humans** The ICNIRP regulations [99], on non ionising radiation exposure, set limits in terms of current density and specific absorption rate for living tissue. These limits are defined by the frequency range that the electromagnetic field lies within; in this case we shall use the regulations for 100 kHz to 10 MHz of current density for trunk and neck of  $100mA\cdot m^{-2}$ , whole body SAR of  $0.4wKg^{-1}$ , local SAR in head and trunk of  $10wKg^{-1}$  and local SAR in limbs of  $20wKg^{-1}$ .

The SAR levels of tissue exposed to wireless electricity electromagnetic fields is investigated in a 2012 paper by Christ et al [100]. In this paper the authors use a numerical body simulation with a primary coil frequency of 8 MHz. The study found that the peak SAR levels occurred nearest to the coil, but with peaks at more distant locations also. The model also found that there was an inhomogeneous distribution

of absorption rates, possibly due to the varying attenuation characteristics of different tissue types, as mentioned earlier. The study found that the limits, as set by the ICNIRP, were reached at 45 watts of power transfer or 750 watts, depending on the chosen threshold. In this case the lowest limit for a localised SAR is that of the head and trunk. Further to this, the study performed an experiment on a liquid filled phantom representation of a human body. On this occasion the frequency used was of 6.7 MHz and the threshold for SAR was reached at power transmission of 39.6 watts.

A 2009 paper, by Shiba and Higaki [101], looks at the SAR and current density in a numerical human body model following exposure to fields of frequency 50 KHz, 300 KHz and 600 KHz. The study found that the SAR levels and current density decreased with increased transmitter frequency. With relation to the limits set by the ICNIRP, SAR levels remained below the threshold in all forms of tissue. Current density levels, however, were above the threshold for the 50 KHz group and below for the 300 and 600 KHz group. What should also be noted is that the highest SAR and current density levels, in terms of tissue type, changes across the three frequency groups. Notable movers include Blood, muscle and the large intestine, whose relative SAR in relation to other tissue types increased with increased frequency, and the large intestines, testis and prostate, whose current density relative to other tissue type increased with increased frequency.

The studies investigating the SAR and current densities in tissue exposed to the electromagnetic field of wireless electricity transfer systems appear to show that in the frequency range that the proposed system would work in will not produce levels that would exceed limits imposed by current standards. However, there are a few shortcomings in these studies that need addressing. Firstly, the studies have tended to towards the use of numerical models of the human body, and thus the accuracy of these models and the adaptability to real life models needs further investigation. Secondly, the thresholds set out by the ICNIRP limits may not be a true indicator of relative risk, as pathological mechanisms are not confined by the same clear cut limits as exposure regulations. Lastly the studies have not addressed the effects of continued exposure, with low SAR and current density levels. Since the regulations that govern EM exposure limits are now 15 years old, future studies may look at SAR and current density levels relative to a more detailed set of exposure parameters, which take into account exposure time amongst other variables.

**2.2.2.2.3 Pathology of Electromagnetic Field Exposure** It remains somewhat unclear what the effects of an electromagnetic field on living tissue are beyond that of localised heating, and damage as a result of this heating. A 2009 paper, by Sage and Carpenter [102], proposes a number of possible mechanisms by which electromagnetic field exposure may cause long term damage to the cell or propagate the development of a cancer. The first pathological pathway is that of DNA damage occurring via the production of reaction oxygen species, these reacting with cellular molecules such as DNA and hence affecting the cells division cycle. Another way that electromagnetic field exposure may influence cell health is via the up or down regulation of gene expression. Studies have indicated that electromagnetic fields may influence gene regulation, and as some of these genes were involved in cell functions such as metabolism, it is reasonable to suggest that they may have an influence over the cells ability to function normally and replicate normally. An interesting point of note is the papers mention of stress proteins, cellular proteins that form due to certain changes in cellular environment, which form at exposure levels below the levels set out by current regulations. This point demonstrates that pathological mechanisms do not conform to a binary distribution either side of chosen safety standards.

The literature investigating the link between certain pathological conditions and electromagnetic field exposure is largely restricted to mobile phone use, as this is the only model currently available which can simulate long term exposure and provide a time frame in which any pathology can become apparent. The picture painted by the literature is however mixed, for example a study, by Lahkola et al [103], indicates that the risk of a meningioma (a cancer of the supportive cells in the central nervous system) was actually lower amongst regular users of mobile phones compared to those who had never used them. This tendency is supported, by Kan et al [104], which showed an odds ratio of 0.9 to 1.25 for the development of brain tumours in mobile phones users compared to controls, the study concluding that little or no correlation exists. On the other hand, a paper, by Sadetzki et al [105], suggested an associated with increased mobile phone use and parotid gland tumours, the results showing in odds ratio of 1.49 to 1.58 when comparing to a high use group to a control, the study also concluding that a dose response association exists.

The literature on the health effects of non ionising radiation in the form of electromagnetic fields appears to be mixed in its overall opinion be it that there is a risk or not.

The literature is currently inadequate for the production of a risk analysis of wireless electricity for capsule endoscopy. Publications are largely designed around long term mobile phone use rather than short term exposure during medical procedures. The mechanisms behind any pathology caused by EM field exposure also needs clarifying, as although the pathways proposed by the Sage and Carpenter 2009 paper are feasible, they lack the evidential data to link them to the pathologies suggested. It should also be noted that the studies mentioned were case controls, and thus subject to a number of biases and inaccuracies, namely selection bias and the vague classification parameters for heavy mobile phone use. Considering that most concerns are regarding long term exposure, and WPT for capsule endoscopy would be during the short procedure time only, these concerns would not relate to the proposed WPT capsule endoscopy.

### **2.2.3 Tactile Sensing**

The following section will explore the current technology of tactile sensing as an onboard examination tool for capsule endoscopy. Driven by the discussion in section 1.3, capsule endoscopy with tactile sensing capabilities is both novel and in line with examination approaches currently used during external examination of the body.

#### **2.2.3.1 The Human Sense of Touch**

In order to understand the sense of touch it helps to understand the mechanisms behind human perception of touch. The human sense of touch comprises both tactile, sensory input from receptors embedded within the skin, and kinaesthetic, forces incurred on the skeleton measured by receptors embedded in muscles, tendons and joints of the body. Detection of small features is typically reliant on tactile sensation, through stimulus of particular mechanoreceptors close to the skin. Vallbo et al. 1984 [106] discuss the workings of the 'tactile unit', describing it as a primary afferent neuron whose sensory endings are primarily responsive to light skin deformations and are mostly located in the dermis. Further more the type of tactile units or more commonly named mechanoreceptors can be broken down in to the following categories; SA I (slow acting) Merkel cell, SA II Ruffini corpuscle, FA I (fast acting) Meissner corpuscle and FA II Pacinian corpuscle.

There are two mechanoreceptors in particular that respond to the type of tactile stimulus regarding palpation, the FA I Meissner corpuscle and SA I Merkel cell. Gerling

et al. [107], Kuroki et al. [108] and more recently Chorley et al. [109] discussed the role of these mechanoreceptors with regards to light touch and edge detection identifying that it is the movement of dermal papillae that stimulate the receptors. The Meissner corpuscles adapt quickly to when stimulus is both applied and removed, and so are sensitive to movement across the skin. They are sited at the base of and between surrounding papillae. Any changes in distance between papillae will be detected by the Meissner corpuscle. The Merkel cell is sensitive to light touch, responding to the shape of the contacting surface. Merkel cells are sited at very specific locations on the tips of the dermal papillae, where they are stimulated by the papillae tip movement, see Fig. 2.21.

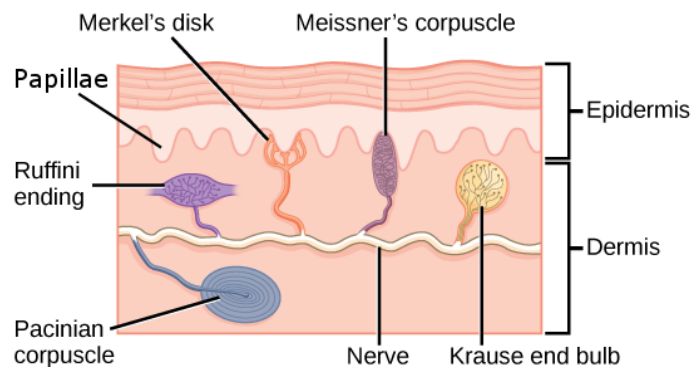


Figure 2.21: Cross section of glabrous skin detailing location of mechanoreceptors, by Steven Telleen, Rice University. Image sourced from <https://cnx.org/contents/D4mGheAC@1/Somatosensation>, permission given under a Creative Commons Attribution License 4.0 license, <https://creativecommons.org/licenses/by/4.0/>. Download for free at <http://cnx.org/contents/0f898685-e002-491c-9a68-b906bbd070cf@1>.

The remaining receptors are the Ruffini endings which are associated with slip detection and Pacinian corpuscle which are associated with high frequency stimulus such as textures, [4]. Table 2.3 summarises the role of each of the mechanoreceptor types. With this understanding of human perception of touch in mind, it is logical that a sensor that monitors surface deformation of a device could be akin to human touch.

### 2.2.3.2 Existing Tactile Sensors

A number of tactile sensors currently exist within the robotics field. Perhaps the most well known is the BioTac [110], [111]. The BioTac is a collection of sensors rather than one individual sensor. The device itself comprises three sensing modalities. One

Table 2.3: Function of Each Mechanoreceptor Type

Category	Type	Role
Slow Acting 1 (SA1)	Merkel Cell	Sensitive to pressure, position, and deep static touch features such as shapes and edges.
Slow Acting 2 (SA2)	Ruffini Corpuscle	Respond to sustained pressure and sensitive to skin stretch.
Fast Acting 1 (FA1)	Meissner Corpuscle	Highly sensitive to light touch, detecting shape and textural changes.
Fast Acting 2 (FA2)	Pacinian Corpuscle	Respond only to sudden disturbances and are especially sensitive to vibration, useful for discriminating texture.

is a hydro-acoustic pressure sensor which is stimulated by an incompressible fluid fed from a reservoir that wraps around the contacting region of the device. As the device contacts an object it forces the incompressible fluid through a channel leading to the hydro-acoustic pressure sensor to measure the force applied. The second modality is impedance sensing electrodes beneath the fluid reservoir. This array of electrodes localise the force contact position. Finally there is a thermistor which measures the temperature of the contacting object. Whilst a competent tactile sensing device with evidence proven with ex-vivo tumour localisation [111], slip detection [112] and tactile exploration of objects [113], the BioTac is both an expensive and complex sensing system. The mechanical complexities of BioTac make it challenging to fit successfully to a capsule endoscopy structure.

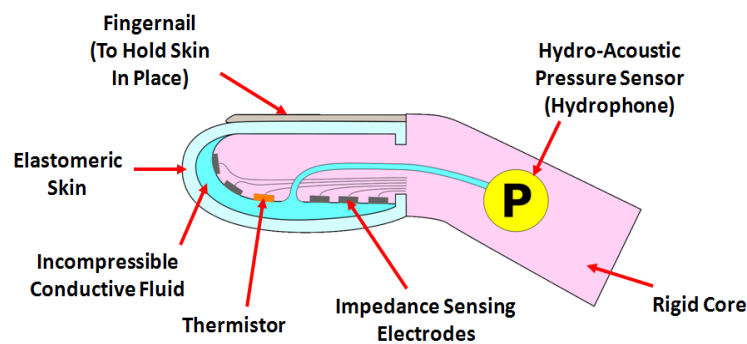


Figure 2.22: BioTac cross section, Lin et al. [110]. ©2009 IEEE

Typically approaches to tactile sensing utilise one modality. The type of sensing method differs; from piezo-resistive and piezo-electric, capacitive, MEMS based and optical based. With regards to piezo-resistive and piezo-electric Uldry et al. [114] surveyed conductive elastomers to identify material formulations, then constructed an

array of strain and temperature sensors, an early tactile skin. Shimojo et al. [115] presented similar work using electrical wires stitched in to pressure conductive wire, and then in a much more compact form Takei et al. 2010 [116] developed nanowire active-matrix circuitry tactile skin.

Early development of capacity tactile sensing fingertip was shown by Fearing et al. in 1991 [117] where an array of capacitive sensor on a finger shape were able to determine curvature of contact. Both Ko et al. 2006 [118] and Lee et al. 2006 [119] presented micro scale capacitive tactile sensing arrays suitable for skin applications. In 2008 Maggiali et al. [120] applied this principle to a scalable robot skin system used on the iCub [121].

MEMS technology has become very well established in recent years, opening many new opportunities for sensing. Kuwana et al. 2013 [122] developed grasping forceps with a triaxial MEMS tactile sensor for quantification of stresses on organs to be applied to laparoscopic forceps. Sohgewa et al. 2014 [123] were able to characterise various material textures with their developed MEMS based micro cantilever embedded in PDMS elastomer. Finally, Charalambides et al. 2015 [124] developed a 3-axis all elastomer MEMS tactile sensor capable of a sensing resolution down to 50 mN and force ranges up to 10N.

Early optical based tactile sensor development inspired by human tactile sensing began when Begej 1988 [125] presented a fiberoptic fingertip with sensing resolution comparable to a human finger ( $100 \text{ taxels} / \text{cm}^2$ ). In 2004 Kamiyama et al. presented a camera system that uses image processing to monitor movement of staged laminated markers in an elastic body. This model is very similar in principle to the Tactip device discussed throughout this work, and has demonstrated sensing ability of 3-axis of force and rotation. Ali et al. 2012 [126] presented the use of this method applicable to endoscopy, utilising fibre-optics to translate markings on the inside of a finger tip back to a CCD camera. Xie et al. 2014 [127] and Back et al. 2015 [128] also use optical fibres, but to translate reflected light from individual moving mechanical contact element arranged in an array on the end of a probe. Back's later development starts to appear similar to the Tactip with external fingerprint features that exaggerate textured stimulus, [4]. The advantage of both these devices and the Tactip is that any delicate components such as cameras can be removed from the point of contact, creating a more robust device. Furthermore miniaturisation of optical systems is limited only by the

lens, image sensor and the deformable material being observed, whilst the modes of sensing in this one device include motion, force and shape deformation.

### **2.2.3.3 Biologically Inspired Tactile Sensing - Tactip**

The Tactip is a biologically-inspired sensing technology, based upon the deformation of the epidermal layers of the human skin. Deformation from device-object interaction is measured optically by tracking the movement of internal papillae pins on the inside of the device skin. These papillae pins are representative of the intermediate epidermal ridges of the skin, whose static and dynamic displacement are normally detected through the skin's mechanoreceptors, see Fig. 2.23. In past publications it has been shown how the Tactip can be used for edge detection [129], lump detection [130] and texture discrimination [131], as well as miniaturisation [132].

There are two mechanoreceptors in particular that respond to the type of tactile interaction that this sensor explores, the Meissner corpuscle and the Merkel cell [106]. The Meissner corpuscles adapts quickly to when stimulus is both applied and removed, and so are sensitive to movement across the skin. They are sited at the base of and between the surrounding papillae. Any changes in distance between papillae will be detected by the Meissner corpuscle. The Merkel cell is sensitive to light touch, responding to the shape of the contacting surface. Merkel cells are sited at very specific locations on the tips of the dermal papillae, see Fig 2.23.A, where they are stimulated by the papillae tip movement. The Tactip system mimics this tactile sensing system by visually tracking the papillae movement as if it were the described mechanoreceptors. Fig. 2.23 shows the design of a traditional Tactip concept which comprises an artificial cast silicone skin, optically clear flesh like gel, camera and internal illumination using LEDs. Whilst in the biological model it is the papillae pin movement that stimulates the mechanoreceptors in the finger, the Tactip design replaces the mechanoreceptors with a camera system capable of tracking pin interaction visually.

### **2.2.3.4 Tactile Sensors for Examination**

Inspection of gastrointestinal tract where long slender instruments are introduced in the human body for diagnostic and therapeutic purposes, although clinically increasingly important, do not allow the surgeon to directly palpate the tissue. This problem has been the subject of many research groups, particularly in the integration of haptic

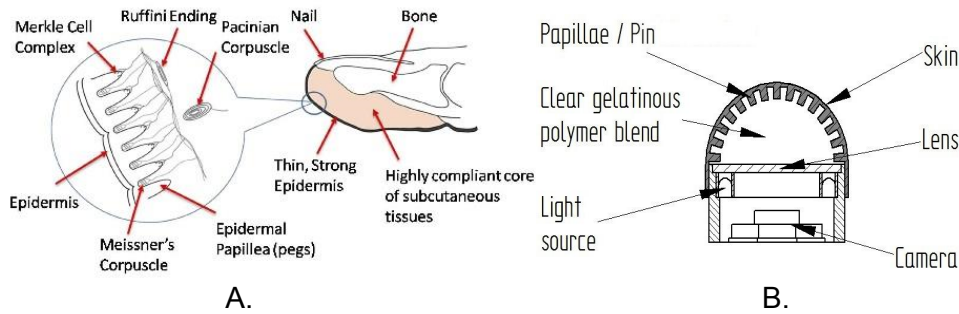


Figure 2.23: A. Biological inspiration for Tactip, B. Tactip tactile sensing device.

feedback to Robot Assisted Minimally Invasive Surgery (RAMIS) to aid in guidance and diagnostics. Trejos et al. [133] show a robotic controlled surgical instrument for remote tumour detection with tactile and force feedback achieved accurate tumour detection with 35% reduced maximum applied force on the tissue than a comparable system with no tactile, only force feedback.

In 2006 Schostek et al. [134] presented work on adding tactile sensing capabilities with a visual feedback display to laparoscopic tooling in order to aid in local tumour surgery, see Fig.2.24. More recently in 2013 Roke et al. [130] took this concept further with the addition of a tactile feedback display using a mechanical matrix of linear actuators to remotely stimulate the operators fingers based on sensor deformation in contact with artificial tissue and tumours, see Fig.2.25. The latter work is intended for remote operated surgical systems such as the DaVinci® robot. Gwilliam et al. [135] further support evidence presented by Sarvazyan et al. [136] that computerised or electronic palpation can be more effective in detecting lumps than the human finger.

In [14] a list of the main challenges of endoscopes includes their limited degrees of freedom and more importantly, lack of sensing capability which presents major risk of excessive force application. Dogramadzi et al. [137] have presented a method to measure in vitro colonoscope forces along the length of the shaft, Rebello [138] discusses endoscopic tips with contact, force and pressure micro-sensors to aid in user feedback. In 2011 Kume et al. [20] investigated the development of an articulated robotic endoscopic tool. Although adding articulation showed evidence that the insertion becomes easier, and learning to operate quicker, they clearly state that tactile feedback would aid in limiting excessive application of force. Further evidence of the lack of, but need for tactile sensing in remote surgical systems is discussed by Chaudhary et al. [21] in

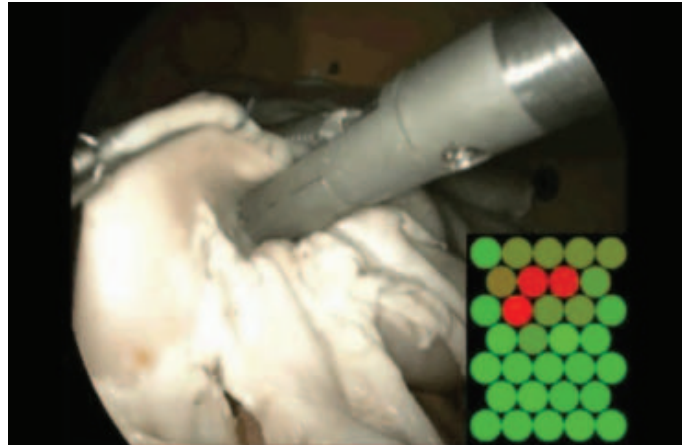


Figure 2.24: Schostek et al. 2006 tactile laproscopic tool, [134]. With permission of Taylor & Francis, 2006.

their review of medical robotics. The capsule endoscopy introduced by Given Imaging PillCam brought a novel approach to gastrointestinal diagnostics but with limitations. The capsule is propelled by peristalsis and its motion can not be controlled. Further research on improving its abilities have been made on traversing the entire abdominal environment to perform biopsy of hepatic tissue with a mobile in vivo camera robot, [139], simple controlled observation of the GI tract, [140] [32] or drug delivery, [78].

One of surgeon's most important skills is their highly enhanced sense of touch [19]. Minimally invasive approaches to diagnostics in medical technology often restricts direct palpation of the patient. Whilst systems for laparoscopic surgery introduce minimally invasive procedures that minimise patient discomfort and improve recovery, they are making much less use of this very human perception. Konstantinova et al. [141] have reviewed the latest developments in tactile sensors for robot assisted minimally invasive surgery with a focus on manual palpation. They state that "*Nowadays, no sensor system exists that is capable of accurately measuring the full complexity of tactile cues on the same level as the human tactile receptive system*", emphasising that this is a needed development for accurate perception in robot assisted medical procedures. In 2004 Dargahi et al.'s [142] review discusses the importance of modelling human tactile perception as a standard in the development of tactile sensing systems.

Other examples of remote palpation using tactile sensors can be found in [143] where the detection of stiff nodules beneath soft tissue is achieved using a resonance sensor. The system is able to detect stiffness changes at least 4 mm away from the biological specimen. Nyberg et al [144] combine Raman spectroscopy with tactile resonance

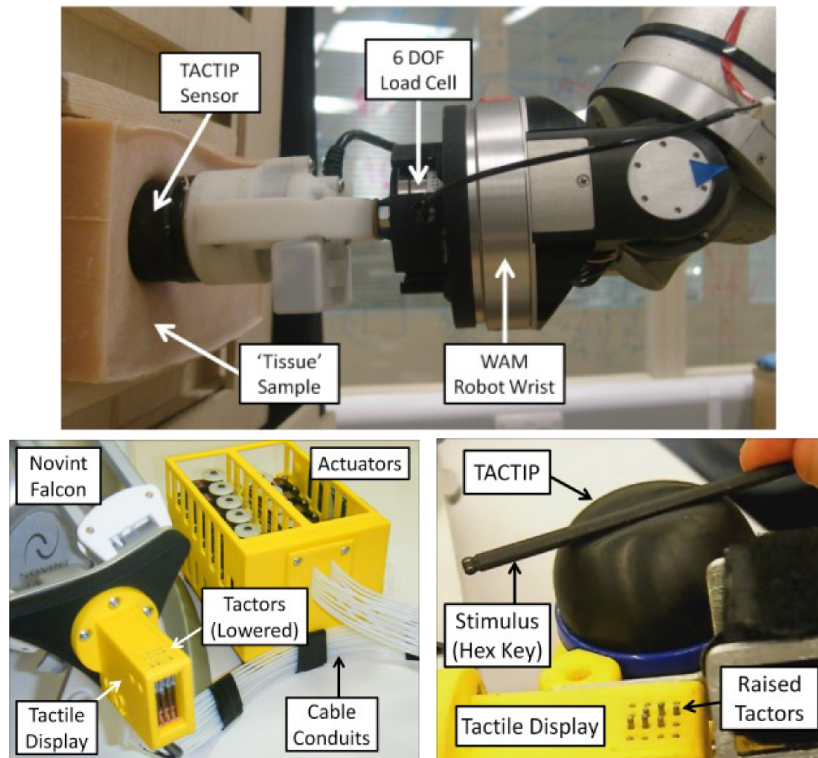


Figure 2.25: Roke et al. 2013 tactile laparoscopic tool, [130]. ©2013 IEEE.

technology to achieve discrimination of normal prostate tissue *ex vivo*. Using stepwise analysis to combine system parameters they achieved 100% sensitivity, with a 91% specificity for discriminating non-epithelial and epithelial tissue. Finally, Chuang et al [145] utilize a tactile sensor with structural electrodes for differentiating the mechanical properties of elastomeric materials. The presented sensor is suitable for mounting on an endoscope for the hardness detection of submucosal tumors. Further work can also be seen using haptic feedback as a means to relay remote tactile sensing. Talasaz et al presents force feedback stimulated by a capacitive tactile sensor mounted to a laparoscopic tool [146], and Tanaka et al, [147] have used a voice coil based tactile array to stimulate the finger with data acquired from a tactile sensor also located on a laparoscopic tool.

Although examples can be found in the scientific literature of technology capable of tactile palpation of the external surfaces of the body or internally through a limited reach tethered system, Ciuti et al. [148] review the frontiers of robotic endoscopic capsules and report that no work has yet focused on remote palpation using an untethered capsule for examination of the GI tract. Capsule endoscopy (CE) utilises a swallowable capsule with a self contained microsystem, similar to a traditional drug delivery cap-

sule. CE provides a platform to achieve similar procedures to more traditional methods of endoscopy but without the difficult and time consuming insertion of an endoscope. This presents a capability to explore the entire length of the GI tract including the small intestines which is not currently possible using any other system. In its current form capsule endoscopy is limited to only visual inspection of the lumen surface. Tissue health deeper than the lumen surface cannot be detected by visual means, however using a tactile palpation technique deep tissue deformities could be sensed.

Modern capsule endoscopy presents an ability to view the small bowel beyond the duodenum and proximal to the colon. There are a number of pathologies that can occur in the small bowel, such as tumours, strictures and ulceration as part of an inflammatory bowel condition such as crohns disease. Shi et al. [18] discusses the importance of the GI tract motility and how failings in motility can be an indication of more serious GI diseases. Shi presents a sensing capsule to measure pressures encountered during the journey through the GI tract as an indication of GI tract motility. The capsule robot sensor presented in this work would be suitable to detect GI tract motility through measuring the deformation of the capsule walls due to forces exerted by GI tract action. As the capsule sensor passes through the GI tract, a map of tract motility can be recorded.

#### **2.2.3.5 Identifying a Novel Technological Approach to Tactile Sensing**

The requirements of a tactile sensing system for a capsule endoscopy robot dictate a sensing system capable of being miniaturised, capable of sensing stimulus similar or equal to that of the human finger and accurate enough to discriminate between healthy and non-healthy tissue. There are six typical ways to transduce tactile energy; capacitive tactile sensors, piezoresistive tactile sensors, piezoelectric tactile sensors, inductive tactile sensors, optoelectric tactile sensors and strain gauges. Each have advantages and disadvantages which suit particular scenarios. Capacitive sensors have great sensitivity and range, however, are susceptible to noise and require complex measurement electronics. Piezoresistive sensors have good resolution but suffer hysteresis and higher power consumption. Piezoelectric sensors offer high frequency response and sensitivity but only produce signal during stimulus change. Inductive sensors can be bulky and use moving parts but provide linear output and uni-directional measurement. Optoelectric sensors have good sensing range, reliability and are immune to electromagnetic inter-

ference but can be bulky. Finally strain gauges are low cost and have good range but are susceptible to temperature changes and electromagnetic interference. The Tactip device, developed at Bristol Robotics Laboratory, [109] [129] [129] [132] [4], presents an excellent biomimetic optical tactile sensing solution. Where previous work has shown the Tactip to be suitable for ex-vivo palpation, texture discrimination and miniaturisation it suggests that the Tactip could be a suitable candidate for in-vivo palpation.

## 2.3 Proposal

This chapter has reviewed a number of problems encountered during internal examination and diagnostics of the human, in particular the gastrointestinal tract. The list below summarises the problems identified;

- Current tools used for internal non surgical examination of human gastrointestinal tract suffer either limited reach or limited control.
- Capsule endoscopy only captures images of the surface of the lumen, however some conditions produce early symptoms such as hard tissue beneath the lumen which is not visually noticeable.
- Remote operated examination tooling neglects the clinician's trained skill of skin and tissue palpation.
- Evidence has shown that both force and tactile feedback improves accuracy of both applied force and sensing of surgical/medical tooling, but is missing from most tooling, and certainly not available for capsule endoscopy.
- Whilst some tethered endoscopy tools provide additional tooling for procedures such as tissue biopsy, capsule endoscopy does not. This is a restricted potential of capsule endoscopy.
- A capsule endoscopy with tactile sensing capabilities will need an effective locomotion method to target the sensing region achieving palpation of internal tissue.
- Additional mechanical and electrical payload on a capsule endoscopy will require additional power which is not currently available from battery technology of a suitable size.

Taking into account the problem identified, the existing attempts to tackle this problem and the reality of what is achievable in the time available, it is proposed that the following work be performed in order to develop and present a novel and beneficial contribution to the medical and robotics research community. Capsule endoscopy has been the first attempt at minimally invasive examination within the gastrointestinal tract. The commercial products; PillCam and Endocapsule, have presented many advantages over traditional endoscopy but are extremely limited by their passive nature. There are two rational approaches to provide actuation to the capsule, through applied external forces or attached actuators. Although a number of groups have researched in to using external magnetic forces to push capsules and micro robots around the body, their applications are limited and lack compatibility with other complimentary practices due to strict environmental conditions. This leads to the conclusion that attached actuators provides a more plausible solution. Having on board actuators can not only provide locomotion, but also means to deposit treatment and take tissue sample.

An un-tethered wireless capsule is only the first part of the solution. A capsule capable of arriving at a specific location along the GI tract then has the opportunity to provide some kind of treatment. This is something that would traditionally require some kind of invasive procedure such as small tooling at the end of an endoscope, laparoscopic tooling or full open surgery. The positive impact on patient comfort is quite obvious if no serious surgery is required for localised treatment such as this. What kind of procedure the capsule should be capable of is a very open ended question. In fact so many opportunities could be pursued, so the real question to answer is what is novel and little or entirely un-researched within this domain. The literature research performed has identified a number of examples of both passive and active capsule robots that perform either tissue biopsy or drug delivery. What appears to be strongly lacking, and yet suggested in a number of publications is tactile sensing and haptic feedback. The ability to relate long standing expertise in tissue palpation to minimally invasive active capsule endoscopy robotics is a new a novel technology that could potentially bring new methods and practices to medicine and robotics.

### 2.3.1 Research Objectives

The proposed work breaks down into three clear research objectives that contribute to answering the research question stated in 1.4, and furthermore, the development of an active capsule endoscopy;

1. **Capsule Endoscopy with Onboard Diagnostic/Treatment Tools.** Whilst active capsule endoscopy robots have been extensively researched, less of that focus has been on the actual treatment opportunities. In particular, remote tactile sensing is under developed and requested by research publications. This work will focus on developing capsule endoscopy capable of providing remote tactile sensing to the operator. The use of tactile sensing should aid in the detection of suspicious regions of tissue either directly on the surface of the lumen or deeper in the surrounding tissue. Furthermore, the developed tactile sensing system should be characterised, and then optimised with a suitable classification method to discriminate between healthy and non healthy tissue.
2. **Active Capsule Endoscopy Locomotion.** Developing a capsule with tactile sensing further strengthens the need for active locomotion. The work of Lederman and Klatzky [149] identifies the need for active exploration in order to fully use the fingers tactile sensing abilities to categorise shape and form of manipulated objects. Within a restricted environment such as the GI tract this is even more important. More information is available from a transition in feedback than one captured moment in time. Seeing and or feeling deformation caused by a lump through exploration is far more accurate, this has been proven recently by Roke et al. [130] using a remote haptic sensing system to identify artificial tumours. If the capsule is capable of directional movement controlled by the operator then following the conclusions presented in these publications, discrimination of tissue features will be more accurate. A capsule will be developed with the ability to transition across a region of interest such that the operator can remotely explore features being inspected.
3. **Wirelessly Powered Capsule Endoscopy.** Acknowledging that current battery technology cannot provide sufficient power for actuation and onboard control for a period long enough to last the journey of the GI tract, many research

groups have focussed on wireless power technology. Wireless power transfer offers a source of power for an unlimited time, however the amount of power is subjected to conditions such as distance from source, orientation and optimisation of the transfer system. Particularly recently, a number of examples of wireless powered capsule endoscopy have reached the research community. These examples present a capsule with onboard camera, communications and early stage locomotion mechanisms. In order to achieve the two previously discussed developments of this work, more power will be required. This power is only reasonably feasible through a wireless power source. During this work, a review and laboratory exploration of WPT will be undertaken. It is acknowledged that the quantity of work required to tackle this challenging RF and physics problem is high, so evidence of feasibility will be considered sufficient in the case of this work, such that future work can take the active tactile sensing capsule forwards with the details of how to achieve more complete WPT.

### **2.3.2 Considerations of Proposal**

The main focus of this work is to find valuable scientific discovery that can aid in furthering the field of robotic capsule endoscopy. As with many other research projects, it is likely that the physical scale of the components developed will be larger than considered practical for clinical application. The miniaturisation process within any development is typically an engineering task that can be very time consuming. Working with small components requires more specialised manufacturing facilities and higher specification materials which are not readily available to university research facilities in a time scale or budget to suit this project. The scientific objectives of this early stage work can be achieved at a larger scale within the time scale of this project. Adding the complication of miniaturisation is a high risk that could hinder any objectives being achieved. Manufacturing, assembly and testing of conceptual ideas is a more manageable task when at a scale suitable for laboratory and workshop bench facilities. However, when deciding on methods and designs for this project, the ease of future miniaturisation should be strongly considered.

A further consideration of this proposal is that an ideal experimental environment would be a real human intestinal tract, or at least a comparable animal tract such as from a pig. Whilst cadaver donations are possible, the laboratory is not equipped

with such facilities. This work is predominately an integration focused project. The objectives are to prove that integrating these technologies provide a new potential in capsule endoscopy. First and foremost these technologies need to work together before they can be tested in an organic environment. The test environment for these early experiments should focus on proving the sensing and locomotion capabilities, with later intentions to move towards an organic environment. Therefore, an environment that uses synthetic materials to characterise the developed system are considered sufficient to prove the system.

## 2.4 Work Plan

The following work plan provides a list of tasks which on completion will answer the research question posed in section 1.4, achieve the objectives detailed in section 2.3.1 and form the structure of this thesis.

1. Capsule endoscopy diagnostic tool.
  - (a) **Develop** a tactile sensing system capable of identifying surface deformation.
  - (b) **Develop** a tactile sensing system capable of identifying artificial tumour like lumps.
  - (c) **Optimise** the developed tactile sensing system in order to discriminate between different lump features. Lump features will differ in size and hardness
  - (d) **Consider** a soft sensing structure to minimise the impact on the patient and allow for compliance around the changing bowel environment.
  - (e) **Consider** a sensing system which can be easily miniaturised in future developments.
2. Capsule endoscopy locomotion.
  - (a) **Develop** a locomotion method to drive the capsule through a GI tract like environment.
  - (b) **Optimise** the locomotion mechanism to identify methods to adapt to a changing environment.

- (c) **Consider** a soft locomotion system to minimise the impact on the patient and allow for compliance around the environment reducing risk of blockage and increasing accuracy of sensing
  - (d) **Consider** a locomotion system that can be easily miniaturised through reduced number of components and complexity.
3. Integration of locomotion and diagnostic tool.
- (a) **Develop** an integrated assembly of the locomotion system and tactile sensing system.
  - (b) **Test** the integrated assembly in a combined test environment used in the development of the locomotion and sensing system. The robot assembly should show capability to traverse and detect a tumour like feature.
4. Wireless power for capsule endoscopy.
- (a) **Review** the potential of WPT as a possible power source for untethered capsule endoscopy.

This chapter is based upon the publications Winstone et al. 2014 "A Novel Bio-inspired Tactile Tumour Detection Concept for Capsule Endoscopy" [131] and Winstone et al. 2015 "Biomimetic Tactile Sensing Capsule" [150].

### 3.1 Introduction

In chapter 2 the current state of GI tract examination was explored. Key problems were identified around issues regarding hard to reach locations within the GI tract. Whilst established technology is successfully used to access the beginning and the end of the GI tract, the middle section, the small intestines offer a greater challenge. The only technology capable of accessing the whole of the GI tract is capsule endoscopy, but with limitations. Capsule endoscopy is a passively driven capsule that passes through the GI tract after being swallowed. The camera system on board observes what the camera is directed towards at any given time, but this is determined by how the peristalsis forces the capsule through. During the passive travel through the body the camera can rotate around and even encounter foreign bodies already inside the GI tract such as food or tumour growth, which can obscure or redirect view. So there is no guarantee that all regions of the GI tract can be observed with this dependance on the natural movements of the GI tract directing the capsule.

In section 1.3 tactile sensing and palpation are discussed as a crucial practice in

medical diagnosis. As haptic technology advances along with tactile sensing technology it has become more plausible to develop systems that can present remote palpation opportunities. This provides the advantages of recorded data, overall consistency in approach and most important minimally invasive access to regions of the body that typically need surgical procedures to access. This highlights a potentially new technology that can introduce medics to an entirely new experience of diagnostics treatment and a simpler less invasive and more comfortable experience for the patients. The following chapter will explore ideas to realise a minimally invasive tactile sensing diagnostic capsule.

In section 2.2.3 tactile sensing technologies are reviewed in relation to medical applications. It was identified that there is a lack of tactile sensing technology in today's medical equipment, and further to this no technology yet exists that utilises tactile sensing technology in a capsule endoscopy. It has therefore been determined that an opportunity for novel work bringing together tactile sensing and capsule endoscopy has been identified. Shi et al. [18] discusses the importance of the GI tract motility and how failings in motility can be an indication of more serious GI diseases. This technology could provide a comfortable early stage diagnostic tool to identify GI tract motility state. Furthermore, conditions growing beneath the lumen may not show visual symptoms on the inner wall of the lumen until much later, whilst formation of lumps and growths beneath the lumen could be identified sooner if palpation were possible.

This chapter reports the design and build of a tactile sensing capsule, and characterise it in a laboratory environment. The tactile sensing capsule has potential for detecting contours and shapes inside a GI tract-like environment. This has been achieved using the biomimetic sensing device Tactip, redesigned to suit the form of a capsule endoscopy. The cylindrical Tactip is characterised through a series of in-vitro experiments.

This chapter tackles the following task that were outlined the work plan, section 2.4:

- 1.(a) **Develop** a tactile sensing system capable of identifying surface deformation.
- 1.(b) **Develop** a tactile sensing system capable of identifying artificial tumour like lumps.
- 1.(d) **Consider** a soft sensing structure to minimise the impact on the patient and allow for compliance around the changing bowel environment.

- 1.(e) **Consider** a sensing system which can be easily miniaturised in future developments.

### 3.1.1 Technology Selection

Whilst all the discussed tactile sensing methods have proven competencies in their given scenarios, they are not all ideally suited to the role of tissue palpation on the exterior of a small endoscopy capsule. The following list describes the requirements on a tactile sensor for such an application;

- The sensor should be compliant to accommodate the changing bowel environment caused by the winding nature of the intestines, potential for contact with foreign bodies and peristaltic action of the gut.
- The sensor should have a sufficient resolution to detect small early stages formations of unhealthy tissues. [151] identified that cancer is known to occur more frequently in larger polyps, with finding cancer present in 1% of adenomas (benign tumour) smaller than 1 cm, 10% of 1-2 cm adenomas, and nearly 50% of adenomas larger than 2 cm. Whilst adenomas form in the colon and rectum, no dimensional statistics could be identified regarding formations in the small intestines. So this standard will be used as an indicative guide for lump / polyp size. [152] state that sizes of 6-10mm is a critical threshold for clinical decision making for polypectomy versus polyp surveillance. A development device which is larger than intended final design can be tested against relatively scaled tumour test models.
- Design of the sensor has to conform to capsule endoscopy. Size of a development device can be relatively larger as longer as it is tested against comparable tumour like features.
- The sensor should be robust against the influence of peristaltic, sudden movement etc.
- It should be possible to miniaturise any larger prototype

Reflecting back on section 2.2.3.1 where the human sense of touch is described, the full range of tactile sensing is achieved through four types of mechanoreceptors spread

throughout the boundaries of the glabrous skin. Many of the technologies discussed in section 2.2.3.2 show tactile sensors which are comparable to just one mechanoreceptor. In some situations this has been proven to be sufficient, however there an array of sensors within the skin is capable of sensing a range of stimulus. It is the intention of this development to build on the acknowledged excellent tactile perception skills of clinicians utilised through palpation techniques during examination procedures. With this in mind, it is logical to replicate the sensing modalities of human tactile perception as closely as possible. For example, if MEMS technology was considered, it would require a MEMS sensor for each mechanoreceptor of the many that we have just discussed. This would be mechanically and electrically complex, potentially fragile and challenging to iteratively reform to fit capsule endoscopy form. In fact, it is likely that only optical based sensors can replicate the role of multiple mechanoreceptors with simple complexity and mechanical design due to the vast number of light sensitive pixels in a compact space of a CCD camera. Both the work of Xie & Back and the BRL's Tactip match this profile of replicating multiple mechanoreceptors, with the Tactip offering a higher density of mechanoreceptors to tactile space if the number of papillae are indicative. Whilst many technologies identified could be potentially suitable to tackling this challenge, the Tactip offers sensing of force, shape deformation, motion in a form that has potential for miniaturisation.

## 3.2 Proof of Concept Study

In the following section the tactile sensing technology identified in subsection 3.1.1 will be detailed and considered in the context of capsule endoscopy. The following section was published as an extended abstract in Living Machines 2014, Milan, Italy.

Modern advances in optical diagnostics have developed capsule endoscopy(CE) such as the PillCam ®from Given Imaging, which is a passive imaging system in the form of a large pill swallowed by the patient. CE is used to inspect the GI tract by use of an internal imaging camera. A capsule endoscopy allows a more comfortable examination for the patient that can reach further into the GI tract than traditional endoscopy. However with up to 8 fps only and direction being determined by the peristaltic motion of the gut, identification of tumours is not guaranteed along the whole length of the GI tract.

The Tactip tactile sensor is proposed to be placed on the outer surface of a CE so that it can trace along the wall of the intestines during travel through the GI tract. Using established signal processing algorithms the Tactip can identify raised bumps which deform the surface of the sensor. Previous work by Roke et al.[130], has shown that the Tactip is capable of tumour detection in the context of remote palpation of artificial tissue.

In previous work, [4] has shown that the Tactip is also capable of texture analysis whilst being dragged along a textured surface. It is the application of tumour detection and lateral movement along a target surface that could enrich the detection capabilities of CE. Tactip is a biologically-inspired sensing device, based upon the deformation of the epidermal layers of the human skin. Deformation from device-object interaction is measured optically by tracking the movement of internal papillae pins on the inside of the device skin. These papillae pins are representative of the intermediate epidermal ridges of the skin, whose static and dynamic displacement are normally detected through the skin's mechanoreceptors, see Fig.2.23.

PillCam® capsule endoscopy is a commercial product used within the medical industry as a minimally invasive endoscopy tool. The pill is swallowed by the patient and an internal camera records the journey through the GI tract. Spada et al. report a case study [12] identifying the advantages of the PillCam over traditional endoscopy. The work concludes that the PillCam can be a feasible and safe diagnostic tool, and may represent an alternative in cases of difficult or incomplete colonoscopies. However, Triantafyllou et al. [13] evaluated whether CE can complete colon examination after failure of conventional colonoscopy. Their findings conclude that in a series of patients with incomplete colonoscopy, CE did not always satisfactorily examine the colon due to insufficient exposure to the entire region at risk.

Fig.3.1 demonstrates the concept of placing a Tactip sensor around the surface of a capsule endoscope. As the capsule passes naturally through the GI tract, the walls of the capsule push against the intestinal wall which will stimulate the Tactip sensor. After extensive research, it was clear that little or no work has been published exploring such a tactile sensor on a capsule endoscope with the intention of tumour detection.

An initial proof of concept experiment has been performed whereby a Tactip sensor has been laterally dragged along the surface of an artificial tissue sample. Embedded within the tissue sample is an artificial tumour. Cancerous tumours typically form as

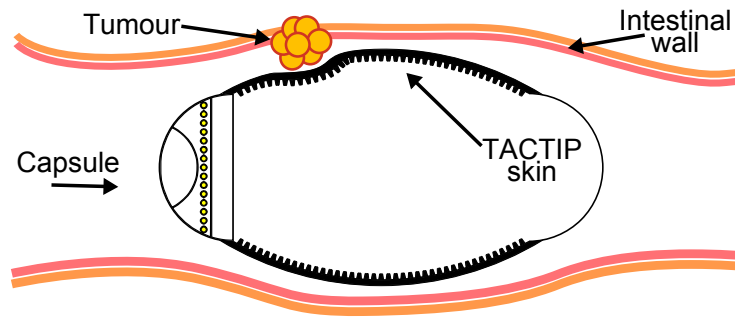


Figure 3.1: Tactile sensing capsule endoscopy.

hard lumps in the soft tissues of the body and many studies have shown that tumours are stiffer than surrounding tissue [153; 154; 155]. The density of the tumour is much greater than the surrounding tissue and so it leaves an impression on the Tactip surface which is easily identifiable with image processing as presented by Assaf et al. [129]. Fig.3.2 demonstrates the internal Tactip view with the output from the image processing algorithm overlaid over the raw camera image. The three images show progression of the Tactip across the tissue sample with the identified tumour moving from right to left.

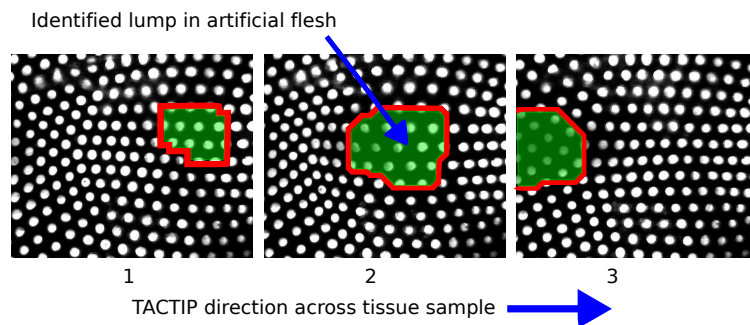


Figure 3.2: Tactip demonstrating lump detection. The Tactip is laterally pushed along an artificial tissue sample from left to right and the embedded tumour is shown moving right to left.

An initial experiment has shown that the Tactip sensor has potential as a tactile sensor for capsule endoscopy with the ability to detect tumour like objects embedded in soft tissue walls. The Tactip design can be modified to fit on to the exterior of the capsule. This would offer either an alternative to the standard image camera, or an additional sensing technology to enrich overall tumour detection.

### 3.2.1 Standard Tactip Design

In section 3.2 the Tactip sensor was introduced and proposed as a tool for sensing deformation caused by palpation. The following section will delve into the original standard Tactip design and detail previous applications. Due to the biomimetic design of the Tactip, its tactile sensing capabilities resemble that of the human finger. The modes of sensing include pressure force, shear force, shape characterisation such as edges and corners and more recently texture discrimination with the addition of artificial fingerprint features [156; 132; 4; 3]. A number of approaches exist to interpret the image data captured during object interaction. Roke et al. 2011 [2] utilised a relatively simple algorithm to detect deformation as a 4 x 4 matrix of pressure values; "The deformation of the sensor membrane is determined by grading the regional movement of the internal papillae against calibrated values. The regions of papillae selected are treated as individual sensels (sensor elements). A simple algorithm is used to average the shade of the pixels within each region of the greyscale image. As an area of the surface is deformed, the underlying papillae deflect away from each other, thereby decreasing the average brightness of the area. This can be seen in Fig.3.3.

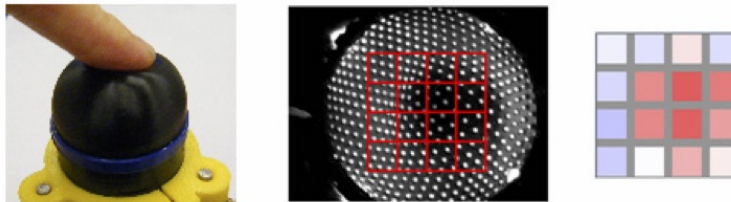


Figure 3.3: Average shading algorithm presented by Roke et al. 2011 [2]

Assaf et al. 2014 [3] have developed an algorithm for real time contour following. The algorithm uses dilation and erosion machine vision techniques to identify low density regions of papillae pins caused by concave deformation of the sensor skin. Dilation is the process of enlarging the boundaries of regions of foreground pixels, whilst erosion is the opposite process of enlarging boundaries of regions of background pixels. In this context it increases the regions of white circles or papillae pin tips until the only remaining black region is that of the deformation caused by object contact. The areas of low density highlight where an object has made contact with the Tactip. This region presents an opportunity for a blob tracking algorithm. A blob tracking algorithm is a

method for tracking regions of adjacent pixels that all share a common characteristic such as colour or brightness. The size of the blob is an indication of the pressure of contact and the shape of the blob is an indication of the object shape. Fig.3.4 demonstrates how this algorithm can discriminate between straight edges and corners. Using this method to identify and analyse edges produces orientation information, which is particularly useful when trying to follow the contours of a shape.

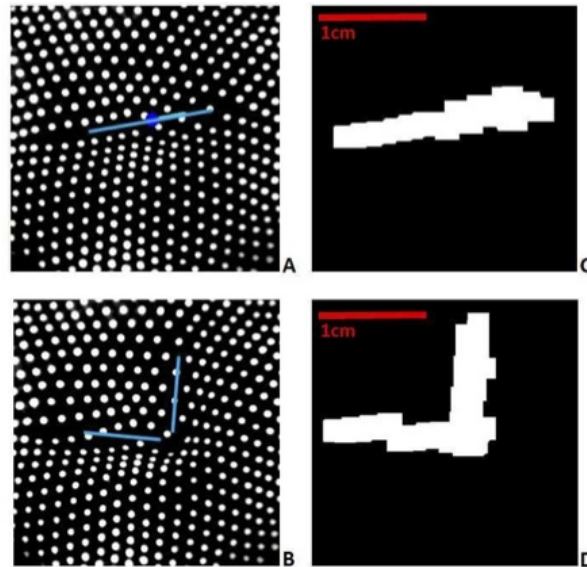


Figure 3.4: Blob detection algorithm presented by Assaf et al. 2014 [3]

Most recently a fingerprint like surface has been developed by Winstone et al. 2013 [4]. In this experiment a high speed camera is used to achieve 1 KHz sample rate whilst monitoring one papillae pin during dragging contact across various textured surfaces. In this context the camera is replicating RA type 2 Pacinian corpuscle mechanoreceptor because of its function in detecting texture stimulus. The results show that the addition of artificial fingerprints is necessary to detect finer textures. The algorithm used is very simple, whereby just one pin at the centre of contact is tracked by the camera. Pixel displacement is recorded and translated into a time based waveform. This waveform is passed through FFT analysis to provide frequency spectrum analysis which can then be passed through a learning classifier system such as an ANN so that history can be incorporated for texture identification. Fig.3.5 shows the Tactip sensor at the end of a 6-axis robot arm being dragged along different surfaces, alongside an internal view of the Tactip to monitor just one pin.

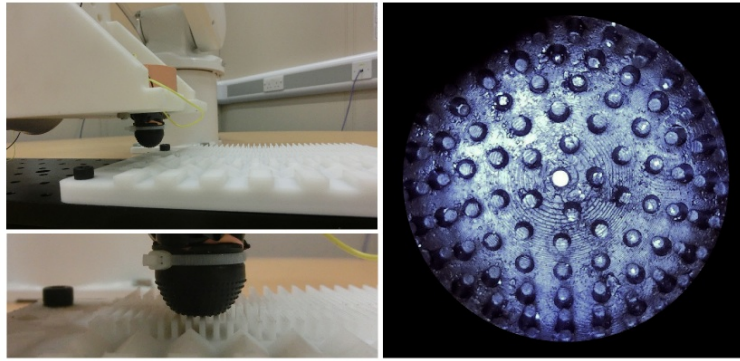


Figure 3.5: Texture discrimination experiment presented by Winstone et al. 2013 [4]. With permission of Springer, Conference on Biomimetic and Biohybrid Systems, Living Machines 2013: Biomimetic and Biohybrid Systems pp 323-334

Developments of the Tactip to date have shown that the sensor is capable of various types of surface deformation, in particular pressure and lump detection, and also surfaces roughness. The algorithms offer a good starting platform for a cylindrical Tactip capable of detecting circumferential pressure and lump deformations.

### 3.2.2 Tactip Design and Manufacture Process

The original Tactip device described by Chorley et al. [109] comprises of a camera looking through a plastic tube to the silicone skin mould with pins that simulate the fingertip papillae. The overall size of the device is 40mm in diameter, a little over twice the diameter of a human fingertip, which is approximately 16-20mm diameter. The skin, hosting approximately 526 pins, each 1.5mm in height and 0.75mm in diameter at the base, was made using a vacuum casting process.

Using 3D printed moulds (Fig.3.6), a soft silicone negative mould is prepared that forms the papillae pins. The material used is a silicone RTV 240, Shore A 20 hardness. This mould shapes an inverted skin, for ease of casting, so that the pins face outwards. A soft mould is used because it allows safe and easy removal of the final silicone skin without tearing or loss of pins. The skin is 0.5mm thick so it presents no problems being inverted. The silicone skin, Vytaflex Shore A 60 silicone rubber, is a two part 1:1 ratio mix with a small amount of black pigment that is susceptible to bubbles unless correctly de-gassed in a vacuum chamber.

The de-gassing process also aids in pulling the silicone in to the mould cavities increasing the chance of a successful mould. A second 3D printed part is then placed

on top of the silicone mould to form the outer wall of the skin. Curing takes around 10 hours. Once set, the silicone skin is cut out, the tips of the pins are painted white to contrast with the black pigmented silicone, aiding the image processing task. Finally an optically clear gelatinous polymer, RTV27905, is poured in to the skin and held in place with a clear acrylic lens.

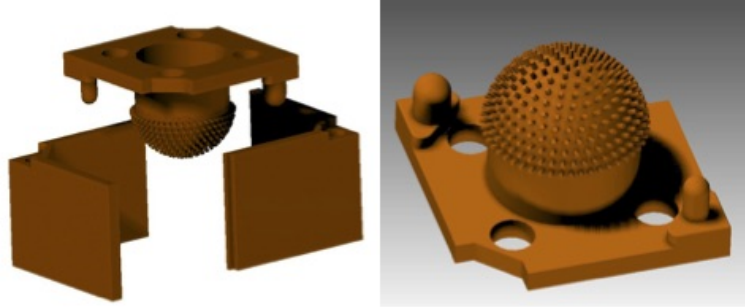


Figure 3.6: 3D printed mould assembly. Note that to aid in successful casting of the skin, the mould is inverted and the skin is later reversed so that the papillae pins face inward, Winstone et al. [132].

### 3.3 Methodology

The following section details the methods explored to modify the standard Tactip design so that it fits the cylindrical form of a capsule endoscope. This process has utilised modern manufacturing processes to overcome challenges presented by manufacturing a cylindrical Tactip, along with the adoption of a new mirrored lens component and new sensing algorithm.

#### 3.3.1 Cylindrical Tactip Concept - Design Challenges

Transforming the original Tactip into a capsule form presents three main challenges.

1. Creating a cylindrical skin. This could be done either using a flat piece of skin and stitching two edges together or it could be cast in a cylindrical shape. This creates complex casting issues, in particular removing the cured skin from the mould. The current Tactip skin design is cast in an inverted state and its orientation is corrected after curing. This process is used in order to achieve successful casting of papillae pins and removal of the cast from the mould. A second casting process forms the optically clear gel encased by the skin. A cylindrical Tactip would have

to seal around a cylindrical window or tube, whilst providing means to inject a gel and release any trapped gas.

2.  $360^\circ$  field of view. Achieving a good quality optical view of a  $360^\circ$  field presented in two dimensions requires additional image processing to unwrap an image. Two options are apparent to capture the data. The first is to scan the field of view by rotating the camera, the second is to redirect light using a mirror system such as a catadioptric panoramic lens mirror. The scanning method introduces new issues in the form of the number of images required for a full scan, in combination with the camera frame rate. The total time for a complete scan would be much greater than using a mirror system. The data acquired with this method would provide less of a challenge preprocessing the image and localisation of image data would be linked directly to the scanning motor position.
3. A final challenge in miniaturisation and implementation is removal of all tethering. Whilst at proof of concept stage, a tethered system is sufficient, practical implementation would require complete untethered freedom. Radio transmission video cameras provide a real time video stream to a compatible receiver. Although it is possible to process data captured onboard with a microprocessor, further effort should be made on proving the benefits of tactile sensing and on using a compact wireless video transmission system, where data captured can be transmitted directly to a control PC where various methods of image interpretation can be explored.

### 3.3.2 Design Solution

Taking this initial proof of concept to fit the constraints of a capsule endoscopy, the Tactip required a physical redesign in order to fit the correct form. This capsule pill form seen in the PillCam and many examples discussed in Chapter 2 is an elongated cylinder with spherical ends. The external surface of a capsule which contacts the intestinal lining is cylindrical, so the Tactip skin must cover the cylindrical surface. This presents a new problem in capturing the surface deformation as the surface now covers a  $360^\circ$  field of view.

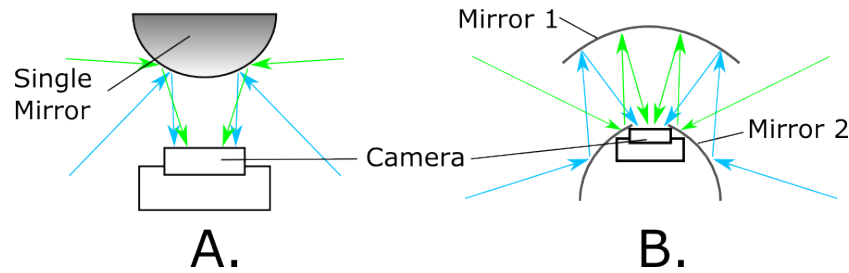


Figure 3.7: Catadioptric panoramic mirrors to achieve 360 degree field of view. A. Single mirror system, B. Double mirror system..

### 3.3.2.1 Optical System Design

Fig.3.7 presents how the concept of a 360° view camera system works. A catadioptric system uses a combination of mirrors and lenses to achieve focus on a subject that would not typically be possible with a lens alone. Parabolic mirrors are used to reflect light in to the lens from a much greater field of view. Fig.3.7.A shows a single mirror system that uses a convex parabolic mirror. The field of view is determined by the combination of the diameter of mirror, distance of the mirror from the lens and the the aperture of the lens. An alternative formation is shown in Fig.3.7.B whereby a double mirror system is used. By altering size, shape, distance and number of mirrors a specific field of view can be acquired. However, these solutions are not perfect as they present distorted and warped images that need to be processed to view in a standard two dimensions format. This distortion is not uniform, for example a subject placed within one region of the field of view will not occupy the same area of the image sensor when reflected through the mirrors, as it would if placed in another region. As such processed images will have regions of stretched or compressed data. Also, the centre of the image is subject to a blind spot. Fig.3.8 presents the proposed method of capturing a 360° view using a catadioptric panoramic lens mirror. The mirror is placed centrally at the opposite end of the camera. The mirror reflects the cylindrical view of the Tactip skin directly to the image sensor translating three dimensions into two dimensions. A commercially available catadioptric mirror system has been identified in the Kogeto Dot 360 which is a 360 lens for an Apple iPhone. It is appropriate in both field of view during a prototyping stage and economically viable during this study.

The form of the image presented to the camera can be seen in Fig.3.9. The span of the Tactip skin rotates around the centre of the image. In doing this the density of

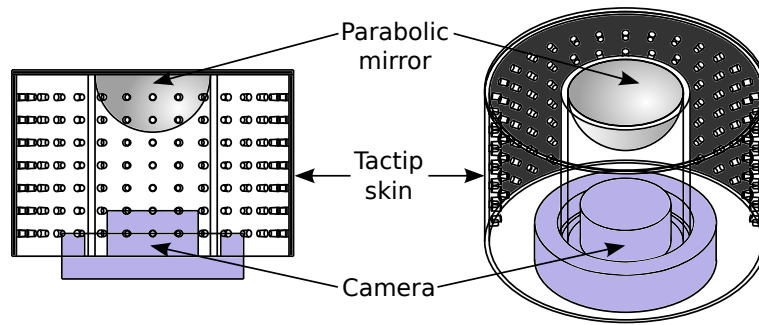


Figure 3.8: Cylindrical Tactip design utilising a catadioptric panoramic lens mirror to achieve a  $360^\circ$  field of view.

pins at the centre of the image is much higher than at the edges. A scaling ratio can be considered where the circumference of the top of the cylinder through the camera view and the circumference of the bottom of the cylinder compared show the distortion of the view. This affects the sensor in a way that if a papillae pin nearest the mirror moves by one pixel in the camera view, the same physical movement of a papillae pin furthest from the mirror would move many times more in the camera view.

A simple and yet effective image processing algorithm for Tactip data has been presented by Roke 2011, [2] where regions of papillae pins are summarised with a function that calculates the average grey scale value within the region. This works because focal points of pressure causes pin separation exposing more black background that dominates the region whilst the white pin tips are pushed away from the pressure point. Areas with more white pin tips have a higher grey scale value than those with more exposed black background. This approach can be applied to the wrapped image seen in Fig.3.9. If the image is split radially and each region occupies the same number of pins as the other regions, then the average grey scale value could be calculated the same way as Roke 2011.

Whilst Roke's approach is capable of detecting pressure points to  $4 \times 4$  grid resolution of the original Tactip, it will not be enough to detect the precise surface deformation needed for tumour classification. Each papillae pin offers two degrees of free information for the area of tactile skin it is directly attached to. By analysing individual pin movement a greater depth of tactile information is available. In order to achieve accurate pin movement, the distorted image acquired from the mirror system must first be unwrapped so that all pins are the same relative size. This distorted image can be

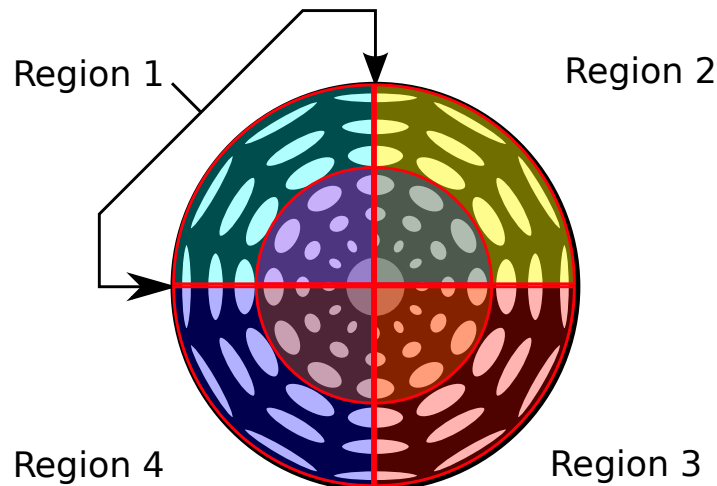


Figure 3.9: View of cylindrical Tactip presented by catadioptric panoramic lens mirror.

simply unwrapped for ease of image process, which is described further on in section 3.4.2.1.

The internal view through the catadioptric mirror occupies  $406 \times 406$  of the  $720 \times 1200$  resolution camera view. Whilst there are 13 rows of pins in the device, only the middle 5 are consistently visible to the camera due to the angle of view of the mirror system. Fig.3.10 details the rows being monitored and their number, where 2 is the middle row. The  $360^\circ$  degree view is presented as a ring which is later unwrapped into a 2D representation, see Fig. 3.11. Axial movement of pins has a relationship of 1 pixel to 0.24 mm, whilst radial movement is more complicated. If the middle row of pins is considered, they are situated within a circumference of 946 pixels. This determines the minimum pin movement that can be detected radially. The outer diameter of the device at the point of this middle row is 63 mm, whilst the tip of the papillae form a diameter of 54 mm, and circumference of 201 mm. This determines that one pixel covers 0.21 mm. The inner row has a smaller physical circumference of 167.5 mm, and pixel circumference of 726 pixel, providing a relationship of 1 pixel to 0.23 mm. Finally the outer row has a physical circumference of 167.7 mm, pixel circumference of 1165 and relationship of 1 pixel to 0.14 mm. The catadioptric mirror has produced a system that provides greater sensitivity to certain areas than others, and the rounded shape of the Tactip further distorts this perspective. Whilst the system can detect between 0.14mm and 0.24mm depending on the papillae pin location within the field of view,

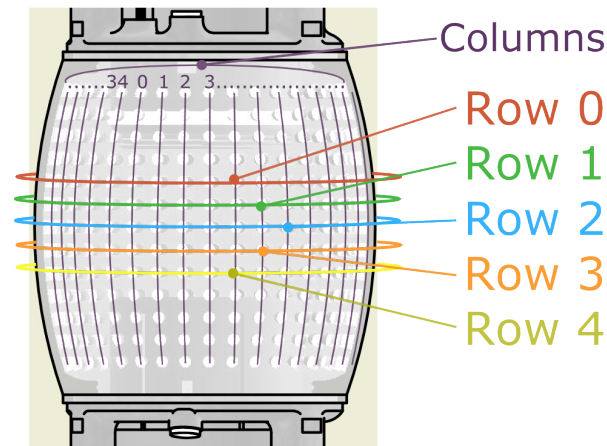


Figure 3.10: Relationship between physical papillae pins and the columns and rows reference in the machine vision analysis.

the evidence exists that suggests that the image processing method super-resolution can be applied to tactile perception to increase the resolution of array based sensing, [157; 158].

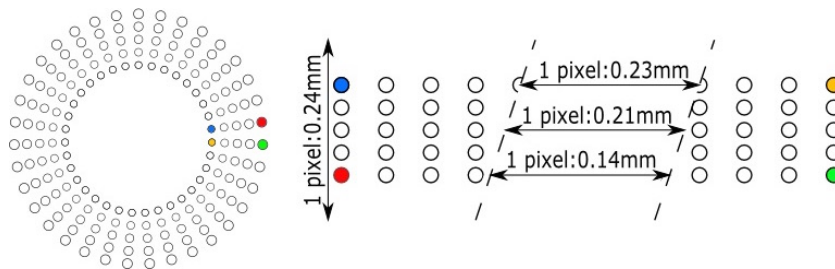


Figure 3.11: Left: Diagram showing pin orientations from raw image before unwrapping. Right: Diagram showing pin orientations from unwrapped image and relative pixel to distance ratio for radial and axial movement.

### 3.3.2.2 3D Printed Cylindrical Tactip Capsule Design

The cylindrical Tactip presents moulding challenges. The traditional Tactip design was moulded in an inverted state in order to encourage the papillae cavities to fill with silicone during the vacuum process. The bulbous cylindrical nature of this new design causes difficulty in using a two part mould, because the internal mould would have to deform once inserted in order to fill the space. The outer rings of a bulbous cylinder have a smaller diameter than the rest of the body so create bottle necks for mould assembly parts to pass through. Whilst it may be possible to design a many multi-part assembly that tackles this problem, it requires a long iterative design process

which would be equally costly. Alternatively with the recent availability of 3D printing rubber materials, the Tactip can be printed in one quick process negating the need for casting the skin.



Figure 3.12: Complete 3D printed cylindrical Tactip skin. Printed from two separate materials, solid vero white, and soft tango black.

Using the Objet 260 connex 3D printer it is possible to print multi-material objects. Materials can be solid, soft or some intermediate density in between. Relating this idea to a cylindrical Tactip it is possible to print a solid frame bonded to a soft skin. Fig. 3.12 shows a 3D printed form of the cylindrical Tactip, with Fig.3.13 presenting a cross sectional view of the assembly of the device. Whilst the printer can produce a range of material properties, it cannot produce optically clear material. The Tactip requires a clear lens that interfaces with the flesh like gel in order to allow containment of the gel and also optical access to the skin deformation. In an ideal situation the Objet machine could print all components of the cylindrical Tactip but for now additional components are required to fulfil these roles. A clear acrylic tube will be used as the lens between the camera and gel. TECHSIL RTV27905 silicone gel is used as the flesh like optically clear medium. Using the multi-material 3D printing, solid vero white end caps are printed with the soft tango black plus rubber skin to form a single part. These end caps have integrated rubber seals which interface with the internal acrylic tube to containing the gel, preventing leaks. Externally, a plastic glue is used to form a structurally solid bond. Once the solid elements of the cylindrical Tactip are assembled, the soft silicone gel can be injected to complete the build process. One of the end caps has been designed with an inlet for a syringe tip. The gel is injected slowly from the base, such that filling the Tactip pushes the air inside the cavity out through the top release hole. When completed, the two holes are sealed and the Tactip is left to set on a rotating platform so that the gel sets uniformly. Fig.3.14 presents an exploded view of the cylindrical Tactip. As with a traditional Tactip design, it comprises an artificial

3D printed skin, optically clear flesh like gel, camera and internal illumination, but in addition uses a catadioptric mirrored lens. The camera used is a Microsoft LifeCam Cinema HD.

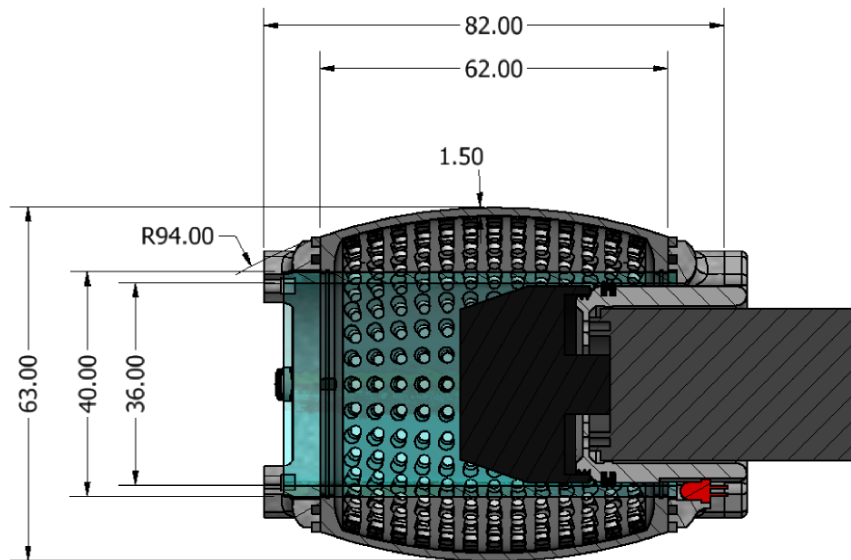


Figure 3.13: Cross section view of Tactip capsule assembly.

Through the use of new 3D printing technology it has been possible to avoid casting a skin, and instead use an Objet Connex 260 printer capable of simultaneously printing in hard and soft materials. This new skin has been designed to fit and seal to an internal clear acrylic tube which acts as both a main body structure and a barrier to contain the flesh like gel. The quality and robustness of such printed material is not yet as good as a cast rubber silicone, however for the purpose of experimentation it greatly speeds up the whole development process.

This current model is larger than a typical capsule endoscopy pill, however, its miniaturisation is achievable. With the restricting factor of the size of the catadioptric mirror system where one-off custom mirrors could be expensive. Mass production would remove this cost to achieve a much smaller mirror system, and accompanying electronics can be miniaturised. All other components are easily miniaturised such as the camera, which is evident in current capsule endoscopes, and materials which have already undergone considerable reduction in [132] & [4] where reduced models suffered no loss in sensitivity.

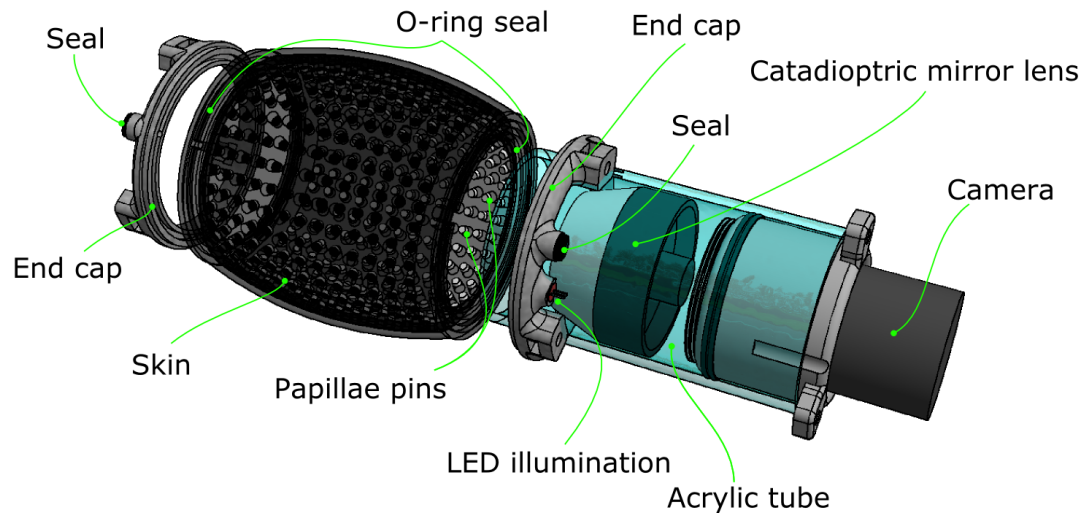


Figure 3.14: Exploded arrangement of cylindrical Tactip capsule endoscopy design.

### 3.3.2.3 Limitations of 3D Printing

There are many advantages to using 3D printing technology during a prototyping process. The original Tactip design required two casting processes, one for the skin and one for the gel. This creates at least a day of curing for each casting process. Add to that painting the papillae tips white, if and when the skin casting process is successful. Essentially the physical build process of the original design takes at least one week to complete, which is before further assembly of electronics and fixtures. 3D printing the cylindrical Tactip requires one day print, and one day curing of the internal gel. The tips of the papillae are coloured by using a different material in the multi-material printer so no painting is required, and any seals required to keep curing gel in place are designed in to the part, so no additional components are needed. The use of 3D printing has dramatically reduced the production time of each design iteration.

Whilst rapid development times are an attractive choice, 3D printing is not without faults. Fig. 3.15 shows tears that have developed on the skin of the cylindrical Tactip during experimentation. 3D printed materials do not yet have the structural integrity of traditionally formed or cast materials, and as such are not as robust. This compromise is acceptable during a prototyping stage of development, especially considering the advantages gained in production speed. However, a real life implementation would require substantially more robust materials.



Figure 3.15: View of fractured 3D printed skin that occurs much quicker than cast silicone skin. The fatigue is caused from repeated contact and friction with another surface where over time the integrity of the flexible rubber breaks down.

### 3.4 Experiment - Characterisation of Cylindrical Tactip, Lump Detection

In the following section the newly developed cylindrical Tactip is tested within a laboratory set up to evaluate its working characteristics. The following experiment was presented at Living Machines 2015; Winstone et al. [150] "Biomimetic Tactile Sensing Capsule", Conference on Biomimetic and Biohybrid Systems, 113-122, 2015, Springer International Publishing.

#### 3.4.1 Experiment Hypothesis

The hypothesis of this experiment is that the newly designed cylindrical Tactip is capable of detecting surface characteristics during travel through cylindrical or tube like environment. This hypothesis and experiment are a precursor to later designs of a tactile sensing capsule endoscopy device that will be complimentary to a soft and compliant robotic actuation capsule endoscopy system.

#### 3.4.2 Experiment Design

The intention of this experiment is to identify the following;

1. Can the cylindrical Tactip sense in 360 degrees whilst moving axially?
2. Can the cylindrical Tactip discriminate between different types of obstructions, i.e. shape, size or density?
3. Can the data be represented in a way easily interpretable by a human?

The experiment environment has four components, a cylindrical Tactip for sensing, a six axis ABB IRB120 robot arm for capsule locomotion, a 74mm internal dia. acrylic tube and six artificial lumps placed randomly along a length of 250mm, see Fig.3.16. The robot arm is used as a mode of capsule locomotion.

The acrylic tube represents the tunnel like intestinal tract. Whilst it shares limited comparison with an organic human tract, it does offer the ability to determine exact positions of deformation of the sensor for proof of concept and characterisation. In subsection 2.3.2 it was declared that this work would focus on proving the integration of technologies before realistic environments can be considered. With this in mind, this environment is suitable to achieve the intentions of this experiment. The future vision is that the capsule would be capable of untethered locomotion through the GI tract with the addition of an appropriate locomotion system, however this experiment focuses purely on the tactile sensing capabilities.

Two sizes of lumps are used in this experiment. The sizes chosen, 10mm and 8mm in height and both 35mm diameter, explore a range of impressions on the Tactip without exceeding a maximum deformation of the sensor. The maximum deformation achievable on cylindrical Tactip is 7mm before the papillae pins contact the internal acrylic lens. A 10mm high lump causes 4.5mm deflection, and the 8mm high lump deflection is 2.5mm. The gap for lumps is between the 63mm outer diameter of the Tactip and 74mm internal diameter of the acrylic tube. It was considered that using larger lumps may cause early fatigue of the Tactip through excess force and friction as shown in Fig.3.15. These lumps are larger than would typically occur in the GI tract, however in order to match the scale of the prototype capsule their size has also been scaled up. Future work would focus on both miniaturisation of the capsule and more accurate tumour representations. There are three types of lump material - white hard plastic shore 85, hard rubber silicone shore 30 and soft rubber silicone shore 15. Using different size lumps with different material hardness it gives an indication of whether the Tactip can distinguish between all of them. In clinical use this could help characterise the actual tumour.

#### **3.4.2.1 Sensing Algorithm**

The algorithm used to interpret tactile interaction with the capsule focuses on papillae pin separation replicating the role of the Meissner's corpuscle mechanoreceptor in the

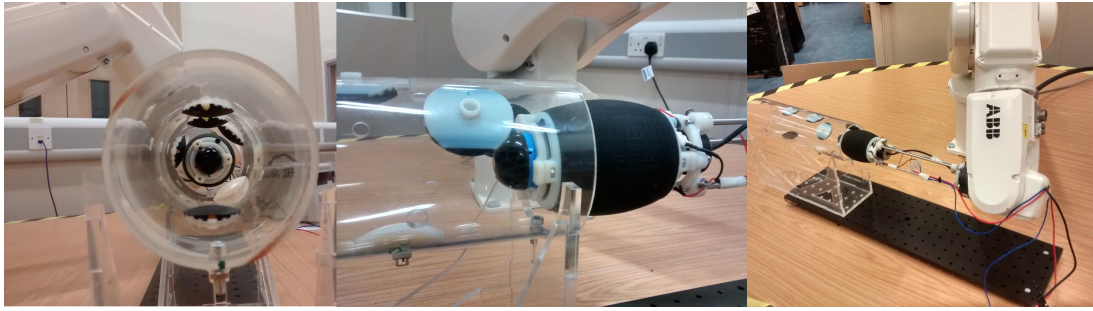


Figure 3.16: Experiment setup, ABB IR120 pushing tactile sensing through rigid tube containing raised lumps..

human finger. When objects contact the capsule skin and deform the surface shape, pins within the region of contact separate from each other whilst moving closer towards adjacent neighbouring pins. This can be seen in Fig.3.17 where the first image shows the Tactip in a relaxed state with no objects in contact with the skin, whilst the second image shows the Tactip in contact with a lump highlighted by the red circle where the papillae pins are clearly separated in the region of contact.

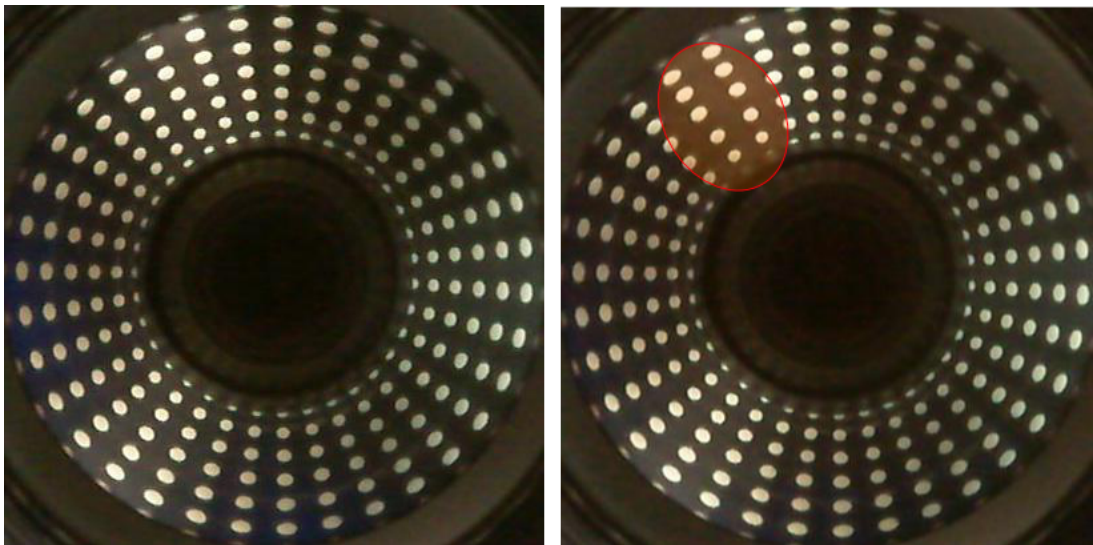


Figure 3.17: Raw camera image showing calibration state on the left, and contact with lump state on the right highlighting the location of the contact.

The first stage of image processing is unwrapping the distorted image acquired through the catadioptric lens. The following algorithm is an effective method of unwrapping a  $360^\circ$  degree image. The algorithm takes a square source image containing the  $360^\circ$  field of view, operating the function to return a translated two dimensional unwrapped image similar to that of a panoramic photograph. Equation 3.1 calculates the corresponding pixel position in the source image relative to the destination image such

that if one were to iterate through the destination image it would become populated with corresponding pixels from the source image.

$$d(x, y) = s((\cos(x * (2\pi/W)) * y) + R, (\sin(x * (2\pi/W)) * y) + R) \quad (3.1)$$

$s$  = 360 source square image array

$R$  = Radius of 360 image (pixels)

$W$  = Width of destination image (pixels)

$d$  = Destination flat image  $W * R$

$x$  = Horizontal pixel co-ordinate (pixels)

$y$  = Vertical pixel co-ordinate (pixels)



Figure 3.18: Unwrapped 360° panoramic image capture with identified pin positions.

Fig.3.18 shows the result of equation 3.1 and also subjected to the next stage of the image processing, blob tracking. Blob tracking is described in subsection 3.2.1. Blob tracking is achieved using the OpenCV feature detection library and provides accurate identification of the papillae pin positions within the camera view. In order to identify the location of deformation or lump contact, pin locations are compared against the relaxed calibrated state. In particular it is the increase in pin separation that highlights the location of skin deformation, so pixel distance between pins is used as the comparison value.

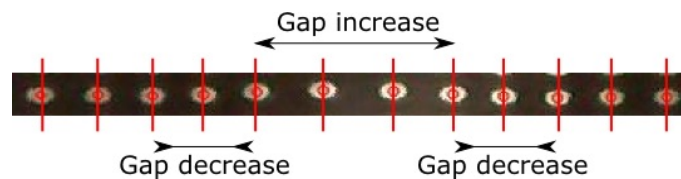


Figure 3.19: Localised group of pins subjected to skin contact showing the pins within the contact region separate.

Gaps between pins that exceed the calibrated state provide a representative value of

deformation at that location. Fig.3.19 shows a localised group of pins subjected to skin contact where the pins within the contact region separate and the adjacent neighbouring pins move towards each other. It is that pin separation value that can be used as a relative skin depression from the nominal radius of the Tactip to derive a reconstruction of the environment. In relation to the ABB IRB120 position co-ordinates, localisation of lumps and an accumulated surface profile of the tube can be achieved through active exploration. By linking the collected points through the tube scan, mesh vertices can be defined and a complete visual representation of the tube based on the Tactip sensor data alone.

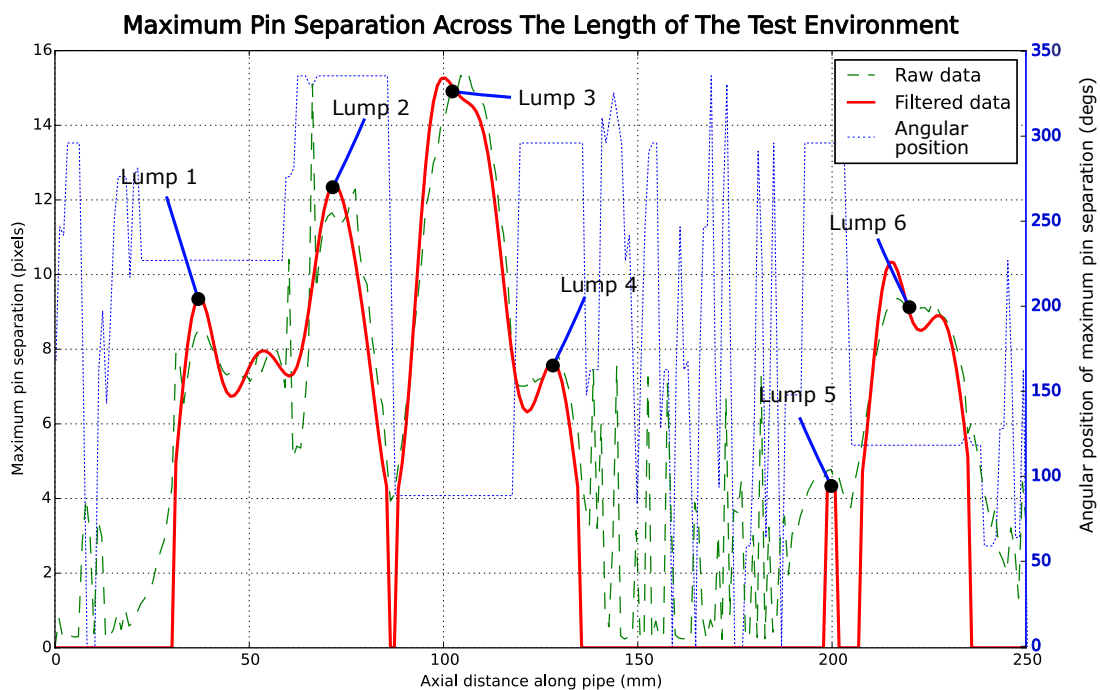


Figure 3.20: Location of maximum pin separation and angular position along length of test pipe.

### 3.4.3 Results

Table 3.1: Results of actual lump positions and Tactip detected lump positions.

Lump No.	Height (mm)	Shore A	Real Axial Position	Measured Axial Position	Std. Dev	Delta (mm)	Real Angular Position	Measured Angular Position	Std. Dev	Delta (degs)
1	10	15	47	38	4.8	-9	233	234	1.2	1
2	10	30	64	71	3	7	346	348	2.4	4
3	10	85	102	101	2.2	-1	92	90	2.8	-2
4	10	15	121	128	3.2	7	307	308	1.1	1
5	8	15	195	200	2.8	5	306	306	.8	0
6	10	15	220	221	2.0	1	125	121	2.9	-4

Using an ABB IRB120 robot arm the cylindrical Tactip has been moved through a 250mm length of 74mm diameter acrylic tube, containing six artificial tumours or lumps, 10 times. Data in the form of an image from the internal camera has been captured at 1mm increments along the length of this tube. The data has then been analysed using the discussed algorithm. The intention of this experiment has been to localise and potentially characterise lumps within a simplified artificial GI tract-like environment. Fig.3.20 presents the average maximum pin separation in pixels at each stage along the pipe. The data received after the image processing is represented by the green raw data line. The data shows some level of noise, which is most likely due to jitter in the blob detection algorithm. The second plot shows that data after being passed through a Butterworth low pass filter, and thresholding the data so that only significant changes in pin separation are acknowledged. This graph shows six clearly defined peaks that coincide accurately with the locations of the lumps in the test environment. The blue dotted on the graph shows the average angular position of the maximum pin separation. When there is no contact with a lump, there is no dominant area of deformation, so the angular position of the peak deformation is drawn to any jitter or noise in the blob detection algorithm. However, when contact is made the difference between noise and actual papillae movement is much greater causing a dominant area of deformation where the lump contacts the Tactip. Table 3.1 summarises the results of axial and angular lump detection. The table shows the exact location of the lumps with their size and material, along side the average measured location of the lumps. The results show a worst case accuracy of +/- 9mm and +/- 4 degrees. Considering that only one the middle row of papillae pins has been used

for this analysis, the axial accuracy may improve if more rows are used. With 35 pins radially per row, a space of just over 10 degrees, and accuracy of  $\pm 4$  degrees is a reasonable result. When reflecting on Fig.3.20, the results show a relationship between pin separation and lump size, whilst material hardness further influences greater pin separation. This is apparent in the maximum pin separation per lump encountered, or the height of the plot in the figure. The least pin separation is noticed with the smallest and softest lump number 5, whilst greatest separation is noticed with the largest and hardest lump number 3. The data captured by the Tactip can be collected together to create vertices and a mesh surface to present a three dimension reconstruction of the test environment. Fig.3.21 shows a three dimensional representation of the collected data.

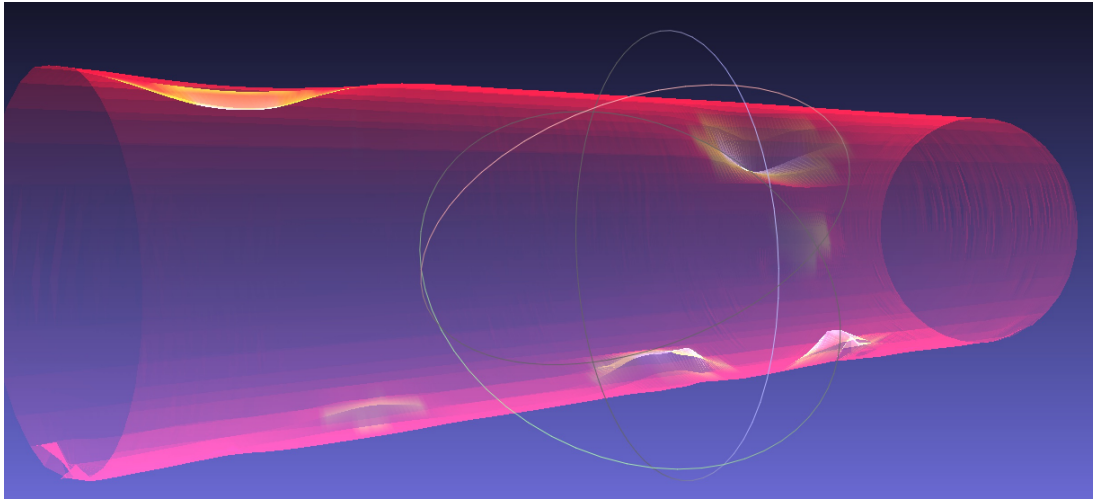


Figure 3.21: 3D reconstruction of test environment built from data captured by the cylindrical Tactip sensor.

### 3.5 Chapter Conclusion

The objectives of this chapter and questions for this experiment, are listed below. The original Tactip device has been redesigned to fit the form of a capsule endoscopy. This new Tactip has been used to identify surface deformation caused by artificial lumps based on the shapes in which submucosal tumours grow around the lumen of the human intestinal tract, addressing tasks 1.(a) and 1.(b). Through experimentation it has been shown that this new Tactip can discriminate between when there is contact or no contact with these lumps. Further to this, a range of lump sizes and hardnesses has been

used such that the data acquired has been subjected to an initial to identify changes between lump size and hardness. Whilst results suggest potential for discrimination, characteristics vary in small amounts. In cases where data is often hard to discriminate it is well suited to machine learning algorithms for further analysis. This approach will be investigated further in Chapter 4. Results so far suggest that the new Tactip has potential in the context of a tactile sensor for capsule endoscopy, but further investigation is needed to prove material density discrimination. In designing the cylindrical Tactip materials and form have been chosen that create a soft system that reduces the chance of blockage through compliance in the surface, addressing task 1.(c). This compliance also allows for better contact with the environment, in particular the lump obstructions which improves opportunity for accurate data. The Tactip device is an image based sensing device. Image based sensors provide the opportunity of scalability to the point of manufacturing constraints for their associated optical lenses and microelectronics, addressing task 1.(e). This means that if a microelectronics board and camera can be sourced small enough, and any lens and mirror components manufactured smaller, the optical components of the Tactip can be reduced in size. Whilst the 3D printing technology used for the prototype is not suitable for small components at this time, other manufacturing processes are able to produce small compliant rubber components that would replicate the Tactip skin and internal papillae pins. Now that this experiment has shown the potential of the design with a prototype of a larger cylindrical Tactip, it would be more feasible to pursue more costly but also appropriate manufacturing and materials suitable for a miniaturised design.

**Addressed Tasks:**

- **Task 1.(a): Develop** a tactile sensing system capable of identifying surface deformation.
- **Task 1.(b): Develop** a tactile sensing system capable of identifying artificial tumour like lumps.
- **Task 1.(d): Consider** a soft sensing system to minimise the impact on the patient and allow for compliance around the environment reducing risk of blockage and increasing accuracy of sensing.
- **Task 1.(e): Consider** a sensing system which can be easily miniaturised in

future development.

### Addressed Questions:

- **Question:** Can the cylindrical Tactip sense in 360 degrees whilst moving axially?
- **Question:** Can the cylindrical Tactip discriminate between different types of obstructions, i.e. shape, form or density?
- **Question:** Can the data be represented in a way that is easily interpretable by a human?

Fig.3.20 shows that the cylindrical Tactip can sense in 360 degrees, whilst Table 3.1 details its capability in determining angular position of greatest surface deformation. This figure and table prove that the Tactip can discriminate between lump characteristic, and finally Fig.3.21 presents an easy to interpret 3D representation of the the sensed data over the length of the capsule travel.

Further to these observations of the data acquired from the experiment this experiment has presented a new application for a biologically inspired tactile sensing device. Whilst first thoughts of applications lead toward replication of typical fingertip type activities, this chapter has proposed a new method of medical diagnostics. The human finger is the most suitable device for a medical practitioner to use in order to inspect a patient for suspicious tissue, however inside the body this is not possible without invasive surgery. A sensor capable of mimicking the capabilities of the human finger that can access the inside of the body without drastic surgery is the first step in creating a minimally invasive remote palpation system. This is a new capability which could lead to a new approach in diagnostics. This chapter has presented an experiment which provides evidence that the cylindrical Tactip is capable of sensing surface deformation. In successfully doing this it has also presented the sensor data as quite accurate three dimensional reconstruction of the test environment. This is a capability that would exceed that of the human tactile perception.

---

## Tactip Data Analysis with Classifier Systems

---

The following chapter is based upon the publication Winstone et al. 2016 "Towards Bio-Inspired Tactile Sensing Capsule Endoscopy for Detection of Submucosal Tumours," [159].

### 4.1 Introduction

In previous chapter 3 a development and testing of the cylindrical Tactip capsule endoscopy sensor was reported. This device has been inspired by the original biomimetic Tactip fingertip sensor and modified to be applicable to inspection of the GI tract, in particular the small intestines. Through an experiment that involved passing the device through a tube with staged lumps of different sizes and density, the sensor data was processed and reconstructed as a 3D representation of the test environment. This has proven that the sensor has the potential to interpret the surface properties with and visually reconstruct the data to be easily interpreted by a human.

In this chapter a further analysis of the output data using more complex techniques is presented. Developing technology that interacts with a patient can not only increase the accuracy of examination but also provides an opportunity to correlate new data with old, identifying patterns that may not be recorded by human interpretation. Such a system would 'classify' data in to groups such as healthy or not healthy, or where possible, with increasing levels of suspicion and severity. This chapter will explore the

use of a classifier system to discriminate between different sizes and hardness of lumps. Typical submucosal tumour like lumps are found growing circumferentially around the lumen of the intestines, and so it will be the objective of this experiment to assess if the cylindrical Tactip can identify when contact is made with a model tumour, determine its circumferential coverage and material hardness.

Building on the recent work showing capabilities of this design [150], this chapter investigates the suitability of the sensor for use with a classifier system to discriminate shape, size and hardness of bowel and intestinal deformities. A bio-inspired remote tactile sensing capsule endoscopy system with a 6-axis robot arm provides localisation and characterisation of symbolic intestinal lining beyond what is typically identifiable through vision alone. This demonstrates a suitability for remote palpation and tactile sensing but also a step towards an automated diagnostics system.

This chapter will tackle the following tasks that were outlined in section 2.4.

- 1.(b) **Develop** a tactile sensing system capable of identifying artificial tumour like lumps.
- 1.(c) **Optimise** the developed tactile sensing system in order to discriminate between different lump features. Lump features will differ in size and hardness

These tasks define a list of specifications that the developed system must meet. By meeting these specifications it will be considered that the system achieves the objectives detailed above. The system should be capable of the following;

1. Identifying a lump through Tactip deformation.
2. Identifying how much of the Tactip is in contact with the lump, i.e has the Tactip only just encountered the lump, or is the peak of the lump in the centre of the Tactip.
3. Identifying how far around the lumen the lump has grown, i.e how far around the circumference of the Tactip the lump is in contact. This will be achieved using model lumps that vary in circumferential distance up to 120°.
4. Identifying whether the lump is hard or soft. Model lumps considered to be hard will be made on the object 260 printer using vero white which is shore A 85, whilst soft lumps made from a much softer Platsil 7315 shore A 15 silicone

rubber. These two materials present examples from either end of the shore A spectrum whilst being easily manufactured in the laboratory.

### 4.1.1 Hypothesis

In this chapter it is hypothesized that typical submucosal tumour like lumps found growing circumferentially around the lumen can be detected and classified using the Tactip capsule device.

## 4.2 Review - Classification of Tactile Data

The data available from the pins of cylindrical Tactip which consistently stay within view of the camera during interaction amount to the middle 5 rows, which provides 175 vectors of displacement. Whilst a functional approach for analysis could be defined, the problem is more suited to classification system. Classification is an approach of machine learning to categorise new data in to sub-populations. By reviewing characteristics of data, patterns can be recognised that determine the best fit data class. With regards to the context of lump detection, classes to be identified could be shape, size of hardness of a lump. Using classifier systems to analyse tactile data is a proven technique. There are many different methods and approaches which are suited to different types of data. In 2005 Kim et al. [160] used a 4x4 MEMS with a sensory array with a maximum likelihood estimation algorithm to classify simple textures and Sullivan et al. 2012 [161] use a naive Bayesian classifier with data from active whisker sensors to discriminate surface textures. Additionally, Winstone et al. 2013 [4] designed an artificial fingerprint on to the external surface of the Tactip to amplify micro features and used an ANN to discriminate between surface textures.

With regard to object and shape detection, Drimus et al. 2014 [162] presented a flexible tactile sensor for classification of rigid and deformable objects using k nearest neighbour classifier system. Su et al 2015 [163] estimated force and slip detection with a biomimetic tactile sensor using an artificial neural network and Bhattacharjee et al. 2012 [164] reported haptic classification and recognition of objects using k-nearest neighbour algorithm.

Classification methods have been applied more specifically to lump and tumour detection. In 2013, Jia et al. [165] used the GelSight sensor, and Hui et al.[166] the

BioTac for lump classification using a support vector machine classifier. Hui et al. [167] it tactile perception of artificial tumours using pairwise comparisons of sensor array readings, first with a gaussian model, and then improving with a pairwise comparison model. This evidence of previous work suggests that a classification method for analysing tactile data is practical and in fact effective for lump discrimination. Selection of appropriate classification tool is discussed later in subsection 4.5.3.

### 4.3 Methods for Exploring Classification of Tactip Data

In order to achieve sufficient understanding the capabilities of a classification algorithm with the data presented by the cylindrical Tactip, similar to those discussed in section 4.2, a number of experiment features must be defined.

Firstly, what is considered an appropriate representation of a submucosal tumour like lump should be defined. It has previously been stated that submucosal tumours grow circumferentially around the lumen within the human intestines. So one variable in the tumour model design should be circumferential length around the Tactip. Cancerous tumours typically form as hard lumps in the soft tissues of the body so tumour hardness can be an indicator for concern. The second variable in the tumour model design will be material hardness. Fig.4.1 details the three stages of the model lumps that will be used in the experiment that range in circumferential length. In section 3.1.1 it was identified that the critical threshold of tumour size for polypectomy is 6-10mm. Using the 11mm diameter of the pillcam as a reference for capsule endoscopy size, the cylindrical Tactip diameter is approximately 6 times the scale at 63mm. So a relative critical threshold for tumour size would be 36-60mm. This suggests that an appropriate model tumour size would align to these dimensions. All lumps maintain the same axial profile, but circumferentially are either  $60^\circ$ ,  $90^\circ$  or  $120^\circ$  around the central axis of the Tactip. This circumferential progression represents the discussed growth of a tumour around the lumen. The second mentioned variable is material hardness. A number of different approaches have been used when creating simulated tumours, from [111] that use 3 mm synthetic tumours ranging from shore 30 A to 60 A to [168] who have used a tumour made from shore 70 A. Considering the lab facilities available to 3D print these models, the materials that can be printed or cast, two material hardnesses will be explored, a soft silicone cast shore A 15 and hard verowhite shore A 85. Each of

the three model tumour sizes will be made in both the soft shore A 15 and hard shore A 85 verowhite. Table 4.1 lists all the test pieces described, in both combinations of hard and soft. From this point forwards they will be referenced by their corresponding identifier label. These model tumour pieces will be used in conjunction with the test environment from the experiments in chapter 3.

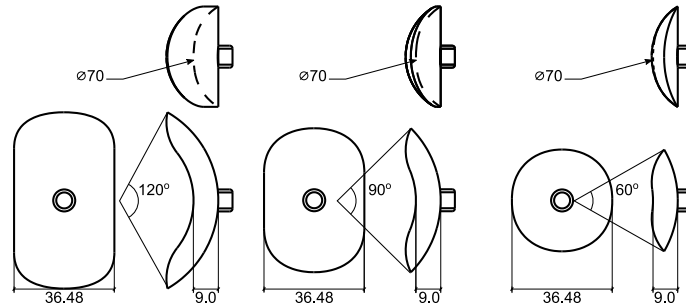


Figure 4.1: Test pieces range in circumferential spread around the pipe,  $120^\circ$ ,  $90^\circ$  and  $60^\circ$  left to right. Test pieces are in two forms, shore A 85 vero white and soft shore 15 silicone.

Circumferential Length	Hardness	Identifier
$60^0$	Shore A 15	Soft-60
$90^0$	Shore A 15	Soft-90
$120^0$	Shore A 15	Soft-120
$60^0$	Shore A 85	Hard-60
$90^0$	Shore A 85	Hard-90
$120^0$	Shore A 85	Hard-120

Table 4.1: Model Submucosal Tumour Test Pieces

Secondly, when exploring tumour density, it would be necessary to understand how the Tactip responds to the defined lump profiles when subjected to varying force. This will provide an indication of the range of forces the current Tactip design can detect relative to the material density of the model tumour in contact. This experiment will be explored in section 4.4.

Finally, the concluding experiment of this chapter will see the cylindrical Tactip moved through the test environment used in chapter 3 with the additional of the defined model tumour test pieces. The development of the classifying system will be in three stages. The first stage will explore whether detection of the lump can be achieved, and also whether partial contact or full coverage of the lump by the Tactip is needed. The second stage will explore the range of circumferential length of the lumps as shown in Fig.4.1. The third stage will explore the discrimination between hard and soft lump.

## 4.4 Experiment 1 - Cylindrical Tactip Relationship With Force

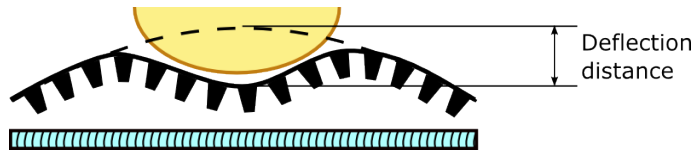


Figure 4.2: The maximum distance the Tactip can deflect before papillae pins touch the internal acrylic surface is 7mm.

In chapter 3 an initial investigation in to how the cylindrical Tactip sensor works and performs was presented. Additional characterisation, in particular an understanding of force sensitivity and range is necessary to understand the limits of this sensor. The advantage of using the Tactip sensing technology over a sensor that is not deformable is that its compliance works in favour of the extendable GI tract environment. A rigid sensor will not be capable of conforming to its surroundings. If a foreign object such as typical bowel material or a tumour was encountered in a tight section of lining, a blockage could occur. However, a compliant sensor may deform enough to escape.

In its current form the cylindrical Tactip can be compressed by 7mm from any direction (Maximum deflection distance, see Fig.4.2, before the internal papillae pins collide with internal acrylic tube. As part of future miniaturisation this proportion that the Tactip can be compressed could be increased if the camera system space occupancy is reduced, allowing a reduction in the diameter of the acrylic tube. Additionally, a flexible internal tube could be used instead of the acrylic tube, to further increase compliance with external compressive forces.

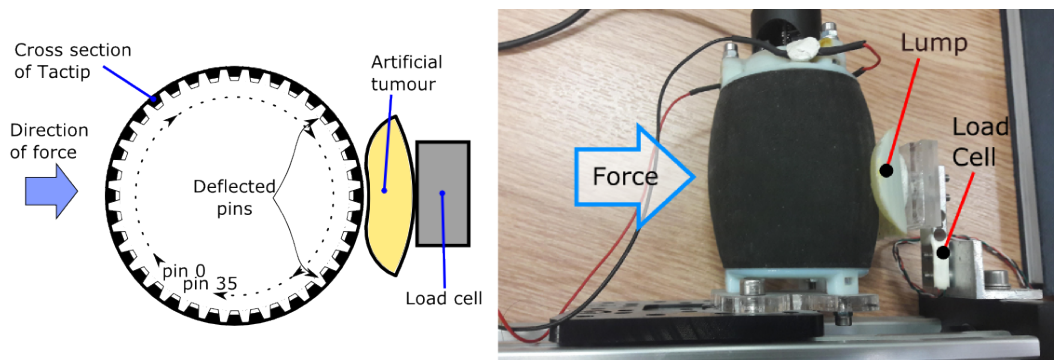


Figure 4.3: Experiment setup for characterisation of sensor force to pin displacement relationship.

To identify the relationship between papillae pin displacement and the force, shape and hardness of lumps an experiment has been performed. Fig.4.3 shows the sensor being pushed on to a lump which is directly connected to a load cell to measure the applied force. The forces required to compress the cylindrical Tactip (Fig. 4.4), saturate at  $8N$ . Furthermore Fig. 4.5 presents the average pin displacement when both loaded and unloaded to identify the extent of hysteresis. The results show a maximum of 0.3 pixel difference between loading and unloading the force. Kamba et al. [169] have identified human intestinal action applies compression forces up to  $1.9N$ . This suggests that with the sensing range of  $8N$  the Tactip could be subjected the peristaltic compressions and still be capable of sensing. Furthermore, previous work [132] has shown that changing materials for the Tactip skin increases compliance and sensitivity of the Tactip device. The design presented is subjected to the properties available from the Object 260 3D rubber printer and tango black plus material. However, it is very feasible that using more compliant materials the cylindrical Tactip would be more easily compressible to suit the weaker forces of the GI tract such that the sensitivity range can be designed to be in line with the forces identified by Kamba et al.

$$f(x) = 0.1425208 + 0.96288229x + -0.04387153x^2 \quad (4.1)$$

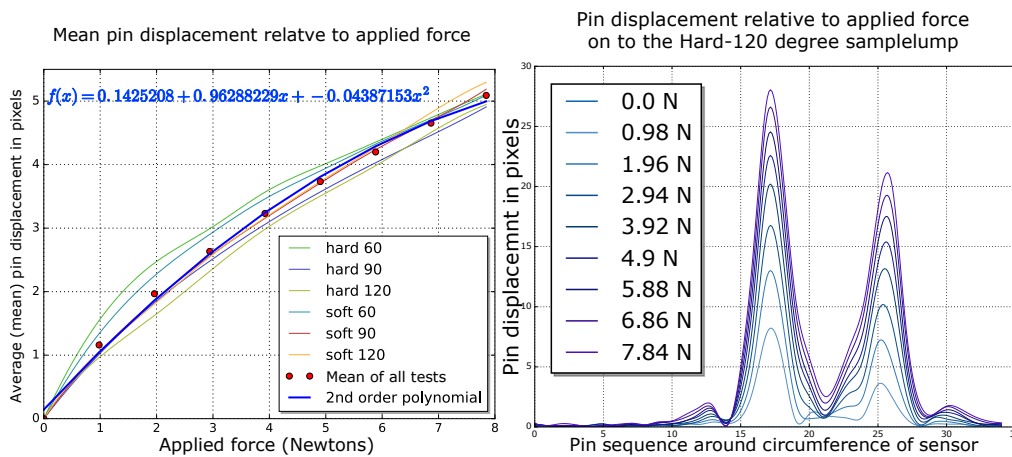


Figure 4.4: The left figure presents the mean pin displacement of the middle three rows when pressed against each of the test lumps with a known force 10 times. The mean average of all the readings from all test lumps is also presented next to a second order polynomial best fit. The right figure shows individual pin displacement of the middle row of pins when subjected to a known force on to the hard  $120^\circ$  test lump.

Fig. 4.4 shows two graphs, the first is a general representation of average pin

displacement against applied forces for a range of different hardness lumps. The mean average of all the readings from all test plumps is also presented next to a second order polynomial best fit described in equation 4.1. The second graph shows the individual pin displacement of the middle of pins at varying forces applied to the large hard-120° test lump. Both graphs show the sensitivity of the sensor even at low forces, and also the shape characteristics detectable by the sensor. Whilst these experiments have used classifier groups that start to detect the presence of a lump in 25% coverage increments in order to reduce complexity of input for the classifier, these graphs show promise for detection of much finer features at low forces.

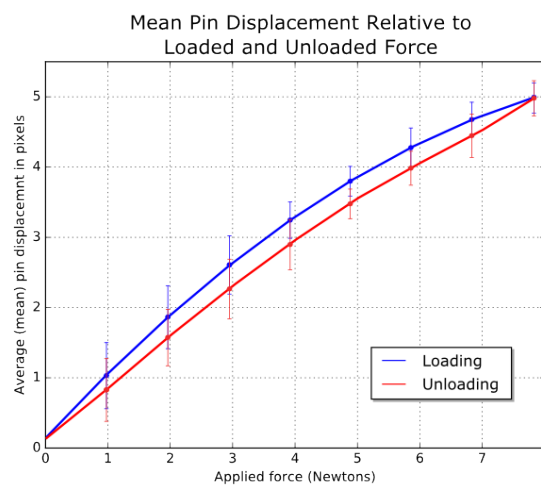


Figure 4.5: Mean results of 10 iterations of applied force to each of the lumps shown in Fig. 4.4, with standard deviated noted with error bars. Loaded force in blue and unloaded force in red.

## 4.5 Experiment 2 - Classification of Tactip Interaction with Artificial Tumour Objects

### 4.5.1 Experiment environment

The experiment setup comprises of four components, a cylindrical Tactip, a six axis ABB IRB120 robot arm, a 74mm internal diameter acrylic tube and a solid or soft test lump placed in a known location within the tube. Section

The robot arm is used as a mode of locomotion for the capsule. The future vision is that the capsule would be capable of untethered locomotion through the GI tract with the addition of an appropriate locomotion system, however current work focuses

purely on the tactile sensing capabilities. In order to collect a large sample set and test the full circumference of the sensing surface, the Tactip is pushed in 1mm increments along a 70mm long tube and then rotated by 10 degrees increments. A total of 36 scans at each millimetre length are made for each test lump providing 2520 images. At each millimetre increment within the tube 36 samples are taken at varying rotational positions, which will prove that the sensor works consistently throughout the area of tactile surface. At each instance an image is grabbed from the camera through the catadioptric lens which captures a 360 degree view, it is then translated into a two dimensional image. The image is further processed before sensor data can be acquired.

In this experiment the sensor is moved with specific increments in order to collect a sufficient sample set for the classifier. The real world application would see the sensor traverse through the lumen either propelled by the peristaltic contractions of the gut, or by being attached to a locomotion platform. The sampling frequency will be restricted by the frame rate of the camera, and the processing time of the algorithm. Worse et al. [170] have studied gastrointestinal transit velocity (velocity in which bodies pass through the GI tract), where fast velocity is considered to be 15cm per minute. If the Tactip was to sample at a minimum of once per mm, then a frame rate of 2.5 fps would be sufficient. If a locomotion system was to guide the Tactip through the gut, then an increased speed would demand a higher frame rate.

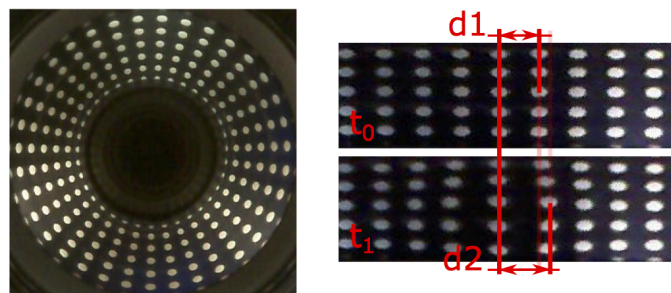


Figure 4.6: Raw camera image showing calibration state on the left at  $t_0$ , and post unwrapping of image, contact with lump state  $t_n$  on the right highlighting the location of the contact.  $d_1$  is the calibrated distance between the pins before any external contact,  $d_2$  shows a new larger distance between the pins at the focal point of contact. Maximum pin displacement is 30 pixels per pin, which is approximately 6 mm physical distance.

### 4.5.2 Sensing algorithm

The algorithm used to interpret tactile interaction with the capsule focuses on papillae pin movement replicating the role of the Meissner's corpuscle and Merkel cell mechanoreceptors as explained in chapter 3 subsection 2.2.3.1. When objects contact the deformable capsule skin, pins within the region of contact separate from each other whilst neighbouring pins move closer to each other. This can be seen in Fig. 4.6 where the first image shows the Tactip in a relaxed state with no objects in contact with the skin, whilst the second image shows the Tactip in contact with a lump highlighted by d2 where the papillae pins have separated in the region of contact. The first stage of image processing is unwrapping the distorted  $360^\circ$  image using the algorithm described in Equation 3.1 which shows how to calculate the corresponding pixel in the source image to the destination image.

After iterating through the source image using Equation 3.1, a two dimensional image is created with the papillae arranged in a grid formation. Using the OpenCV feature detection library, papillae pin positions can be tracked and compared to previous states. In order to identify the location of deformation or lump contact, pin locations are compared against the relaxed calibrated state. In particular it is the increase in pin separation that highlights the location of skin deformation, so pixel distance between pins is used as the measurement value. Fig. 4.7 shows a matrix of vectors that represent the movement of each pin when pressed against a lump. The apex of the lump is noted by the region surrounded by vectors oriented away in all directions. This flow of vectors extends to the area of contact with the lump.

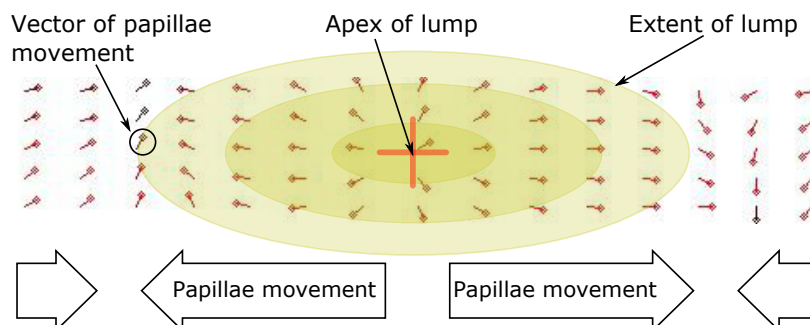


Figure 4.7: Representation of difference in pin position with vectors. Location of lump is inferred through the centre of vector activity. The extent of the lump contact is inferred by the boundaries of vector flow.

Gaps between pins, the vector magnitudes between neighbouring papillae pins along

circumferential rows, that exceed the calibrated state provide a representative value of deformation at that location. Fig. 4.8 shows a localised group of pins subjected to skin contact where the pins within the contact region separate and the adjacent neighbouring pins move towards each other. It is these pin location deviations from calibrated state that form the input data to a classifier system. Encoded within the list of pin positions are the deformation features of the skin.

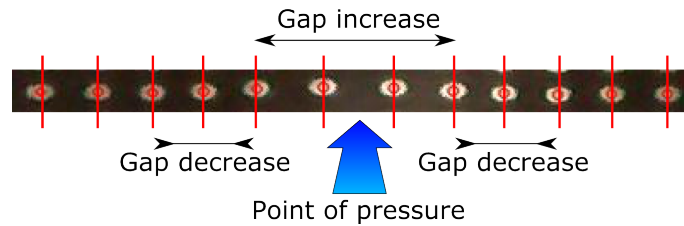


Figure 4.8: Localised group of pins subjected to skin contact showing the pins within the contact region separate.

The delta value of pin position can be represented visually as shown in Fig. 4.9. In this figure examples of contact with each of the three lump sizes are shown and the source image is placed above the processed image. The delta value of each pin's movement is used as a colour intensity parameter for each cell in the grid. Additionally the vector angle is presented with the line and marker (coloured circle).

### 4.5.3 Classifier systems

The objectives of this chapter outlined in section 4.1.1 and section methods outlined in 4.3 detail that the approach for processing tactile data from the Tactip interaction with artificial tumour lumps will be optimised using a classifier algorithm. In three phases this method will explore grouping data in to classified groups of lump detection, lump detection with size classification and finally lump detection with size classification and hardness classification.

Within a clinical context where accuracy of results is equally as importance as clarity, both patients and clinicians benefit from not only a result, but also a gauge of confidence accompanying that result. The following section discusses two different classifier systems which individually achieve either high binary accuracy, or a range of confidence results. It is considered that the combination of these two systems can provide both high accuracy with a good supporting explanation for the result.

A Support Vector Machine (SVM) is a supervised learning model discriminative

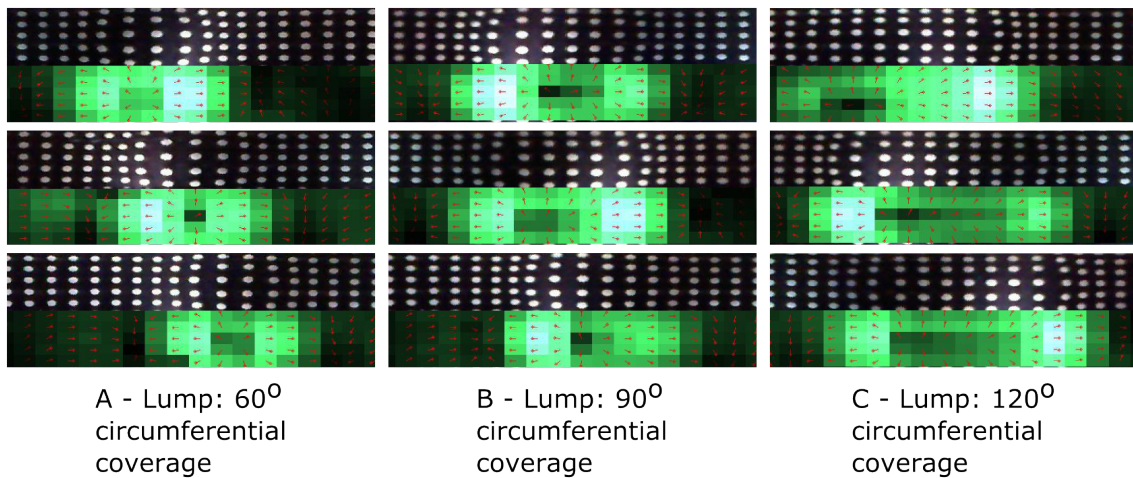


Figure 4.9: Examples of contact with each of the three lump sizes. The unwrapped captured image sits above the visual representation of captured data. Each cell corresponds to one of the papillae pins, where its colour is determined by that pins vector magnitude. The angle of the vector is shown by the vector and marker (coloured circle) layered above the cell.

classifier, formally defined by a separating hyperplane, used for classification and regression analysis. It is a non-probabilistic binary linear classifier that ring-fences results in to a strict category. A binary classifier is suitable in this context of study to classify data without confidence. As data groups become less easily distinguishable, perhaps due to smaller differences in material hardness, an output of confidence will be useful to identify difficult areas of classification. An alternative is a multilayer perceptron Classifier Neural Network (CNN). A CNN is a feedforward artificial neural network model which can provide confidence based decision output rather than the explicit binary classification output of the SVM. This may be more useful within the context of tumour classification considering the variance found in natural tumorous growths. Whilst SVMs are less prone to over fitting, they are non-parametric models, meaning their size can increase with the size of the training set. A CNN however is a parametric model, so its size is fixed. This could be a consideration for a system that may constantly update itself with new patient information. Results of the two methods will be

compared with the same input data.

In order to simplify the classification process, pin vector data is sorted in to a list such that the values range from maximum to minimum. In doing so the radial position of the focal point of contact is lost from that data. However, this information is available through simpler algorithmic means than a using a classifier, and bears little relevance to the classification of the lump. In its sorted form the data can be plotted, where the changes in the plot shape due to the lump type would be as shown in Figure 4.10. In summary, with lumps of larger height the indentation of the sensor is greater so the maximum pin separation increases. Current experiments have only explored classification of one lump at one time, although with further training of the classifier using more complex lump scenarios identification of multiple lumps would be possible.

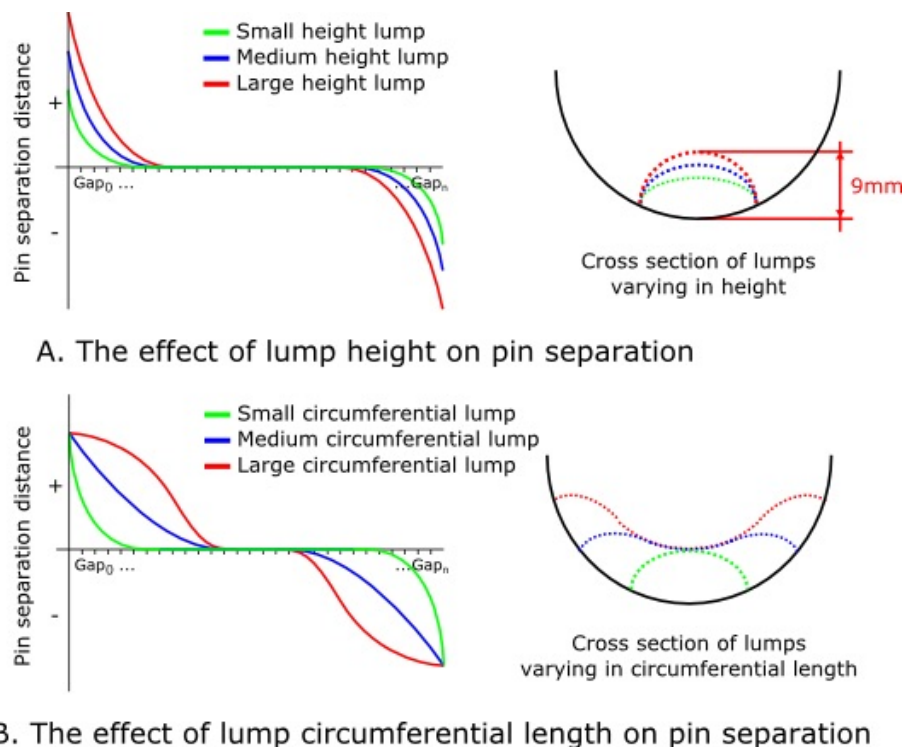


Figure 4.10: Example of the effects of lump size and shape (as described in Fig. 4.1 and 4.11) on sensor data used as input to classifier system. A. shows that as the lump height increases, the maximum pin deviation increases also. B. shows that increased circumferential coverage of the Tactip causes greater total pin deviation through a larger quantity of pins achieving achieving maximum deviance.

## 4.6 Results

### 4.6.1 Lump detection

Considering the limited size of capsule endoscopy, its payload would be restricted to an onboard camera and necessary electronics to achieve transfer of the image data. In a perfect scenario the image processing to determine pin movement would happen on board the capsule so that the output data is a list of vectors, reducing the bandwidth requirements. This presents a motivation to reduce both camera and computation in order to reduce the load of any onboard power source. The following experiments investigate whether consideration of only the middle row of pins (row 2, see Fig.3.10) is sufficient for detection of lumps, and the trade off of accuracy against computational complexity.

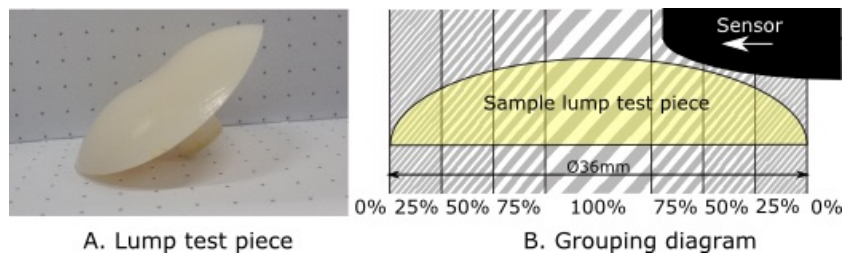


Figure 4.11: A. 3D printed lump test piece used for lump detection experiment. B. Diagram showing how samples are grouped in relation to sample coverage and central position of sensor.

The first experiment tests whether a classifier system can detect whether a lump is present and what percentage of the lump is covered by the sensor. A binary classifier cannot provide confidence with results as a measure of how much a lump is present, so the samples are grouped in to regions of 0.0%, 25.0%, 50.0%, 75.0% and 100.0% lump coverage, see Fig. 4.11.B. A sample set of 2520 has been used which is randomised and split 50/50 between training and test data. The data is fed to both SVM and CNN classifiers 10 separate times, Table 4.2 presents the results and precision of both. The CNN is capable of providing confidence data and so the average confidence for the CNN is shown in the table. The results show a positive ability to detect the presence of a lump. Focus should be paid to 100% coverage detection rather than partial detection as this is where the lump is fully covered by the sensing envelope. In this case more than 90% accuracy can be achieved using the SVM and more than 80% with the CNN. Detection of no lump has greater success, but there are clear strengths in 'lump' /

'no lump' scenario. Results with partial detection where the sensor covers 25-75% of the lump are less positive but still achieve around the 70% region. It is notable that the standard deviation in the results increases with lower accuracy from the classifier. These results show a clear ability to detect lump presence and the ability to classify to what extent a lump has been covered. Additionally the average confidence provided by the CNN shows the average confidence in the output class in all results. The results showing SVM outperforming CNN match other's comparison between SVM and NNs, [171; 172; 173]. Shao et al. [174] state that their results show SVN to have superior generalisation capability. Whilst SVM may show superior accuracy, in a clinical context, patient and clinicians would favour a confidence output which is not offered by a binary classification system (SVM).

Coverage/Group	Mean SVM Precision	Std. Dev.	Mean CNN Precision	Std. Dev.
0%	0.98	0.01	0.97	0.01
25%	0.74	0.04	0.59	0.12
50%	0.70	0.05	0.77	0.04
75%	0.69	0.07	0.70	0.04
100%	0.92	0.02	0.83	0.3
Ave / Total:	0.81		0.77	
Ave confidence:	N/A		0.79	

Table 4.2: Lump detection SVM and CNN precision results. Test data was fed in to the classifier systems 10 times to produce an average result and associated standard deviation.

#### 4.6.2 Circumferential lump size

Typically a submucosal tumour will begin to form in one region of the intestinal wall and spread around that wall circumferentially. In order to detect this, the sensor would need to discriminate between the spread of deformed pins around the circumference as shown in Fig. 4.10.B. Fig. 4.1 shows the 3D printed hard test lumps varying in circumferential length. In this experiment three test pieces are used to detect lump size. This increases the number of classifier groups from five (one group for each 25% coverage increment) to thirteen (0% coverage plus the remaining 4 coverage increments for each of the 3 lump sizes). The same principle of lump coverage is used in combination with lumps that cover  $60^\circ$ ,  $90^\circ$  and  $120^\circ$  of the sensor circumference. The additional 2 test lumps increase the number of samples acquired to 7560. Again data is fed to both a SVM and CNN classifiers 10 separate times, and Table 4.3 presents the results and

precision of both.

The results show little negative effect on the classifier detection rates for both SVM and CNN. This suggests that the classifier has potential to further discriminate sensor readings with more complex features. As with the previous lump detection experiment, the SVM leads the CNN with accuracy. There is a small increase in CNN average confidence but this is too small to be considered an improvement.

### 4.6.3 Lump hardness



Figure 4.12: Soft test pieces spread circumferentially around sensor,  $60^\circ$ ,  $90^\circ$  and  $120^\circ$  left to right. Soft lumps are made from cast Platsil 7315 rubber silicone.

The final aim of this work is to discriminate between hard and soft tissue. Three new test pieces have been made the same shape and size as the previous circumferential length test pieces, only the new pieces are made using a soft shore A 15 silicone as opposed to the original hard shore A 85, see Fig. 4.12. This forms a soft and deformable surface that will create a different interaction with the sensor compared to a rigid material test piece. These differences will be relatively small compared to the previous experiments so it is expected that the accuracy of the classifiers will decrease. Table 4.3 shows both the first results for classification of hard and soft lumps in combination with varying circumferential length and the second optimised results explained in the next section. The first section of the table shows the results when only the middle row of pin data is used as an input for the classifier, the same input as the previous experiments. The results show a decline in accuracy of 3 and 5 percent for the SCV and CNN respectively from the previous size discrimination experiment. Table 4.4 isolates the grouping to hard or soft, in which the results are complimentary of Table 4.3. The next section details efforts to improve accuracy by increasing the level of detail in the classifier input format.

Coverage/Group	Input: 1 row		Input: 3 rows	
	SVM precision (std-dev)	CNN precision (std-dev)	SVM precision (std-dev)	CNN precision (std-dev)
0%	0.91 (0.01)	0.90 (0.02)	0.97 (0.01)	0.95 (0.02)
Hard-60°25%	0.41 (0.12)	0.28 (0.11)	0.77 (0.05)	0.79 (0.02)
Hard-60°50%	0.61 (0.03)	0.66 (0.03)	0.80 (0.02)	0.53 (0.04)
Hard-60°75%	0.76 (0.03)	0.57 (0.05)	0.88 (0.02)	0.50 (0.07)
Hard-60°100%	0.95 (0.02)	0.90 (0.01)	0.98 (0.01)	0.76 (0.03)
Hard-90°25%	0.57 (0.09)	0.52 (0.08)	0.79 (0.02)	0.74 (0.04)
Hard-90°50%	0.71 (0.02)	0.68 (0.03)	0.75 (0.03)	0.50 (0.04)
Hard-90°75%	0.86 (0.03)	0.86 (0.03)	0.88 (0.02)	0.44 (0.07)
Hard-90°100%	0.98 (0.01)	0.70 (0.04)	0.94 (0.01)	0.84 (0.02)
Hard-120°25%	0.64 (0.04)	0.44 (0.07)	0.84 (0.03)	0.81 (0.01)
Hard-120°50%	0.57 (0.03)	0.43 (0.08)	0.80 (0.04)	0.52 (0.03)
Hard-120°75%	0.86 (0.04)	0.73 (0.04)	0.88 (0.02)	0.51 (0.05)
Hard-120°100%	0.97 (0.01)	0.82 (0.03)	0.95 (0.01)	0.81 (0.03)
Soft-60°25%	0.41 (0.05)	0.19 (0.09)	0.82 (0.04)	0.72 (0.04)
Soft-60°50%	0.45 (0.04)	0.32 (0.08)	0.84 (0.03)	0.53 (0.06)
Soft-60°75%	0.62 (0.02)	0.35 (0.09)	0.87 (0.02)	0.52 (0.07)
Soft-60°100%	0.80 (0.03)	0.78 (0.05)	0.80 (0.03)	0.65 (0.04)
Soft-90°25%	0.46 (0.08)	0.41 (0.06)	0.68 (0.04)	0.63 (0.05)
Soft-90°50%	0.50 (0.06)	0.40 (0.05)	0.73 (0.03)	0.51 (0.04)
Soft-90°75%	0.54 (0.07)	0.53 (0.03)	0.73 (0.04)	0.47 (0.03)
Soft-90°100%	0.80 (0.04)	0.42 (0.06)	0.84 (0.02)	0.66 (0.07)
Soft-120°25%	0.70 (0.03)	0.54 (0.07)	0.66 (0.03)	0.69 (0.03)
Soft-120°50%	0.75 (0.04)	0.57 (0.04)	0.77 (0.03)	0.65 (0.04)
Soft-120°75%	0.85 (0.03)	0.58 (0.07)	0.80 (0.02)	0.53 (0.05)
Soft-120°100%	0.92 (0.02)	0.78 (0.03)	0.90 (0.02)	0.80 (0.03)
Ave / Total:	0.81	0.73	0.90	0.79
Ave confidence:	N/A	0.70	N/A	0.76

Table 4.3: Hardness shape detection SVM and CNN precision results. Test data was fed in to the classifier systems 10 times to produce an average result and associated standard deviation.

#### 4.6.4 Optimisation

The previous experiments have used a simplified classifier input of the middle row of pins only. This has been sufficient for discrimination to this point however the success and accuracy discriminating size and density has declined. In an attempt to increase accuracy, more data has been included in the input data that incorporates the row of pins above and below the middle row currently used. These three rows are separately sorted maximum to minimum as shown in Fig. 4.13, where the input is a list of values from the three rows of thirty five pins each. The second sections of Tables 4.3 and 4.4 detail the benefits of this increased data. By using three times the data the

Coverage/Group	Input: 1 row		Input: 3 rows	
	SVM precision	CNN precision	SVM precision	CNN precision
Hard shore A 85	0.78	0.78	1.00	1.00
Soft sore A 15	0.71	0.63	1.00	0.99
Ave confidence:	N/A	0.69	N/A	0.99

Table 4.4: Hardness detection SVM and CNN precision results

average accuracy has increased by almost 10 percent in the SVM and 6 percent in the CNN. When considering lump density on its own accuracy reaches 100 percent and 99 percent respectively. The increased data has a clearly positive effect on the accuracy of the classifier systems.

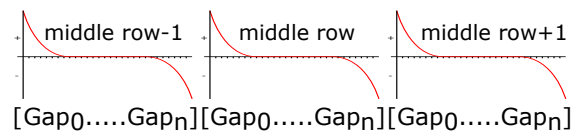


Figure 4.13: Visualisation of the optimised classifier input data format. The new format consists of the pin delta values for the middle row of pins and one row above and below. Each row's data is kept separate but they are concatenated together to form a 135 element long array. As with the previous experiment, each row's data is sorted from maximum to minimum values.

## 4.7 Chapter Conclusion

Whilst the previous chapter showed the principles in building the cylindrical Tactip sensing device and basic functionality towards deformation sensing, addressing research task 1.(b), this chapter has used learning systems to abstract the sensor data and classify different kinds of synthetic tumours based around the natural growth of submucosal tumours, addressing research task 1.(c). The hypothesis has been explored by collecting sample data of the cylindrical Tactip in contact with a variety of tumour like lumps and presenting the data to a classifier system. This has confirmed that the cylindrical Tactip is capable of discriminating between size, shape and hardness, characteristics which help define a tumour. When the complexity of the classifier grouping increased with the introduction of different hardness lumps the accuracy of the classifier decreased, but this was countered with a more complex data format passed to the classifier which improved accuracy to a more acceptable average of 90%. This is a promising start towards achieving a remote palpation system inside the GI tract that will help return

the use of one of surgeon's most important skills their highly enhanced sense of touch.

This chapter has presented a new application for a biologically inspired tactile sensing device. Whilst first thoughts of applications of the Tactip lead toward replication of typical fingertip type activities, it has proposed a new method of medical diagnostics. This has been achieved by combining artificial tactile sensing with classifier algorithms to discriminate and identify different object characteristics in the context of tumour growth around the lumen. With the use of new 3D printing technology it has been possible to develop and prove this system quickly. Whilst the environment used to test the hypothesis is not typical to a human digestive tract, it is a step towards it. Future work with this device would expect further progress towards a more realistic digestive tract environment using compliant lumen like surfaces.

---

### Integration of Capsule Locomotion and Tactile Sensing

---

The following chapter is based upon the publication Winstone et al. 2016 "Single motor actuated peristaltic wave generator for a soft bodied worm robot" [1].

#### 5.1 Introduction

In previous chapters a review of background issues has been explored to identify a need to enter the body for more accurate diagnostic procedures whilst avoiding drastic surgical methods to gain entry. As remote operated medical technology has been developed it has neglected the clinician's sense of touch which has been identified as a crucial expert skill. So it has been proposed that a tool that is capable of entering the body without surgery, able to relay tactile sensing information to the clinician or operator, will close this gap. In chapter 3 the idea of tactile sensing has been applied to capsule endoscopy. The Tactip sensor has been redesigned to fit the form of a capsule endoscopy, and performance investigated inside a laboratory constructed environment. The results show the capability to sense surface deformation caused by artificial lumps based on submucosal tumours that grow around the lumen of the intestines. Further development of this sensor was shown in chapter 4 where the algorithms developed to interpret the sensor data were optimised using a classification system. This system was able to discriminate between different lump size, shape and hardnesses.

This chapter investigates the area of locomotion as identified in subsection 2.2.1. A

design approach has been taken in order to build a mechanically simple drive mechanism that can be miniaturised and optimised for a given environment. This drive mechanism design has been first simulated and then compared against a non optimised design in a physical robot. The first result of this chapter is a robot design that moves along a pipe like structure along with mechanical gearbox parameters that maximise the pulling capabilities of the robot whilst also achieving a simpler drive mechanism for future miniaturisation.

The locomotion method developed in this chapter has then been integrated with the tactile sensing system developed in the previous chapters. The second result of this chapter is an integrated system capable of moving and sensing through the test environment used in previous chapters. By showing that the robot can move across a test piece symbolic of a submucosal tumour and using the tactile sensing system to detect the presence of the tumour, it validates the theories of operation suggested in chapter 2. In particular this chapter tackles the following tasks that were outlined in section 2.4. These tasks provide a specification for this chapter.

- 2.(a) **Develop** a capable locomotion method to drive the capsule through a GI tract like environment.
- 2.(b) **Optimise** the locomotion mechanism to identify methods to adapt to a changing environment.
- 2.(c) **Consider** a soft locomotion system to minimise the impact on the patient and allow for compliance around the environment reducing risk of blockage and increasing accuracy of sensing
- 2.(d) **Consider** a locomotion system that can be easily miniaturised through reduced number of components and complexity.
- 3.(a) **Develop** an integrated assembly of the locomotion system and tactile sensing system.
- 3.(b) **Test** the integrated assembly in a combined test environment used in the development of the locomotion and sensing system. The robot assembly should show capability to traverse and detect a tumour like feature.

## 5.2 Peristaltic Locomotion Actuator Mechanism

This section explores the design, development and testing of a peristaltic worm inspired locomotion system. The robot has three segments and one actuator that achieves optimised worm like peristaltic motion. Each segment consists of two solid circular disks that have a tendon connected through to the drive mechanism using a Bowden cable and a soft rubber skin that deforms under the compression of the tendon. The hypothesis is that a tuned peristaltic waveform can achieve increased locomotion distance and clamping strength compared to an untuned waveform. This is tested using an initial development robot capable of demonstrating varying waveform types with multiple actuators, one for each worm segment. Three experiments have been created to test the locomotion design: (i) moving along a flat surface, (ii) moving through a confined tunnel (iii) moving through a confined tunnel whilst pulling a payload. Results from these experiments have identified optimal parameters for a smart gearbox capable of achieving the same optimal peristaltic waveform signal as the more complex development platform but with only one actuator driving all three worm segments. Unlike other examples of peristaltic worm robots [68; 67; 54; 56; 57; 55; 58; 69], this example uses a control method embedded within the mechanics of the design removing the need for excessive number of actuators. This contributes to miniaturisation, reduces power consumption and simplifies the overall design and size.

During forward linear locomotion of an earthworm each individual segment of the body is performing the same action as the other segments, only at a different phase. This suggests that each individual segment could be actuated from the same actuator if the phase of each segment can be offset. The work of Boxerbaum et al. [57] presents an effective mechanism that actuates multiple tendons from one rotary actuator. Using bowden cables, the rotational movement of the motor can be translated into linear movement or contraction of a segment. With each Bowden cable positioned at a phase offset the corresponding worm segment will contract at a unique period in the motor's cycle. Omori et al. [54] state that a minimum of three worm segments are required to achieve peristaltic motion so from this point on a robot with three segments will be considered. Fig. 5.1 demonstrates the principle of this mechanism with three segments. An axially positioned motor rotates a free moving cam housing to which all tendons are attached. As the cam rotates it pulls an individual tendon by different displacements

based on its angular position or phase offset. The displacement of a tendon at any given time 'h' relates to the angle of the motor and the phase offset of the tendon, see equation 5.1. As shown in Fig. 5.1, and further in Fig. 5.14, the output of this mechanism for each segment is a sinusoidal wave through the contracting tendon. The value of 'h' is directly proportional to the distance a segment axially contracts by, and in turn radially expands by.

$$h = \sqrt{(tx - (r1 \cdot \cos(\theta)))^2 + (ty - (r1 \cdot \sin(\theta)))^2} \quad (5.1)$$

Where;

$h$  = Tendon displacement at armature angle  $\theta$  (mm)

$r1$  = Distance from motor shaft centre to spur gear centre (mm)

$tx$  = Tendon exit point horizontal distance from centre (mm)

$ty$  = Tendon exit point vertical distance from centre (mm)

$\theta$  = Angular position of armature  $\theta$  (radians)

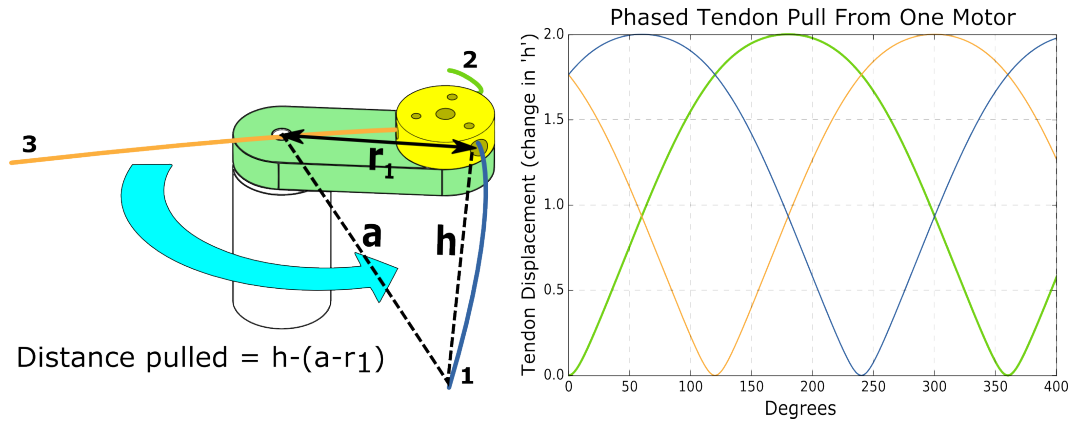


Figure 5.1: Phased linear tendon pull with a single rotary actuator.

### 5.2.1 State Driven Actuator Mechanism

Earthworm locomotion is based on waves of muscular contractions traveling the length of the body. However, it is not a fluid motion of each segment being in the constant transition. Segments that clamp or root to the environment hold their state for the full length of time in which the remaining segments complete their transition to either

extension or contraction, see State Table. 5.1. As such the sinusoidal control of segment tendons is not sufficient to achieve such behaviour. Instead, a waveform that contains three stages; pull, push and hold is required. Whilst a rotational motor output can directly translate to a sinusoidal movement, a more complex mechanism is needed to achieve this new waveform.

Table 5.1: Three Segment Worm Locomotion State Table

State	Segment 1	Segment 2	Segment 3
$t_0$	<i>Clamp</i>	Stretch	Contract
$t_1$	Contract	<i>Clamp</i>	Stretch
$t_2$	Stretch	Contract	<i>Clamp</i>
$t_3$	<i>Clamp</i>	Stretch	Contract
$t_4$	Contract	<i>Clamp</i>	Stretch

Three worm segments are considered, one for each of the described states. As the swing arm rotates between the contracting and extended tendon points, the pull on the clamping segment must remain the same length throughout the duration of the transition. This determines the loci of the output of the gearbox as a three sided shape with each side having a degree of curvature. In order to achieve such a loci with a specific number of sides, a number of examples of working systems should be considered; e.g. the geometric drawing toy Spirograph demonstrates how two counter rotating wheels can produce multi-sided shapes.

The two counter rotating wheels that generate a triangular loci from an outer point of the second wheel generate the waveform and shape produced in Fig. 5.2. By varying the ratio between the radius of the first and second wheel the waveform can be varied to achieve either a longer but more unstable clamping phase or a shorter but more stable clamping phase. To achieve the most stable clamping phase where the tendon retains stationary tension throughout, the distance of the loci point to the tendon attachment point must remain the same during the clamping phase. During this period the remaining two tendons either undergo a pulling or releasing transition. By translating this triangular loci to linear movement of the tendons that contract and radially expand the worm segments, a bio-mimetic locomotion method can be achieved.

The gear arrangement is designed as shown in Fig. 5.3 where  $r_1$  shows the distance from the motor shaft to the spur gear and  $r_2$  is the distance from the central axis of the gear to the offset point to which the tendons A,B and C are attached to. In order to determine how much a tendon is displaced at any given motor position ( $\theta$ ), a simple

## The Effect of Radii Ratio on Resulting Loci Path

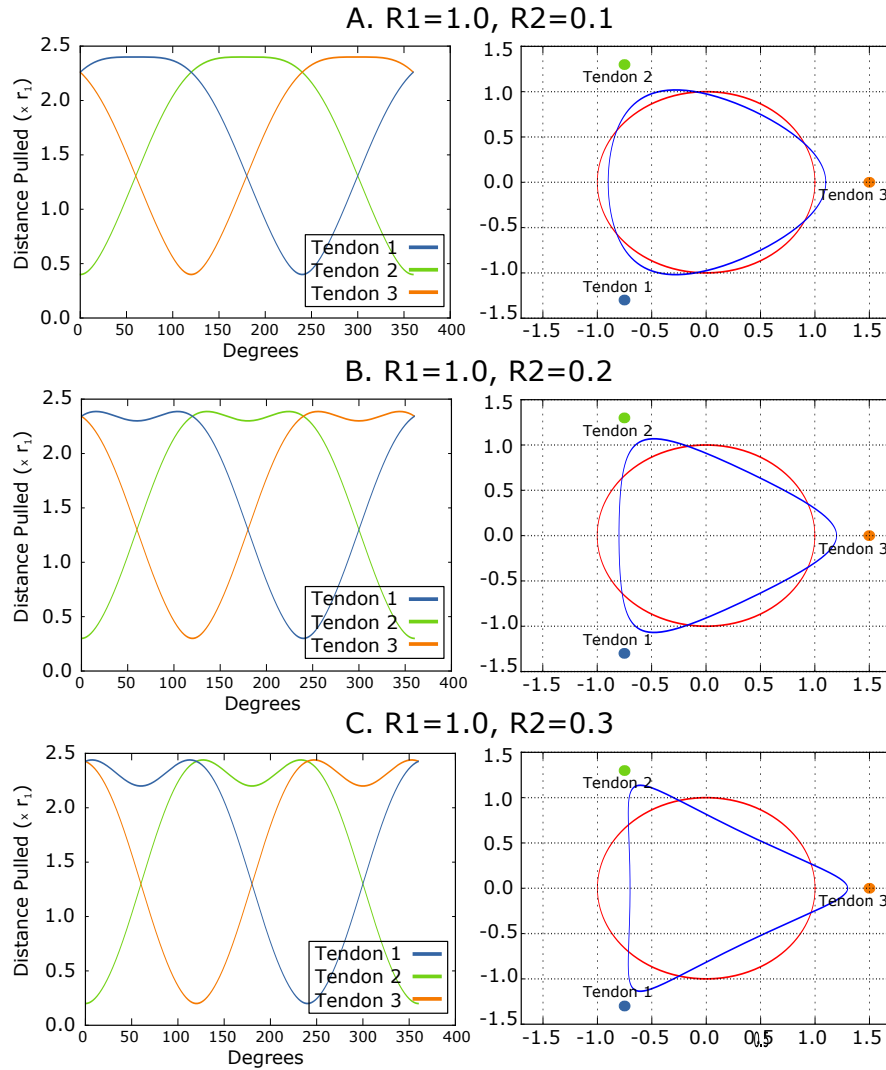


Figure 5.2: The left column of graphs show the tendon pull or waveform against angular position of the motor, the right column of graphs show the loci generated. The loci path produced by the gear mechanism changes according to the ratio between the two radii. A longer period of flat or most tendon tension signified in A. shows more effective segment clamping than in C. where clamping relaxes mid way through the clamping stage. References to  $R1$  and  $R2$  related to  $r1$  and  $r2$  in equations 5.2 and 5.3 respectively.

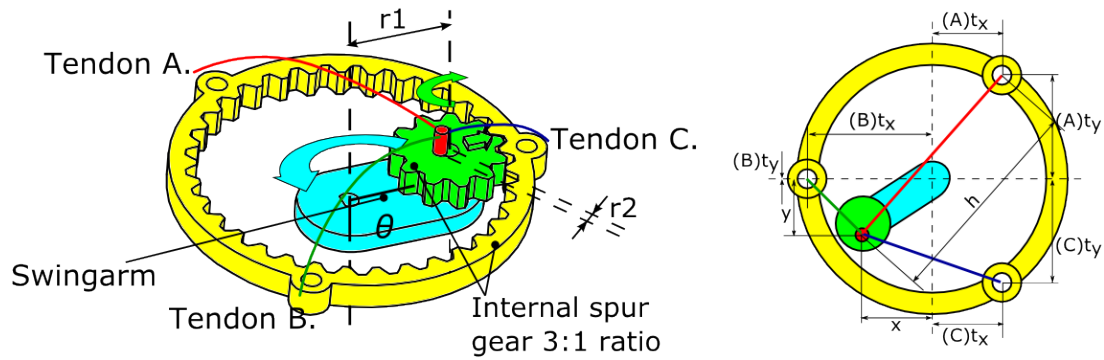


Figure 5.3: Diagram of the planetary gear arrangement needed to achieve the correct waveform.

calculation can be applied to sum the vectors of the two gears radii to achieve an x,y position and then calculate the distance to the tendon exit point.

$$x = (r1 \cdot \cos(\theta)) + (r2 \cdot \cos(-2 \cdot \theta)) \quad (5.2)$$

$$y = (r1 \cdot \sin(\theta)) + (r2 \cdot \sin(-2 \cdot \theta)) \quad (5.3)$$

$$h = \sqrt{(tx - x)^2 + (ty - y)^2} \quad (5.4)$$

Tendon displacement 'h', gearbox scenario Where;

$h$  = Tendon displacement at armature angle  $\theta$  (mm)

$x$  = X coordinate of tendon attachment wheel

$y$  = Y coordinate of tendon attachment wheel

$r1$  = Distance from motor shaft centre to spur gear centre

$r2$  = Distance from spur gear centre to tendon wheel offset

$tx$  = Tendon exit point horizontal distance from centre

$ty$  = Tendon exit point vertical distance from centre

$\theta$  = Angular position of armature  $\theta$  (radians)

### 5.3 Optimising Parameters

In the following analysis, it is assumed that the worm segments radial expansion will make contact with an outside surface when its axial contraction reaches 1.8 times  $r_1$ . This value is chosen in order to identify optimal parameters for a given contact point.

Ultimately, these parameters will only be optimal for a given sized environment, but the designed mechanism could tune these parameters to suit a changing environment as the robot moves around. The maximum a rotating swing arm of length  $r_1$  can pull a tendon is  $2r_1$ . This allows further expansion for a flexible skin of a worm segment to comply and obtain a footing with the surface. This analysis focuses on identifying gearbox parameters that are optimised for the environmental size, such that the worm could compensate for different pipe diameters and obtain stronger clamping force.

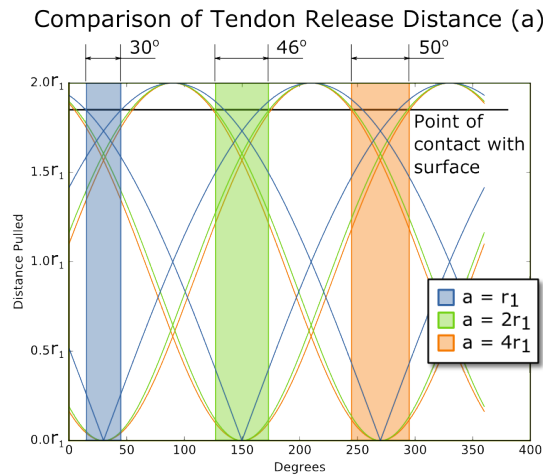


Figure 5.4: Effect of changing tendon release point, 'a', in a basic swingarm with no gearbox. Shaded regions shows periods of no clamping and no effective movement.

### 5.3.1 Tendon Offset

A number of factors affect the performance and efficiency of this design. Consider a system that uses a swing arm of length  $r_1$  attached to a motor. A tendon release point is placed at distance 'a' (Fig. 5.1) from the centre of rotation. The distance from the tendon release point to the end of the swing arm,  $h$ , will vary through the rotation of the motor as shown in Fig. 5.1. Although a rotation can translate to a sinusoidal waveform, the distance of the tendon release point to the centre of rotation affects the conformance to an exact sinusoidal form. Fig. 5.4 demonstrates the effect of changing length  $a$  from a distance of  $r_1$  to  $4r_1$ . This shows that a tendon positioned further away from the point of rotation produces a sharper trough shape, see Fig. 5.4. In the context of achieving the perfect waveform for effective peristaltic worm locomotion, attention should be focused on maximising the period in which the wave is above the point of contact so that the least amount of time is spent transitioning between phases whilst having no contact with the surface. Fig. 5.4 shows shaded regions that relate to each

configuration of length  $a$ , highlighting the crossover point with the contact threshold. Essentially the wider the shaded region the greater the time the configuration is not clamping during a transition. This shows that a tendon release point at a distance of  $r_1$  from the centre of rotation achieves clamping for the longest period,  $90^\circ/120^\circ$  compared to the furthest distance of  $4r_1$ ,  $70^\circ/120^\circ$ .

A gearbox mechanism driven by this previous example of a swing arm of length  $r_1$  attached to the motor is considered. The gearbox enables a counter rotating gear at a ratio 3:1 that connects to the free rotating pulley wheel that connects to the tendons as shown in Fig. 5.3. As with previous examples of varying the tendon release point 'a', the effect of using the gearbox mechanism is the same, however the ineffective periods are greatly reduced to  $9^\circ/120^\circ$  when the distance is  $r_1$ , and  $61^\circ/120^\circ$  when the distance is  $4r_1$ , see Fig. 5.5.a.

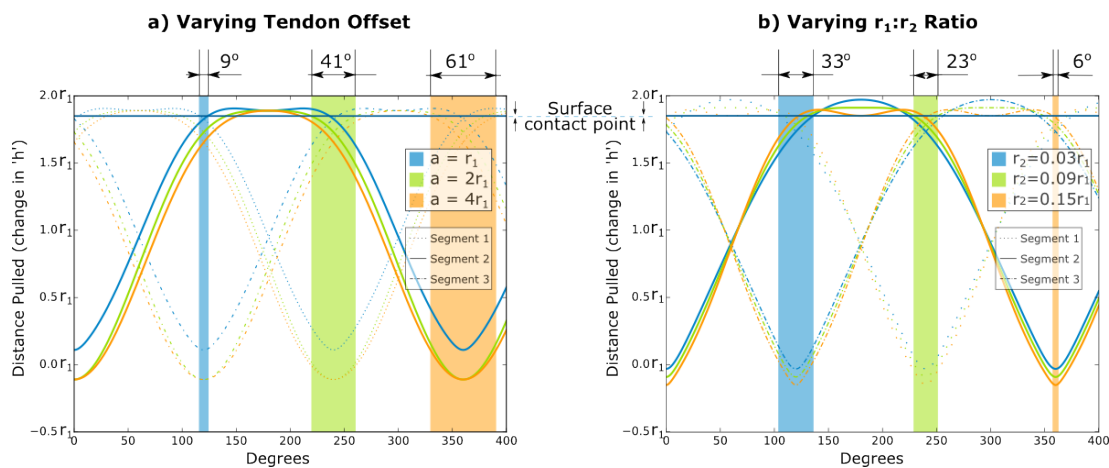


Figure 5.5: (a) Comparison of effective clamping period when varying tendon offset in gearbox mechanism, where  $r_2 = 0.09$ . (a) Comparison of effective clamping period when varying  $r_1 : r_2$  ratio in gearbox mechanism, where  $a = 1.2r_1$ .

### 5.3.2 $r_1:r_2$ Ratio

The main attributing variable of the gearbox is the ratio between  $r_1$  and  $r_2$  as shown in Fig. 5.3. The effect of changing this ratio is shown in Fig.5.5.b where an increased  $r_2$  in relation to  $r_1$  increases the period of time over the clamping threshold. However, a further increase of  $r_2$  creates a dip at the peak of the wave which can cause the wave to drop below the contact threshold momentarily compromising contact with all sides of the robot. If the contact threshold is  $1.8 r_1$  the ideal ratio between  $r_1$  and  $r_2$  is 1:0.15 where the period of clamping is increased to  $144^\circ/120^\circ$ .

### 5.3.3 Efficiency Improvement of Gearbox

When a worm segment contracts, it clamps to the contact surface for the entirety of its cycle, allowing the remaining segments to advance axially. At any given time, one of the segments is clamped to the contact surface, achieving an overall stronger and more effective clamping. A waveform for such a situation is shown in Fig. 5.6 noted as an ideal waveform. A sine waveform generated by the simple rotating swing arm pulling offset tendons is shown with no gearbox, and finally with the gearbox waveform. Highlighted are the periods of no clamping when the contact surface is engaged at an axial compression of 1.8 times  $r_1$ . The parameters for the gearbox waveform use the  $r_1 : r_2$  ratio of 1:0.15 and the tendon offset of  $1.2r_1$  to allow for the addition of  $r_1$  to  $r_2$  at the peak of the waveform. Fig. 5.6 shows that whilst an ideal waveform achieves 100% clamping per cycle, the gearbox derived waveform achieves a  $6^\circ$  or 5% reduced clamping period. However, a simpler swing arm generated sine waveform achieves a  $23^\circ$  or 19.2% reduced clamping per cycle.

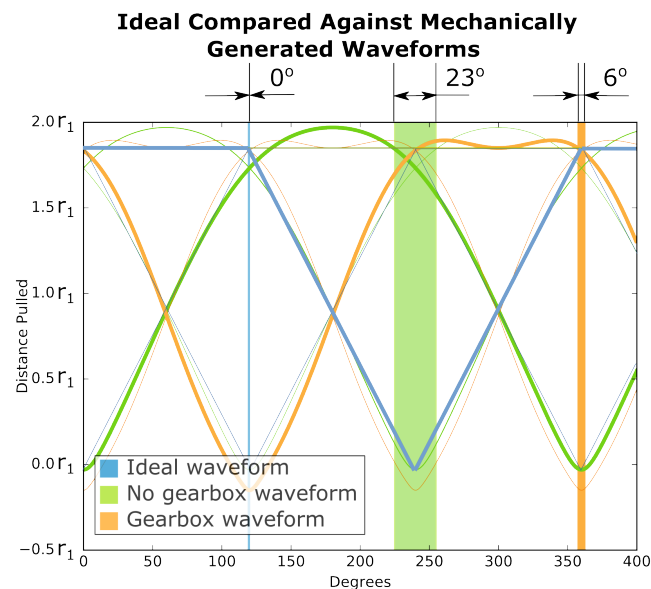


Figure 5.6: Comparing an ideal waveform (segment clamping occurs for 100% of cycle), sine wave generated waveform (tendon attached to end of swingarm) and optimised gearbox generated waveform (tendon attached offset  $r_2$  of gearbox).

## 5.4 Robot Design - Gearbox Design Test Platform

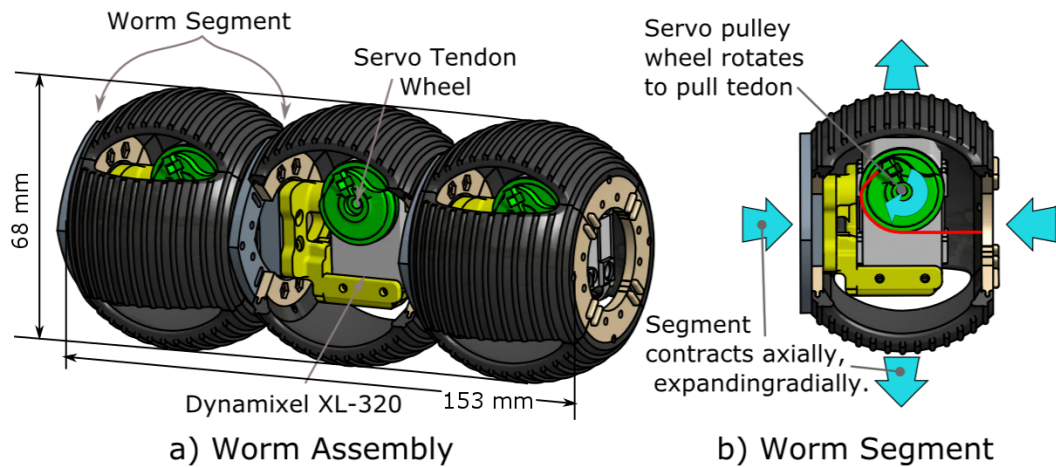


Figure 5.7: Dynamixel driven robot built to test out each waveform and compare performance and identify optimal gearbox parameters. a) Assembly of three worm segments, each containing a Dynamixel xl-320 servo. b) One worm segment showing how the dynamixel servo rotation pulls the tendon compressing the segment.

Before designing the gearbox mechanism proposed in this chapter, the waveforms suggested must be compared. This has been achieved through building a robot worm body with actuators in each segment, as shown in Fig. 5.7. The robot worm has been printed on an Objet 260 3D rubber printer where flexible worm segment skins are made of Tango Plus, and the rigid sections, Vero White. Each worm segment comprises 4 rubber segment skins. These skins expand radially when contracted axially. A Dynamixel XL-320 motor and pulley connect both ends of the segment with a tendon cable. When the segment expands radially it gains friction with the supporting or contacting surfaces.

### 5.4.1 Experiment 1 - Force Distribution Test

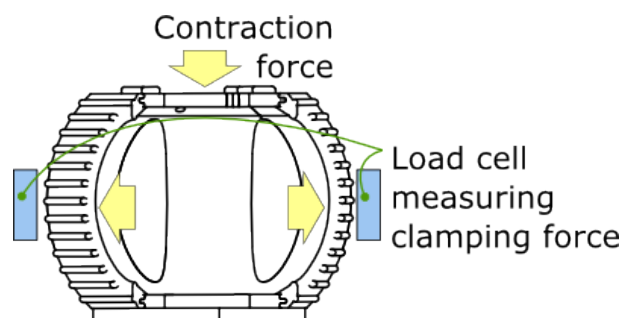


Figure 5.8: Force distribution experiment arrangement Axial contraction force applied to achieve radial expansion applying relative force on to force measurement load cell.

In order to understand the performance of this test platform, a relationship between a segment contraction and the force distributed to the radial expansion needs to be understood, see Fig.5.8. Fig. 5.9 displays results of load cell measurements of the forces imposed on the contacting surface when the segment is compressed by an axial force. One segment has been compressed from above, whilst the forces applied by each of the segment walls to their contacting surfaces are measured by load cells. The results show that the forces are distributed equally. The inclusion of the actuator inside the segment limits space for compression of the segment to 80% of the original axial length. To achieve this axial compression of 20%, 4 N of force is required axially through the tendon. The radius of the servo pulley is 10 mm and so the minimum torque of the motor required to achieve this compression is  $0.04Nm$ . The Dynamixel XL-320 can achieve 0.4 Nm and is an appropriate actuator for this requirement.

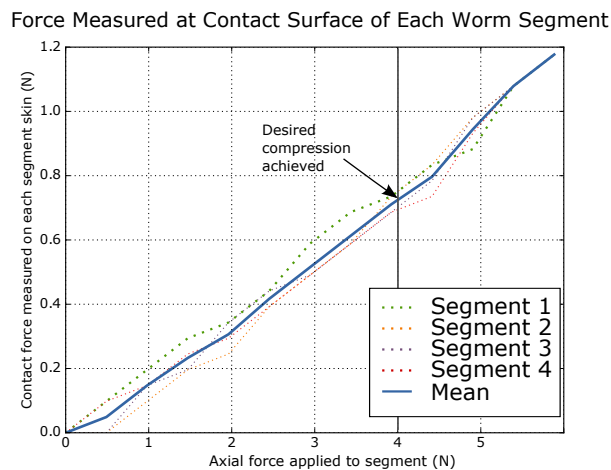


Figure 5.9: Force distribution measurement of each segment when subjected to axial compression.

#### 5.4.2 Experiment 2 - Locomotion on a Flat Surface

The test platform worm robot has been subjected to three tests;

- 1. locomotion on a flat surface
- 2. locomotion within a confined tunnel where all worm's segments contact during the clamping phase
- 3. locomotion whilst pulling a payload

In these experiments, one cycle is considered to be a segment going through all transitions. This corresponds to one full rotation of the swing arm. 50 cycles of the

three waveforms are passed to the worm robot and the corresponding distance travelled across an acrylic surface is measured. 155.0 mm was achieved by the standard sine waveform, 175.0mm by the generated gearbox waveform and 175.0mm by the ideal waveform. In summary, the sine waveform is 86.57 % of the ideal waveform whilst the gearbox waveform is 98.87 % of the ideal waveform. This highlights that, on a flat surface a worm with one actuator would sacrifice only 1.13 % drop in performance if the gearbox mechanism is used compared to a simple swing arm mechanism that loses 13.43 %. The movement of the tip of the robot's segment skin during contraction has been tracked, see Fig.5.10, showing the distance achieved per cycle.

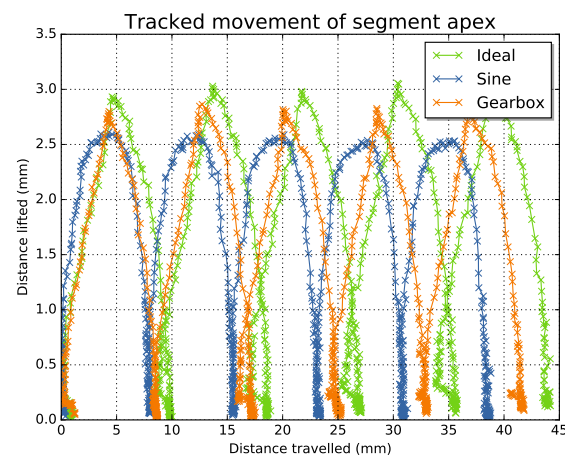


Figure 5.10: Tracked segment apex of worm robot travelling across a flat surface.

### 5.4.3 Experiment 3 - Locomotion Through a Confined Space

A confined tunnel has been constructed from transparent acrylic with a width equal to the measured expansion of a segment when it is contracted to 1.8 times  $r_1$ , 76 mm, see Fig. 5.12 and Fig. 5.11. Given the limitation of space in the segment allowing for 20 % axial contraction, 9.6 mm,  $r_1$  will be considered to be half of this distance, 4.8 mm. When a segment is contracted to 1.8 times  $r_1$  it expands radially to 76 mm, which determines the width of the tunnel. The first experiment within the tunnel simply measures the distance travelled when all four segment skins contact the surrounding environment. In the following experiments with a confined space, 20 cycles of the three waveforms are passed to the worm robot. This is reduced from the previous 50 due to the length of the confined space that could be made which was restricted by the laser cutter work envelope used to manufacture the test environment. Table 5.2 shows the

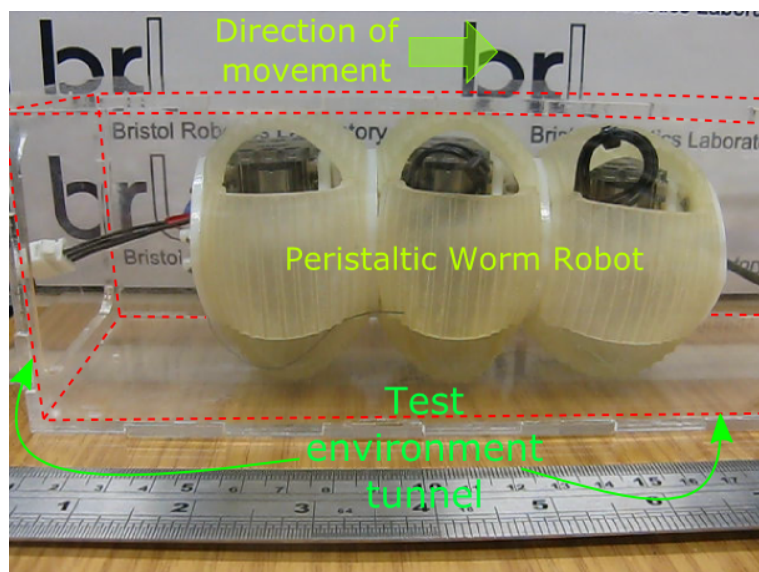


Figure 5.11: Side view looking on to tunnel created for confined space experiment.

results of this experiment, where the efficiency of the gearbox waveform compared to the two other waveforms is in line with the locomotion on a flat surface. However, in all cases, the distance achieved is greatly reduced due to the resistance incurred from the four segments skins in contact with a surface compared to only one skin surface contacting when on a flat surface.

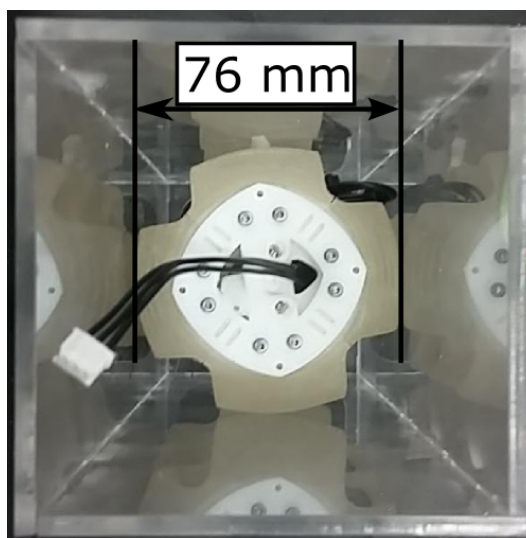


Figure 5.12: Front view looking in to tunnel created for confined space experiment. The width of the tunnel is 76 mm to match the diameter of the worm when a segment is contracted to  $1.8r_1$ .

#### 5.4.4 Experiment 4 - Locomotion Through a Confined Space With Payload

The final experiment investigates how well the worm robot can pull a payload whilst inside the confined space. In this instance brass weights were attached to the back of the worm to be pulled by the robot. The static coefficient between the acrylic surface and brass weights has been empirically measured to provide the static force required to move the payload. With a static coefficient  $U_s$  of 0.24, 100g payload requires a force of 0.24N to overcome the static friction, equally a payload of 1Kg requires a force of 2.4N. On a flat surface the maximum the worm can pull is 400g, (a force of 0.94N), using the gearbox or the ideal waveform. Inside a confined space where all segment skins contact a surface, the maximum the worm can pull is 1.6 Kg, (a force of 3.77N), using the same two waveforms. In comparison, the sine waveform could only pull a maximum of 800g, (a force of 1.88N). Table 5.2 shows a range of pull forces applied and the distances achieved. As expected, the greater the force, the less distance is achieved. The worm robot weighs a total of 225 g and yet the results show that it can demonstrate a maximum pull force of 3.77 N, when all four segment skins are in contact. As with the previous experiment, the results of each waveform are in line with the previous results, however, the pull force of 2.4 N was not able to be pulled when the robot was driven by the sine waveform as it does not produce enough clamping force. These results show a dramatic performance difference between a simple sine wave control of the tendons and a purposefully designed gearbox waveform intended to achieve a longer period of segments clamping.

If the results of these experiments are compared with the assumptions presented in Fig. 5.6, it is clear that while the sine waveform can no longer pull the payload, the results are fairly consistent. The performance drops of sine and geared are 20% and 5% respectively. This shows good evidence that adjusting the gearbox parameters can optimise the robot worm performance to that near an ideal waveform, whilst using only one actuator.

Table 5.2: Distance travelled through confined space executing 20 motor rotation cycles.

Pull force (New-tons)	Waveform	Distance (mm)	Std. Dev (mm)	% of ideal waveform
<b>0 N</b>	Ideal (Simulated)	56	2.5	100.0
	Gearbox (Simulated)	54	1.8	96.4
	Sine (Simulated)	48.5	2.1	81.6
	Gearbox (Real)	53.5	1.7	95.5
<b>0.24 N</b>	Ideal (Simulated)	47.5	2.7	100.0
	Gearbox (Simulated)	45	1.3	94.7
	Sine (Simulated)	39	1.9	82.1
	Gearbox (Real)	42.5	1.5	89.5
<b>0.48 N</b>	Ideal (Simulated)	40	1.7	100.0
	Gearbox (Simulated)	37.5	2.5	94
	Sine (Simulated)	32.5	2.1	81.25
	Gearbox (Real)	36.5	2.7	91.3
<b>1.2 N</b>	Ideal (Simulated)	36.5	3.1	100.0
	Gearbox (Simulated)	35	1.9	96.5
	Sine (Simulated)	26	2.7	71.7
	Gearbox (Real)	34.5	1.7	94.5
<b>2.4 N</b>	Ideal (Simulated)	31.5	2.2	100.0
	Gearbox (Simulated)	30	3.1	96
	Sine (Simulated)	n/a	n/a	n/a
	Gearbox (Real)	28.5	2.9	90.5

#### 5.4.5 Transferring Mechanism Parameters to a Gearbox Drive Mechanism

A state driven actuator mechanism has been designed in a soft bodied worm robot with three actuated segments. Fig. 5.13 shows the front view of the robot giving details of the actuator mechanism. It also shows  $r_1$  and  $r_2$ , the two radii that determine the output loci shape that pulls the segment tendons. On one hand,  $r_1$  can be considered as the main sinusoidal carrier wave whilst  $r_2$  provides the offset to shape the loci.

Fig. 5.14 shows a side view of the worm robot. Each of the segments has a tendon connected through to the drive mechanism using a Bowden cable. The drive mechanism pulls each tendon to produce the gearbox waveform shown in Fig. 5.6 where each segment's waveform has a  $120^\circ$  offset from its neighbour. The body of the robot has been printed on an Objet 260 3D printer capable of printing in multiple material including rubbers. The segment walls and actuator mechanism are made from Vero white, a hard 3D printable material and the soft skin is printed using Tango plus, a soft rubber capable of deformation under influence of a tendon but with enough resistance to return to shape when the tendon forces are released. Fig. 5.15 shows the robot printed and

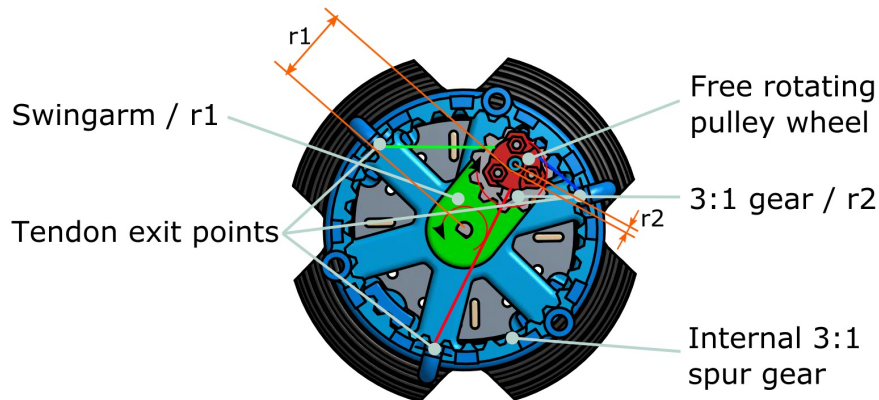


Figure 5.13: Front view of worm robot showing the gearbox mechanism made from two connected counter rotating gears.

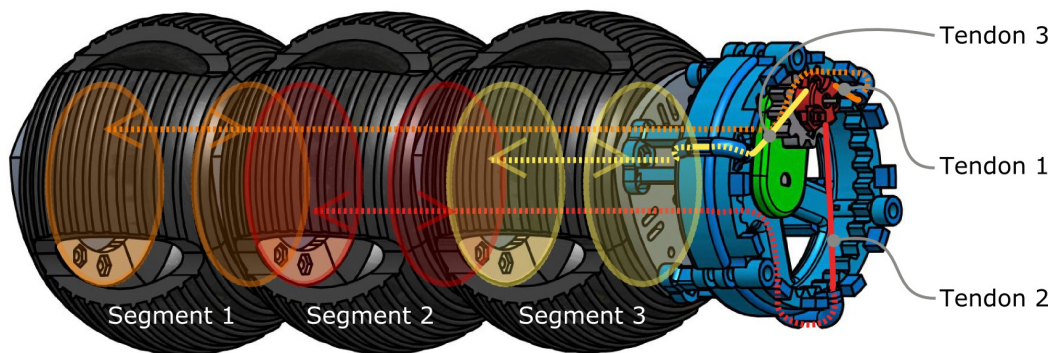


Figure 5.14: Side view of the robot worm design showing the front gear mechanism, soft body worm segments and tendon routing from gearbox to associated segment.

assembled. Note the three separate stages each segment is in when the robot is at rest. The robot has only one actuator, a Dynamixel XL-320. The surface of each segment has a raised profile to subtly recreate setae found naturally in many annelids.

This new single motor actuated robot has been run through the same performance metric as the test platform, see Table 5.2. The performance observed was as expected to be in line with the predicted performance of the gearbox waveform, only suffering a slight decline in total distance achieved. This is mostly likely due to the effect of the weight of the gearbox mounted at the front of the robot causing slight distortion in the soft body of the robot. This distortion could have lead to suboptimal surface contact during periods of the robot locomotion. Despite the slight performance drop this has confirmed that by exploring the gearbox parameters with the initial test platform, a

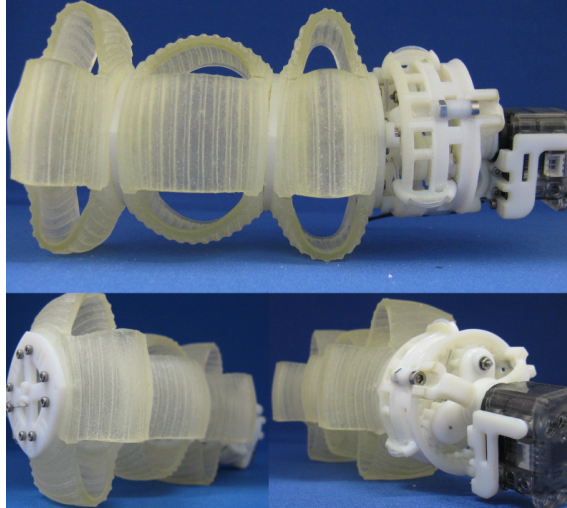


Figure 5.15: 3D printed worm robot with the gearbox that drives optimised peristaltic worm locomotion.

simplified single motor actuated peristaltic worm has been built with comparable performance to a robot worm with additional actuators dedicated to each worm segment.

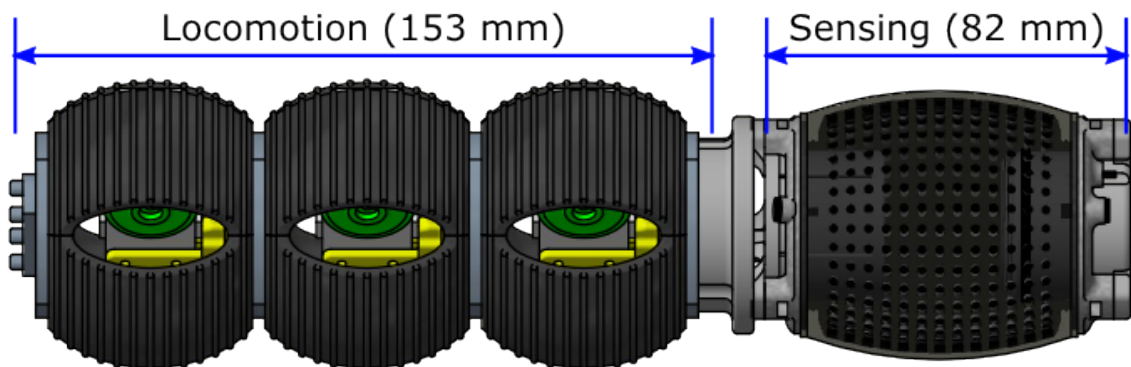


Figure 5.16: CAD model of integration of locomotion and sensing modules.

## 5.5 Integration

The following experiment sees the integration of the cylindrical tactip and the soft bodied peristaltic worm robot. Fig.5.16 presents how the two elements are arranged in CAD, where a new component is added to fix the two together and Fig.5.17 shows the real robot and sensor assembled. The peristaltic worm movements push the whole assembly forwards as developed in section 5.4, where the Tactip is the first to contact any new surface. The external surface of the Tactip will deform in relation to external

forces caused by the forward locomotion and contact surface features.



Figure 5.17: Built assembly of integrated of locomotion and sensing modules.

Combining the experiment environments from chapter 3, chapter 4 and chapter 5 a new environment can be created to test the new integrated system for locomotion and sensing. Placing a test piece symbolic of a submucosal tumour inside the environment, the robot system can be tested for effectiveness of detecting lumps previously developed in chapter 3 and chapter 4. Fig.5.18 shows the integrated assembly inside the previously used experiment environment, now with the addition of an artificial tumour lump 'Hard-60'. The figure details the direction of travel showing the Tactip sensor half way over the lump obstruction.

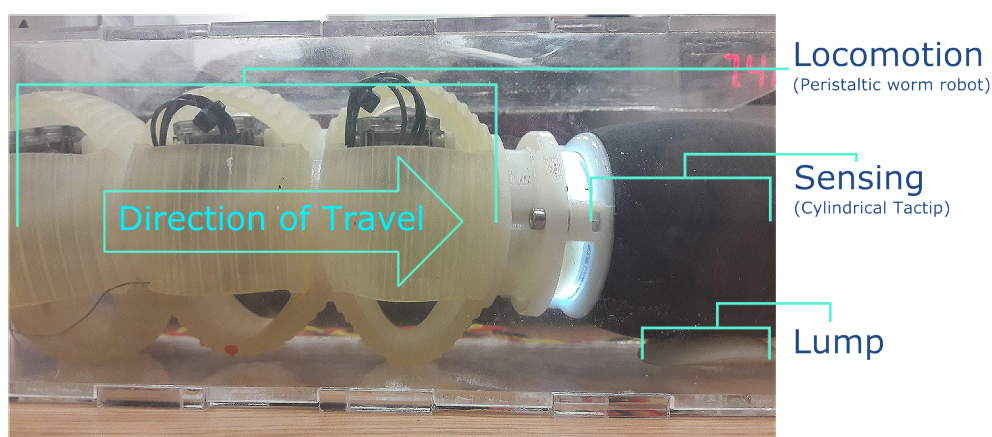


Figure 5.18: Integrated robot assembly inside test environment with addition of artificial tumour lump.

### 5.5.1 Experiment 5 - Locomotion of Soft-Bodied Peristaltic Robot with Integrated Cylindrical Tactip Tactile Sensor

During this experiment, the following procedure is executed whilst recordings of sensor data are taken;

- The robot will traverse through the test environment using the optimised driving waveform identified earlier in chapter 5.
- The robot will encounter the tumour like lump obstruction as used in chapter 3 and chapter 4, and continue to traverse over it.
- The Tactip sensing module will constantly be recording the image data throughout the experiment.
- The sensor data recorded will be pre-processed as in chapter 3 and chapter 4.
- Additional information will be available through the sensor from that will be generated from the locomotion. Tools will be identified to both isolate and remove this information leaving purely the object interaction.
- A comparison will be made between the quality of the data obtained in this experiment and that from experiments in chapter 3, chapter 4.

#### 5.5.1.1 Locomotion

Fig. 5.6 details the control signal waveforms considered to drive the peristaltic worm locomotion, in particular the ideal waveform which has been identified as the most effective when pulling a load. The ideal waveform was used for this experiment. In chapter 5 a mechanism has been presented that can achieve good performance using one motor that almost matches that of multiple motors, one for each worm segment. However, the facilities for manufacturing robust components that last multiple uses are not available within the laboratory, where 3D printing is favoured. The 3D printed gear components used in chapter 5 have not maintained their form to remain effective for further experimentation and so the multiple motor worm robot was used instead. When running the control signal waveform through the robot worm, a full cycle where a segment goes through full extension, contraction and clamping takes approximately 5.9 seconds.

### 5.5.1.2 Sensing

The algorithm used to process the raw sensor data will be the same as in previous chapters. The papillae pin matrix is split in to a 5 row by 35 column matrix as show in Fig. 3.10. Whilst at times 7 rows can be seen, during deformation the end rows can fall out of view of the internal mirror system, and 5 rows have been proven to consistently stay within view, and sections 4.6.4 and 4.6.3 have shown that the middle row and also adjacent rows to the middle are sufficient for effective sensing. During the entirety of the travel of the robot, images are captured from the camera at around 7.51 frames per second. Whilst this is quite slow, the robot is moving slowly through the test environment so all deformation will be captured. The position of the papillae pins will be monitored with the object tracking algorithm combined with nearest neighbour algorithm used in chapter 3 and chapter 4. 751 papillae vectors are summarised by being grouped in to their associated rows, with a sum of total deformation per row presented in graphs in the following section.

## 5.6 Results

Section 5.5.1.2 explains how the movement of papillae pins is grouped in to five rows, with each groups total pin movement analysed for interpretation. Fig.5.19 shows the sensor readings throughout an experiment lasting just over five minutes. In this experiment the robot traveled through the test environment described previously, encountered a hard artificial tumour like obstruction, and traversed over it. In Fig.5.19 a number of interesting observations can be made;

- The sensor detects deformation at all times. This means that not only is obstruction information detected, but general deformation caused by the experiment environment.
- When an obstruction is first encountered the sensor deformation increases which can be seen at around 150 seconds.
- Row 0 is the leading row in the sensor. It is this reason that row 0 encounters any contact or obstruction first, so in Fig.5.19 row 0 displays activity first, and whilst traveling unobstructed, an increased amount of deformation compared to other rows.

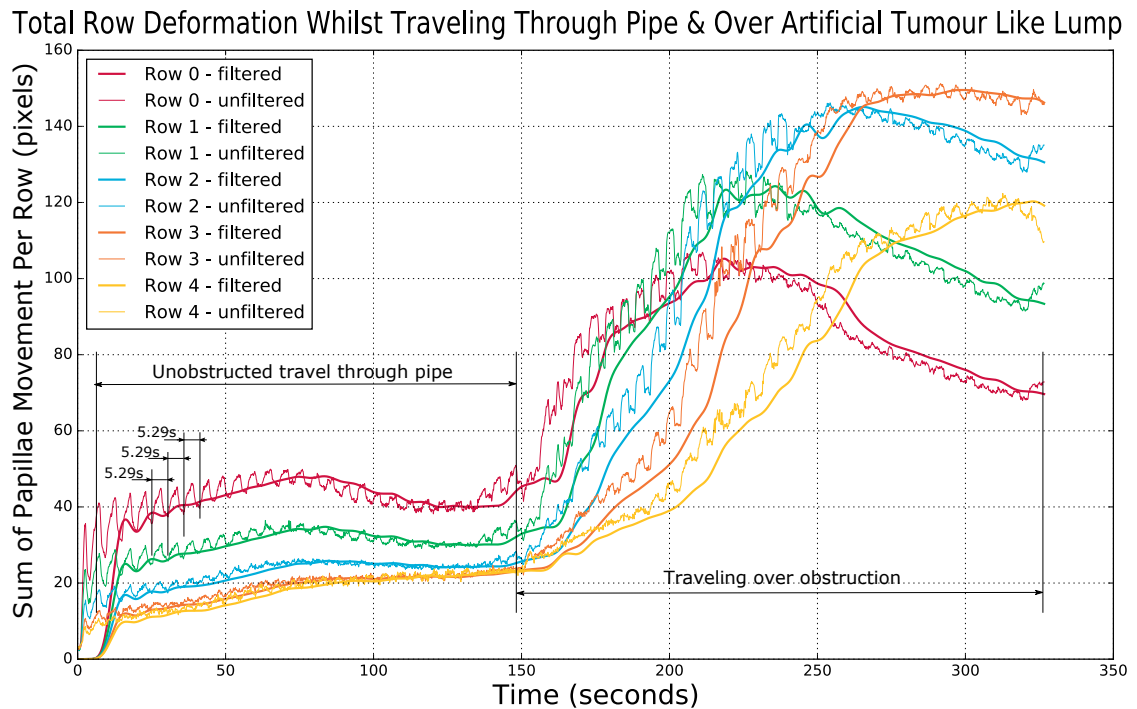


Figure 5.19: Total row deformation whilst traveling through test environment driven by the peristaltic worm locomotion robot developed in chapter 5. Note plots for raw data and data after a low-pass Butterworth filter has been applied. This isolates sensor data from object interaction.

- When the sensor encounters an obstruction row 0 may deform first but it is the middle rows which deform the most.
- There is a consistent wave form found in all of the row readings, with a duty cycle of 5.29 seconds. Cutting out the higher frequencies provides a much smoother data plot. This is shown in Fig.5.19 with the filtered plots. This data is created by applying a low-pass Butterworth filter to the unfiltered data with a cut-off frequency of 0.11 Hz, which is below the locomotion frequency of 0.19 Hz.
- Applying a high-pass filter to the data isolates the 'noise' or data created from the robot moving along the test environment. Fig.5.20 presents this noise data, which shows a consistent frequency with duty cycle of 5.9 seconds, equal to that of the robot's locomotion sequence.

Further more, Fig.5.21 shows a series of 3D plots of individual pin displacement over time, one for each row. These plots show a clear sequential increase in papillae pin movement at the 150 seconds, and at a focal point of the 20<sup>th</sup> column of pins. These

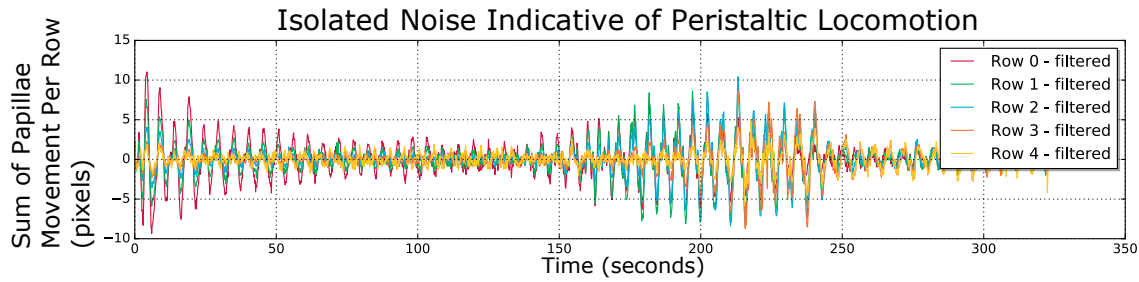


Figure 5.20: Row data after a high-pass Butterworth filter has been applied. This isolates the sensor data generated from the peristaltic cycles of the locomotion.

observations show that the integrated robot and sensor are capable of traveling along the test environment, traverse the lump obstruction, and after some relatively simple data processing distinguish between environmental noise and deformation caused by the obstruction.

### 5.6.1 Integration Data Classification Predictions

In order to tie together the developments of the previous chapters, the data recorded during the integration experiment has been passed to the classifier systems used in Chapter 4. Fig. 5.22 presents both the SVM and CNN system predictions of both the percentage of obstruction coverage and the predicted obstruction type. The results are laid over previous results of pixel movement per row to indication events of sensor stimulation and their correlation with obstruction predictions. The obstruction used in the experiment was the 'Hard-60' lump which can be seen as the predominant prediction from both SVM and CNN, however the CNN presents a higher occurrence of false predictions of 'Hard-120' lump. The CNN results provide the addition of confidence values, which show an interesting insight in to the effect of transitioning between the percent coverage groups. Confidence appears to settle once 100 % coverage is achieved. These results have shown that the previous development can be pulled together and show promise of the initial concept of this work.

## 5.7 Chapter Conclusion

In section 5.1 the objectives of this chapter were outlined and relate to the initial proposal detailed in section 2.3. Two outputs were expected from this chapter;

### Individual Row Papillae Pin Displacement Through Traverse

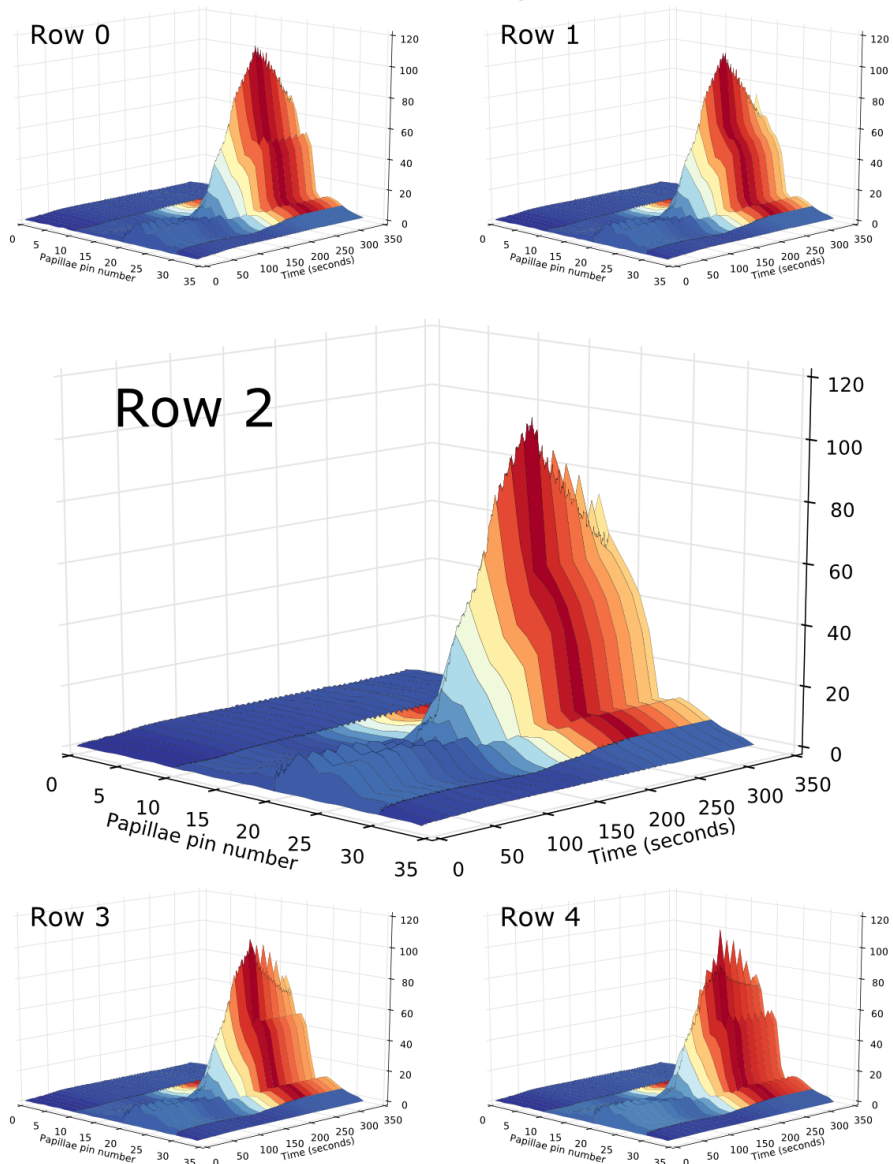


Figure 5.21: 3D plots of individual papillae pin movement throughout experiment period for each of the 5 captured rows.

- Present a robot design that moves along a pipe like structure along with parameters that maximise the pulling capabilities of the robot whilst also achieving a simpler drive mechanism for future miniaturisation. This has been addressed between sections 5.2 and 5.4
- Present an integrated system capable of moving and sensing through the test environment used in previous chapters. This has been addressed in section 5.5.

The robot development has shown the removal of the complexity of controlling multiple actuators and instead embedded the control sequence within a novel drive mechanism, addressing task 2.(d). This drive mechanism has been implemented in to a 3D printed soft robot body with three segments, addressing task 2.(c). Experiments with the robot have shown successful peristaltic locomotion comparable with a robot worm that requires multiple actuators, and that a tuned waveform generated by the gearbox mechanism can achieve better locomotion distance and payload carrying capabilities than a simplified sine waveform, addressing tasks 2.(a) and 2.(b).

The second output of this chapter has presented the integration of the tactile sensing developed in chapter 3 and optimised in chapter 4, with the locomotion system developed for the first output of this chapter, addressing task 3.(a). By combining both tactile sensing and locomotion it has been possible to explore the concept of an active capsule endoscopy by moving the robot towards and over a submucosal tumour model whilst recording tactile sensor reading. The data received has then been processed using both the method developed in chapter 3 and then chapter 4. These algorithms enabled identification of the model tumour, addressing task 3.(b). The results has shown promising data with easily distinguishable environment noise from desired tactile data. Further more, the data was then passed to the classifier systems developed in previous chapters to bring both the tactile sensing and locomotion developments together. The predictions generated by the classifiers show promising accuracy, with the SVM being more accurate in line with the results of Chapter 4.

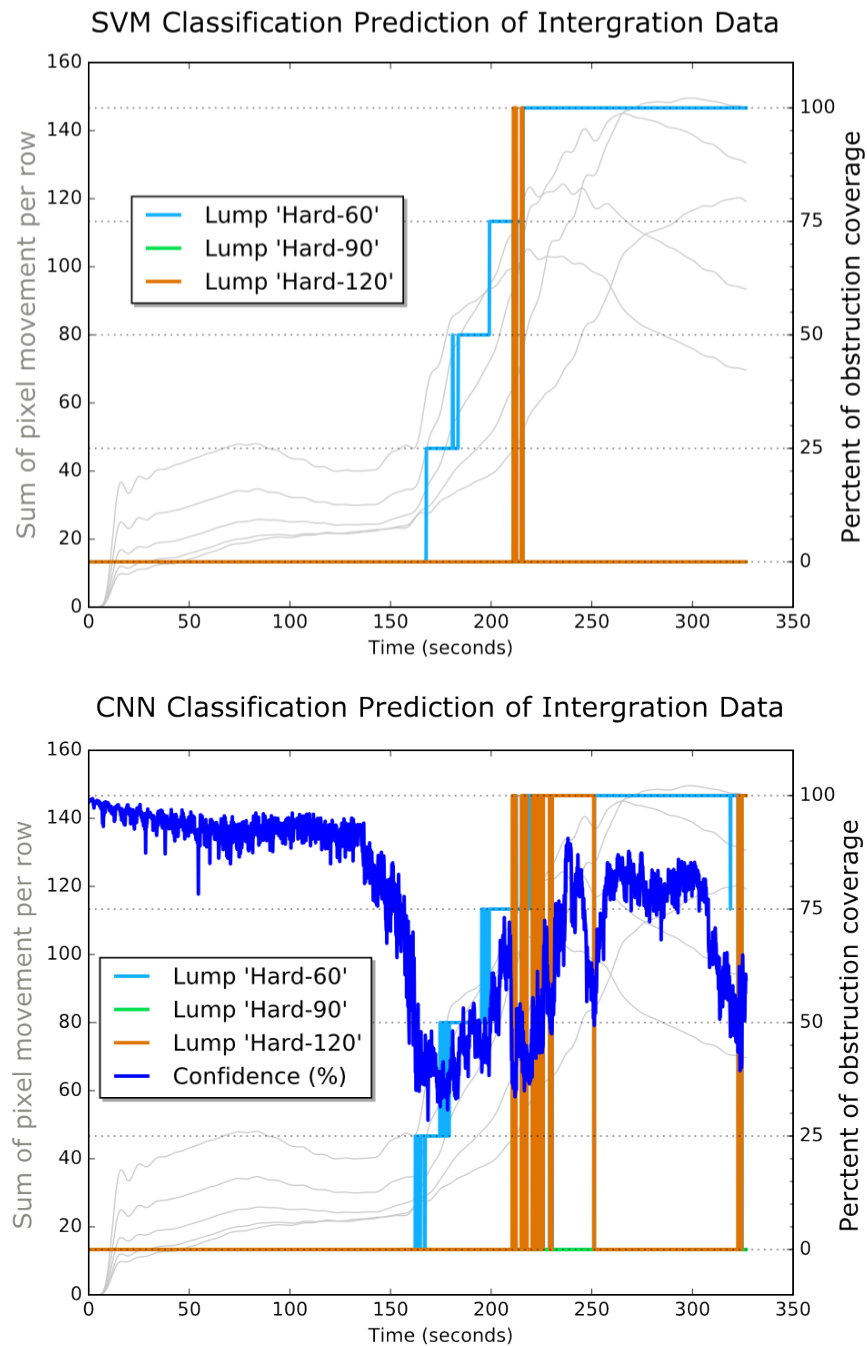


Figure 5.22: Top: Lump predictions from integration data passed to SVM used in previous experiments. Bottom: Lump predictions from integration data passed to CNN used in previous experiments. In addition, the CNN results are accompanied by a confidence percentage. Both results are layered over previous observations of pin movement presented in Fig. 5.21 to show correlation between prediction and sensor stimulus.

---

## A Review of Wireless Power for Capsule Endoscopy

---

### 6.1 Introduction

In Chapter 2 it was identified that the limitations in battery technology prevent the opportunity for additional payload being added to capsule endoscopy. Each additional camera, processor or actuator will require more power, reducing the operating time of the device. This chapter proposes that wireless power technology could be a solution by providing a constant source of power throughout the procedure. Section 2.2.2 has identified other work in the field applying wireless power to capsule endoscopy, [89; 73; 42]. In Section 2.3.1 it was stated that due to the scale of work required to build an effective WPT system for capsule endoscopy, a review and laboratory exploration of WPT would be sufficient to achieve the task 4.(a) within the timescale of this entire work. Task 4.(a) is listed below;

- **Review** the potential of WPT as a possible power source for untethered capsule endoscopy.

This chapter will discuss the concepts and principles of WPT and present laboratory based exploration of those principles. The outcome of this chapter will be an understanding of how WPT could be a practical power source for untethered capsule endoscopy.

## 6.2 Wireless Power Design Principles

Wireless power transfer (WPT), also known as wireless energy transfer (WET), is the process of transferring power from an energy source to a device without wires. Traditional WPT is based upon the concept of induction charging and can be seen being used in electric tooth brush chargers and handheld device charging pads. The leading approach to WPT is radio and resonance charging, which utilises magnetic resonance of an electromagnetic circuit. Whilst induction charging is restricted to very near field charging, resonance charging can transfer high powers over multiple feet. In the following section the principles of WPT will be discussed in order to be able to design a working system.

WPT is achieved using an air cored transformers. Whilst standard transformers have the advantage of nearly perfect conditions for energy transfer, air cored do not. The main contributing factor to these imperfect conditions is poor coupling between primary and secondary circuits, called mutual inductance, see Section A.1.5, and the coefficient of coupling 'k', with more explanation and equations relating to Bio-savart law, see Appendix item A.1.2 and Lenz's law see Section A.1.3. The equations presented in Section A.1.5 have been validated by comparing measured mutual inductance and predicted mutual inductance, shown in Fig.6.1. Two identical  $13.3\mu H$  coils of ten turns and  $20mm$  length were placed so that they are axially aligned at varying distances of separation and the mutual inductance measured.

Mutual inductance 'M' is derived by measuring the total inductance of the two coil connected in series to an inductance meter, and deducting that reading from the sum of L1 and L2. Measurements along the axis were compared against calculate predictions of the mutual inductance using the equations shown in Section A.1.5 and summarised with the coupling coefficient 'k' in Fig.6.1. Both measured and calculated coupling follow the same curve indicating that the calculations are accurate in this sinatnce

### 6.2.1 Circuit Design Principles

The primary RCL transmitting inductor circuit is supplied with a varying AC waveform to cause the induced magnetic field to expand and collapse. This achieves the change in magnetic field over time to induce emf as stated by Lenz's law. Magnetic field strength is proportional to the current through the coil, so ideal conditions would encourage

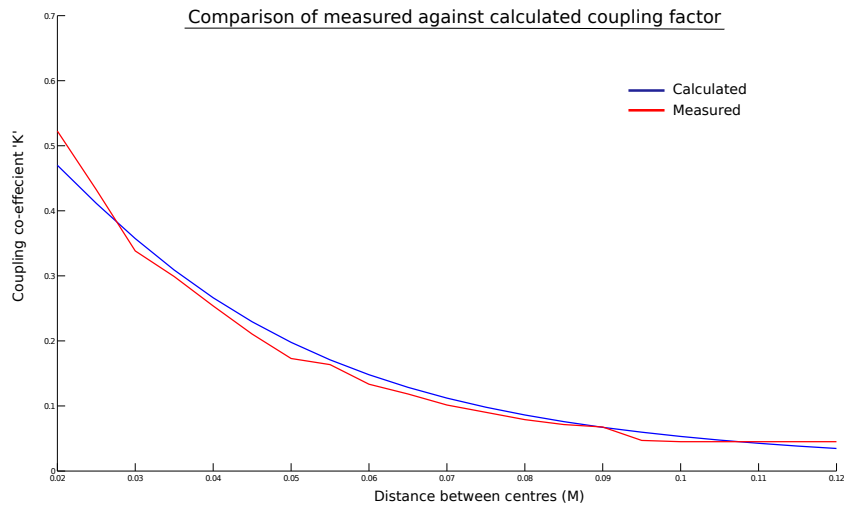


Figure 6.1: Measured against calculated mutual inductance of two identical ten turn  $13.3\mu H$  coils.

maximum current flow. The phenomenon of reactance in AC circuits states that a circuit has a resonant frequency where impedance is at a minimum and maximum current is drawn. A resonant circuit causes maximum current draw, which achieves maximum field strength to be generated by the inductor solenoid. A basic circuit design for WPT comprises of two in air cored transformer circuits, see Fig.A.11. Each circuit is tuned to the same resonant frequency. Each component value can be calculated as shown in Section A.2.2.2 for coil resistance, A.2.2.3 for coil inductance and A.2.2.4 for tuning capacitance.

## 6.2.2 Predicting System Performance

There are a number of circuit and inductor parameters that affect the performance of a WPT system. The first measure to consider is the effect of distance between the primary and secondary circuits. The emf induced in the secondary circuits provides a measure of system performance. Utilising the equation for emf A.5 derived from the equation for flux density A.4 section A.3.1 presents an example scenario predicting emf induced in a secondary coil. The data shows a rapid decline in emf with increased coil separation.

The next factor to gauge a WPT system is the efficiency or figure of merit 'U' of the system based up the coupling coefficient 'k' and quality factor 'Q' of the primary and secondary circuits, described in equation A.30. Section A.3.2 explains that 'U' is based on the 'Q' factor of both circuits and the coupling coefficient between both circuits.

Furthermore, system efficiency  $\eta$ , equation A.32 is derived from 'U' normalised between 0 and 1. These equations state that efficient WPT is achieved with a combination of strong coupling 'k' and high 'Q' circuits. Coupling between circuits is affected by the mutual inductance between coils, which itself is effected by coil parameters such as number of windings, length and diameter. High quality factor is effected by low resonant load of a circuit, high inductance and low capacitance of a circuit. Fig.6.2 demonstrates the effect of both k and Q on system efficiency. The graph shows that even with poor k below 0.1 with sufficient Q, efficiency of over 90 percent is theoretically possible, however achieving high Q is very challenging because even the smallest load will have a dramatic effect.

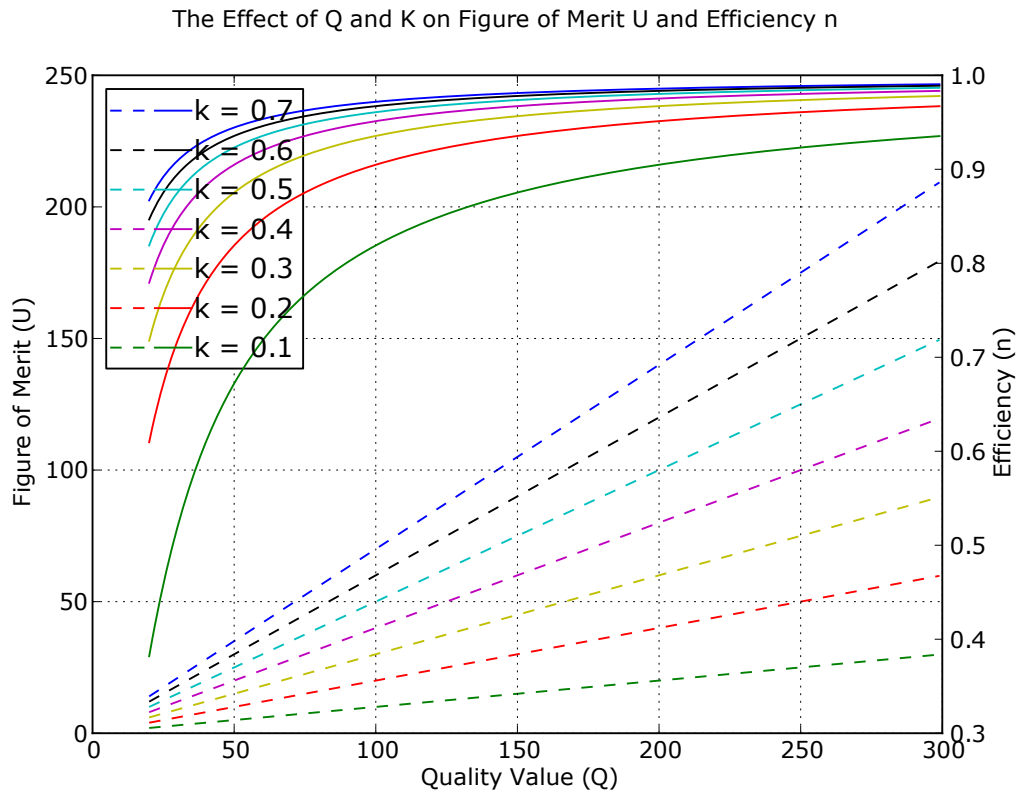


Figure 6.2: Demonstration of the effect of both k and Q on system efficiency. Broken lines represent U and solid lines represent  $\eta$

### 6.2.3 Exploring Coil Design

Fig.6.3 demonstrates the influence of solenoid length, radius and number of turns on Q. The graphs show that a short, large radius coil with a greater number of turns provides a higher Q resonant circuit. Considering that more turns in a shorter coil with larger

radius increases  $Q$ , space restrictions will inevitably lead to smaller conducting winding material which has increased resistance. Larger resistances greatly impact  $Q$  values so selecting high quality conductive material is recommended.

Fig.6.4 demonstrates the influence of solenoid length, radius and number of turns on mutual inductance  $M$  and in turn coupling coefficient  $k$ . As with  $Q$ , short solenoids with increased turns and radius have greater mutual inductance. In the context of capsule endoscopy, size restrictions limit coil radius and length, so efforts should be made towards more turns and shorter solenoid length.

Hoang and Bien state that "high quality factor coils are considered as one of the most critical features for a superior system", [5]. They further go on to categorise coupling based power transfer in to three types. First is low efficiency non-resonant inductive coupling. Second is low- $Q$  resonant coupling which uses resonant two coil circuits, mostly discussed in this chapter. Finally a high- $Q$  resonant system uses a four coil arrangement to further optimise transfer efficiency, see Fig.6.5. Whilst high  $Q$  circuits greatly improve transfer efficiency over greater distances, the output impedance of the signal source negatively effects the primary circuit  $Q$ . Equally, any load seen on the secondary a similar negative effect on the  $Q$  factor of the secondary. If the effect of these loads can be isolated from the coupling of the transmitting circuit then the transmitting circuit could achieve higher  $Q$  values and greater efficiency. The primary side of a high- $Q$  resonant system has a lower  $Q$  signal circuit wirelessly integrated with a high  $Q$  transmitting circuit. On the secondary side a high  $Q$  receiving circuit is wirelessly integrated with a low  $Q$  load circuit. In this system, source and load losses due to low  $Q$  are isolated from the transmission coupling, allowing for high  $Q$  coupling over distance. This is the same approach as used by MIT back in 2007 [87]. Hoang and Bien compare the efficiencies of these three discussed systems in Fig.6.6. This graph shows the advantages of high  $Q$  coupling over standard resonant and non resonant coupling.

Many of the studies into coil size ratios focus on flat spiral coils. Zierhofer et al. explain that flat spiral coils provide significantly improved coupling coefficient compared to coils with turns distributed along circumference [175]. An additional advantage of flat spiral coils is better form factor for electrical products such as mobile phones or medical implants. A recent study in to optimal coil size ratios by Waters et al. [176] has found that although vastly dissimilar coils yield poorer maximum transfer efficiency,

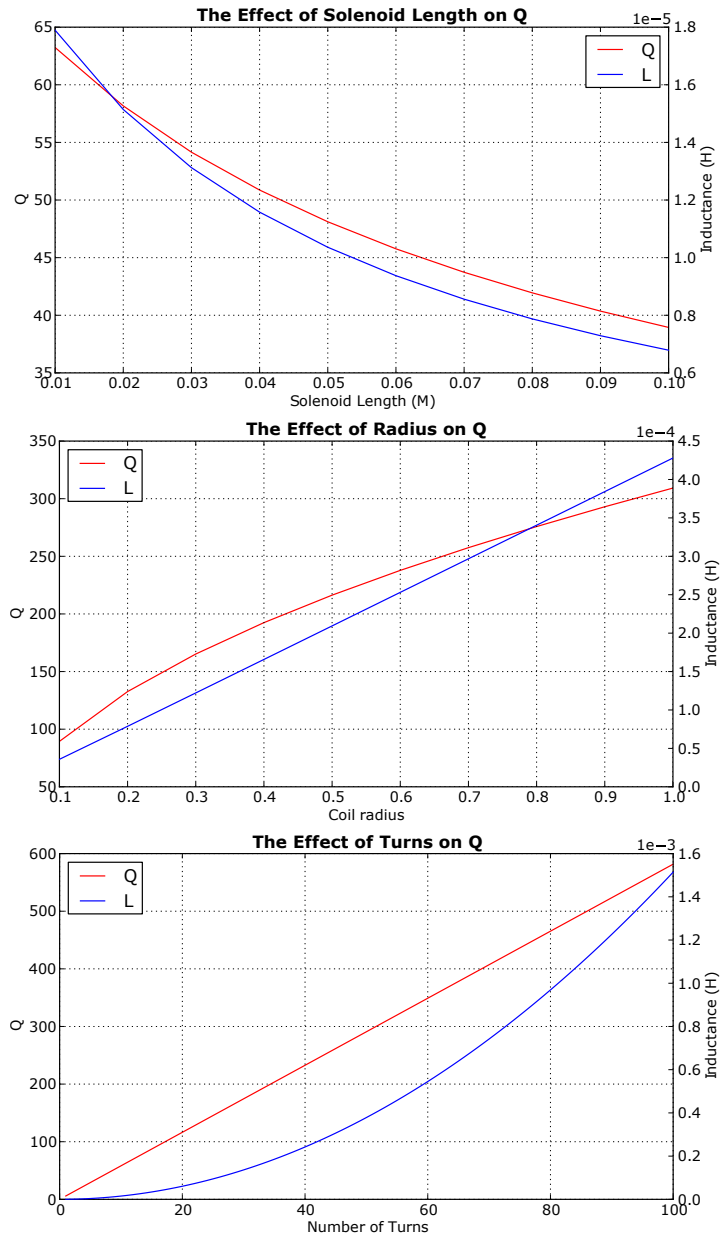


Figure 6.3: Demonstration of the effect of solenoid parameters on Q and inductance.

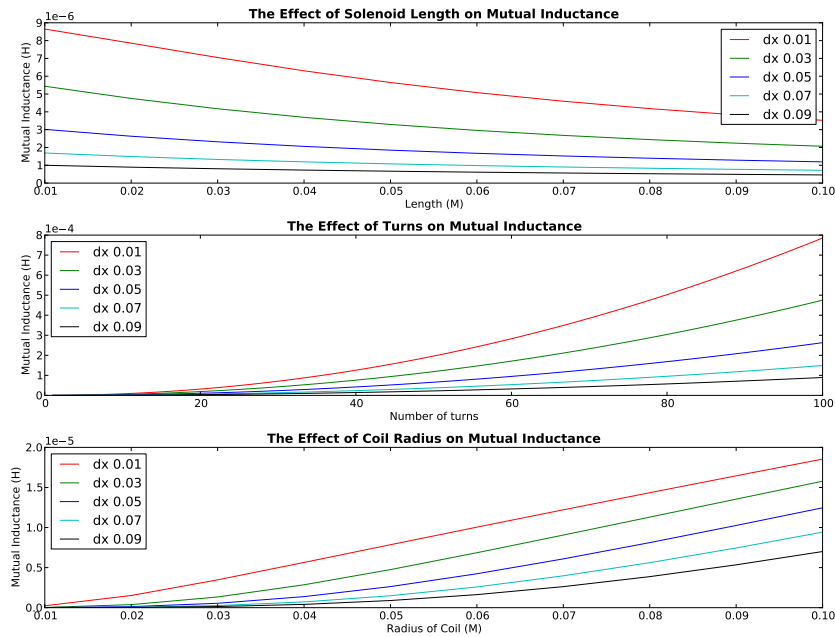


Figure 6.4: Demonstration of the effect of solenoid parameters on mutual inductance at various distances of separation.

they do not exhibit such drastic efficiency drop off and so can actually transfer better efficiency at further distances than similar coils.

In the context of WPT for capsule endoscopy, there are considerable size restrictions on the receiving circuit. Transmission distance is more strongly related to the magnetic field generated by the primary circuit. As such, the primary coil can more easily take advantage of the characters discussed, such as flat, multiple turns and large radius. Utilising the high Q principle the source load could be isolated, however, extra coils on the receiving capsule endoscopy may be too large to integrate. A capsule endoscopy would be moving in 3D and achieving varying orientation and misalignment can strongly affect coupling. Lenaerts et al. [89] suggests that orientation issues can be overcome using a coil on each plane at either the primary or secondary side. Lenaerts identified that using a receiver coil on each plane with only one primary coil was considerably more effective than using a transmitting coil on each plane with one receiving coil. Further to this idea, the primary circuit could be the secondary as it passes through the patient re-orientating itself to achieve maximum efficiency. This concept could be realised in a form similar to a MRI machine.

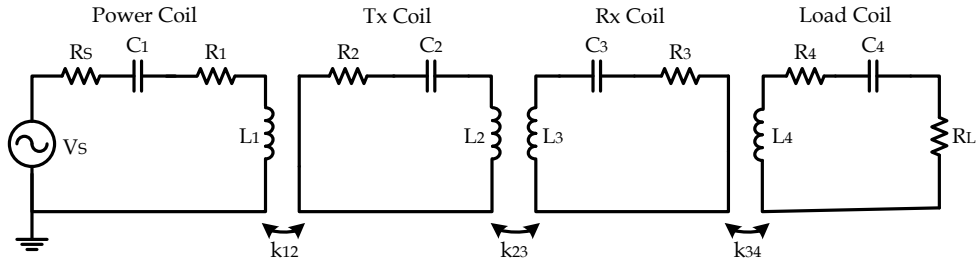


Figure 6.5: Four coil high-Q resonant circuit diagram. Taken from figure 6(c), [5]. Huy Hoang and Franklin Bien (2012). Maximizing Efficiency of Electromagnetic Resonance Wireless Power Transmission Systems with Adaptive Circuits, Wireless Power Transfer - Principles and Engineering Explorations, Dr. Ki Young Kim (Ed.), ISBN: 978-953-307-874-8, InTech, Available from: <http://www.intechopen.com/books/wireless-power-transfer-principles-and-engineering-explorations/maximizing-efficiency-of-electromagnetic-resonance-wireless-power-transmission-systems-with-adaptive>. Image acquired through Creative Commons Attribution 3.0 Unported License, <https://creativecommons.org/licenses/by/3.0/>.

#### 6.2.4 Identifying Requirements For Endoscopy Applicable WPT

The knowledge gained in previous sections suggests potential for WPT in the context of capsule endoscopy, however examples used are with coils beyond the size constraints of a capsule endoscopy. This section will explore a theoretical implementation of WPT for coils more suitable to the proposed application. Firstly, the coil dimensions will be defined. Regarding the secondary coil, the current PillCam technology is a cylinder shape with diameter of 11mm. This is a tight size requirement to match, given that coil diameter has a large impact on coil coupling. In order to maximise coil coupling a larger maximum diameter of 20mm is suggested and suitable to pass through the GI tract. Using 0.5mm copper at a length of 20mm there would be 40 turns in the coil. The primary coil can be much larger to offset the limitations of the secondary. The coil could be arranged flat to the patient's body or even around similar to an MRI machine. In order for this to be possible a minimum of 600mm diameter is suggested. Finally, using 1mm copper and a length of 50mm it will have 50 turns.

Accurate prediction of mutual inductance 'M' between very dissimilar coils is very challenging, so for the intention of this study it will be assumed such that a coupling coefficient 'k' of 0.1 can be achieved. In this case, M will be 68  $\mu$ H. With these parameters set, the figure of merit 'U', see section A.3.2, can be calculated. 'U' would calculate to be  $1.257 \times 10^{-6}$ . Finally with 'U' understood, system maximum achievable efficiency  $\eta_{opt}$  can be calculated, see section A.3.2.  $\eta_{opt}$  calculates to 0.15, or 15%. The

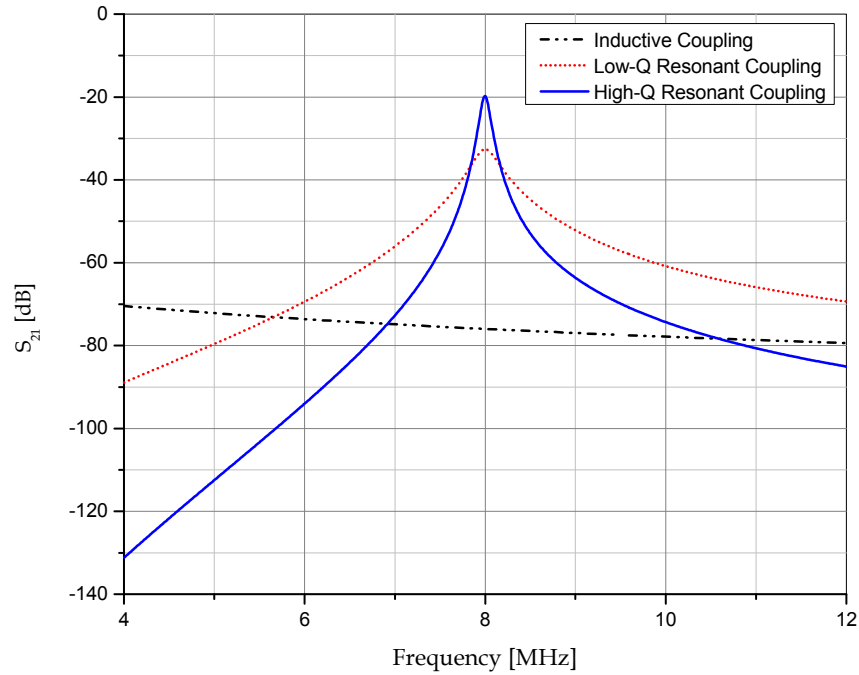


Figure 6.6: Comparison of performance between non-resonant, low-Q resonant and high-Q resonant power transfer system taken from [5].

secondary load will be assumed to be, camera 5 W, motor 5 W and MCU with wireless communications 2 W, the total being 9 W. With these figures, the secondary circuit load of 9 W, then the required input to the transmission circuit would need to be at least 60 W plus any losses within the amplifier circuit. These predictions are for a maximum potential efficiency where in most cases circumstances such as placement, orientation and environment permeability could reduce this potential dramatically.

Where;  $L1 = 6.10 \text{ mH}$

$L1 = 75.8 \text{ uH}$

$M = 68 \text{ uH}$

$k = 0.1$

$U = 1.257 * 10^{-6}$

$\eta_{opt} = 0.15$

It should be noted that this is a simple exercise where often equations have become inaccurate with greatly dissimilar coil parameters. As such, any future system should be measured empirically where possible for more accurate assumption of efficiency.

### 6.3 Proof of Concept Circuit design

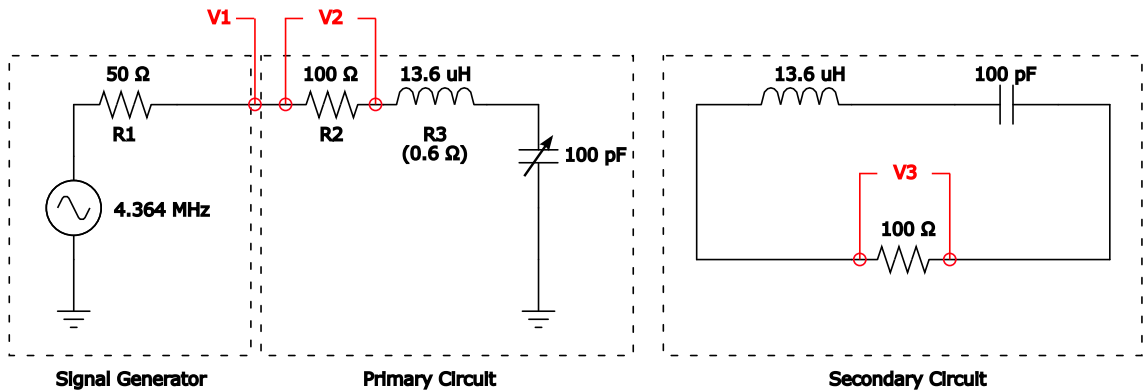


Figure 6.7: Circuit diagram of initial WPT prototype powered directly from signal generator.

The following section describes a physical air-cored transformer circuit based on the principles discussed in sections 6.2. The system comprises two LCR circuits, class E amplifier and digital signal generator. Each LCR circuit has the same 10 turn, 0.1m dia., 0.02m long 13.6  $\mu\text{H}$  inductor coil and 100 pF capacitor. The LCR circuit has been designed to resonate at 4.316 MHz. A variable capacitor is used on the secondary side to compensate for any unwanted stray capacitance or inductance, see Fig.6.7

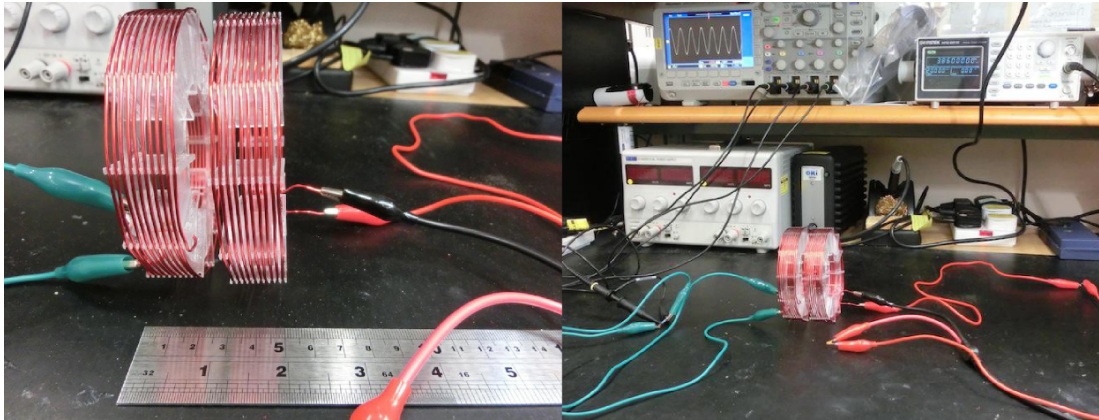


Figure 6.8: Left: Close up of WPT coil arrangement. Right: Experiment set up showing the coils, signal generator and oscilloscope.

#### 6.3.1 Amplifier Circuit

This section details the principles behind the amplification circuit used to provide current for sufficient magnetic field in order to achieve a practical transfer distance and power. A first consideration when designing an amplifier for WPT is the frequency

range of the amplifier. It is not possible to design an amplifier that works equally at low and at high frequencies due to the AC characteristics of each component. Working at higher frequencies provides requires higher specification components and tools to build and test the circuit. Typically the drive element of the circuit, a transistor or MOSFET needs to be able to rise and fall within the time requirements of the frequency. Not only do these components need to be quick enough but they also need to be able to produce a stable signal that does not suffer distortion. Some comparison can be made with RF radio design, with many of the research examples using WPT work between 4.5MHz and 12MHz, see Section A.2.1.3, however, with WPT the power requirements are higher.

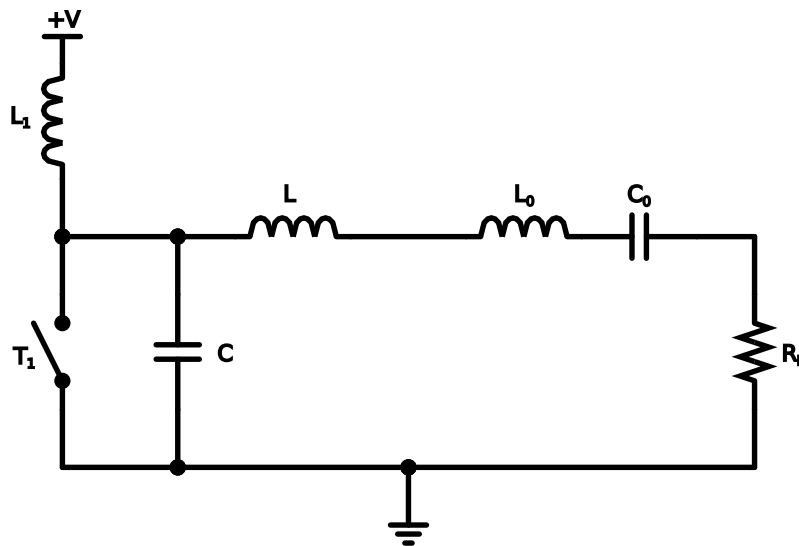


Figure 6.9: Typical Class E amplifier circuit.

The most common method of describing the operation of a power amplifier is with it's class. Typical applications are limited to classes A through to C, whilst more untypical applications extend the range to E and sometimes F. Each class has particular characteristics such as high voltage, high current or wide bandwidth which make that class more appropriate for a given application. The wireless power transfer system requires a fast switching power amplification. The class E amplifier is the most suited to this scenario. This choice is confirmed by [177; 178; 179; 36], all of which use the class E amplifier design for their primary circuit. Fig. 6.9 shows a typical circuit design for a Class E amplifier. The design intention of a class E amplifier is to eliminate the effects of the capacitances within the MOSFET on the efficiency. A major characteristic is that the MOSFET is switched on only when there is no voltage across the device, which

eliminates switching losses. These capacitances are dealt with by incorporating them in to the resonant circuit much like how a resonant LCR circuit has zero reactance at resonance.

### 6.3.1.1 Class E Amplifier Design

The following section describes the prototype Class E amplifier circuit. Using the example class E designs outlined in "RF Power Amplifiers", [180], component values have been calculated using the equations in Section A.4. An initial class E power amplifier was first built on prototype board, see Fig.6.10 and with circuit diagram shown in Fig.6.11. The signal generator source does not provide enough power to enable the IRF540 MOSFET so a UCC27523 MOSFET driver is required to pre-amplify the input signal. This converts 10V<sub>p-p</sub> to 12V<sub>p-p</sub> with enough current to switch the IRF540 MOSFET. The MOSFET then outputs 12V<sub>p-p</sub> at a current drawn by the circuit, and is no longer limited to the capabilities of the signal generator. In this scenario the primary coil is being used as the sole inductor of the LCR circuit, whilst the ten parallel capacitors are the offset capacitance to tune to resonance. The reason ten are used instead of one, is an attempt to lower the Equivalent Series Resistance (ESR) compared to using only one 100pF capacitor. The remaining components are required to enable the MOSFET to drive at RF frequencies. Without these precise values, the charge and discharge periods of the MOSFET will be too long to achieve a change of state for higher frequencies.

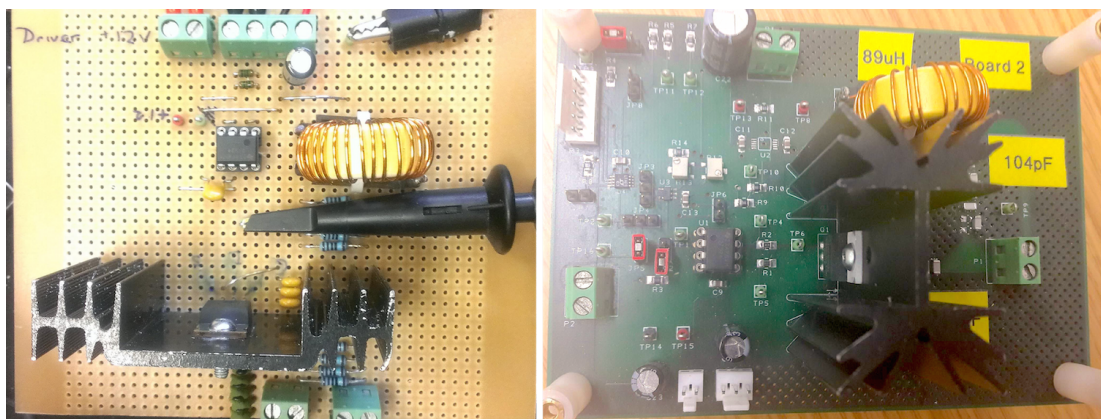


Figure 6.10: Left: Class E power amplifier prototype circuit. Right: Class E power amplifier PCB circuit

Although functional, this first prototype amplifier was very prone to failure, with

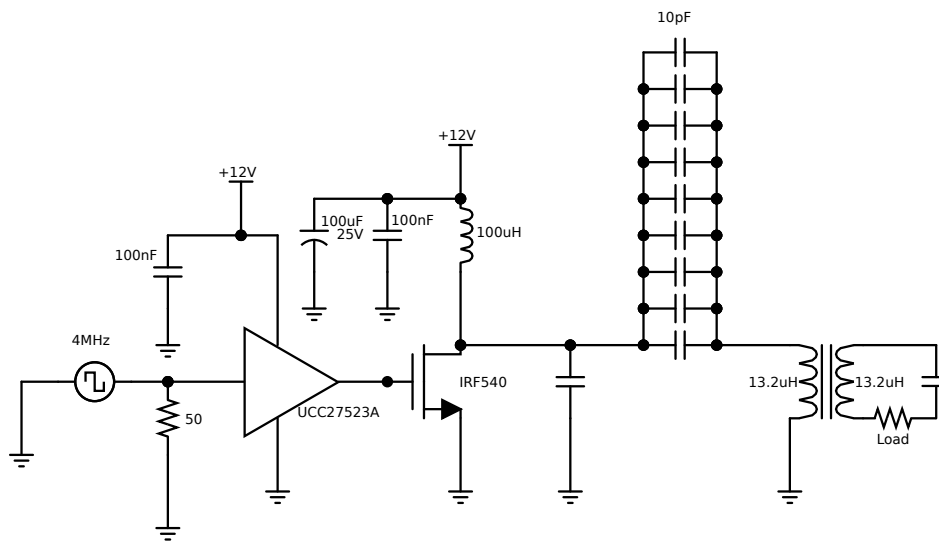


Figure 6.11: Class E power amplifier design schematic.

components over heating regularly, solder melting and the MOSFET driver burning out when the circuit is subjected to a sudden change. The materials used make prototyping easy however are poorly suited to high frequency high current power systems. This is mostly due to thin copper tracks close to each other creating high capacitance between conductive surfaces. Learning from this first design, an improved design that tackles the problems such as component breakdown and overheating, was made in PCB form, see Fig.A.16. The new design has incorporated the following features;

- Onboard I2C power monitoring chip.
- Three methods of supplying waveform signal, I2C programmable oscillator, potentiometer controlled oscillator and external supplied signal.
- Increased sized heat sink.
- Heat extraction fan.
- Lower capacitance printed circuit design.

Fig.6.12 demonstrates the WPT system powering a 3W 12V bulb, inferring 3W of power transfer over a reasonable air gap. When no secondary coil is present and the primary circuit is at resonance the amplifier draws peak current. If a secondary

is introduced, the mutual coupling and inductance shift both coils resonant frequency, which in turn increases their impedance reducing their current draw, reducing their magnetic field strength. A variable capacitor is used on the secondary to alter the resonant frequency and optimise the power transfer to the secondary.

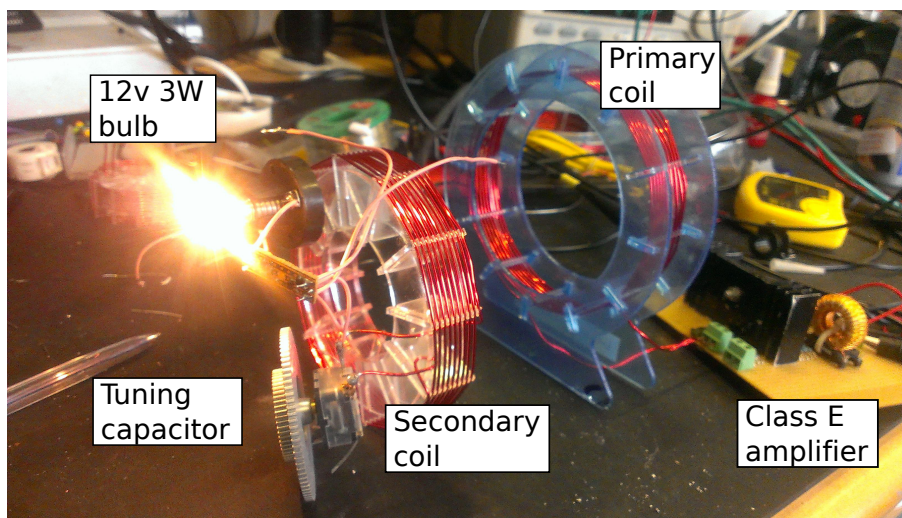


Figure 6.12: WPT system powering a 3W light bulb.

### 6.3.1.2 Benchmark of Class E Amplifier Design

Fig.6.13 presents an axial scan using standard identical coils as discussed previously. Each coil is  $13.3\mu H$  and  $\varnothing 0.1m$ . It should be noted that when the voltage at the receiver drops below 5.5 volts the I2C power monitor will not operate so no power can be measured. The results show that power peaks around 100mm separation, which is coincidentally the diameter of the primary coil. The peak frequency is between 4.1 and 4.2 MHz, and it should be noted that the rate of change in peak frequency greatly decreases once the separation between the coils is greater than the diameter of the primary coil. Figures 6.13 and 6.14 show progressive scans at two different loads to represent the effect of a changing load on the reflected load to the primary side of the system.

Although the improvements on the first design have created a more robust amplifier, the new design still have some issues remaining;

- 100v capacitors arcing during high current situations. This was remedied in the short term by replacing the 100v capacitors with 400v capacitors.
- Coil connection terminals arcing / over heating during high current situations.

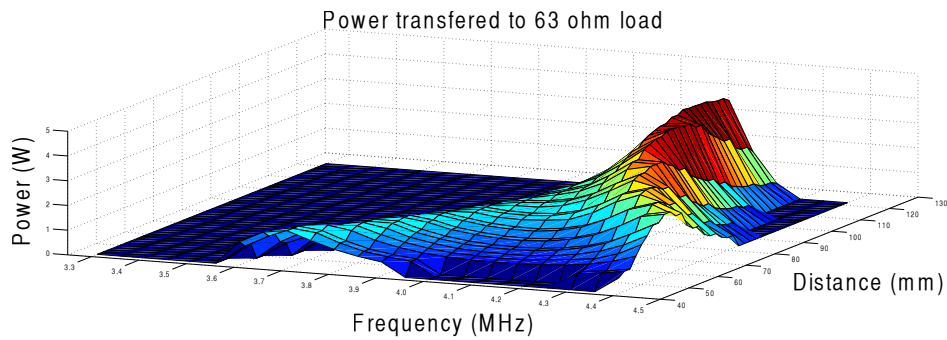


Figure 6.13: Axial scan of power transfer from 40mm to 120mm separation.

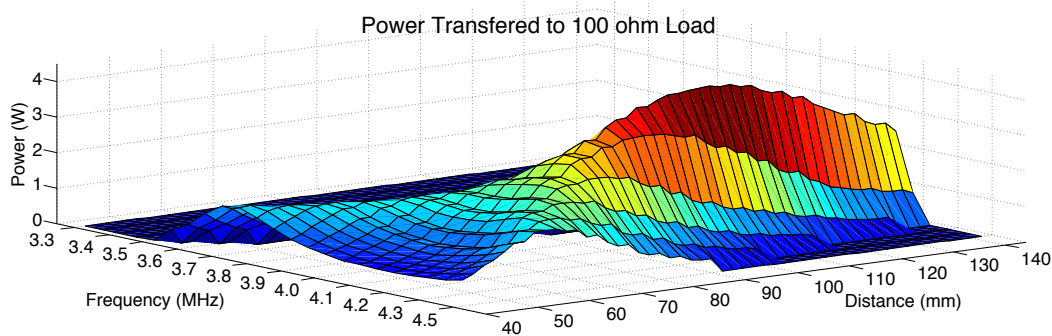


Figure 6.14: Axial scan of power transfer from 40mm to 140mm separation.

- Power can only be measured when voltage to monitoring chip exceeds 5.5 volts.
- When supply voltage is set to 12 volts it is possible to burn out the mosfet driver when the current is high or there is a vast quick change in system coupling. Keeping supply voltage to 10 volts and using a power supply that has a quick response to the current limit being exceeded at around 2 amps almost entirely prevents this. This effect is more common when the secondary load is much smaller, at greater distance, and poorer coupling more current is drawn through the primary.

### 6.3.1.3 WPT Circuit Efficiency

Figure 6.15 shows maximum power transfer as a ratio of input power to output power. These graphs show that optimal efficiency is achieved at a distance just close to the coil diameters, however actual maximum output continues to increase until just after the distance of the coil diameters. It should be noted that in publications discussed and due to the decline in coupling as coils separate efficiency always starts at a peak

and declines with distance however in these graphs closer range does not behave the same. It seems as though close predictions on efficiency such as shown in Fig.6.2 are not as accurate as further distance predictions. It is currently thought that this may be due to the effects of close coupling and mutual inductance at close range strongly affecting reflected load and small differences in resonant frequencies due to additional inductances in the resonant circuits. This would be easier to eliminate with a high-Q system as discussed previously in section 6.2.3

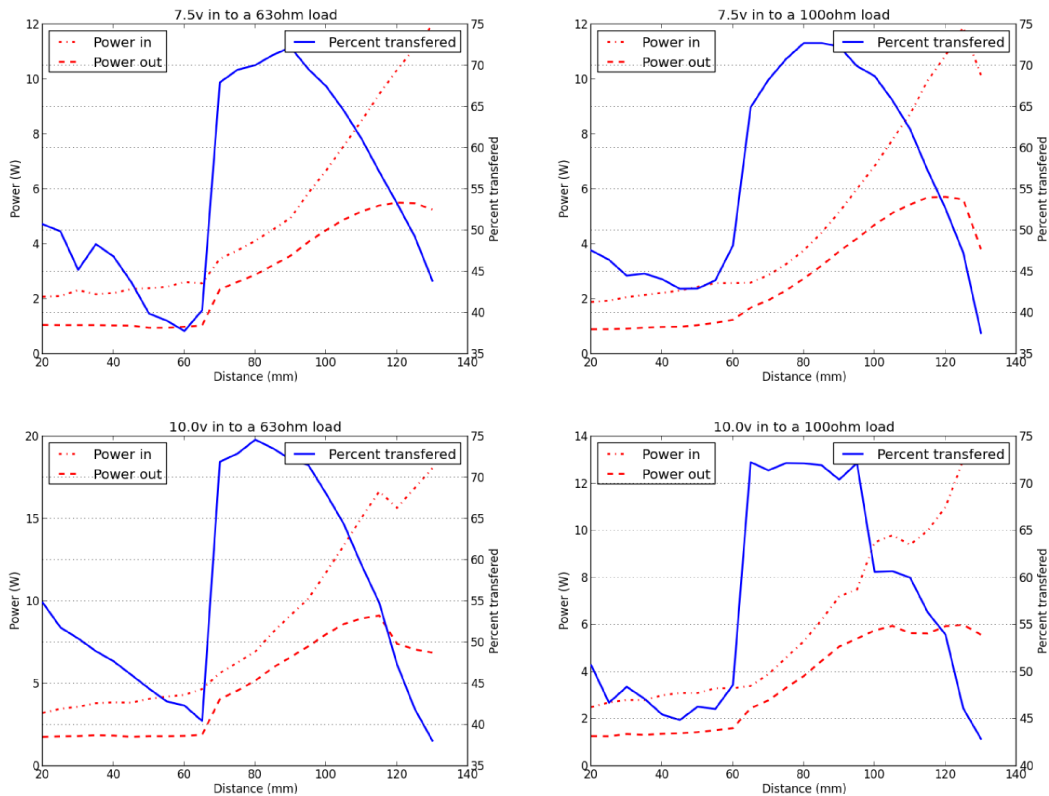


Figure 6.15: Real efficiency scan 20mm to 130mm coil separation, TL: 7.5v input signal with 63 ohm load on secondary, TR: 7.5v input signal with 100 ohm load on secondary, BL: 10.0v input signal with 63 ohm load on secondary, BR: 10.0v input signal with 100 ohm load on secondary.

## 6.4 Chapter Conclusion

Chapter 2 identified that the limitations in battery technology prevent the opportunity for additional payload being added to capsule endoscopy. It was proposed that WPT could be a feasible solution that can provide continuous power if the necessary conditions can be achieved. Whilst WPT development was considered a large task, Objective

4.(a) stated that a review of potential of WPT as a possible power source for untethered capsule endoscopy was needed. Without a power solution the capsule endoscopy design would have to be tethered in order to host additional actuation and payload. Future work will be able to build on the findings and suggestions in the chapter to design and integrate WPT with the capsule endoscopy design.

This chapter has discussed the considerations of WPT and its effects on the human body, concepts and principles of WPT and present laboratory based exploration of those principles. Findings suggest that WPT for capsule endoscopy procedure is safe. Through this research, design attributes have been identified which improve WPT efficiency; high Q circuits, flat wide coils with multiple turns, and isolating transmitter and receiver loads from coupling circuit. Where physical restrictions on components impact efficiency, altering other variables can offset losses to maintain a feasible power transfer system. Furthermore, it is also suggested that the receiver has three coils, one on each plane to compensate for orientation misalignment when the capsule endoscopy is moving through the body.

This final chapter concludes this study by summarising the work undertaken, the achievements and contributions made to this area of knowledge and discussions for future work that could be conducted.

## 7.1 Summary of Research Findings

### 7.1.1 Background Issues

The initial introduction to the work in chapter 1 outlined the intentions to explore the problems encountered during internal examination and diagnostic procedures of the human body. Particular focus has been paid on remote operated miniature robotics for endoscopic procedures. Chapter 2 first investigates the environment of the GI tract and the tools used to examine it. The limitations of passive capsule endoscopy and restricted travel of traditional endoscopy reveal the need for an endoscopy system with both greater access throughout the GI tract and increased diagnostic systems.

Other methods of diagnosis were next reviewed regarding palpation, and its importance in looking for signs of nonuniform density tissue beneath the skin that may be indicative of a tumour. This has led the review towards robotic technology developed with force and tactile feedback for inspection of human tissue. No examples of capsule endoscopy with tactile sensing could be found. This was validated by the review of the

”frontiers of robotic endoscopic capsules” [148] where Ciuti et al. report that only very recent and preliminary technologies [131], the work presented in chapter 3, demonstrate remote tactile palpation for untethered capsule endoscopy. The growth of submucosal tumours beneath the intestinal lumen cannot be visually identified until they breach the lumen surface, however, clues of their presence can be identified through nonuniform tissue density characteristics. Integrating a method of tactile sensing of the lumen with capsule endoscopy could provide opportunity to sense these nonuniform tissue density characteristics. This observation has identified an opportunity for novel research, and is in line with Chaudhary’s recommendations for medical technology development detailed in the chapter 2, [21].

The passive travel of capsule endoscopy does not provide the surface exploration required to create models of shape size and texture described by [149] so section 2.2.1.2 presents research in to developing miniature medical robots and capsule endoscopy with a method of locomotion to achieve this control. Furthermore a broader exploration into robotic locomotion for environments similar to the GI tract; tunnels and pipes. Reflection on how nature solves locomotion through similar environments has lead to an analysis of worm locomotion and findings of a range of studies in to robotic worm locomotion, in particular peristaltic worm locomotion.

The idea of adding additional payload for sensing and locomotion increases the power requirements of the system. Battery technology is restricted by a relationship between battery capacity and physical size, so to carry more power means a bigger battery. The proposed solution is to used wireless power technology to provide a continuous power source to the robot. Wireless power transmission is a complex field of study which could occupy a whole PhD. It is not expected that a complete solution can be identified within this work, but an understanding of possibility through a comprehensive review.

Section 2.2.3 explores the benefits of tactile sensing technologies applied to medical procedures. Furthermore a review is presented of the suitable technologies that have been developed to interact with human tissue. After a discussion on the ways to transduce tactile energy, a novel technological approach to tactile sensing has been identified in the soft and compliant optical based BRL Tactip sensor.

### 7.1.2 Aims and Objectives Revisited

Section 2.3.1 outlined the objectives for this study based on the research questioned proposed in section 1.4. Section 2.3 proposes three areas of research, capsule endoscopy with onboard diagnostic tools, capsule endoscopy locomotion and wireless power for capsule endoscopy. It is these objectives, and tasks detailed in the work plan, section 2.4, which will be used to measure the success of the findings.

#### Research Objectives

1. Capsule Endoscopy with Onboard Diagnostic/Treatment Tools.
2. Active Capsule Endoscopy Locomotion.
3. Wirelessly Powered Capsule Endoscopy.

## 7.2 Contributions to Aims and Objectives

The following section details how the work undertaken contributes to achieving these aims and objectives.

### 7.2.1 Tactile Sensing

Chapter 3 has tackled the research aim of a sensing system applicable to examination inside the body and addressed tasks 1.(a),1.(b),1.(d) and 1.(e) With an understanding of the role and mechanisms of tactile sensing an initial proof of concept study explores the possibility of sensing tumour like objects in soft artificial tissue using the Tactip system. This led to a deeper study using a reformed Tactip to sense deformation inside a pipe environment. The results of the experiment showed that the cylindrical Tactip data could be processed to recreate the three dimensional sensing environment, and also that the different obstruction characteristics provided noticeable variances in the sensor output. In part, this has contributed to satisfying research objective 1. 'Capsule Endoscopy with Onboard Diagnostic/Treatment Tools'. A summary of the three contributions from chapter 3 follows;

- Proof of concept study to investigate applicability of the Tactip sensor for tactile sensing applied to capsule endoscopy. This concept was presented at Living Machines 2014 [131].

- Developed a new cylindrical version of Tactip to suit the pill capsule form required for endoscopy. This utilised the flexibility of a multi-material 3D printer to create a cylindrical soft sensor with 360° field of tactile sensing. A new catadioptric mirror system was incorporated to adapt the vision system to the new 360° field of view.
- Characterised the new cylindrical Tactip inside a tunnel like environment with artificial tumour like lumps. The sensor data provided the ability to identify lump and reconstruct the sensing environment in a 3D rendering. These results were presented at Living Machines 2015 [150].

### 7.2.2 Classification of Tactip Data

Taking the findings from chapter 3, chapter 4 has optimised the sensing algorithm to achieve a higher level of processing. This addresses tasks 1.(b) and 1.(c). Classifier systems have been used to discriminate between artificial submucosal tumour like lumps which vary in shape and hardness. Using the same laboratory test environment as previous experiments, this experiment has explored ways to discriminate between lump shape size and material hardness of artificial tumour lumps. This has fulfilled the remaining requirements towards research objective 1. 'Capsule Endoscopy with Onboard Diagnostic/Treatment Tools'. A summary of the three contributions from chapter 4 follows;

- Characterised the cylindrical Tactip relationship between force and deformation with a range of artificial tumour lumps.
- Optimised the data processing algorithm to incorporate a classifier system to discriminate between shade, size and hardness of artificial tumour lumps. These results were published in IEEE Sensors Journal [159].

### 7.2.3 Locomotion

Chapter 5 explores the development of a soft-bodied peristaltic worm locomotion robot with a novel gearbox mechanism designed to allow for miniaturisation with reduced number of actuators. This addresses tasks 2.(a),2.(b),2.(c),2.(d),3.(a) and 3.(b). Developed through simulation and then in a real robot, optimal gearbox parameters were

identified and then integration of sensing and locomotion systems achieved. An experiment was presented whereby the peristaltic worm robot pushes the cylindrical Tactip through a the test environment, whilst the Tactip captures data. The data is then processed using the algorithms developed to identify the submucosal like artificial lump obstruction encountered during travel. The results showed successful detection of the artificial submucosal lump and easy discrimination between environmental noise and tactile information. These achievements satisfy research objective 2. 'Active Capsule Endoscopy Locomotion'. A summary of the three contributions from chapter 5 follows;

- Designed a novel gearbox mechanism which defines the timing and motion of Bowdon cable tendons used to actuate segments of a worm robot. This provides an opportunity to reduce the number of actuators in a robot design, allowing for easier miniaturisation.
- Validated gearbox parameters with a test robot platform, identifying optimal parameters to match an environment of given size. These results were presented at IEEE BIOROB 2016 [1].
- Integrated the worm locomotion robot with the tactile sensing module. The integrated system was tested inside the locomotion test environment with the addition of an artificial tumour lump whilst sensor data was captured. Data was analysed to identify the presence and type of the lump and discriminate lump data from environmental noise data caused by the locomotion.

#### 7.2.4 Wireless Power

Chapter 6 tackles task 4.(a) by expanding on the review of WPT for capsule endoscopy in Chapter 2 and answers the following questions;

- Is WPT for capsule endoscopy safe for the human body?
- What are the principles of WPT?
- How can WPT be optimised for greater transmission distance?
- How could WPT be adapted for capsule endoscopy?

Chapter 6 approaches these questions by exploring the principles of WPT system, from laws of electromagnetic interactions to efficiency optimisation for air-cored

transformers. From this study it was identified that WPT can achieve higher efficiencies through high-Q resonant circuits. Further more high-Q circuits can be achieved through flat wide coils with multiple turns and isolating transmitter and receiver loads from coupling circuit. Finally, Section 6.3 implemented these findings to develop a working prototype of WPT. A class E amplifier was designed and built through two iterations and transfer efficiency was measured over various distances. This work has contributed towards research object 3. 'Wirelessly Powered Capsule Endoscopy'.

### 7.3 Limitations of this Study

The future vision of this study is a small robot that can enter the body through an exposed orifice, travel to a desired region of the intestinal tract and then examine the area looking for signs of ill health beneath the lumen surface. This work has made early strides towards this, however there are a number of limitations that need to be resolved in moving forwards. The first limitation is this test environment. Focus has been on understanding the characteristics of the tactile sensing system with known object, structure and force. In reality, human bodies are not rigid and predictable. Whilst the findings presented do show how the tactile sensing works against a rigid structure, with more time this should be developed further to explore tumours beneath a soft flexible surface. The same situation exists with the development of the locomotion system. In order to work successfully in the human body, the locomotion must work within a flexible pipe, which is beyond what has been presented here. This limitation has been a factor of time to achieve all objectives outlined in chapter 2, but these further developments are believed to be technically achievable in light of the findings already presented.

The concept of wireless power presented in this study identified the scope of the work required to achieve a working system suitable for this application. Unfortunately that scope in addition to the other objectives was far beyond achievable within this PhD period and so an investigatory study was made. From the findings collected, a starting point for development has been established for future work. In this state a working wireless power system for capsule endoscopy has not been developed, but an understanding of how one could be has been achieved.

## 7.4 Future Work

### Natural Test Environment

Now that the sensing and locomotion elements of this system have been tested individually and also combined, they are ready to be developed towards a more clinical environment. Both sensing and locomotion should next be capable of operating in a soft environment closer to that found naturally in the intestinal tract. The first step to achieving this would be to develop a soft flexible silicone pipe environment. The robot will then be tested inside this new environment to measure its capabilities in movement and sensing. It may be the case that characteristics of both technologies will need fine tuning or redesigning to overcome any new challenges that arise from the environment. For example a flexible environment may increase the complexity and noise in the data obtained from the sensor which may cause the sensor to need a higher resolution of papillae pins, or additional fingerprint like surface features as explored by Winstone et al. [4] to amplify skin deformation. Once successfully operating in a flexible compliant environment, the next stage would be to use an organic test environment such as pig intestines. In doing this, it would be as close as the system can be tested before being used with human patients.

### Robust Miniaturised Tactile Sensing Capsule

A number of other future developments should be pursued regarding the tactile sensing technology presented. The first would be to aid in a reduced sized capsule Tactip. The optics system, the camera and the catadioptric mirror, are purchased items designed for a different purpose. If both these components could be replaced with bespoke designed alternatives then their size could be greatly reduced, meaning the whole system could be reduced in size. The dependency on 3D printing materials, whilst reducing development time and costs, has placed restrictions on material properties and size. If a cast silicone skin could be developed to replace the 3D printing Tactip skin, then the sensing device would benefit from both a more robust structure and also greatly reduced size as previously shown in [132].

### Adaptive Locomotion System

Whilst this work has presented a method to optimise locomotion to a fixed environment size, it has also provided gearbox variables that have potential to be altered during

locomotion. If such a mechanism was developed the robot would be able to adapt to a changing environment size, such that in a tighter or wider pipe the robot could achieve its maximum forward movement and strength. This could be achieved using discrete actuators such as SMAs or Piezo Ceramic motors to make adjustments to the  $r_1 : r_2$  ratio, or tendon offset  $a$ . In doing this, the system could be compliant to varying environment dimensions

### **Locomotion feedback**

The nature of the locomotion robot's skin being flexible means that just as with the tactile sensing capsule, it could be possible to measure skin deformation optically from inside the robot body. If papillae were added to the inside surface of the worm skin, then contact information and locomotion feedback could be observed in the same way that the cylindrical Tactip works. This could lead to a system that has combined tactile sensing along the length of the robot and not just at the front. This would present new challenges for the optics and algorithm due to the extra movement that would be observed, however section 5.6 identified that locomotion causes a predictable change in sensing data that can be filtered out quite easily.

### **Wireless Power**

Chapter 6 has presented an exploration into wireless power in order to identify whether it is a suitable solution for the increased power requirements on more capable capsule endoscopy. It has not been possible to develop a working power source for the other developments of this work due to the effort required for this complex activity. In doing such it would have been at the sacrifice of the other achievement in this work. As such this development is still required in order to realise an untethered capsule endoscopy with locomotion and tactile sensing capabilities. This should be achieved by using a 3 coil receiver arrangement, to compensate for changing orientation, and if possible also using the four coil high 'Q' circuit for each phased receiver and shown in [5]. Once a working system is achieved it should be tested alongside the locomotion and sensing components in the realistic soft intestinal tract environment suggested previously.

### **Beyond Capsule Endoscopy**

The achievements presented in this work have focussed on capsule endoscopy as a means to gain access to the intestinal tract without surgical procedures. This type of

environment shares parallels with other problems in a variety of fields. Firstly, human medicine shares many practices with veterinary medicine. In veterinary medicine the patient can be much larger, reducing the need for miniaturisation. In animals the risks associated with sedation can be much greater in animals. This capsule endoscopy could offer a lower risk method to access the intestinal tract if the patient is considerably weak.

Industrial pipe inspection has been the focus of many of the examples for locomotion identified in subsection 2.2.1. The economic implication of failure in systems providing water or energy to large numbers of customers can be huge. In many cases in order to provide safe access for a human the system must be shut down, however, a robot can potentially enter and maintain the system with minimal changes to the operational system. For example, cracks and fractures are typically early signs of failure that have to be addressed to avoid more severe consequences later. This robot worm and tactile system could be applicable in such situations. Small features such as cracks could potentially be detected by implementing the findings of the earlier Tactip work that utilised fingerprint for texture discrimination, [4].

Finally this work could also be considered in the context of exploration of unknown or unsafe environments such planetary exploration or disaster zones. With further development this robot could be designed to burrow through soil or the debris of fallen buildings. The robot could be released from a Mars rover to explore soil, rocks and regions that current rovers cannot reach, and at little expense or economic risk.

# Appendices

## A.1 Electromagnetic equations

### A.1.1 Magnetic Field Strength

The Oxford Dictionary defines a magnetic field as "a region around a magnetic material or a moving electric charge within which the force of magnetism acts." It is often defined in terms of the Lorentz force it exerts on moving electric charges. A quantity of magnetism is measured in flux. Flux describes the total amount of magnetic field in a given region. It is analogous to electric field in that it can exert force on a charged particle. Magnetic field strength  $H$  is the result of magnetic flux density over the material permeability. Magnetic flux is defined as the scalar product of the magnetic flux density  $B$  and the area, and is measured in the unit weber and the symbol  $\Phi$ .

A two dimensional cut away of a three dimensional field is shown in Fig.A.1. The basic field shown, is produced either by a permanent bar magnetic, or charged elementary particle and is defined as a dipole magnetic field. This means that it has polar attraction from north to south, much like charged particles positive to negative.

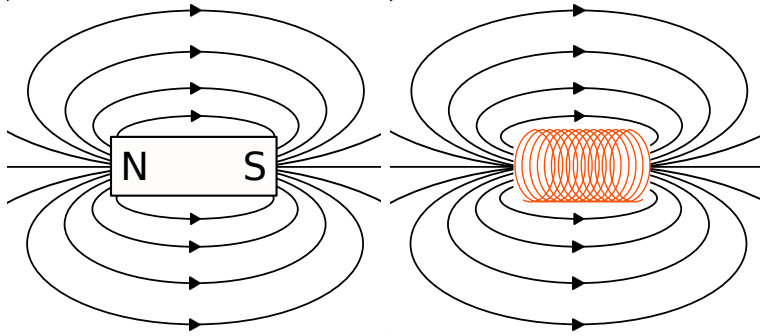


Figure A.1: Example magnetic field produced by permanent bar magnet, left, and conductive coil, right.

Magnetic fields are produced by either permanent magnets (a material is magnetised and creates its own persistent magnetic field, typically made from ferromagnetic materials) or electromagnets (magnetic fields produced by electric charge passing through a conductive material, creating magnetic force). Typically an electromagnet is constructed with conductive wire, wrapped in a helical coil form. Electromagnets differ from permanent magnets in that their strength can be controlled by a number of characteristics. The following equations, A.1, A.2 explain how the strength of an electromagnet is derived.

$$H = \frac{B}{\mu} \quad (\text{A.1})$$

Where;

**H** = Magnetic field strength, A/m

**B** = Magnetic flux density, Tesla

$\mu$  = Permeability of material

### A.1.2 Magnetic Flux Density

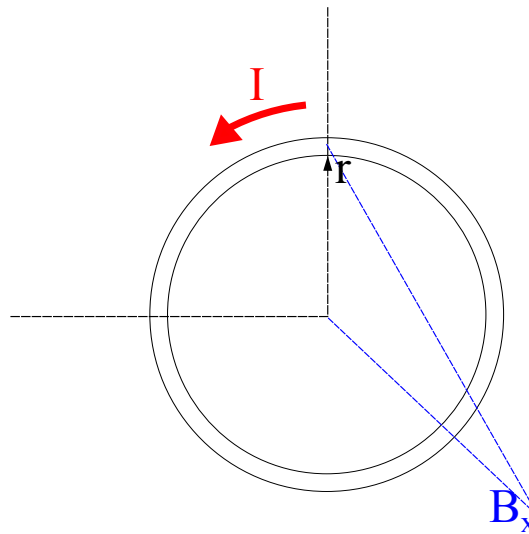


Figure A.2: Bot-Savart current loop

Biot-savart law defines the magnetic field generated around a conductive loop due to an electric current. At a given point 'x' along the loop axis, the magnetic field can be calculated as shown in equation A.2;

$$B_x = \frac{\mu_o I r^2}{2(r^2 + X^2)^{3/2}} \quad (\text{A.2})$$

Where;

**B** = Magnetic flux density, Tesla

$\mu_o$  = Permeability of free space

**r** = Radius of coil, meters

**I** = Current through coil, amp

**X** = Distance from centre of coil, meters

The equation shows that a number of conditions affect the field strength of an electromagnet. The radius of the helical coil and the amount of current passing through the coil are the main contributors to the magnetic field strength produced. With an increase in distance from the centre of the coil the magnetic field strength decreases at a rapid rate. A typical electromagnet is made up of multiple conductive turns.

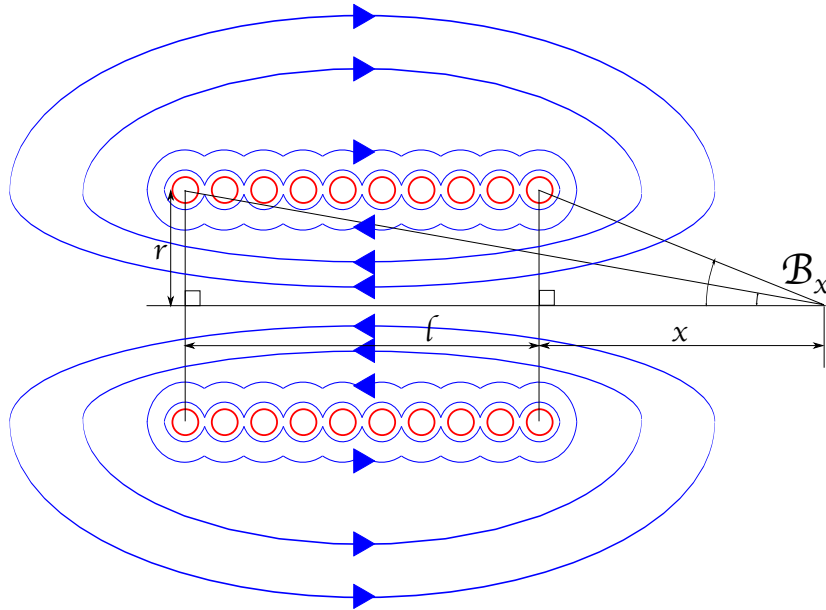


Figure A.3: Solenoid magnetic field

If Biot-savart law is integrated across the length of these turns, a general rule to calculate the magnetic field generated at a given point along the solenoid axis as shown in Fig.A.3 can be derived, see equationA.3.

$$B_x = \frac{\mu_o N I}{2L} \left[ \frac{x + L}{\sqrt{r^2 + (x + L)^2}} - \frac{x}{\sqrt{r^2 + x^2}} \right] \quad (\text{A.3})$$

Where;

**B** = Magnetic flux density, Tesla

$\mu_o$  = Permeability of free space

**r** = Radius of coil, meters

**I** = Current through coil, amps

**L** = Length of solenoid, meters

**x** = Distance from centre of coil, meters

Total magnetic flux is related to the magnetic flux density and the cross-sectional area of a solenoid, and is derived from the following equation.

$$\Phi = BA \quad (\text{A.4})$$

Where;

$\Phi$  = Magnetic flux, weber

$\mathbf{B}$  = Magnetic flux density, Tesla

$\mathbf{A}$  = Area of closed coil winding,  $m^2$

### A.1.3 Magnetic induction

Fig.A.4 demonstrates a permanent bar magnet moving through an induction coil. The magnet has a permanent static magnetic field which when moved through the coil the field changes in relation to the coil, over the time of movement. It is this change of field that exerts force on the charged particles in the coil, that causes emf. If the bar magnet was to stop moving, the magnetic field would not be moving, meaning that no emf would be induced in the coil.

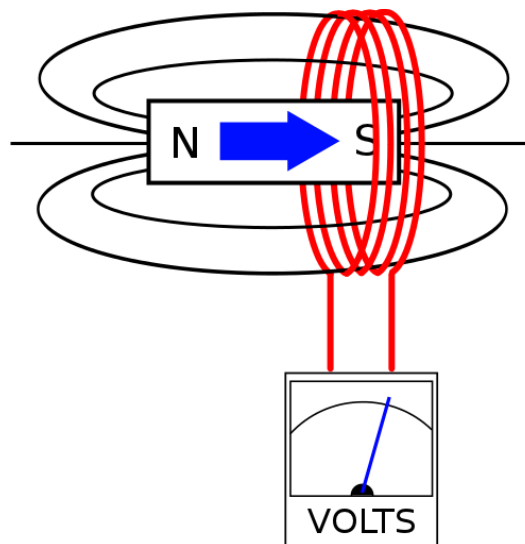


Figure A.4: Permanent bar magnet moving through an induction coil produces emf voltage.

Emf is proportional to the amount of conductive material in which the magnetic field interacts with. This means that an induction coil with more turns will have more conductive material interacting with a changing magnetic field, providing a larger emf value. This is made clear with the equation that derives the emf value, equation A.5.

$$\xi = -N \frac{\Delta\Phi}{\Delta t} \quad (\text{A.5})$$

Where;

$\xi$  = Electromotive force, volts

$N$  = Number of turns in coil

$\Phi$  = Magnetic flux, weber

$t$  = time, seconds

The magnetic field generated by the bar magnet in Fig.A.4, could be equally generated by a electromagnetic coil. The advantage of using an electromagnet is that the coil can remain static, whilst the magnetic field can be varied in relation to the input signal driving the coil. Typically an AC signal is used to expand and collapse the magnetic field in a primary coil, such that the change in flux over time determines the emf induced in the secondary coil. This is demonstrated in Fig.A.5. Similarly to how if the bar magnet stops moving no emf is induced, if the input signal to the primary coil stops changing, no emf is induced. Essentially this is the theory behind a conventional transformer, using an air core, instead of a more effective iron core.

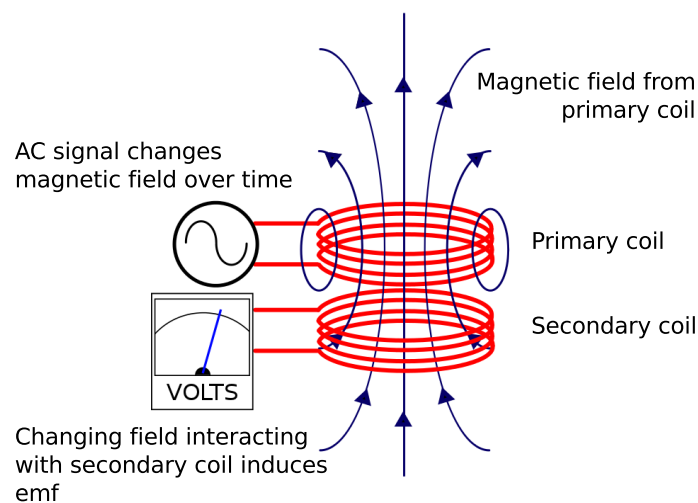


Figure A.5: Primary coil produces emf voltage in secondary coil.

#### A.1.4 Transformer theory

The traditional transformer works using the explained principle of generating a magnetic field with a primary electromagnetic coil to induce an emf in the secondary induction coil. All descriptions so far present electromagnetic induction using coils or permanent magnetics in free space, or air. Permeability is a quantity measuring the influence of a substance on the magnetic flux in the region it occupies. The permeability

of free space ( $\mu_o$ ) is particularly poor,

$$\mu_o = 4\pi * 10^{-7} \tag{A.6}$$

This means that any generated magnetic field expands in all directions, creating low density of flux quickly as distance increases from the source. Using a core inside the electromagnet helps focus the magnetic field, increasing flux density in desirable areas. An ideal characteristic of a core is high permeability. In a transformer a core is shared between both primary and secondary coils, often in a ring shape. Fig.A.6 presents the fundamental form of a transformer.

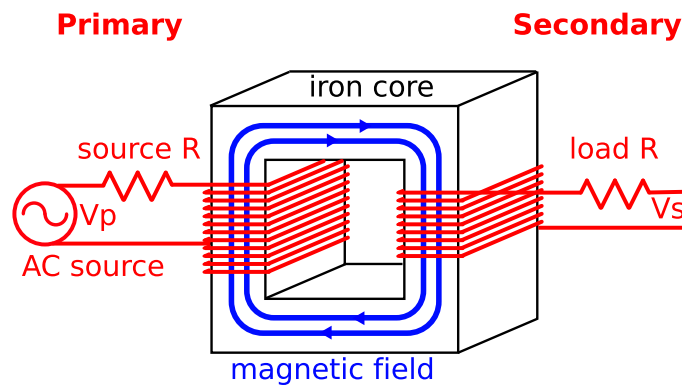


Figure A.6: Fundamental formation of a transformer.

Equation A.7 describes the relationship between input voltage and output voltage of a transformer based up the ratio of turns. A perfect transformer has no loss of magnetic field outside of the iron core, and with a high quality core, loss is negligible. The induced emf is calculated with the same equation A.5, noting that the permeability co-efficient will be dramatically higher using an iron core. Iron cored transformers are many times more efficient than air cored transformers at low frequencies.

$$\frac{V_s}{V_p} = \frac{N_s}{N_p} \tag{A.7}$$

Where;

$V_s$  = Voltage secondary

$V_p$  = Voltage primary

$N_s$  = Turns secondary

$N_p$  = Turns primary

### A.1.5 Mutual Inductance

The term mutual inductance describes the inductive relationship between the primary and secondary coils in a transformer circuit. When the magnetic field generated by the primary interacts with the secondary coil, an emf is produced in the secondary, which in turn creates its own magnetic field. Finally this magnetic field interacts with the original primary coil. This coupling effect presents itself as an additional inductance in the circuit known as mutual inductance;

$$M = \frac{N_2 \Phi_{12}}{I_1} \quad (\text{A.8})$$

Where;

$M$  = Mutual inductance, Henries

$N_2$  = Number of turns in secondary coil

$\Phi_{12}$  = Magnetic field linking primary to secondary

$I_1$  = Current through primary, amps

In a traditional iron core transformer scenario coupling between coil is usually considered to be almost one hundred percent, however when there are no high permeability core materials, only air, coupling is very much lower. Given that  $M$  relates to the magnetic field generated by the primary, then mutual inductance can be calculated at various distances of coil separation. Despite the inclusion of current in equation A.8, mutual inductance is not related to current and is explained by transposing previous equations for  $\Phi$ , A.4, and  $B$ , A.3. If A.8 is expanded out you are left with the following equation;

$$M = \frac{\mu_o N_1 N_2 I \pi r_1^2}{2LI} \left[ \frac{x + L}{\sqrt{r^2 + (x + L)^2}} - \frac{x}{\sqrt{r^2 + x^2}} \right] \quad (\text{A.9})$$

With basic algebraic manipulation equation A.9 can be minimised to equation A.9 where current is no longer a component of the solution.

$$M = \frac{\mu_o N_1 N_2 \pi r_1^2}{2L} \left[ \frac{x + L}{\sqrt{r^2 + (x + L)^2}} - \frac{x}{\sqrt{r^2 + x^2}} \right] \quad (\text{A.10})$$

Where;

$M$  = Mutual inductance, Henries

$\mu_o$  = Permeability of free space

$N_1$  = Number of turns in primary coil

$N_2$  = Number of turns in secondary coil

$r_1$  = Radius of primary coil, meters

$L$  = Length of primary coil, meters

$x$  =Distance between coil centres, meters

Further description of the coupling effect of two coils can be defined with the coupling co-efficient ' $k$ ', which ranges between zero and one as a relationship of shared inductive coupling where a value of '1' is one hundred percent coupling.

$$k = \frac{M}{\sqrt{L_1 L_2}} \quad (\text{A.11})$$

## A.2 Circuit Design Principles for Wireless Power

### A.2.1 Circuit principles

A basic circuit to drive a primary coil comprises of an AC signal of sufficient voltage and current. The source will have resistance, the coil natural inductance, and typically a capacitor is used in series, reasons for which are described later. This forms a circuit named a RCL circuit, which is a harmonic oscillator for current and will resonate in a similar way as an LC circuit will.

When an AC signal passes through this circuit, particular characteristics of each component play a part in how the circuit reacts. Remembering that magnetic flux density is proportional to current change over time, and current is proportional to voltage over resistance, an ideal circuit will have minimal resistance. In an AC circuit, certain components cause a phase difference between voltage and current. In purely resistive circuits, both voltage and current are in phase. In purely inductive circuits,

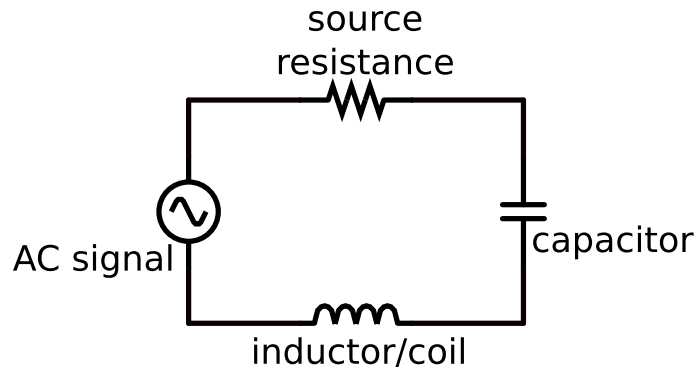


Figure A.7: RCL primary circuit.

the inductance opposes change in current, and so the voltage leads current by  $90^\circ$ . A purely capacitive circuit, the capacitance opposes change in voltage, and so the current leads the voltage by  $90^\circ$ .

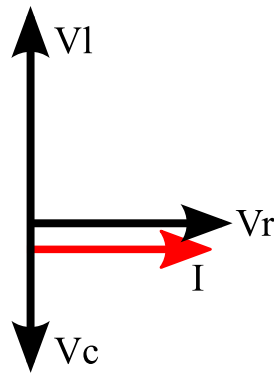


Figure A.8: Voltage phase difference between AC components.

### A.2.1.1 Impedance

In AC circuits, analogous to Ohm's law resistance in DC circuits, impedance ( $Z$ ) describes the voltage current relationship. Equation A.12 describes Ohm's law for DC circuits, whilst equation A.13 describes the impedance of an AC circuit.

$$R = \frac{V}{I} \quad (\text{A.12})$$

$$Z = \frac{V}{I} \quad (\text{A.13})$$

Impedance is affected by the phenomenon of reactance. Reactance is the resistance to voltage presented by a component in an AC circuit, and is dependant on both

component values and circuit frequency. As stated previously, voltage across a resistor in an AC circuit is in phase with current, so the reactance of a resistor is simply the resistance. Inductors and capacitors demonstrate different behaviours.

The reactance presented by a capacitor is calculated with the following equation.

$$X_c = \frac{1}{2\pi fC} \quad (\text{A.14})$$

Where;

**X<sub>c</sub>** = Capacitive reactance, ohms

**f** = frequency, hertz

**C** = Capacitance, farads

Capacitive reactance is low when either or both frequency or capacitance are high. Inductive reactance is low when either or both frequency or inductance are low. The reactance presented by an inductor is calculated with the following equation.

$$X_l = 2\pi fL \quad (\text{A.15})$$

Where;

**X<sub>l</sub>** = Inductive reactance, ohms

**f** = frequency, hertz

**L** = Inductance, henrys

As voltage through a capacitor is 180° out of phase with voltage through an inductor, their reactance opposes each other. The total circuit reactance (**X**) is the vector sum of **X<sub>l</sub>** and **X<sub>c</sub>**. Circuit impedance is the vector sum of circuit resistance and circuit reactance, see equation A.16.

$$X = X_l - X_c \quad (\text{A.16})$$

$$Z = \sqrt{R^2 + X^2} \quad (\text{A.17})$$

Where;

$\mathbf{Z}$  = Impedance, ohms

$\mathbf{R}$  = Resistance, ohms

$\mathbf{X}$  = Reactance, ohms

Fig.A.9 shows how impedance relates to the resistance and reactance of a circuit. It should be noted that if capacitive reactance is much greater than inductive reactance, or vice versa, then the impedance of the circuit increases. If the capacitive reactance and inductive reactance are roughly equal, then the reactance becomes negligible, and impedance equals the resistance only.

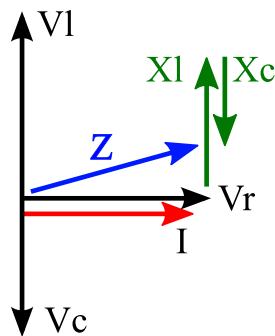


Figure A.9: Total reactance is the sum of all reactance vectors.

### A.2.1.2 Resonance

When the reactance of a circuit is equal to zero, because magnitude of vectors  $X_c$  and  $X_l$  are equal to each other, a condition called resonance is achieved. In a series RCL circuit at resonance the impedance is equal only to the resistance of the circuit, and so maximum current flow is achieved. Therefore maximum power is determined by resistance only. Given that reactance is determined by either component values, or frequency, then a circuit can be tuned by varying these factors until resonance is achieved. Fig.A.10 shows current flow of fixed L and C over a range of input signal frequencies. Different internal resistances are used to show the effect on current output. A series RCL high Q circuit has low internal resistance. Resonance occurs at peak current / power, and tuning either frequency or component values is typically used in order to achieve maximum power of a physical system. The term Q factor is the ratio

of reactance to resistance at a given frequency. A parallel RCL circuit differs from a series RCL circuit in that at resonance impedance is at maximum. This is why a series circuit is used to power a transmission coil.

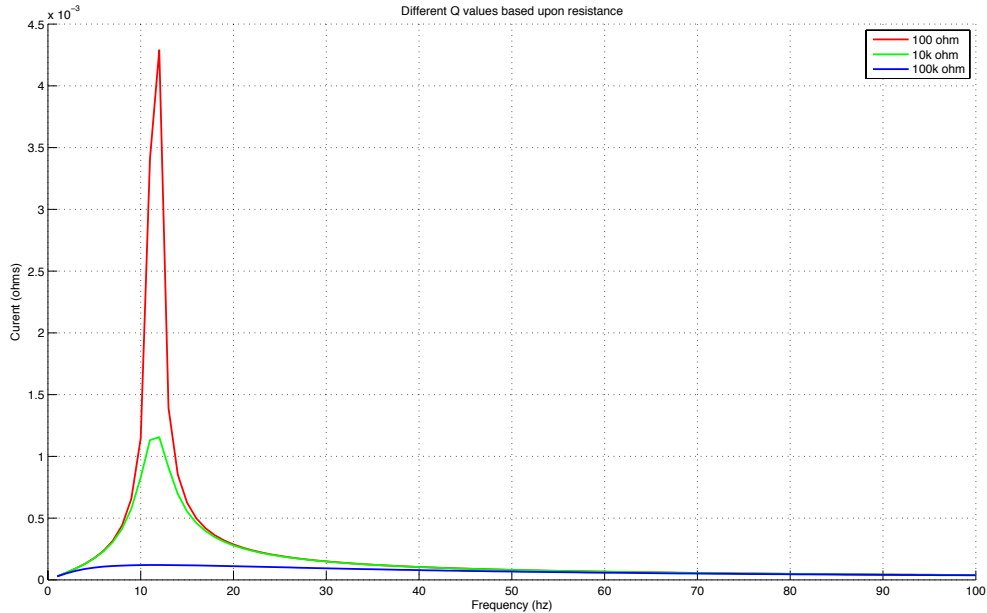


Figure A.10: The peak values symbolise the resonant frequency of a specific combination of capacitor and inductor.

### A.2.1.3 Frequency

There is a vast array of academic examples of WPT that use a range of different operating frequencies. Table.A.1 provides a small sample of references that use operating frequencies from Hz range to high MHz range. Whilst some report reasoning for their chosen frequency others do not. Considering the context of this work, additional factors need to be considered such as the effect of particular frequencies on human tissue and the effect of human tissue on the WPT.

[98] investigate the optimal frequency for wireless power transmission in to dispersive tissue. They conclude that whilst WPT in to biological tissue usually operates below 10MHz, the optimal frequency is in the GHz-range when the dimension of the transmit antenna is much smaller than a wavelength. Only when the dimension is comparable to a wavelength does the optimal frequency reduce below the GHz-range. Considering that the GHz-range is dramatically higher than the range used currently, it provides potential for much smaller receive coils. A final interesting conclusion is that at higher frequencies the effect of the receive coil orientation is desensitised because

it is no longer within the near field of the transmitter. Outside the context of human medium, Garnica et al. further suggest that higher frequencies are more efficient in [181] where they state that increasing coupling and reducing parasitic resistance are two ways to increase efficiency of a WPT system. Coupling is related to the size of the coils, and also the frequency where increased frequency presents increased coupling.

Most evidence suggests that a higher frequency is more efficient, however a tradeoff will always be made between theoretical and practical realities of what can be built. The cost and availability of high frequency source signals, and the ability to build high frequency amplifiers is a factor in what should be chosen. Selection of appropriate components that have fast enough rise and fall times along and effective circuit design will aid in higher frequency amplification. In the reality of what is achievable, and with focus on the project objectives, the most rational approach to choosing operating frequency is to keep in mind the capabilities of equipment available and developed within those boundaries. Keeping development frequencies between 4MHz and 12MHz is suggested.

Table A.1: Comparison of frequency used in wireless power system examples.

Source	Frequency	Justification
Mohamadi et al. [182]	50Hz	Ease of build
Low et al. [183]	134KHz	Ease of build
Xin et al. [97]	400KHz	Ease of build
Shiba et al. [101]	300-600KHz	Ease of build
Bhuyan et al. [85]	720KHz	For the frequency range 100 KHz - 4MHz, no biological effects have been reported, [184]
Lenaerts et al. [89]	1MHz	Ease of build
Sample et al. [185]	7.6MHz	None given
Cannon et al. [186]	8.3MHz	None given
Kurs et al. [187]	9.9MHz	None given
Bhattacharya et al. [188]	10MHz	None give
Hirayama et al. [189]	13.2MHz	None given
Chen et al. [190]	15.56MHz	High frequency for increased coupling
Pannier et al. [191]	27MHz	None given

## A.2.2 Component Calculations

### A.2.2.1 Basic circuit design

A theoretical air cored transformer circuit will be considered in order to explore the concept of wireless power transfer. Fig.A.11 presents a basic air cored transformer circuit diagram. The primary transmitting coil  $L_p$  is use in series with primary capacitor  $C_p$  to achieve resonance. The total resistance of the circuit is summarised as  $R_p$ , however an accurate equivalent circuit and calculation with be explored later. The secondary circuit is show with induction coil and in series capacitor to achieve resonance at the same frequency as the primary circuit.

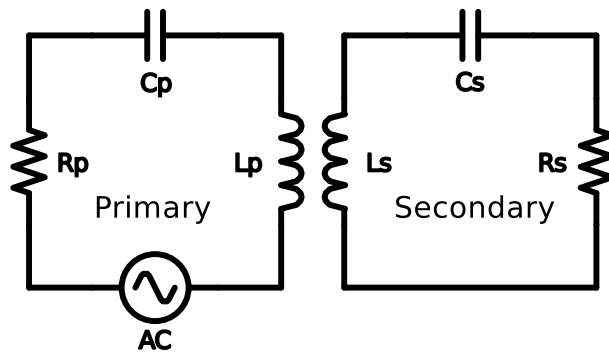


Figure A.11: Simple air cored transformer circuit.

### A.2.2.2 Resistance of a coil

Using equations described earlier, circuit conditions can be calculated. Consider using two equal wound coils of 10 turns, coil diameter 100mm, and core diameter of 1mm wound at a pitch of 2mm, the remaining components will be calculated such that resonance can be achieved at around 4.5 MHz, and secondary coil induced emf at defined distances can be determined.

First the resistance of the coil can be calculated using the following equation;

$$R = Rho * L/A \quad (A.18)$$

Where;

**R** = Resistance, ohms

**Rho** = Resistance constant for given material, Copper is  $1.68 * 10^{-8}$  ohm-centimeters

$\mathbf{L}$  = Length of wire, meters

$\mathbf{A}$  = Cross sectional area of core,  $\text{m}^2$

Therefore the coil resistance can be calculated;

$$R = 1.68 * 10^{-8} * \frac{10 * \pi * 0.1}{\pi * 0.005^2} = 67\text{m}\Omega \quad (\text{A.19})$$

### A.2.2.3 Inductance of a coil

The calculations for inductance are typically started from the analysis of a perfect current sheet inductor, [192]. This inductor is assumed to have an infinitely thin conducting material wound one layer with no space between windings. At low frequencies this inductor creates a uniform magnetic field along its length. For a perfect construction of a current sheet inductor, the follow equation calculates the inductance value.

$$L_s = \frac{\mu_o \pi D^2 N^2}{4l} \quad (\text{A.20})$$

Where;

$\mathbf{L}_s$  = Inductance, henrys

$\mu_o$  = Permeability of free space

$\mathbf{D}$  = Diameter of coil, meters

$\mathbf{N}$  = Number of turns

$\mathbf{l}$  = Length of coil

This is a theoretical model that neglects the influence of additional characteristics. H.Nagoaka presented the coefficient  $K_L$  [193] that deals with non-uniformity of field distribution caused by the relationship of coil radius  $r$  and coil length  $l$ .

$$K_L = \frac{2l}{\pi D} \left( \frac{(\ln(\frac{4D}{l}) - \frac{1}{2})(1 + 0.383901(\frac{l}{D})^2 + 0.017108(\frac{l}{D})^4)}{1 + 0.258952(\frac{l}{D})^2 + 0.093842(\frac{l}{D})^2 + 0.002029(\frac{l}{D})^4 - 0.000801(\frac{l}{D})^6} \right) \quad (\text{A.21})$$

Where;

$K_L$  = Nagoaka coefficient

$l$  = length of coil, meters

$D$  = Diameter of coil, meters

Considering  $K_L$ , equation A.20 can now be modified so that  $L_s$  can be calculated with the following equation.

$$L_s = \frac{\mu_o \pi D^2 N^2}{4l} K_L \quad (\text{A.22})$$

Two further coefficients,  $K_s$  and  $K_m$ , account for the physical pitch of the coil windings and coil radius, and mutual inductance between adjacent windings respectively.

$$K_s = \frac{3}{2} - \ln\left(\frac{p}{r}\right) \quad (\text{A.23})$$

$$K_m = \ln(2\pi) - \frac{3}{2} - \frac{\ln(N)}{6N} - \frac{0.33084236}{N} - \frac{1}{120N^3} + \frac{1}{504N^5} - \frac{0.0011923}{N^7} + \frac{0.0005068}{N^9} \quad (\text{A.24})$$

E.B.Rosa [194] modified equation A.22 to account for  $K_s$  and  $K_m$  as follows;

$$L = L_s - \frac{\mu_o N D}{2} (K_s + K_m) \quad (\text{A.25})$$

For the proposed coil design the discussed values are as follow;

$$K_L = 0.3182$$

$$L_s = 15.701 * 10^{-6}$$

$$K_s = 4.8283$$

$$K_m = 0.2664$$

$$L = 12.500 * 10^{-6} \mu H$$

#### A.2.2.4 Calculating the tuning capacitance

With known inductance, and known frequency the necessary capacitance can be calculated. At resonant frequency in a serial RCL circuit, reactance is equal to zero, i.e.  $X_L - X_C = 0$ , or in further detail,

$$2\pi f L = \frac{1}{2\pi f C} \quad (\text{A.26})$$

This can be rearranged to provide the value of  $C$  at resonance, in this case  $100.07pF$ .

$$C = \frac{1}{4\pi^2 f^2 L} \quad (\text{A.27})$$

#### A.2.2.5 Reflected Load

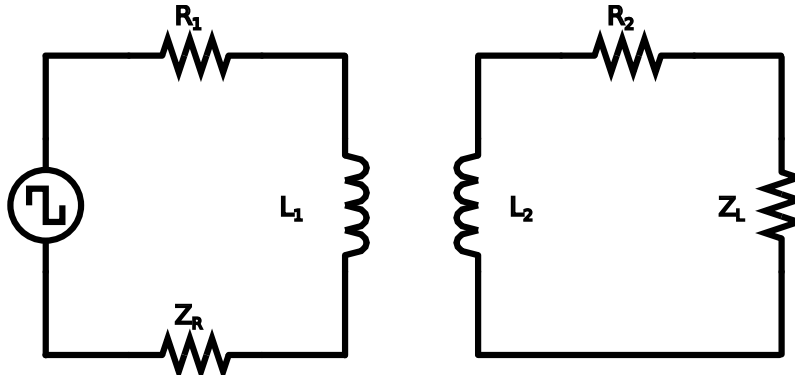


Figure A.12: Reflected Load.

In order to estimate how much current will be drawn by the WPT circuit the perceived or reflected load seen by the power source must be calculated. This reflected load is an impedance that represents the total impedance of the secondary circuit whilst accounting for the affect of coupling between the two coils. Fig.A.12 shows the account-able impedances in a basic air core transformer.  $R_1$  and  $R_2$  are the natural resistances, and impedance if not at resonance, of the series tuned inductor and capacitor.  $Z_L$  is the load resistance of the device that the system is trying to power and  $Z_R$  is the reflected load based upon the coupling between the two inductors. Equation A.28 explains how the secondary circuit presents itself to the power source as an impedance.

$$Z_R = \frac{\omega^2 M^2}{R_2 + j\omega L_2 + Z_L} \quad (\text{A.28})$$

#### A.2.2.6 Equivalent T Circuit Linear Transformer

If a wireless power transfer system is considered as a linear transformer, an equivalent T circuit would look as shown in Fig.A.13 where the component values are derived as follows;

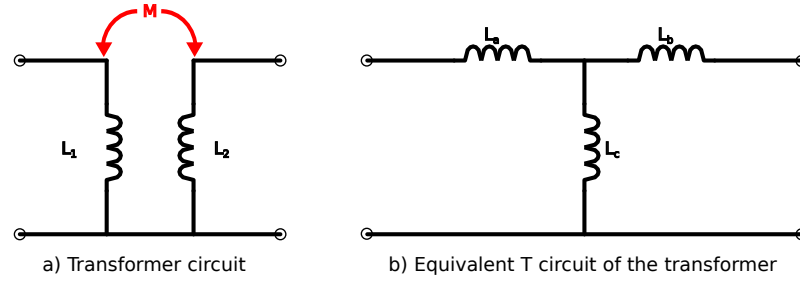


Figure A.13: Reflected Load.

$$L_a = L_1 - M, \quad L_b = L_2 - M, \quad L_c = M \quad (\text{A.29})$$

### A.3 Estimating The Effect of Solenoid Parameters on Efficiency

#### A.3.1 Estimating The Effect of Distance on emf

The following study models the effect of distance on the emf induced in the secondary circuits. Using equations A.3, A.4 and A.5 the emf can be determined over varying distances of coil separation. The following example uses a theoretical 4.5MHz supply signal of  $V_{S_{p-p}} = 3.33$  volts and  $(I_{p-p}) = 166.7\text{mA}$  to drive the primary circuit with 0.1 m dia., 0.02 m long and 10 turn inductor. Fig.A.14 presents estimated emf over varying distances. The steep drop off early on aligns with the effect of distance on coupling coefficient 'k' in Fig.6.1. Table.A.2 presents more specific details of induced emf and various distances.

Table A.2: This table shows the induced emf in the secondary coil at different stages of coil separation.

Coil separation (m)	0.00	0.01	0.02	0.03	0.04	0.05	0.06
$\xi$ (v)	1.48	1.39	1.18	0.93	0.70	0.52	0.38
Coil separation (m)	0.07	0.08	0.09	0.10	0.11	0.12	0.13
$\xi$ (v)	0.29	0.22	0.17	0.13	0.10	0.08	0.06
Coil separation (m)	0.14	0.15	0.16	0.17	0.18	0.19	0.20
$\xi$ (v)	0.05	0.04	0.04	0.03	0.03	0.02	0.02

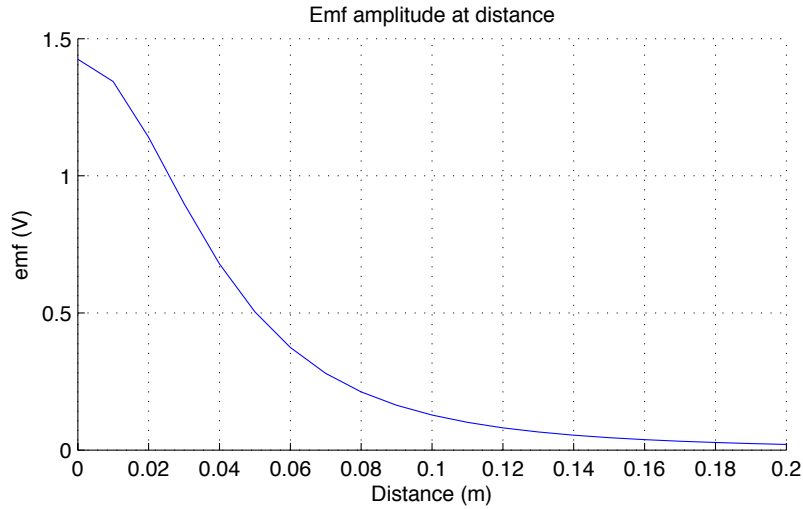


Figure A.14: Estimated emf output over a range of distances.

### A.3.2 Estimating Maximum Achievable Efficiency

The following section explores the effect of the coupling coefficient 'k' and quality factor 'Q' on the maximum achievable efficiency  $\eta$ .  $\eta$  is dependant on the figure of merit 'U', see equations A.30. 'U' is dependant on both the coefficient of coupling 'k' between the two coils, see equation A.11, and the quality factor 'Q' of each coil, see equation A.31.

$$U = K\sqrt{Q_1Q_2} \quad (\text{A.30})$$

$U$  = Figure of merit

$K$  = Coupling coefficient, equation A.11

$Q_1$  = Quality factor of the primary coil, equation A.31

$Q_2$  = Quality factor of the secondary coil, equation A.31

The coupling co-efficient 'k' can be inferred from the mutual inductance which has been shown to change over distance in section A.1.5 and equation A.11. The quality factor 'Q' of a resonant circuit is a factor of the operating frequency. This can be seen in equation A.31 where Q is dependant on the circuit load 'R'. The circuit load of a resonant circuit is dependant on its impedance and frequency such that at resonance the impedance is minimum.

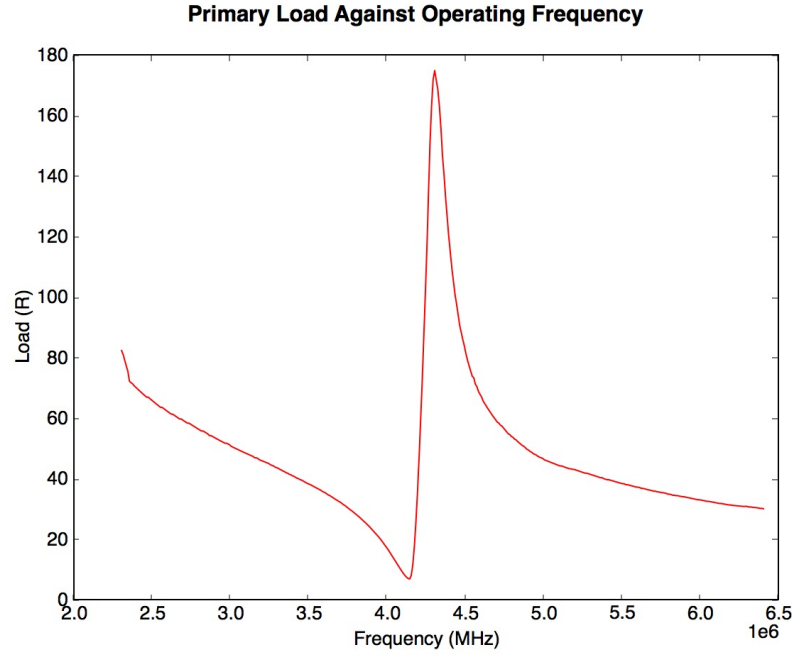


Figure A.15: Primary resonant circuit load over frequency range.

Fig.A.15 shows the resultant load of an isolated primary circuit ( $R = 6.56\Omega$ ,  $C = 104pF$ ,  $L = 13.3\mu H$ , 10 turn, 0.1 m dia. and 0.02 m length inductor) subjected to a sweeping input frequency from 2.4 to 6.4 MHz. Note that the optimal frequency is 4.14 MHz, where the load is  $6.56\Omega$ . The resonant frequency should be  $4.279MHz$ ; however, a difference of  $-0.14MHz$  indicates a stray inductance in the circuit of  $910nH$  and total inductance should now be considered to be  $14.2\mu H$ . This again highlights challenges in using real components and measurement equipment.

$$Q = \frac{1}{R} \sqrt{\frac{L}{C}} \quad (\text{A.31})$$

$Q$  = Quality factor

$R$  = Resistive load of resonant circuit

$L$  = Inductance of resonant circuit

$C$  = Capacitance of resonant circuit

At resonance of 4.14 MHz,  $Q$  for the secondary circuit where  $L = 13.3\mu H$ ,  $C = 104pF$  and  $R = 100\Omega$  is 3.576 whilst the  $Q$  for the primary where  $L = 14.2\mu H$ ,  $C = 104pF$ ,  $R = 6.56\Omega$  is 56.35. Further to describing the system capabilities as a

figure of merit, optimal efficiency  $\eta$  can be calculated using the following equation, and ranges from 0.0 to 1.0;

$$\eta_{opt} = \frac{U^2}{(1 + \sqrt{1 + U^2})^2} \quad (\text{A.32})$$

$\eta_{opt}$  = Maximum achievable efficiency

$U$  = Figure of merit, equation A.30

#### A.4 Class E Amplifier Design Equations

$$\text{Load resistance, } R = \frac{8}{\pi^2 + 4} * \frac{V_1^2}{P_{Omax}} \quad (\text{A.33})$$

$$\text{DC resistance, } R_{dc} = \frac{\pi^2 + 4}{8} * R \quad (\text{A.34})$$

$$\text{Amplitude of output voltage, } V_{rm} = \frac{4}{\sqrt{\pi^2 + 4}} * V_1 \quad (\text{A.35})$$

$$\text{Max voltage across switch capacitor, } V_{C1m} = 3.562 * V_1 \quad (\text{A.36})$$

$$\text{Max voltage across shunt capacitor, } V_{Sm} = V_{C1m} \quad (\text{A.37})$$

$$\text{DC input current, } I_1 = \frac{8}{\pi^2 + 4} * \frac{V_1}{R} \quad (\text{A.38})$$

$$\text{Max switch current, } I_{Sm} = \left( \frac{\sqrt{\pi^2 + 4}}{2} + 1 \right) * I_1 \quad (\text{A.39})$$

$$\text{Current amplitude through resonant circuit, } I_m = \frac{\sqrt{\pi^2 + 4}}{2} * I_1 \quad (\text{A.40})$$

Assuming a good quality factor for the amplifier to be  $QL = 7$ ;

$$\text{Inductor, } L = \frac{QL * R}{\omega} \quad (\text{A.41})$$

$$\text{Capacitor, } C_1 = \frac{8}{(\pi * (\pi^2 + 4) * \omega * R)} \quad (\text{A.42})$$

$$C_{1ext} = C_1 - C_0 \quad (\text{A.43})$$

$$\text{Capacitor, } C = \frac{1}{\omega * R * [QL - \frac{\pi * (\pi^2 - 4)}{16}]} \quad (\text{A.44})$$

$$\text{Peak voltage across resonant capacitor, } V_{Cm} = \text{frac} I_m \omega * C \quad (\text{A.45})$$

$$\text{Peak voltage across resonant inductor, } V_{Lm} = \omega * L * I_m \quad (\text{A.46})$$

$$\text{Choke inductance must be more than, } L_f = 2 * (\frac{\pi^2}{4} + 1) * \frac{R}{f} \quad (\text{A.47})$$

$$\text{Peak voltage across the RF choke is, } V_{LFm} = V_{Sm} - V_1 \quad (\text{A.48})$$

power loss in  $r_{Lf}$ ,

$$P_{rLf} = r_{Lf} * I_1^2 \quad (\text{A.49})$$

$$\text{RMS of switch current, } I_{Srms} = \frac{I_1 * \sqrt{\pi^2 + 28}}{4} \quad (\text{A.50})$$

$$\text{Transistor conduction power loss, } P_{rds} = r_{ds} * I_{Srms}^2 \quad (\text{A.51})$$

$$\text{rms current, } I_{C_1rms} = \frac{I_1 * \sqrt{\pi^2 - 4}}{4} \quad (\text{A.52})$$

$$\text{Conduction power loss in } r_{C_1}, P_{rC_1} = r_{C_1} * I_{C_1rms}^2 \quad (\text{A.53})$$

$$\text{Power loss in resonant rL, } P_{rL} = \frac{r_L * I_m^2}{2} \quad (\text{A.54})$$

$$\text{Power loss in resonant rC, } P_{rC} = \frac{r_C * I_m^2}{2} \quad (\text{A.55})$$

Drain current fall time frequency,

$$\omega t f = 2 * \pi * 1.2 * 10^6 * 20 * 10^{-9} \quad (\text{A.56})$$

$$P_{tf} = \frac{(\omega t f)^2 * P_{Omax}}{12} \quad (\text{A.57})$$

$$\text{Power loss (exluding the gate-drive power), } P_{Ls} = P_{rLf} + P_{rds} + P_{rC1} + P_{rL} + P_{rC} + P_{tf} \quad (\text{A.58})$$

$$\text{The effeciency of the amplifier, } \eta = \frac{P_{Omax}}{P_{Omax} + P_{Ls}} \quad (\text{A.59})$$

$$\text{Gate driver power, } P_g = f * V_{gsm} * Q_g \quad (\text{A.60})$$

$$\text{Power added effeciency, } \eta_{PAE} = \frac{P_{Omax} - P_g}{P_{Omax} + P_{Ls}} \quad (\text{A.61})$$

$$\text{Power gain, } K_p = \frac{P_{Omax}}{P_g} \quad (\text{A.62})$$

$$\text{Equivalent capacitance when switch of off, } C_{eq} = \frac{C * C_1}{C + C_1} \quad (\text{A.63})$$

$$\text{Resonant frequency, } f_{01} = \frac{1}{2 * \pi * \sqrt{L * C}} \quad (\text{A.64})$$

$$\text{Resonant frequency, } f_{02} = \frac{1}{2 * \pi * \sqrt{L * C_{eq}}} \quad (\text{A.65})$$

## A.5 Class E Amplifier Ver 2.0 Schematic Design

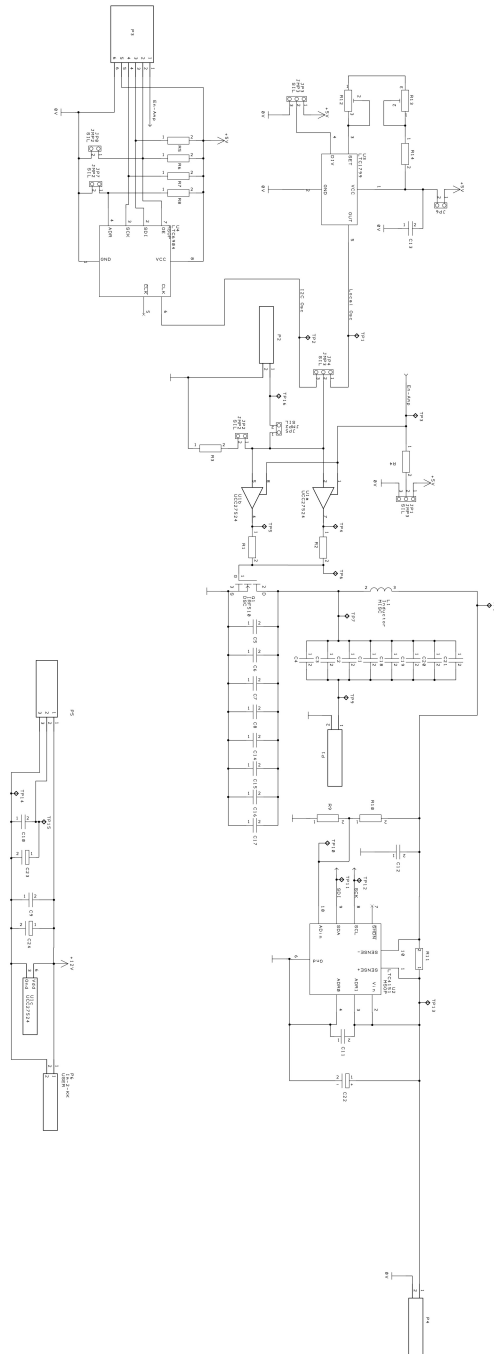


Figure A.16: Class E power amplifier schematic version 2.

---

## Bibliography

---

- [1] B. Winstone, T. Pipe, C. Melhuish, M. Callaway, A. C. Etoundi, and S. Dogramadzi, "Single motor actuated peristaltic wave generator for a soft bodied worm robot," *Proceedings of the IEEE RAS and EMBS International Conference on Biomedical Robotics and Biomechatronics*, vol. 2016-July, pp. 449–456, 2016.
- [2] C. Roke, C. Melhuish, T. Pipe, D. Drury, and C. Chorley, "Deformation-Based Tactile Feedback Using a Biologically-Inspired Sensor and a Modified Display," *Technology*, pp. 114–124, 2011.
- [3] T. Assaf, C. Roke, J. Rossiter, T. Pipe, and C. Melhuish, "Seeing by touch: evaluation of a soft biologically-inspired artificial fingertip in real-time active touch.," *Sensors (Basel, Switzerland)*, vol. 14, pp. 2561–77, jan 2014.
- [4] B. Winstone, G. Griffiths, T. Pipe, and J. Rossiter, "TACTIP - Tactile Fingertip Device , Texture Analysis Through Optical Tracking of Skin Features," *Biomimetic and Biohybrid Systems: Third International Conference, Living Machines*, pp. 323–334, 2013.
- [5] H. Hoang and F. Bien, "Maximizing efficiency of electromagnetic resonance wireless power transmission systems with adaptive circuits," *Wireless Power Transfer Principles and Engineering Explorations*, 2012.
- [6] N. Nakaniwa, A. Namihisa, T. Ogihara, A. Ohkawa, S. Abe, A. Nagahara, O. Kobayashi, J. Sasaki, and N. Sato, "Newly developed autofluorescence imaging

- videoscope system for the detection of colonic neoplasms,” *Digestive Endoscopy*, vol. 17, no. 3, pp. 235–240, 2005.
- [7] R. S. MACKAY and B. JACOBSON, “Endoradiosonde,” *Nature*, vol. 179, pp. 1239–1240, jun 1957.
- [8] R. Shrestha, S. K. Mohammed, M. M. Hasan, X. Zhang, and K. A. Wahid, “Automated Adaptive Brightness in Wireless Capsule Endoscopy Using Image Segmentation and Sigmoid Function,” *IEEE Transactions on Biomedical Circuits and Systems*, vol. 10, no. 4, pp. 884–892, 2016.
- [9] “PillCam, [www.givenimaging.com](http://www.givenimaging.com),” 2013.
- [10] “Olympus - EndoCapsule System EC-1 — Medical Systems.”
- [11] D. R. Cave, D. E. Fleischer, J. a. Leighton, D. O. Faigel, R. I. Heigh, V. K. Sharma, C. J. Gostout, E. Rajan, K. Mergener, A. Foley, M. Lee, and K. Bhattacharya, “A multicenter randomized comparison of the Endocapsule and the Pillcam SB,” *Gastrointestinal endoscopy*, vol. 68, pp. 487–94, sep 2008.
- [12] C. Spada, M. E. Riccioni, L. Petruzzello, M. Marchese, R. Urgesi, and G. Costamagna, “The new PillCam Colon capsule: difficult colonoscopy? No longer a problem?,” *Gastrointestinal endoscopy*, vol. 68, pp. 807–8, oct 2008.
- [13] K. Triantafyllou, P. Tsibouris, C. Kalantzis, K. Papaxoinis, T. Kalli, N. Kalantzis, and S. D. Ladas, “PillCam Colon capsule endoscopy does not always complement incomplete colonoscopy,” *Gastrointestinal endoscopy*, vol. 69, pp. 572–6, mar 2009.
- [14] A. Menciassi, M. Quirini, and P. Dario, “Microrobotics for future gastrointestinal endoscopy,” *Minimally invasive therapy & allied technologies : MITAT : official journal of the Society for Minimally Invasive Therapy*, vol. 16, pp. 91–100, jan 2007.
- [15] M. De Bona, a. Bellumat, E. Cian, F. Valiante, a. Moschini, and M. De Boni, “Capsule endoscopy findings in patients with suspected Crohn’s disease and biochemical markers of inflammation,” *Digestive and liver disease : official journal of the Italian Society of Gastroenterology and the Italian Association for the Study of the Liver*, vol. 38, pp. 331–5, may 2006.

- [16] A. K. H. Chong, A. Taylor, A. Miller, O. Hennessy, W. Connell, and P. Desmond, “Capsule endoscopy vs. push enteroscopy and enteroclysis in suspected small-bowel Crohn’s disease,” *Gastrointestinal Endoscopy*, vol. 61, pp. 255–261, feb 2005.
- [17] C. Excellence, “Wireless capsule endoscopy for investigation of the small bowel Interventional Procedure Guidance 101,” Tech. Rep. December, National Institute for Clinical Excellence, 2004.
- [18] Q. Shi, J. Wang, D. Chen, J. Chen, J. Li, and K. Bao, “In Vitro and In Vivo characterization of wireless and passive micro system enabling gastrointestinal pressure monitoring.,” *Biomedical Microdevices*, vol. 16, pp. 859–68, aug 2014.
- [19] N. H. Cox and J. R. Soc, “Palpation of the skin, an important issue,” *Journal of the Royal Society of Medicine*, vol. 99, pp. 598–601, jan 2006.
- [20] K. Kume, T. Kuroki, T. Sugihara, and M. Shinngai, “Development of a novel endoscopic manipulation system: The Endoscopic operation robot.,” *World journal of gastrointestinal endoscopy*, vol. 3, pp. 145–50, jul 2011.
- [21] A. Chaudhary, D. Atal, and S. Kumar, “Robotic Surgical SystemsA Review,” *International Journal of Applied . . .*, vol. 9, no. 11, pp. 1289–1294, 2014.
- [22] T. Honda, K. Arai, and K. Ishiyama, “Micro swimming mechanisms propelled by external magnetic fields,” *Magnetics, IEEE Transactions on*, vol. 12, no. 5, pp. 5085–5087, 1996.
- [23] M. Sendoh, K. Ishiyama, and K.-I. Arai, “Fabrication of magnetic actuator for use in a capsule endoscope,” *IEEE Transactions on Magnetics*, vol. 39, pp. 3232–3234, sep 2003.
- [24] D. Bell and S. Leutenegger, “Flagella-like propulsion for microrobots using a nanocoil and a rotating electromagnetic field,” in *IEEE International Conference on Robotics and Automation*, pp. 1128–1133, 2007.
- [25] K. B. Yesin, K. Vollmers, and B. J. Nelson, “Modeling and Control of Untethered Biomicrobots in a Fluidic Environment Using Electromagnetic Fields,” *The International Journal of Robotics Research*, 2006.

- 
- [26] J.-B. Mathieu, G. Beaudoin, and S. Martel, “Method of propulsion of a ferromagnetic core in the cardiovascular system through magnetic gradients generated by an MRI system.,” *IEEE transactions on bio-medical engineering*, vol. 53, pp. 292–9, feb 2006.
- [27] Z. Yi, W. Qimin, and Z. Peiqing, “Dynamic Analysis and Experiment of a 3mm Swimming Mirrorobot,” in *International Conference of Intelligent Robots & Systems*, pp. 1746–1750, 2004.
- [28] R. Dreyfus, J. Baudry, M. L. Roper, M. Fermigier, H. a. Stone, and J. Bibette, “Microscopic artificial swimmers.,” *Nature*, vol. 437, pp. 862–5, oct 2005.
- [29] S. Guo, Q. Pan, and M. B. Khamesee, “Development of a novel type of microrobot for biomedical application,” *Microsystem Technologies*, vol. 14, pp. 307–314, sep 2007.
- [30] K. Abdelnour, A. Stinchcombe, M. Porfiri, J. Zhang, and S. Childress, “Wireless Powering of Ionic Polymer Metal Composites Toward Hovering Microswimmers,” *IEEE/ASME Transactions on Mechatronics*, vol. 17, pp. 924–935, oct 2012.
- [31] M. Quirini, S. Member, A. Menciassi, S. Scapellato, C. Stefanini, and P. Dario, “Design and Fabrication of a Motor Legged Capsule for the Active Exploration of the,” *IEEE/ASME TRANSACTIONS ON MECHATRONICS*, vol. 13, no. 2, pp. 169–179, 2008.
- [32] M. Quirini and S. Scapellato, “An approach to capsular endoscopy with active motion,” *IEEE EMBS*, vol. 29, pp. 2827–30, jan 2007.
- [33] H. Park, S. Park, E. Yoon, and B. Kim, “Paddling based microrobot for capsule endoscopes,” *... and Automation, 2007 ...*, no. April, pp. 10–14, 2007.
- [34] S. Yang, K. Park, J. Kim, T. S. Kim, I. J. Cho, and E. S. Yoon, “Autonomous locomotion of capsule endoscope in gastrointestinal tract,” *Proceedings of the Annual International Conference of the IEEE Engineering in Medicine and Biology Society, EMBS*, pp. 6659–6663, 2011.
- [35] P. Valdastri, R. J. Webster, C. Quaglia, M. Quirini, S. Member, A. Menciassi, and P. Dario, “A new mechanism for mesoscale legged locomotion in compliant tubular environments,” *Robotics, IEEE ...*, vol. 25, no. 5, pp. 1047–1057, 2009.
-

- [36] R. Carta, B. Lenaerts, J. Thoné, G. Tortora, P. Valdastri, A. Menciassi, R. Puers, and P. Dario, “Wireless Power Supply as Enabling Technology Towards Active Locomotion in Capsular Endoscopy,” in *Euroensors*, pp. 1369–1372[1] R. Carta, B. Lenaerts, J. Thoné, G. T, 2008.
- [37] P. Gao, G. Yan, and Z. Wang, “A robotic endoscope based on minimally invasive locomotion and wireless techniques for human colon,” ... of *Medical Robotics* ..., no. January, pp. 256–267, 2011.
- [38] W. Chen, G. Yan, and Z. Wang, “A wireless capsule robot with spiral legs for human intestine,” *Int J Med Robotics Comput Assist Surg*, no. May, 2013.
- [39] J. Gao, G. Yan, Z. Wang, F. Xu, W. Wang, P. Jiang, and D. Liu, “Locomotion enhancement of an inchworm-like capsule robot using long contact devices,” *The international journal of medical robotics + computer assisted surgery : MRCAS*, no. July, 2016.
- [40] J. Norton, A. Hood, A. Neville, D. Jayne, P. Culmer, A. Alazmani, and J. Boyle, “RollerBall: A mobile robot for intraluminal locomotion,” *Proceedings of the IEEE RAS and EMBS International Conference on Biomedical Robotics and Biomechanics*, vol. 2016-July, pp. 254–259, 2016.
- [41] R. Carta, J. Thoné, and R. Puers, “A 3D Ferrite Coil Receiver for Wireless Power Supply of Endoscopic Capsules,” *Procedia Chemistry*, vol. 1, pp. 477–480, sep 2009.
- [42] R. Carta, J. Thoné, and R. Puers, “A wireless power supply system for robotic capsular endoscopes,” *Sensors & Actuators*, vol. 162, pp. 177–183, aug 2010.
- [43] B. a. Trimmer, A. E. Takesian, B. M. Sweet, C. B. Rogers, D. C. Hake, and D. J. Rogers, “Caterpillar locomotion : A new model for soft- bodied climbing and burrowing robots,” *7th International Symposium on Technology and the Mine Problem, Monterey, CA May 2-5, 2006*, pp. 1–10, 2006.
- [44] S. G. Roh, S. M. Ryew, J. H. Yang, and H. R. Choi, “Actively Steerable Inpipe Inspection Robots for Underground Urban Gas Pipelines,” in *ICRA*, pp. 761–766, 2001.

- [45] O. Ttar, D. Mândru, and I. Ardelean, “Development of mobile minirobots for in pipe inspection tasks,” *Mechanika*, vol. 68, no. 6, pp. 60–64, 2007.
- [46] H. M. Kim, J. S. Suh, Y. S. Choi, T. D. Trong, H. Moon, J. Koo, S. Ryew, and H. R. Choi, “An In - pipe Robot with Multi - axial Differential Gear Mechanism,” pp. 252–257, 2013.
- [47] W. Neubauer, “A spider-like robot that climbs vertically in ducts or pipes,” *Proceedings of IEEE/RSJ International Conference on Intelligent Robots and Systems (IROS’94)*, vol. 2, pp. 1178–1185, 1994.
- [48] T. Roßmann and F. Pfeiffer, “Control of an eight legged pipe crawling robot,” *Experimental Robotics V*, vol. 232, pp. 335–346, 1998.
- [49] A. Zagler and F. Pfeiffer, “MORITZ a pipe crawler for tube junctions,” *2003 IEEE International Conference on Robotics and Automation (Cat. No.03CH37422)*, vol. 3, pp. 2954–2959, 2003.
- [50] Menciassi, Arianna and P. Dario, “Bio-inspired solutions for locomotion in the gastrointestinal tract: background and perspectives,” *Philosophical transactions of the Royal Society of London. Series A, Mathematical Physical and Engineering Sciences*, no. October 15; 361, 2003.
- [51] D. Zarrouk, I. Sharf, and M. Shoham, “Conditions for worm-robot locomotion in a flexible environment: theory and experiments,” *IEEE transactions on biomedical engineering*, vol. 59, pp. 1057–67, apr 2012.
- [52] E. Aguayo and E. Boemo, “Locomotion of a Modular Worm-like Robot using a FPGA-based embedded MicroBlaze Soft-processor,” *Proceedings of the 7th International Conference on Climbing and Walking Robots (CLAWAR)*, pp. 869–878, 2001.
- [53] A. Yamashita, K. Matsui, R. Kawanishi, T. Kaneko, T. Murakami, H. Omori, T. Nakamura, and H. Asama, “Self-localization and 3-D model construction of pipe by earthworm robot equipped with omni-directional rangefinder,” *2011 IEEE International Conference on Robotics and Biomimetics, ROBIO 2011*, pp. 1017–1023, 2011.

- [54] H. Omori and T. Nakamura, “Development of mobile robots based on peristaltic crawling of an earthworm,” *Robotics 2010: Current . . .*, 2010.
- [55] S. Seok, C. D. Onal, K.-J. Cho, R. J. Wood, D. Rus, and S. Kim, “Meshworm: A Peristaltic Soft Robot With Antagonistic Nickel Titanium Coil Actuators,” *IEEE/ASME Transactions on Mechatronics*, vol. 18, pp. 1485–1497, oct 2013.
- [56] A. Boxerbaum and A. Horschler, “Worms, waves and robots,” in *IEEE ICRA*, pp. 3537–3538, 2012.
- [57] A. S. Boxerbaum, K. M. Shaw, H. J. Chiel, and R. D. Quinn, “Continuous wave peristaltic motion in a robot,” *The International Journal of Robotics Research*, vol. 31, pp. 302–318, jan 2012.
- [58] K. a. Daltorio, A. S. Boxerbaum, A. D. Horschler, K. M. Shaw, H. J. Chiel, and R. D. Quinn, “Efficient worm-like locomotion: slip and control of soft-bodied peristaltic robots,” *Bioinspiration & biomimetics*, vol. 8, no. 3, p. 035003, 2013.
- [59] K.-J. Cho, J.-S. Koh, S. Kim, W.-S. Chu, Y. Hong, and S.-H. Ahn, “Review of manufacturing processes for soft biomimetic robots,” *International Journal of Precision Engineering and Manufacturing*, vol. 10, pp. 171–181, oct 2009.
- [60] J. G. Cham, S. A. Bailey, J. E. Clark, R. J. Full, and M. R. Cutkosky, “Fast and Robust: Hexapedal Robots via Shape Deposition Manufacturing,” *The International Journal of Robotics Research*, vol. 21, no. 10, pp. 869–882, 2002.
- [61] S. Kim and M. Spenko, “Whole body adhesion: hierarchical, directional and distributed control of adhesive forces for a climbing robot,” *Robotics and . . .*, no. April, pp. 10–14, 2007.
- [62] Y.-s. Kwon and B.-j. Yi, “Design and Motion Planning of a Two-Module,” *IEEE Transactions on Robotics*, vol. 28, no. 3, pp. 681–696, 2012.
- [63] P. Debenest, M. Guarnieri, and S. Hirose, “PipeTron series - Robots for pipe inspection,” *Proceedings of the 2014 3rd International Conference on Applied Robotics for the Power Industry*, pp. 1–6, 2014.
- [64] A. Bekhit, A. Dehghani, and R. Richardson, “Kinematic Analysis and Locomotion Strategy of a Pipe Inspection Robot Concept for Operation in Active

- 
- Pipelines,” *International Journal of Mechanical Engineering and Mechatronics*, vol. 1, no. 1, 2012.
- [65] L. Phee, a. Menciassi, S. Gorini, G. Pernorio, a. Arena, and P. Dario, “An innovative locomotion principle for minirobots moving in the gastrointestinal tract,” *Proceedings 2002 IEEE International Conference on Robotics and Automation (Cat. No.02CH37292)*, vol. 2, no. May, pp. 1125–1130, 2002.
- [66] J. Steigenberger and C. Behn, “Gait generation considering dynamics for artificial segmented worms,” *Robotics and Autonomous Systems*, vol. 59, pp. 555–562, jul 2011.
- [67] K. Wang, G. Yan, P. Jiang, and D. Ye, “A wireless robotic endoscope for gastrointestinal,” *IEEE Transactions on Robotics*, vol. 24, pp. 206–210, feb 2008.
- [68] T. Kubota and K. Nagaoka, “Earth-worm typed drilling robot for subsurface planetary exploration,” in *Robotics and . . .*, pp. 1394–1399, 2007.
- [69] M. P. Nemitz, P. Mihaylov, T. W. Barraclough, D. Ross, and A. A. Stokes, “Using Voice Coils to Actuate Modular Soft Robots: Wormbot, an Example,” *Soft Robotics*, vol. 3, no. 4, p. soro.2016.0009, 2016.
- [70] B. Gramescu, C. Nitu, and N. Alexandrescu, “Modeling of a Mobile Robot with Worm-like Movement,” in *EUROCON 2005 - The International Conference on "Computer as a Tool"*, pp. 1204–1207, IEEE, 2005.
- [71] H. Omori, T. Murakami, H. Nagai, T. Nakamura, and T. Kubota, “Planetary subsurface explorer robot with propulsion units for peristaltic crawling,” *Proceedings - IEEE International Conference on Robotics and Automation*, pp. 649–654, 2011.
- [72] J. Zuo, G. Yan, and Z. Gao, “A micro creeping robot for colonoscopy based on the earthworm,” *Journal of medical engineering & technology*, vol. 29, no. 1, pp. 1–7, 2005.
- [73] G. Yan, D. Ye, P. Zan, K. Wang, and G. Ma, “Micro-Robot for Endoscope Based on Wireless Power Transfer,” *ICMA*, pp. 3577–3581, aug 2007.
- [74] S. H. Yeo, I.-M. Chen, R. S. Senanayake, and P. S. Wong, “Design and Development of a Planar Inchworm Robot,” *Proceedings of the 17th International Sym-*
-

- posium on Automation and Robotics in Construction and Mining (ISARC2000)*, pp. 1–6, 2000.
- [75] W. Rone and P. Ben-Tzvi, “Multi-segment continuum robot shape estimation using passive cable displacement,” *Robotic and Sensors Environments ( . . . , no. 1334227*, pp. 3–8, 2013.
- [76] A. Horschler, A. Kandhari, K. Daltorio, K. Moses, K. Andersen, H. Bunnelle, J. Kershaw, W. Tavel, H. Chiel, R. Bachmann, and R. Quinn, “Worm-Like Robotic Locomotion with a Compliant Modular Mesh,” in *Biomimetic and Bio-hybrid Systems* (S. P. Wilson, P. F. Verschure, A. Mura, and T. J. Prescott, eds.), vol. 9222 of *Lecture Notes in Computer Science*, (Barcelona), pp. 26–37, Springer International Publishing, 2015.
- [77] A. Moglia, A. Mencias, M. O. Schurr, and P. Dario, “Wireless capsule endoscopy: from diagnostic devices to multipurpose robotic systems,” *Biomedical microdevices*, vol. 9, pp. 235–43, apr 2007.
- [78] S. P. Woods and T. G. Constandinou, “Towards a micropositioning system for targeted drug delivery in wireless capsule endoscopy,” *IEEE Engineering in Medicine and Biology Society. Conference*, vol. 2011, pp. 7372–5, jan 2011.
- [79] S. Yim, E. Gultepe, D. Gracias, and M. Sitti, “Biopsy using a Magnetic Capsule Endoscope Carrying, Releasing and Retrieving Untethered Micro-Grippers,” *IEEE transactions on bio-medical engineering*, sep 2013.
- [80] M. Simi and G. Gerboni, “Magnetic torsion spring mechanism for a wireless biopsy capsule,” *ASME Journal of Medical Devices*, 2013.
- [81] P. Allen, N. Patronik, M. Zenati, and C. Riviere, “A mobile robot driven by miniature onboard motors for cardiac intervention,” in *Annual Northeast Bio-engineering Conference*, pp. 9–10, 2008.
- [82] L. Qiuhong, D. Guoqing, and Y. Detian, “The prototype of a piezoelectric medical microrobot,” *. . . and Human Science, 2002 . . .*, pp. 73–78, 2002.
- [83] B. Kim, S. Lee, J. Park, and J.-O. Park, “Design and Fabrication of a Locomotive Mechanism for Capsule-Type Endoscopes Using Shape Memory Alloys (SMAs),” *IEEE/ASME Transactions on Mechatronics*, vol. 10, pp. 77–86, feb 2005.

- 
- [84] B. Kim, M. Lee, Y. Lee, Y. Kim, and G. Lee, “An earthworm-like micro robot using shape memory alloy actuator,” *Sensors and Actuators A: ...*, vol. 125, pp. 429–437, jan 2006.
- [85] S. Bhuyan, S. K. Panda, K. Sivanand, and R. Kumar, “A compact resonance-based wireless energy transfer system for implanted electronic devices,” *ICEAS*, pp. 1–3, dec 2011.
- [86] X. Li, H. Zhang, F. Peng, Y. Li, T. Yang, B. Wang, and D. Fang, “A wireless magnetic resonance energy transfer system for micro implantable medical sensors.,” *Sensors (Basel, Switzerland)*, vol. 12, pp. 10292–308, jan 2012.
- [87] F. Hadley, “Goodbye wires!,” 2007.
- [88] W. Gruener, “Intel imagines wireless power for your laptop,” 2008.
- [89] B. Lenaerts and R. Puers, “Inductive powering of a freely moving system,” *Sensors & Actuators*, vol. 123-124, pp. 522–530, sep 2005.
- [90] T. Deyle and M. Reynolds, “Surface based wireless power transmission and bidirectional communication for autonomous robot swarms,” *2008 IEEE International Conference on Robotics and Automation*, pp. 1036–1041, may 2008.
- [91] M. Sivaprakasam, M. Humayun, and J. Weiland, “Power Supply Topologies for Biphasic Stimulation in Inductively Powered Implants,” *2005 IEEE International Symposium on Circuits and Systems*, pp. 2743–2746, 2005.
- [92] P. Li, J. C. Principe, and R. Bashirullah, “A wireless power interface for rechargeable battery operated neural recording implants.,” *Conference proceedings : ... Annual International Conference of the IEEE Engineering in Medicine and Biology Society. IEEE Engineering in Medicine and Biology Society. Conference*, vol. 1, pp. 6253–6, jan 2006.
- [93] G. Kosa, P. Jakab, F. Jolesz, and N. Hata, “Swimming capsule endoscope using static and RF magnetic field of MRI for propulsion,” in *IEEE International Conference on Robotics and Automation*, pp. 2922–2927, Ieee, may 2008.
- [94] G. Kósa, P. Jakab, G. Székely, and N. Hata, “MRI driven magnetic microswimmers.,” *Biomedical microdevices*, vol. 14, pp. 165–78, feb 2012.

- [95] S. Kottou and D. Nikolopoulos, “How Safe is the Environmental Electromagnetic Radiation?,” *J Phys Chem . . .*, vol. 4, no. 3, 2014.
- [96] F. Zhang, X. Liu, S. a. Hackworth, R. J. Sclabassi, and M. Sun, “In vitro and in vivo studies on wireless powering of medical sensors and implantable devices,” *2009 IEEE/NIH Life Science Systems and Applications Workshop*, pp. 84–87, apr 2009.
- [97] W. Xin, G. Yan, and W. Wang, “Study of a wireless power transmission system for an active capsule endoscope,” *The international journal of medical . . .*, no. December 2009, pp. 113–122, 2010.
- [98] A. S. Y. Poon, S. O’Driscoll, and T. H. Meng, “Optimal Frequency for Wireless Power Transmission Into Dispersive Tissue,” *IEEE Transactions on Antennas and Propagation*, vol. 58, pp. 1739–1750, may 2010.
- [99] F. O. R. Limiting, E. To, V. Electric, and M. Fields, “ICNIRP GUIDELINES FOR LIMITING EXPOSURE TO TIME VARYING ELECTRIC , MAGNETIC AND ELECTROMAGNETIC,” tech. rep., INTERNATIONAL COMMISSION ON NONIONIZING RADIATION PROTECTION, 1998.
- [100] A. Christ, M. G. Douglas, S. Member, J. M. Roman, E. B. Cooper, A. P. Sample, B. H. Waters, J. R. Smith, and N. Kuster, “Evaluation of Wireless Resonant Power Transfer Systems With Human Electromagnetic Exposure Limits,” *IEEE TRANSACTIONS ON ELECTROMAGNETIC COMPATIBILITY*, pp. 1–10, 2012.
- [101] K. Shiba and N. Higaki, “Analysis of SAR and Current Density in Human Tissue Surrounding an Energy Transmitting Coil for a Wireless Capsule Endoscope,” in *2009 20th International Zurich Symposium on Electromagnetic Compatibility*, pp. 321–324, Ieee, jan 2009.
- [102] C. Sage and D. O. Carpenter, “Public health implications of wireless technologies,” *Pathophysiology : the official journal of the International Society for Pathophysiology / ISP*, vol. 16, pp. 233–46, aug 2009.
- [103] a. Lahkola, T. Salminen, J. Raitanen, S. Heinävaara, M. J. Schoemaker, H. C. Christensen, M. Feychting, C. Johansen, L. Klæboe, S. Lönn, a. J. Swerdlow,

- T. Tynes, and a. Auvinen, “Meningioma and mobile phone use—a collaborative case-control study in five North European countries.,” *International journal of epidemiology*, vol. 37, pp. 1304–13, dec 2008.
- [104] P. Kan, S. E. Simonsen, J. L. Lyon, and J. R. W. Kestle, “Cellular phone use and brain tumor: a meta-analysis.,” *Journal of neuro-oncology*, vol. 86, pp. 71–8, jan 2008.
- [105] S. Sadetzki, A. Chetrit, A. Jarus-Hakak, E. Cardis, Y. Deutch, S. Duvdevani, A. Zultan, I. Novikov, L. Freedman, and M. Wolf, “Cellular phone use and risk of benign and malignant parotid gland tumors—a nationwide case-control study.,” *American journal of epidemiology*, vol. 167, pp. 457–67, feb 2008.
- [106] A. Vallbo and R. S. Johansson, “Properties of cutaneous mechanoreceptors in the human hand related to touch sensation.,” *Human neurobiology*, vol. 3, no. 1, pp. 3–14, 1984.
- [107] G. J. Gerling and G. W. Thomas, “The effect of fingertip microstructures on tactile edge perception,” *World Haptics Conference: First Joint Eurohaptics Conference and Symposium on Haptic Interfaces for Virtual Environment and Teleoperator Systems, Proceedings*, pp. 63–72, 2005.
- [108] S. Kuroki, H. Kajimoto, H. Nii, N. Kawakami, and S. Tachi, “Proposal of the stretch detection hypothesis of the meissner corpuscle,” *Lecture Notes in Computer Science (including subseries Lecture Notes in Artificial Intelligence and Lecture Notes in Bioinformatics)*, vol. 5024 LNCS, pp. 245–254, 2008.
- [109] C. Chorley, C. Melhuish, T. Pipe, and J. Rossiter, “Development of a Tactile Sensor Based on Biologically Inspired Edge Encoding,” *Design*, 2008.
- [110] C. H. Lin, T. W. Erickson, J. A. Fishel, N. Wettels, and G. E. Loeb, “Signal processing and fabrication of a biomimetic tactile sensor array with thermal, force and microvibration modalities,” *2009 IEEE International Conference on Robotics and Biomimetics, ROBIO 2009*, no. November 2016, pp. 129–134, 2009.
- [111] M. Arian and C. Blaine, “Using the BioTac as a tumor localization tool,” *IEEE Haptics Symposium*, pp. 443–448, 2014.

- [112] J. Reinecke, A. Dietrich, F. Schmidt, and M. Chalon, “Experimental comparison of slip detection strategies by tactile sensing with the BioTac® on the DLR hand arm system,” *Proceedings - IEEE International Conference on Robotics and Automation*, pp. 2742–2748, 2014.
- [113] D. Xu, G. E. Loeb, and J. A. Fishel, “Tactile identification of objects using Bayesian exploration,” *Proceedings - IEEE International Conference on Robotics and Automation*, pp. 3056–3061, 2013.
- [114] J.-P. Uldry and R. A. Russell, “Developing conductive elastomers for applications in robotic tactile sensing,” *Advanced Robotics*, vol. 6, no. 2, pp. 255–271, 1992.
- [115] M. Shimojo, A. Namiki, M. Ishikawa, R. Makino, and K. Mabuchi, “A tactile sensor sheet using pressure conductive rubber with electrical-wires stitched method,” *IEEE Sensors Journal*, vol. 4, no. 5, pp. 589–596, 2004.
- [116] K. Takei, T. Takahashi, J. C. Ho, H. Ko, A. G. Gillies, P. W. Leu, R. S. Fearing, and A. Javey, “Nanowire active-matrix circuitry for low-voltage macroscale artificial skin.,” *Nature materials*, vol. 9, no. 10, pp. 821–6, 2010.
- [117] R. S. Fearing and T. O. Binford, “Using a Cylindrical Tactile Sensor for Determining Curvature,” *IEEE Transactions on Robotics and Automation*, vol. 7, no. 6, pp. 806–817, 1991.
- [118] C.-T. Ko, S.-H. Tseng, and M. S.-C. Lu, “A CMOS Micromachined Capacitive Tactile Sensor With High-Frequency Output,” *Journal of Microelectromechanical Systems*, vol. 15, pp. 1708–1714, dec 2006.
- [119] H.-K. Lee, S.-I. Chang, and E. Yoon, “A Flexible Polymer Tactile Sensor: Fabrication and Modular Expandability for Large Area Deployment,” *Journal of Microelectromechanical Systems*, vol. 15, pp. 1681–1686, dec 2006.
- [120] M. Maggiali, G. Cannata, P. Maiolino, G. Metta, M. Randazzo, and G. Sandini, “Embedded Distributed Capacitive Tactile Sensor,” *11th Mechatronics Forum Biennial International Conference*, no. 039, pp. 1–5, 2008.
- [121] P. Maiolino, M. Maggiali, G. Cannata, G. Metta, and L. Natale, “A flexible and robust large scale capacitive tactile system for robots,” *IEEE Sensors Journal*, vol. 13, no. 10, pp. 3910–3917, 2013.

- 
- [122] K. Kuwana, A. Nakai, K. Masamune, and T. Dohi, “A grasping forceps with a triaxial MEMS tactile sensor for quantification of stresses on organs,” *Proceedings of the Annual International Conference of the IEEE Engineering in Medicine and Biology Society, EMBS*, pp. 4490–4493, 2013.
- [123] M. Sohgawa, K. Watanabe, T. Kanashima, M. Okuyama, T. Abe, H. Noma, and T. Azuma, “Texture measurement and identification of object surface by MEMS tactile sensor,” *Proceedings of IEEE Sensors*, vol. 2014-Decem, no. December, pp. 1706–1709, 2014.
- [124] A. Charalambides, J. Cheng, T. Li, and S. Bergbreiter, “3-axis all elastomer MEMS tactile sensor,” *Proceedings of the IEEE International Conference on Micro Electro Mechanical Systems (MEMS)*, vol. 2015-Febru, no. February, pp. 726–729, 2015.
- [125] S. Begej, “Fingertip-Shaped Optical Tactile Sensor for Robotics Applications,” in *IEEE International Conference on Robotics and Automation*, IEEE, 1988.
- [126] B. Ali, M. A. Ayub, and H. Yussof, “Characteristics of a New Optical Tactile Sensor for Interactive Robot Fingers,” *International Journal of Social Robotics*, vol. 4, no. SUPPL.1, pp. 85–91, 2012.
- [127] H. Xie, H. Liu, L. D. Seneviratne, and K. Althoefer, “An optical tactile array probe head for tissue palpation during minimally invasive surgery,” *IEEE Sensors Journal*, vol. 14, no. 9, pp. 3283–3291, 2014.
- [128] J. Back, P. Dasgupta, L. Seneviratne, K. Althoefer, and H. Liu, “Feasibility study- novel optical soft tactile array sensing for minimally invasive surgery,” *IEEE International Conference on Intelligent Robots and Systems*, vol. 2015-Decem, no. c, pp. 1528–1533, 2015.
- [129] T. Assaf, C. Chorley, J. Rossiter, T. Pipe, C. Stefanini, and C. Melhuish, “Real-time Processing of a Biologically Inspired Tactile Sensor for Edge Following and Shape Recognition,” *TAROS*, 2010.
- [130] C. Roke, a. Spiers, T. Pipe, and C. Melhuish, “The effects of laterotactile information on lump localization through a teletaction system,” *2013 World Haptics Conference (WHC)*, pp. 365–370, apr 2013.
-

- [131] B. Winstone, C. Melhuish, and S. Dogramadzi, “A Novel Bio-inspired Tactile Tumour Detection Concept for Capsule Endoscopy,” in *Biomimetic and Biohybrid Systems: Third International Conference, Living Machines*, pp. 442–5, 2014.
- [132] B. Winstone, G. Griffiths, C. Melhuish, and T. Pipe, “TACTIP - Tactile Fingertip Device , Challenges in reduction of size to ready for robot hand integration,” in *IEEE Robotics and Biomimetics (ROBIO)*, (Guangzhou), pp. 160–166, 2012.
- [133] A. L. Trejos, J. Jayender, M. Perri, M. Naish, R. Patel, and R. Malthaner, “Robot-assisted Tactile Sensing for Minimally Invasive Tumor Localization,” *The International Journal of Robotics Research*, vol. 28, no. 9, pp. 1118–1133, 2009.
- [134] S. Schostek, C.-N. Ho, D. Kalanovic, and M. O. Schurr, “Artificial tactile sensing in minimally invasive surgery - a new technical approach.,” *Minimally invasive therapy & allied technologies : MITAT : official journal of the Society for Minimally Invasive Therapy*, vol. 15, pp. 296–304, jan 2006.
- [135] J. C. Gwilliam, Z. Pezzementi, E. Jantho, A. M. Okamura, and S. Hsiao, “Human vs. robotic tactile sensing: Detecting lumps in soft tissue,” *2010 IEEE Haptics Symposium*, pp. 21–28, mar 2010.
- [136] A. P. Sarvazyan, “Computerized palpation is more sensitive than human finger.,” in *Proceedings of the 12th International Symposium on Biomedical Measurements and Instrumentation.*, pp. 523–24, 1998.
- [137] S. Dogramadzi, G. S. Virk, G. D. Bell, R. S. Rowland, and J. Hancock, “Recording forces exerted on the bowel wall during colonoscopy: in vitro evaluation.,” *The international journal of medical robotics + computer assisted surgery : MRCAS*, vol. 1, pp. 89–97, dec 2005.
- [138] K. Rebello, “Applications of MEMS in Surgery,” *Proceedings of the IEEE*, vol. 92, pp. 43–55, jan 2004.
- [139] M. E. Rentschier, J. Dumpert, S. R. Platt, D. Oleynikov, S. M. Farritor, and K. Iagnemma, “Mobile in vivo biopsy robot,” *Proceedings - IEEE International Conference on Robotics and Automation*, vol. 2006, no. May, pp. 4155–4160, 2006.

- 
- [140] S. Park, H. Park, and B. Kim, “A paddling based locomotive mechanism for capsule endoscopes,” *Journal of mechanical science and technology (KSME Int. J.)*, vol. 20, no. 7, pp. 1012–1018, 2006.
- [141] J. Konstantinova, A. Jiang, K. Althoefer, P. Dasgupta, and T. Nanayakkara, “Implementation of tactile sensing for palpation in robot-assisted minimally invasive surgery: A review,” *IEEE Sensors Journal*, vol. 14, no. 8, pp. 2490–2501, 2014.
- [142] J. Dargahi and S. Najarian, “Human tactile perception as a standard for artificial tactile sensing - a review,” *International Journal of Medical Robotics and Computer Assisted Surgery*, vol. 01, no. 01, p. 23, 2004.
- [143] A. P. Åstrand, V. Jalkanen, B. M. Andersson, and O. A. Lindahl, “Detection of Stiff Nodules Embedded in Soft Tissue Phantoms , Mimicking Cancer Tumours , Using a Tactile Resonance Sensor,” *Journal of Biomedical Science and Engineering*, no. March, pp. 181–193, 2014.
- [144] M. Nyberg, V. Jalkanen, K. Ramsler, B. Ljungberg, a. Bergh, and O. a. Lindahl, “Dual-modality probe intended for prostate cancer detection combining Raman spectroscopy and tactile resonance technology—discrimination of normal human prostate tissues ex vivo,” *J Med Eng Technol*, vol. 39, no. 3, pp. 198–207, 2015.
- [145] C. Chuang, Yung-Kang, T. Li, I. Chou, and Y. Teng, “Piezoelectric tactile sensor for submucosal tumor hardness detection in endoscopy,” in *Solid-State Sensors, Actuators and Microsystems (TRANSDUCERS), 2015 Transducers - 2015 18th International Conference on*, pp. 871–875, IEEE, 2015.
- [146] A. Talasaz and R. V. Patel, “Integration of force reflection with tactile sensing for minimally invasive robotics-assisted tumor localization,” *IEEE Transactions on Haptics*, vol. 6, no. 2, pp. 217–228, 2013.
- [147] Y. Tanaka, M. Fujiware, and A. Sano, “Lump detection with tactile sensing system including haptic bidirectionality,” in *World Automation Congress (WAC), 2014*, pp. 1–6, 2014.
- [148] G. Ciuti, R. Calì, D. Camboni, L. Neri, F. Bianchi, A. Arezzo, A. Koulaouzidis, S. Schostek, D. Stoyanov, C. M. Oddo, B. Magnani, A. Menciassi, M. Morino,
-

- M. O. Schurr, and P. Dario, “Frontiers of robotic endoscopic capsules: a review,” *Journal of Micro-Bio Robotics*, 2016.
- [149] R. Klatzky and S. Lederman, “Hand Movements: A Window into Haptic Object Recognition,” *Cognitive psychology*, vol. 19, no. 3, pp. 342–368, 1987.
- [150] B. Winstone, “Biomimetic Tactile Sensing Capsule,” in *Living Machines*, (Barcelona), pp. 113–122, Springer, 2015.
- [151] T. Muto, H. J. Bussey, and B. C. Morson, “The evolution of cancer of the colon and rectum.,” *Cancer*, vol. 36, no. 6, pp. 2251–70, 1975.
- [152] R. M. Summers, “Polyp size measurement at CT colonography: what do we know and what do we need to know?,” *Radiology*, vol. 255, no. 3, pp. 707–20, 2010.
- [153] P. Dario, “Tactile sensing: Technology and applications,” *Sensors and Actuators: A. Physical*, vol. 26, no. 1-3, pp. 251–256, 1991.
- [154] K. Hoyt, B. Castaneda, M. Zhang, P. Nigwekar, P. A. di Sant’Agnese, J. V. Joseph, J. Strang, D. J. Rubens, and K. J. Parker, “Tissue elasticity properties as biomarkers for prostate cancer,” *Cancer biomarkers : section A of Disease markers*, vol. 4, no. 4-5, pp. 213–225, 2008.
- [155] S. Phipps, T. H. J. Yang, F. K. Habib, R. L. Reuben, and S. a. McNeill, “Measurement of tissue mechanical characteristics to distinguish between benign and malignant prostatic disease.,” *Urology*, vol. 66, pp. 447–50, aug 2005.
- [156] C. Chorley, C. Melhuish, T. Pipe, and J. Rossiter, “Tactile Edge Detection,” *Sensors (Peterborough, NH)*, pp. 2593–2598, 2010.
- [157] N. F. Lepora, U. Martinez-Hernandez, M. Evans, L. Natale, G. Metta, and T. J. Prescott, “Tactile Superresolution and Biomimetic Hyperacuity,” *IEEE Transactions on Robotics*, vol. 31, no. 3, pp. 605–618, 2015.
- [158] N. F. Lepora and B. Ward-Cherrier, “Superresolution with an optical tactile sensor,” *IEEE International Conference on Intelligent Robots and Systems*, vol. 2015-Decem, pp. 2686–2691, 2015.

- 
- [159] B. Winstone, C. Melhuish, T. Pipe, M. Callaway, and S. Dograma, “Towards Bio-inspired Tactile Sensing Capsule Endoscopy for Detection of Submucosal Tumours,” *IEEE Sensors Journal*, vol. 17, no. 3, pp. 848–857, 2017.
- [160] S.-H. Kim, J. Engel, C. Liu, and D. L. Jones, “Texture classification using a polymer-based MEMS tactile sensor,” *Journal of Micromechanics and Microengineering*, vol. 15, no. 5, pp. 912–920, 2005.
- [161] J. C. Sullivan, B. Mitchinson, M. J. Pearson, M. Evans, N. F. Lepora, C. W. Fox, C. Melhuish, and T. J. Prescott, “Tactile discrimination using active whisker sensors,” *IEEE Sensors Journal*, vol. 12, no. 2, pp. 350–362, 2012.
- [162] A. Drimus, G. Kootstra, A. Bilberg, and D. Kragic, “Design of a flexible tactile sensor for classification of rigid and deformable objects,” *Robotics and Autonomous Systems*, vol. 62, no. 1, pp. 3–15, 2014.
- [163] Z. Su, K. Hausman, Y. Chebotar, A. Molchanov, G. Loeb, G. S. Sukhatme, and S. Schaal, “Force Estimation and Slip Detection for Grip Control using a Biomimetic Tactile Sensor,” *IEEE-RAS International Conference on Humanoid Robotics (Humanoids)*, pp. 297–303, 2015.
- [164] T. Bhattacharjee, J. M. Rehg, and C. C. Kemp, “Haptic classification and recognition of objects using a tactile sensing forearm,” *IEEE International Conference on Intelligent Robots and Systems*, pp. 4090–4097, 2012.
- [165] X. S. Jia and E. H. Adelson, “Lump Detection with a GelSight Sensor,” in *World Haptics Conference (WHC), 2013*, no. c, (Daejeon), pp. 175–179, IEEE, 2013.
- [166] J. C. T. Hui and K. J. Kuchenbecker, “Evaluating the BioTac’s Ability to Detect and Characterize Lumps in Simulated Tissue,” in *Haptics: Neuroscience, Devices, Modeling, and Applications: 9th International Conference, EuroHaptics 2014, Versailles, France, June 24-26, 2014, Proceedings, Part II* (M. Auvray and C. Duriez, eds.), vol. 8619, pp. 295–302, Berlin, Heidelberg: Springer Berlin Heidelberg, 2014.
- [167] J. C. T. Hui, A. E. Block, C. J. Taylor, and K. J. Kuchenbecker, “Robust tactile perception of artificial tumors using pairwise comparisons of sensor array

- readings,” *IEEE Haptics Symposium, HAPTICS*, vol. 2016-April, pp. 305–312, 2016.
- [168] S. Mckinley, A. Garg, S. Sen, D. V. Gealy, J. P. Mckinley, Y. Jen, and K. Goldberg, “Autonomous Multilateral Surgical Tumor Resection with Interchangeable Instrument Mounts and Fluid Injection Device,” tech. rep., University of California, Berkeley, 2015.
- [169] M. Kamba, Y. Seta, A. Kusai, M. Ikeda, and K. Nishimura, “A unique dosage form to evaluate the mechanical destructive force in the gastrointestinal tract,” *International Journal of Pharmaceutics*, vol. 208, no. 1-2, pp. 61–70, 2000.
- [170] J. WorsØe, L. Fynne, T. Gregersen, V. Schlageter, L. a. Christensen, J. F. Dahlerup, N. J. Rijkhoff, S. Laurberg, and K. Krogh, “Gastric transit and small intestinal transit time and motility assessed by a magnet tracking system,” *BMC Gastroenterology*, vol. 11, no. 1, p. 145, 2011.
- [171] E. Byvatov, U. Fechner, J. Sadowski, and G. Schneider, “Comparison of Support Vector Machine and Artificial Neural Network Systems for Drug/Nondrug Classification,” *Journal of Chemical Information and Modeling*, vol. 43, no. 6, pp. 1882–1889, 2003.
- [172] R. Burbidge, M. Trotter, B. Buxton, and S. Holden, “Drug design by machine learning: support vector machines for pharmaceutical data analysis,” *Computers & Chemistry*, vol. 26, no. 1, pp. 5–14, 2001.
- [173] M.-C. Lee and C. To, “Comparison of Support Vector Machine and Back Propagation Neural Network in Evaluating the Enterprise Financial Distress,” *International Journal of Artificial Intelligence & Applications*, vol. 1, no. 3, pp. 31–43, 2010.
- [174] Y. Shao and R. S. Lunetta, “Comparison of support vector machine, neural network, and CART algorithms for the land-cover classification using limited training data points,” *ISPRS Journal of Photogrammetry and Remote Sensing*, vol. 70, pp. 78–87, 2012.
- [175] C. Zierhofer and E. Hochmair, “Geometric approach for coupling enhancement

- of magnetically coupled coils,” *Biomedical Engineering, IEEE . . .*, vol. 43, no. 7, pp. 708–714, 1996.
- [176] B. H. Waters, B. J. Mahoney, G. Lee, and J. R. Smith, “Optimal coil size ratios for wireless power transfer applications,” *2014 IEEE International Symposium on Circuits and Systems (ISCAS)*, vol. 1, pp. 2045–2048, jun 2014.
- [177] T. Sowlati, S. Member, C. A. T. Salama, J. Sitch, G. Rabjohn, and D. Smith, “Low Voltage , High Efficiency GaAs Class E Power Amplifiers for Wireless Transmitters,” *IEEE Journal of Solid-state Circuits*, vol. 30, no. 10, pp. 1074–1080, 1995.
- [178] G. Lee, C. Thompson, T. Hwang, R. A. Chinga, and J. Lin, “A 63W 14MHz Class-E amplifier for wireless power transmission,” *2012 Asia Pacific Microwave Conference Proceedings*, pp. 469–471, dec 2012.
- [179] A. N. Laskovski and M. R. Yuce, “Class-E oscillators as wireless power transmitters for biomedical implants,” *2010 3rd International Symposium on Applied Sciences in Biomedical and Communication Technologies (ISABEL 2010)*, pp. 1–5, nov 2010.
- [180] M. K. Kazimierczuk, *RF Power Amplifiers*. Wiley-Blackwell, 2008.
- [181] J. Garnica, J. Casanova, and J. Lin, “TWPT4-2 High Efficiency Midrange Wireless Power Transfer System,” in *IEEE MTT-S International*, no. 5, pp. 73–76, 2011.
- [182] T. Mohamadi, “Modeling and Deesigning Wireless Energy Transfer Circuit in High Voltage Based on Magnetic Coupling,” in *International Conference on Electrical Engineering and Informatics*, 2011.
- [183] Z. N. Low, S. Member, R. A. Chinga, R. Tseng, J. Lin, and S. Member, “Design and Test of a High-Power High-Efficiency Loosely Coupled Planar Wireless Power Transfer System,” *Transactions on Industrial Electronics*, vol. 56, no. 5, pp. 1801–1812, 2009.
- [184] P. Sharma and S. Guha, “Transmission of time varying magnetic field through body tissue,” *Journal of Biological Physics*, vol. 3, no. 2, pp. 95–102, 1975.

- [185] A. P. Sample, S. Member, D. T. Meyer, and J. R. Smith, “Analysis , Experimental Results , and Range Adaptation of Magnetically Coupled Resonators for Wireless Power Transfer,” *IEEE Transactions on Industrial Electronics*, vol. 58, no. 2, pp. 544–554, 2011.
- [186] B. Cannon, H. J, and D. Stancil, “Magnetic Resonant Coupling As a Potential Means for Wireless Power Transfer to Multiple Small Receivers,” *IEEE TRANSACTIONS ON POWER ELECTRONICS*, vol. 24, no. 7, pp. 1819–1825, 2009.
- [187] A. Kurs, A. Karalis, R. Moffatt, J. D. Joannopoulos, P. Fisher, and M. Soljacic, “Wireless power transfer via strongly coupled magnetic resonances.,” *Science (New York, N.Y.)*, vol. 317, pp. 83–6, jul 2007.
- [188] S. Bhattacharya and Y. K. Tan, “Design of static wireless charging coils for integration into electric vehicle,” *2012 IEEE Third International Conference on Sustainable Energy Technologies (ICSET)*, pp. 146–151, sep 2012.
- [189] H. Hirayama, Y. Okuyama, N. Kikuma, and K. Sakakibara, “Equivalent circuit of induction fed magnetic resonant WPT system,” in *2011 IEEE MTT-S International Microwave Workshop Series on Innovative Wireless Power Transmission: Technologies, Systems, and Applications*, pp. 239–242, Ieee, may 2011.
- [190] W. Chen, R. Chinga, and S. Yoshida, “A 25.6 W 13.56 MHz wireless power transfer system with a 94% efficiency GaN Class-E power amplifier,” ... *Digest (MTT), 2012 ...*, pp. 25–27, 2012.
- [191] J. Pannier, D. Hendrickx, and T. Nobels, “WIRELESS POWER TRANSFER FOR INDUSTRIAL APPLICATIONS THROUGH STRONGLY COUPLED MAGNETIC RESONANCES.”
- [192] K. Y. Kim, *WIRELESS POWER TRANSFER PRINCIPLES AND ENGINEERING EXPLORATIONS Edited by Ki Young Kim*. intechweb.org, 2012.
- [193] H. Nagoaka, “The inductance coefficients of solenoids,” *Journal of the college of science, Imperial University, Tokyo, Japan.*, vol. 27, no. 6, pp. 1–33, 1909.
- [194] E. B. Rosa and F. W. Grover, “Formulas and tables for the calculation of mutual and self-inductance.,” *US Government Printing Office*, 1916.